Switching and imaging of magnetic structures in iron oxides



Jiahao Chen

Linacre College

University of Oxford

A thesis submitted for the degree of

Doctor of Philosophy

Michaelmas 2022

This thesis is dedicated to
my parents
for giving me the opportunity to adventure

Acknowledgements

I can still remember the excitement and ambition when I received the offer from Oxford nearly five years ago as a naive young master's graduate expectantly packaging for a mysterious trip to a new country. And it turned out to be a rather nontrivial trip indeed. On the journey of pursuing the DPhil, I am finally awarded the opportunity to acknowledge the lovely people who influence me so much during this memorable period.

First, I would like to show my highest respect and gratitude to my supervisor Paolo Radaelli, who gave me a chance to initialise this extraordinary journey. His wisdom and intuition of science have always been the beacon to lead me in the voyage of searching for the truth. He is always sharp at finding the problem and giving the best solution at some intense moments during the experiments, acting more like a captain to guide the sailors for directions. Paolo is a true educator for mentoring his students to discover what excites and motivates one's inner heart, from the point of science attitude to an enormous scope of life philosophy. Whenever there are puzzles from experimental results or difficulties in promoting projects, he is always willing to listen and lend his hand as much as possible, but exceeding the duty is never his style. He is a responsible supervisor who focuses on cultivating independent research ability, which is essential for a DPhil student stepping into a young researcher. Furthermore, when unexpected turbulence sweeps on my career, his strong sense of responsibility and morality played a pivotal role in the mainstay so that I could successfully finish the course under colossal pressure. The thank and gratitude for his support are beyond any words I can express.

Then I would like to thank Dr Hariom Jani and Mr Jheng-Cyuan Lin, the best friends and colleagues I have ever met. Hariom is passionate and curious about an extensive range of scientific topics, and his encouragement has been significant to me during the last few years of the DPhil. He is playing the role of mentor and a senior member within our group, although he has not officially joined Oxford until this thesis has been done. Jheng-Cyuan is always wise in finding the right way for problem shooting and is accommodating in many beamtime experiments; sometimes, he is an expert acting like a beamline scientist. Although he is very experienced in physics, he joined the group later than me; he taught me many experiment skills and enhanced the understanding of my projects. Hariom and

Jheng-Cyuan are reliable partners for their remarkable work. We enjoy the period of intensive collaboration on the hematite project, and the payment of the publishing results is the best witness of our teamwork.

I also would like to thank Prof. Andrew Boothroyd, who is always encouraging to the attendance at the afternoon tea break; Dr Dharmalingam Prabhakran, who is so kind to help with techniques and provides high-quality samples; Prof. Stephen Blundell, who is erudite and talented in physics and music, Prof. Thorsten Hesjedal who is always cheering up and Prof. Amalia Coldea, she is very active in organising academic activities across the department. I want to acknowledge Dr Jieyi Liu, Dr Viviane Pecanha Antonio, Dr Rebecca Scatena, Dr Anuradha Vibhakar, Dr Laura Schade, Dr Jian Rui Soh, Dr Noah Winterfield Price, Dr Francis Chmiel, Dr Shilei Zhang, Dr Zhiping Wang, Dr Ding Pei, Dr Yiwei Li, Dr Junjie Liu, Mr Jack Harrison, for providing gracious help and happiness within the department and the surrounding pubs. Although it is a bit lagging, I still would like to congratulate my colleagues Anu and Laura for successfully obtaining the degree. And I also send my best wishes to Jack to have a thriving PhD in due course.

I also would like to thank my friends gathered by luck: Josh Wang, Mengxi Wang, Rui Gao, Yangsiyu Lu, Shaoling Zhong, Dinglan Tang, Woody Wu, Ivan wang, Pengjin Wang, Mengjue Wang, Ri Cao, Xudong Tao and so on. You have been an indispensable part of my life in Oxford, full of joy and fun. I will never forget the many beautiful places of the UK countryside together with Josh, Mengxi, Rui, Yangsiyu, Shaoling, Dinglan and Pengjin; the trips are always relaxing and enlightening. Thank you all for being good companions during the expeditions.

I want to thank my friends and colleagues in China who provide selfless support during the problematic pandemic. I want to give special thanks to Prof. Jiayu Dai and Prof. Wenxin Tang, who supported me when I returned to China in 2020. A large part of the work in the last chapter has been done on the computing clusters provided by Prof. Dai and Prof. Tang. The living costs were covered when I continued my study in Chongqing and Changsha so I could focus on the work without concern. And I also like to thank the team members in the Warm Dense Matter group: Prof. Zengxiu Zhao, Prof. Dongdong Kang, Dr Kaiguo Chen, Dr Xiaoxiang Yu, Dr Bo Chen, Dr Qunchao Tong, Dr Fangyu Guo; PhD candidate Mr Jianpeng Liu, Mr Jinsen Han, Mr Li Wang, Mr Haizhong Wu, Mr Fan Xiao; as well as SPLEEM group: Prof. Yihua Wang, Dr Lei Yu, Dr Xiaodong Yang, Mr Aosen Xiong.

I want to acknowledge the institutions that support me in realising this dream. I acknowledge China Scholarship Council (CSC) for the full scholarship grant, Linacre College for generously supporting the college facilities and last year's writing-up bursary, CMP department for providing experimental facilities and office, and the central University, who help to protect my student right and interest from political pressures.

Last but not least, I would like to thank my parents, who consistently support me in spirit and life. And my beloved Ms Han Yang, who stepped into my life at the final stage of DPhil but witnessed so many anecdotes like an old friend, thank you for the consistent love and support. It is a great pity to leave Oxford so early without a formal farewell to my loved ones, streets, buildings and glorious memories. If chances are allowed, I wish I could return to Oxford with my family to recall the days of matriculation and compensate for the regrets of the absence of the degree ceremony.

Abstract

Spintronics is a multidisciplinary science aiming to develop the next-generation electronic device at the age when Moore's Law has met its limit. Magnetic oxides, as a traditional material widely applied in CMOS and memory devices, have attracted tremendous attention in spintronics because of many important compounds such as multiferroics and antiferromagnets; both are dominant platforms for studying strong correlation physics. In this thesis, I look at a new type of multiferroic single crystal $Ba_{0.5}Sr_{1.5}Mg_2Fe_{12}O_{22}$ and a time-honoured antiferromagnet α-Fe_2O_3 thin film. I investigate the magnetic domains and the coupling between different magnetic orders for multiferroic candidates. As for the antiferromagnets, I developed a state-of-art imaging technique for probing antiferromagnetic domains, and a series of topological structures were discovered to profit from this technique.

I study the fundamental multiferroic properties of a novel Y-type hexaferrite $Ba_{0.5}Sr_{1.5}Mg_2Fe_{12}O_{22}$ by utilising soft X-ray resonant magnetic diffraction and transport techniques. The investigation focuses on the coupling between magnetic, ferroelectric, and structural order, especially on domains. The puzzling physical properties arising from switching the multiferroic domains are elucidated from the perspective of the magnetic structure. The multiferroic phase accompanies an incommensurate phase while switching the polarised magnetic domains. Furthermore, the imaging of the multiferroic phase is performed on the two-fold fan structure by utilising the X-ray magnetic circular dichroism effect. The manipulation of the magnetic domain is tried by static electric voltage and THz electric pulses; the experiment results show that the multiferroicity in Y-type hexaferrite can be switched in domain scale by an external electric field, even likely at a transient time scale of picoseconds. The result provides promising evidence for applying type-II multiferroics for ultrafast spintronic materials.

I also study the domains and topological structures in α-Fe_2O_3, a room-temperature antiferromagnet, by developing an advanced imaging technique based on an X-ray photoemission electron microscope (X-PEEM). Using the XMLD-PEEM method based on XAS spectroscopy for antiferromagnetism, a family of exotic topological structures are identified at room temperatures, such as meron, anti-meron and bimeron structures. This technique highlights that the in-plane Neel vectors can be mapped for the in-plane domains at room temperature above the Morin transition

and the in-plane domain walls at low temperatures below the Morin transition. The intermediate nucleation process from OOP to the IP phase can also be depicted by constructing such a vector map.

Not confined to the experiment, more in-depth studies are taken on high-performance computing clusters, where many simulations on the dynamical behaviour of the topological structures found in experiments are performed by the atomic micromagnetic tool called VAMPIRE. The complex superexchange interactions in α-Fe_2O_3 are constructed with atomistic resolution. The Landau-Lifshitz-Gilbert dynamics reveal the generation and annihilation of the topological meron and bimeron structures. Furthermore, the spin wave emission by non-trivial topological structure is also demonstrated in an ultrafast time scale that the experiment cannot observed so far.

Publication list

- Chmiel, Francis P., D. Prabhakaran, Paul Steadman, **Jiahao Chen**, Raymond Fan, Roger D. Johnson, and Paolo G. Radaelli. "Magnetoelectric domains and their switching mechanism in a Y-type hexaferrite." Physical Review B 100, no. 10 (2019): 104411.

- Jani, Hariom, Jheng-Cyuan Lin, **Jiahao Chen**, Jack Harrison, Francesco Maccherozzi, Jonathon Schad, Saurav Prakash et al. "Antiferromagnetic half-skyrmions and bimerons at room temperature." Nature 590, no. 7844 (2021): 74-79.

∗ **Jiahao Chen**, Francis P. Chmiel, Jieyi Liu, Dharmalingam Prabhakaran, and Paolo G. Radaelli. "Switching of ferrotoroidal domain via the intermediate state in a multiferroic Y-type hexaferrite." *Ready to submit*

∗ **Jiahao Chen**, Jani, Hariom, Jheng-Cyuan Lin,Xiansi Wang, Jiayu Dai, and Paolo G. Radaelli. "Spin wave generation from antiferromagnetic topological textures." *In preparation*

Contents

List of Figures **xvii**

List of Tables **xxi**

List of Abbreviations **xxiii**

1 Introduction **1**

1.1 Multiferroics 2

1.1.1 Classification of multiferroics 5

1.1.2 Coupling mechanism 7

1.2 Antiferromagnetism and its excitation 10

1.2.1 Types of antiferromagntism 11

1.2.2 Antiferromagnetic spin wave excitation 12

1.3 Magnetic topology 16

1.3.1 Topological textures in magnetic materials 16

1.3.2 Domains and domain walls 18

1.4 Thesis outline 20

2 Experiment methods **21**

2.1 Introduction 21

2.2 Theory backgrounds of magnetic phenomena 22

2.2.1 Basis of magnetic diffraction 22

2.2.2 Basis of magnetic absorption 31

2.3 Experiment instruments 37

2.3.1 X-ray tube 37

2.3.2 Synchrotron facility 38

2.4 Micromagnetic simulation 40

2.4.1 Introduction of atomistic micromagnetics 41

2.5 Conclusion 45

3 Switching of multiferroic Y-type hexaferrite 47
3.1 Introduction . . . 48
3.1.1 Structures of Y-type hexaferrite . . . 48
3.1.2 Block model for magnetic structure . . . 50
3.1.3 Magnetic phase diagram . . . 51
3.2 Electric control of the multiferroic phase . . . 55
3.2.1 Ferroelectricity switched by the electric field . . . 55
3.2.2 Ferroelectricity switched by the magnetic field . . . 57
3.2.3 Ferroelectric polarity switched by the electric field . . . 60
3.3 Identification of the intermediate phase . . . 63
3.3.1 Transport evidence . . . 64
3.3.2 X-ray diffraction evidence . . . 65
3.3.3 Intermediate phase diagram . . . 68
3.4 Models of phase switching . . . 69
3.4.1 Cone rotation model . . . 70
3.4.2 Rotation model with phase coexistence . . . 77
3.5 Conclusions . . . 83

4 Magnetic domain imaging and ultrafast switching 85
4.1 Introduction . . . 85
4.2 Domain size controlled by electric bias fields . . . 86
4.2.1 XMCD imaging on magnetic domain . . . 86
4.2.2 Electric field control of the single domain . . . 89
4.3 Domain switching by THz pulse train . . . 91
4.3.1 Development of the experiment setup . . . 91
4.3.2 Results and discussion . . . 96
4.4 Conclusion . . . 98

5 Imaging of antiferromagnetic structures in hematite 99
5.1 Introduction–Magnetic structure of hematite . . . 100
5.2 Anisotropic XMLD effect in hematite . . . 102
5.2.1 Angular dependence of XMLD for In-Plane order . . . 102
5.2.2 Angular dependence of XMLD for Out-Of-Plane order . . . 105
5.2.3 Images constructed by anisotropic XMLD effect . . . 107
5.3 Results and discussion . . . 112
5.3.1 Domain wall analysis . . . 112
5.3.2 Intermediate state at Morin transition . . . 113
5.3.3 AFM topological structures . . . 114

6 Spin wave dynamics in AFM topological structures 119
6.1 The hematite model for micromagnetics 120
6.2 Spin dynamics in bimeron annihilation 130
6.2.1 Trivial bimeron annihilation 130
6.2.2 Non-trivial bimeron annihilation 131
6.3 Analysis of annihilation 135
6.3.1 Spin wave spectrum 135
6.3.2 Dispersion model 139
6.3.3 Topological charge transition 143
6.4 Conclusion 145

7 Conclusion and outlook 147

Appendices

A Theory of magnetic diffraction 153

B Calculation of topological number in lattice spin field 157

References 161

List of Figures

1.1 Schematic diagram showing the symmetries and degrees of freedom of correlated electrons 3
1.2 Schematic diagram of CoFe/BFO heterostructure and their domain images 6
1.3 Competing exchange interaction results different magnetic order. . . 9
1.4 Illustration of the inverse Dzyaloshinskii-Moriya interaction. 10
1.5 Schematic comparison of different types of antiferromagnetic ordering. 12
1.6 Semiclassical depiction of spin wave excitation. 14
1.7 Demonstrations of Néel type and Bloch type skyrmion structure. . . 17
1.8 Different types of domain walls. 19

2.1 Scattering geometry diagram. 27
2.2 The diagram of scattering process. 29
2.3 XMCD effect in L edge X-ray absorption for Fe. 34
2.4 XMLD effect in L-edge X-ray absorption for NiO. 35
2.5 X-ray absorption spectra and application for imaging. 36
2.6 The lab-based X-ray diffractometer from Smartlab Rigarku. 38
2.7 Synchrotron facility and accelerator based X-ray radiation. 39

3.1 Schematics of the crystal structure and magnetic structure of Y-type hexaferrite $Ba_2Mg_2Fe_{12}O_{22}$. 51
3.2 Crystalline characterisation of Y-type hexaferrite $Ba_2Mg_2Fe_{12}O_{22}$ by X-ray diffractometer. 52
3.3 Magnetometry and magnetic phase transition of $Ba_{0.5}Sr_{1.5}Mg_2Fe_{12}O_{22}$. 53
3.4 Magnetometry on the two fan transversal phase. 54
3.5 Experimental demonstration of ferroelectricity in multiferroic BSMFO. 56
3.6 The ferroelectric polarisation measured by magnetocurrent scheme. 58
3.7 Magnetic switching of electrical polarisation at low temperatures. . 59
3.8 TFTC structure is depicted in magnetic reciprocal space. 61
3.9 Magneto-current measurements on the electrical polarisation at 10 K under different bias field combinations. 63
3.10 Temperature dependence of the switching. 65

3.11 The signature of phase coexistence during the switching of the TFTC phase. 67
3.12 Phase diagram of the switching dynamics. 68
3.13 Illustration of TFTC magnetic components. 71
3.14 The rotational model for TFTC structure switching. 75
3.15 The modified model for TFTC structure rotation. 76
3.16 Experiment results of the linear polarisation diffration. 78
3.17 Magnetometry and coexisted model fitting. 79
3.18 Linear polarisation diffraction channels at Γ point and Z point. . . 82

4.1 Fe L-edge spectrum from BSMFO. 86
4.2 Circular dichroism on helical phase BSMFO. 87
4.3 The magnetic characterisation for TFTC phase. 88
4.4 The procedures of the domain manipulation on multiferroic TFTC structure. 89
4.5 THz generation from LNO. 92
4.6 THz free space TDS characterisation. 93
4.7 THz free space TDS spectra. 94
4.8 THz pump-Xray probe experimental setup 95
4.9 THz pulse switching on the magnetic domains. 97

5.1 Magnetic structure of α-Fe_2O_3. 101
5.2 XMLD imaging for the IP phase. 104
5.3 XMLD imaging for OOP phase. 106
5.4 Construction of α-Fe_2O_3 vector map. 108
5.5 Construction of OOP image. 111
5.6 Illustration of anti-phase domain wall. 112
5.7 Illustration of IP and OOP coexisted domain at Morin temperature. 114
5.8 Topological properties of the IP AFM textures at $T>T_M$. 116

6.1 Superexchange bondings in corundum structure α-Fe_2O_3. 121
6.2 Néel order simulation by LLG-heun method. 123
6.3 Anisotropy parameter changes with temperature. 125
6.4 Simulation of Morin transition in cooling process. 127
6.5 Simulation of Morin transition in warming process. 128
6.6 Illustration of the plotting layers of atoms within the crystalline structure. 129
6.7 The dynamical process of $Q = 0$ bimeron structure annihilation. . . 130
6.8 The modelling of Néel phase transition. 132
6.9 Illustration of non-trivial bimeron annihilation. 133

6.10 The spectrum of the spin wave. 135
6.11 Real and reciprocal space analysis of spin waves. 136
6.12 2D FFT on annihilated spin wave. 138
6.13 The magnon dispersion in antiferromagnetic hematite. 141
6.14 Topological charge analysis in time and real space. 144

B.1 A simplified model for 2D spin lattice in plaquette geometry 158

List of Tables

1.1 Spatial-inversion and time-reversal symmetry in ferroics 4

3.1 Different types of hexaferrite. 49
3.2 Parameters for the TFTC fraction function $\delta(H,T)$. 80
3.3 Temperature-dependent switching velocity for SQUID switching model. 81

6.1 Parametrising exchange interactions by nearest neighbouring ion pairs for corundum structure. 122

List of Abbreviations

ME . . . . . Magneto-electric

AFM . . . . . Antiferromagnetism

FM . . . . . Ferromagnetism

PEEM . . . . . Photoemission electron microscope

DMI . . . . . Dzyaloshinskii-Moriya interaction

i-DMI . . . . . inverse Dzyaloshinskii-Moriya interaction

BSMFO . . . . $Ba_{0.5}Sr_{1.5}Mg_2Fe_{12}O_{22}$

XMCD . . . . X-ray magnetic circular dichroism

XMLD . . . . X-ray magnetic linear dichroism

X-PEEM . . . X-ray photoemission electron microscope

SQUID . . . . Superconducting quantum interference device

VSM . . . . . vibrating sample measurement

XPS . . . . . X-ray photoelectron spectroscopy

XAS . . . . . X-ray absorption spectroscopy

OPA . . . . . Optical parametric amplifier

OR . . . . . Optical rectification

DFG . . . . . Difference frequency generation

LLG . . . . . Landau-Lifshitz-Gilbert

DFT . . . . . Density functional theory

LC . . . . . Longitudinal cone

TFTC . . . . . Two fan transversal cone structure

ZFC . . . . . Zero field cooling

FC . . . . . Field cooling

1 Introduction

Contents

1.1 Multiferroics 2
1.1.1 Classification of multiferroics 5
1.1.2 Coupling mechanism 7
1.2 Antiferromagnetism and its excitation 10
1.2.1 Types of antiferromagntism 11
1.2.2 Antiferromagnetic spin wave excitation 12
1.3 Magnetic topology 16
1.3.1 Topological textures in magnetic materials 16
1.3.2 Domains and domain walls 18
1.4 Thesis outline 20

As the largest field of physics, condensed matter physics (CMP) focuses on symmetry-breaking phenomena in a system's condensed phases, including an almost limitless range of problems such as superconductivity, superfluidity and magnetism, to name three examples of many [1–3]. The search for relevant and measurable order parameters in a system was the overarching theme for CMP in the 1960s and 1970s until the emergence of the quantum hall effect in 1980 by Klitzing, Dorda and Pepper [4]. Then a series of important discoveries associated with the quantum hall effect, such as fractional quantum hall effect, quantum anomalous hall effect (QAHE), and quantum spin hall effect (QSHE) [5, 6] burst in the following decades, revolutionising the traditional concept of order parameters with topological order. Another parallel

realm (from the trace of development) in CMP is the strongly correlated electron system, which can be traced back to the study of the Mott insulator and high-temperature superconductivity. Although the mechanism of superconductivity remains elusive, the non-trivial collective behaviours of electrons have fostered an appreciation for a variety of emergent phenomena, such as topological insulators, which is a 3D bulk system that QSHE effect pertains distinct from two-dimensional electron gases (2DEGs). Similar breakthroughs in traditional magnetism witness the surging of study on emergent excitations such as magnons, monopoles and skyrmions.

A novel terminology named Quantum Materials was invented to refer to the systems with exotic emergent properties resulting from the behaviours of collective electrons, which is a brand new perspective on the well-known phenomena associated with strong correlated electron systems. In the shield of the generic concept of quantum materials, we aim to uncover the emergent phenomena in quantum magnetism throughout the thesis, including many novel topics such as multiferroics, topological spin structures, antiferromagnetic excitations *et al.*

1.1 Multiferroics

The interplay among the electronic degrees of freedom produces various forms of symmetry-breaking, such as inversion (I), time-reversal (T) and gauge (G) symmetries, leading to various emergent phenomena that appear only through the collective behaviours of electrons [7], as shown in Figure 1.1. As Landau theory suggests, phase transition's essence is the change in the symmetry, which is usually described by an order parameter. The inversion symmetry breaking results in the ferroelectricity leading to spontaneous polarization. Then time-reversal symmetry breaking is often accompanied by magnetism, in which spin acts as the order parameter and reverses the sign while T symmetry applies. The gauge symmetry is central to superconductivity or superfluidity, which is associated with charge conservation. When the (θ) in the phase of the wavefunction changes as $\psi \rightarrow e^{i\theta}\psi$, the G symmetry is broken, and this can elegantly describe conventional superconductivity according to BCS theory.

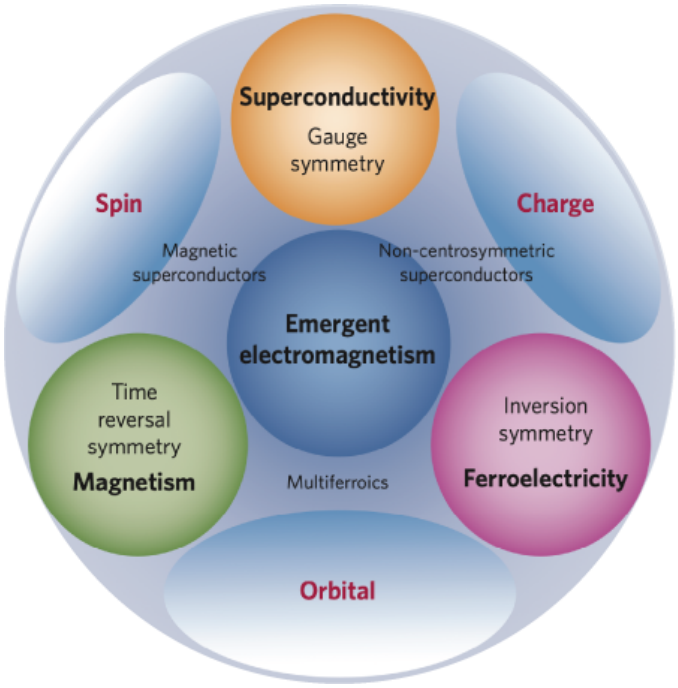


Figure 1.1: Schematic diagram showing the symmetries and degrees of freedom of correlated electrons that result in the emergent phenomena in modern condensed matter physics. Adapted with permission from Nature Materials [8].

The multiferroic material, where T and I symmetries are simultaneously broken, bridges the gap between ferromagnetic and ferroelectric systems and is a particular category of magnetoelectric coupled materials. The original definition for multiferroic is that at least two 'ferroic' properties: ferroelectricity, ferromagnetism and ferroelasticity, are found in a single-phase ferroic material [9]. The symmetries for these ferroic properties are shown in Table 1.1, which demonstrates why the multiferroics are rare from the perspective of symmetry constraints [10]. Magnetoelectric (ME) coupling, on the other hand, is a more generic concept that may exist whatever the nature of magnetic and electrical order parameters, such as in paramagnetic ferroelectrics [11]. As a characteristic property for multiferroics, magnetoelectric coupling plays a crucial role in realising the non-volatile switching of magnetic state via coupling with other ferroic orders, making multiferroics one of the promising candidates for energetically efficient memory devices [12–16].

The ME coupling can be phenomenologically described by Landau theory by writing the free energy F of the system in terms of an applied magnetic field H

Characteristic symmetry	Spatial-inversion (I)	Time-reversal (T)
Ferroelastic	Yes	Yes
Ferroelectric	No	Yes
Ferromagnetic	Yes	No
Multiferroic	No	No

Table 1.1: Spatial-inversion and time-reversal symmetry in ferroics

and an applied electric field E. For a non-ferroic, stress-free medium as an example, free energy F under the Einstein summation convention can be written as:

$$-F(E,H) = \frac{1}{2}\epsilon_0\epsilon_{ij}E_iE_j + \frac{1}{2}\mu_0\mu_{ij}H_iH_j + \alpha_{ij}E_iH_j + \frac{\beta_{ijk}}{2}E_iH_jH_k + \frac{\gamma_{ijk}}{2}H_iE_jE_k + ... \tag{1.1}$$

The first term on the right describes the contribution from electrical response to an electric field, where the relative permittivity reflecting the property of the medium $\epsilon_{ij}(T)$ is a second-rank tensor that is typically independent of the electric field component E_i, the permittivity of free space is denoted as ϵ_0; the second term is the magnetic equivalent of the first term, where $\mu_{ij}(T)$ is the relative permeability of the medium in second-order tensor form, and μ_0 is the free space permeability; the third-rank tensors $\beta_{ijk}(T)$ and $\gamma_{ijk}(T)$ represent quadratic magnetoelectric coefficients. The tensile form of the coefficients incorporates all magnetoelectric effects as expansions continue. The ME effect can be established by differentiating free energy F concerning E_i and H_j, obtaining $P_i(H_j)$ and $M_i(E_j)$ respectively, in field free case (where E_i and H_j are zero for the first term of the derivative):

$$P_i = \alpha_{ij}H_j + \frac{\beta_{ijk}}{2}H_jH_k + ... \tag{1.2}$$

$$\mu_0 M_i = \alpha_{ij}E_j + \frac{\gamma_{ijk}}{2}E_jE_k + ... \tag{1.3}$$

This less rigorous derivation on the ME coupling $P_i(H_j)$ or $M_i(E_j)$ neglects the field hysteresis of the $\epsilon_{ij}(T)$ and $\mu_{ij}(T)$. The above equations provide two methods to obtain the magnetoelectric coefficient. According to Equation 1.2, the electrical response can be measured in terms of either current or voltage, that is $\alpha = \partial P/\partial H$ leading to the empirical expression when omitting higher-order coupling; Equation 1.3 provide the magnetic response concerning the external electric field when the sample is addressed in a magnetometer.

1.1.1 Classification of multiferroics

Multiferroic materials can be classified into type-I and type-II multiferroics, simply by the empirical judgment from the size of the ME coefficient; that is, type-I is often observed with a smaller α value and type-II witnesses a much higher coupling value. However, the primary difference between these two classes is the origin of their ferroelectricity. More specifically, the cause of inversion symmetry breaking for type-I is from crystalline, while type-II is caused by magnetic order.

Type I multiferroic materials

In type-I multiferroics, the ferroelectric phase transition occurs independently from the magnetic phase transition at a different critical temperature. Although the co-existence of the two orders will generally result in some coupling between the polarisation and magnetic structure, the ferroelectric and magnetic order parameters are not directly coupled, often being described as 'weakly' coupled [17]. The very early material that exhibited weak ME coupling was Cr_2O_3 in 1957, where the anisotropic magnetoelectric coefficients were measured near the antiferromagnetic Néel temperature of 307 K [18, 19].

Although type-I multiferroics are weakly ME coupled, they are proper ferroelectrics. They have a sizeable ferroelectric polarisation of up to several hundred $\mu C/cm^2$, with additional property of working at high critical temperatures. These characteristics make type-I multiferroics ideal for applications. The most studied candidate of type-I multiferroic is perovskite-structure $BiFeO_3$ (BFO): the ferroelectricity arises from the structural distortions induced by stereochemically active lone pairs of electrons, whereas the magnetism comes from the Fe^{3+} with its five 3d electrons. The ferroelectricity of bulk crystal orders at 1100 K [20], whereas antiferromagnetic order emerges at 643 K [21], making it one of the few room-temperature multiferroics. The ME coupling in $BiFeO_3$ is achieved by the electric field control of the Néel vector of the antiferromagnetic phase reported by many groups [22–24]. Although the intrinsic ferromagnetism in antiferromagnetic BFO is weak [25], the control of the ferromagnetism layer via BFO substrate

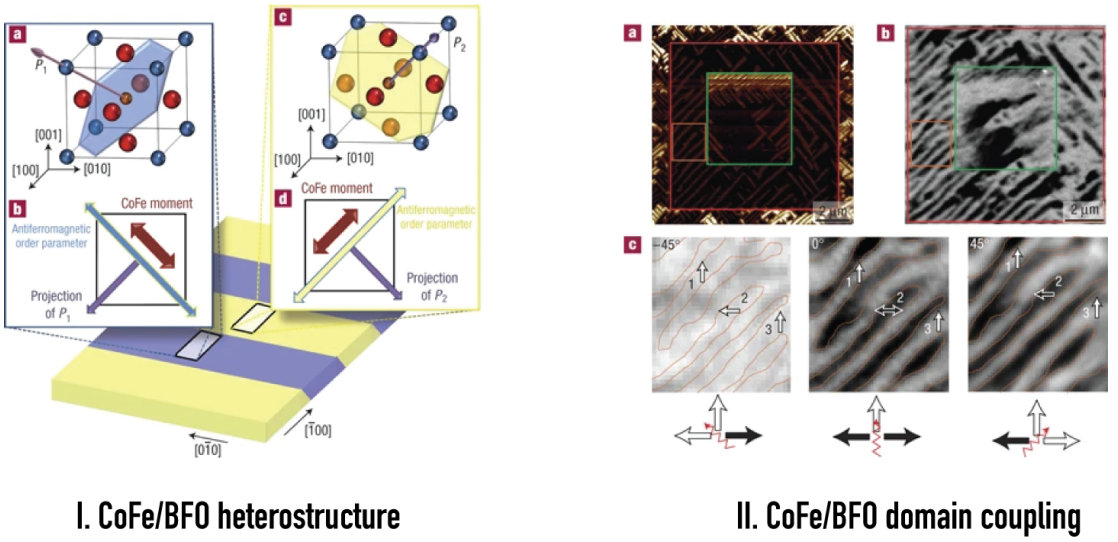


Figure 1.2: I. Schematic diagram of CoFe/BFO heterostructure. (a, c) Two adjacent domains in the [001]-oriented BFO crystal, in which the [111] polarisation directions, as well as the antiferromagnetic plane (perpendicular to P direction), are identified. (b, d) The corresponding projections of the polarisation direction for Néel vector in BFO and M directions in CoFe. II. CoFe/BFO domain coupling. (a) In-plane PFM image showing the ferroelectric domain structure of a BFO film with a large (red square) and small (green square) electrically switched region. (b) Corresponding XMCD-PEEM image taken at the Co L-edge for a CoFe film. The domain structures from two different methods match with good agreement. (c) Rotation of the sample about the incoming right-circularly polarised lights for the CoFe layer. Adapted and reprinted by permission from Nature Materials [22].

through the external electric field is proved promising, as shown in Figure 1.2. The antiferromagnetic domains in BFO demonstrate stripe feature in a (001)-oriented BFO film, in which the [111] polarisation directions, as well as the antiferromagnetic plane (perpendicular to this polarisation direction), are coupled in each respective domain, forming a zig-zag repetition. The corresponding magnetisation directions in the CoFe layer are associated with the Néel vector direction of the AFM domain, which is verified by the stripe domain images from Co L edge PEEM and PFM on BFO.

The mechanism underlying the interfacial magnetic coupling between ferromagnets and antiferromagnets is far from well understood. Nevertheless, the importance of interfaces in mediating magnetoelectric coupling and enabling the production of multiferroics-based devices is self-explanatory [26]. The study of interfacial control by strain has been an important topic in multiferroic devices.

Type II multiferroic materials

In a type-II multiferroic, the ferroelectric polarisation arises simultaneously with the magnetic ordering at the transition driven by a magnetic order parameter. As the magnetic ordering induces the polarisation, type-II multiferroics are thus 'improper' ferroelectrics that encompass much higher ME coupling. In contrast to type-I multiferroics, the ordering temperatures tend to be relatively low. This is because the non-centrosymmetric magnetic structures required to drive the system into the ferroelectric state generally arise from magnetic frustration [17]. The spontaneous polarisations are typically much lower than type-I multiferroics, on the order of 0.1 μC/cm^2.

Among the type-II multiferroics, the most well know class is the rare earth manganite family, which was first discovered in 2003 when Kimura *et al.* observed the cycloidal magnetic ordering of $TbMnO_3$ induced a ferroelectric polarisation [27]. A similar effect was followed in $TbMn_2O_5$, in which a magnetic field could reverse the ferroelectric polarisation [28]. The polarisation that arose in $REMnO_3$ or $REMn_2O_5$ (RE represent rare earth) is found due to the magnetoelastic distortion of lattice because of the spin frustration effect [27, 29], both magnetic orders are not simple but with a particular distortion such as spiral or cycloidal. The critical question of coupling modes between magnetic order and the induced ferroelectricity, as well as the role of spin frustration, leads to further discussion of the exchange interaction between the non-linear spin order.

1.1.2 Coupling mechanism

By looking at the coupling mechanism in type-II multiferroic systems, we can see that the nonlinear magnetic order is essential for these frustrated magnetic systems. From the perspective of spatially varying magnetisation M in an inhomogenous magnetic order, the induced polarisation can be written as [30]:

$$P^i = T^{ijkl} M^j \partial_k M^l \tag{1.4}$$

where T^{ijkl} is a parity-even materials tensor describing the coupling. Evaluating the coefficients of T^{ijkl} in a cubic system, this simplifies to

$$\mathbf{P} \propto [(\mathbf{M} \cdot \nabla)\mathbf{M} - \mathbf{M}(\nabla \cdot \mathbf{M})] \tag{1.5}$$

This spatially varying magnetisation $\boldsymbol{M}$ is present in all non-collinear magnetic structures, such as the helicoidal or spiral spin arrangements, as a result of spin frustration. The period of magnetic states in frustrated systems depends on the strengths of competing interactions, which leads to the spiral order and is often incommensurate with the crystalline period. Taking the example of the one-dimension Ising chain model with a ferromagnetic interaction $J < 0$ between neighbouring spins, where ferromagnetic parallel spin order is the ground state. When introducing the antiferromagnetic interaction $J' > 0$ between the next-nearest neighbouring spins, the total Hamiltonian $H = \sum_n [J\boldsymbol{S}_n \cdot \boldsymbol{S}_{n+1} + J'\boldsymbol{S}_n \cdot \boldsymbol{S}_{n+2}]$ of the frustrated spin chain gives rise to the spiral ground state:

$$\boldsymbol{S}_n = S[\boldsymbol{e_1} \cdot \cos Qx_n + \boldsymbol{e_2} \cdot \sin Qx_n]$$

where $\boldsymbol{e_1}$ and $\boldsymbol{e_2}$ are two orthogonal unit vectors, the wave vector Q is given by $\cos(Q/2) = -J'/(4J)$. For $J'/|J| > 1/4$, the classical ground state is a magnetic spiral, as demonstrated by Figure 1.3 (a). In contrast, when $J'/|J| > 1/2$, the chain of Ising spins orders into the up-up-down-down state, as shown in Figure 1.3 (b). A plausible microscopic mechanism inducing ferroelectricity in magnetic spirals is discussed by Katsura and Nagaosa [31] by introducing the spin current model. However, a more comprehensive introduction of the microscopic mechanisms is discussed in ref [32], the main three interactions being the inverse Dzyaloshinskii-Moriya interaction, exchange-striction, and *d-p* hybridisation. The polarisation induced by these contributions is expressed as [33, 34]:

$$\mathbf{P} = \overbrace{P_{\mathrm{DM}}\mathbf{r}_{ij} \times (\mathbf{S}_i \times \mathbf{S}_j)}^{\text{Dzyaloshinskii-Moriya}} + \overbrace{P_{\mathrm{ES}}\,(\mathbf{S}_i \cdot \mathbf{S}_j)\,\mathbf{r}_{ij}}^{\text{Exchange-striction}} + \overbrace{P_{\mathrm{d-p}}\left[(\mathbf{r}_{ij} \cdot \mathbf{S}_i)\,\mathbf{S}_i - (\mathbf{r}_{ij} \cdot \mathbf{S}_j)\,\mathbf{S}_j\right]}^{d-p \text{ hybridisation}} \tag{1.6}$$

where r_{ij} is a vector connecting the positions of the two spins, $\boldsymbol{S}_i$ and $\boldsymbol{S}_j$.

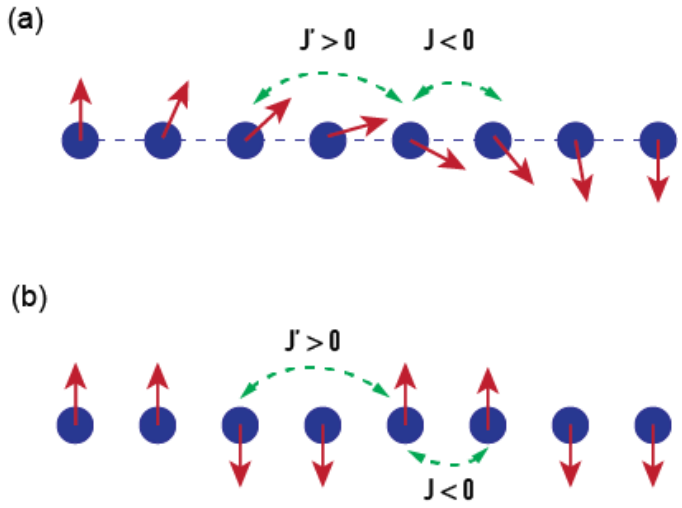


Figure 1.3: Competing exchange interaction results in different magnetic orders. (a). Spiral magnetic order induced from spin frustration $J'/|J| > 1/4$. (b). spin $\uparrow\uparrow\downarrow\downarrow$ mode from stronger frustration $J'/|J| > 1/2$.

The first term describes the inverse Dzyaloshinskii-Moriya interaction (i-DMI), which is antisymmetric exchange interaction composing the basis of the *spin current* model. This mechanism is often seen in orthogonal crystal lattices like $RMnO_3$ and hexagonal lattices like $Ba_2Mg_2Fe_{12}O_{22}$ [32, 35, 36]. Ligands usually mediate the super-exchange between spins of transition metal ions, as shown in the $RMnO_3$ in Figure 1.4 (a); the inverse DM interaction forces the oxygen ions to deviate from the equilibrium position, thus breaking the inversion symmetry. The Hamiltonian $\mathcal{H}_{DM} = \boldsymbol{D}_{ij} \cdot (\boldsymbol{S}_i \times \boldsymbol{S}_j)$ describes the i-DMI coupling between two adjacent non-collinear spins, whose intensity depends on the strength of spin-orbital coupling. As shown in the schematic graph (b), if all ligands in the structure are displaced in the same direction, this leads to a net polarisation. The *spin current model* describes the $\boldsymbol{S}_i \times \boldsymbol{S}_j$ by $\boldsymbol{j}_{i,j}$, and the net polarisation can therefore be obtained by $P \propto r_{ij} \times \boldsymbol{j}_{i,j}$ [37].

The second term, which forms a ferromagnetic exchange interaction, is the exchange-striction term. A magnetically ordered phase will cause the crystal structure to deform, potentially producing a local polarisation. The magnetic ions may displace uniformly for specific spin configurations, giving rise to a net polarisation. This term can give rise to ferroelectricity even in a collinear magnetic

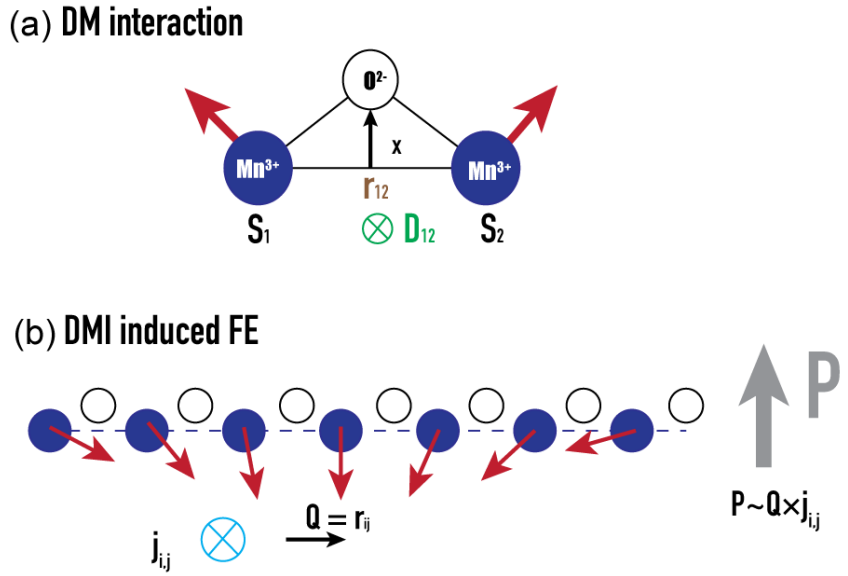


Figure 1.4: (a) The diagram of antisymmetric inverse Dzyaloshinskii-Moriya interaction, given by $\mathcal{H}_{DM} = \boldsymbol{D}_{ij} \cdot (\boldsymbol{S}_i \times \boldsymbol{S}_j)$. The Dzyaloshinskii vector $\boldsymbol{D}_{ij} \propto \lambda \boldsymbol{x} \times \boldsymbol{r}_{ij}$ describes the displacement of the O^{2-} ligand inducing the inversion symmetry breaking. (b) The net polarisation generated from spiral order is described by the spin current model. Re-adapted from ref [29].

structure, such as in the orthomanganites $HoMnO_3$ [38] and $TmMnO_3$ [39], and does not depend on the spin-orbital interaction.

The final term results from a spin-orbit-induced variation in the metal-ligand *d-p* hybridisation. It can describe the magnetically induced polarisation resulting from some non-collinear magnetic order in triclinic, monoclinic and trigonal crystal structures. In contrast to the inverse DM interaction, which only gives a polarisation for a cycloidal magnetic structure, the *d-p* hybridisation term can produce a polarisation for a proper-screw (helical) magnetic structure. This mechanism successfully describes the magnetically induced ferroelectricity in delafossite compounds such as $CuFeO_2$ [40] and $CuCrO_2$ [41].

1.2 Antiferromagnetism and its excitation

Antiferromagnetism (AFM) are materials that have a spontaneous, long-range magnetic order with net zero moment. AFM commonly refers to the complete absence of a net magnetic moment. However, materials with long-range, antiferromagnetic-

like ordering with an additional average moment far smaller than the moment of a single ion per magnetic unit cell can also exist, featuring a weak ferromagnet. Antiferromagnetic ordering exists up to the Néel temperature T_N, above which the thermal fluctuations on the spins will transfer the system into a paramagnetic state.

Antiferromagnetism was discussed separately by Landau and Néel concerning abnormal behaviours found in paramagnetic materials. They proposed different magnetic geometries. For Néel, this was a staggering order where each magnetic moment is aligned antiparallel to its nearest neighbours (G-type antiferromagnetism), whilst Landau favoured layers of parallel moments aligned antiparallel to neighbouring layers (A-type antiferromagnetism). Since these first discussions, numerous antiferromagnetic structures have been observed, including both of these. The first was reported by Shull and Smart, where they observed that the magnetic cell of MnO was twice that of the crystallographic cell by neutron scattering measurements.

1.2.1 Types of antiferromagntism

Some of the known antiferromagnetic materials are not absolute non-magnetic, a typical example is the α-Fe_2O_3, which is an AFM system but found with weak ferromagnetism due to bulk-DM interaction [43–46]. Here, we introduce several common types of ideal antiferromagnetic arrangement, by approximation, in three-dimensional space. In an A-type antiferromagnet (Figure 1.5 (a)), the magnetic moments are coupled ferromagnetically within a given spin plane but are antiparallelly coupled between neighbouring planes [47]. However, if the intra-plane coupling is ferromagnetic and the inter-plane coupling is antiferromagnetic, this structure is termed a C-type antiferromagnet (Figure 1.5 (b)). The third common antiferromagnet type, featuring inter-plane and intra- plane antiferromagnetic coupling, is known as a G-type antiferromagnet (Figure 1.5 (c)). All three AFM configurations are collinear antiferromagnetism, where the moments lie along joint axes. There are different types of antiferromagnetism which are non-collinear in nature; for example, the metallic AFM IrMn shows a triangular lattice where the moments are rotated at 120° with respect to each other [42]. The antiferromagnetism

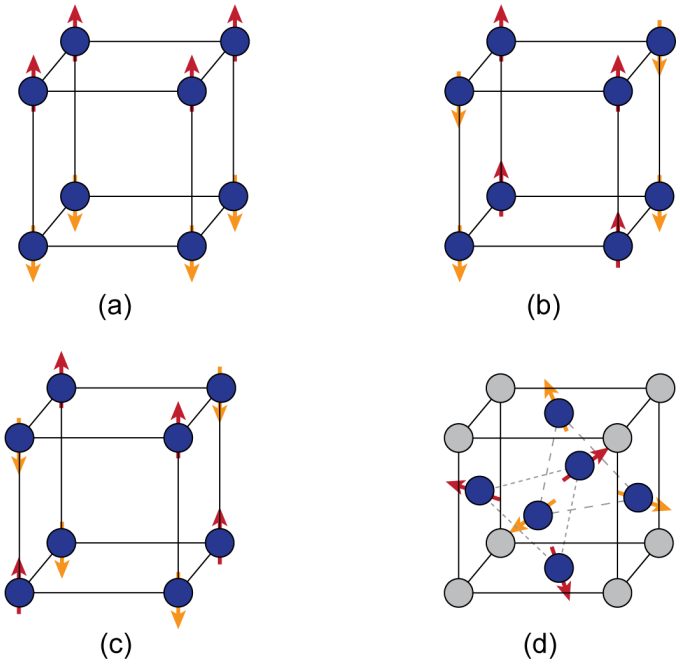


Figure 1.5: Schematic comparison of different types of antiferromagnetic ordering. (a) A- type order where there are layers of ferromagnetically ordered moments. (b) Shows C- type ordering where the moments experience antiferromagnetic coupling along two directions whilst (c) demonstrates the antiferromagnetic coupling along three directions present in a G-type antiferromagnet. (d) An example of a non-collinear antiferromagnetic ordering such as found in IrMn. Structure adapted from ref. [42]

is then provided by three, rather than two, antiferromagnetically coupled moments (Figure 1.5 (d)). The AFM candidate discussed in this thesis is $\alpha-Fe_2O_3$, a collinear AFM order (if not including bulk-DM interaction) more like the A-type.

1.2.2 Antiferromagnetic spin wave excitation

Spin wave excitation, in which the corresponding quantised quasi-particle is called *magnon* (this term is used to refer to the quantised spin wave mode for the rest of the paragraph), also exists in the antiferromagnetic system, which exhibits intriguing properties in contrast to the counterpart in ferromagnetism. Starting from the ferromagnetic spin wave, the dispersion relationship of the ferromagnetic magnon describes the propagation of the quasi-particles in the ferromagnetic lattice, analogous to the phonon dispersion in atomic lattice vibration.

The ground state of a simple ferromagnetic spin chain has all spins parallel along the same direction, as shown in Figure 1.6. Considering N spins with magnitude

S in a chain coupled by Heisenberg interaction from the nearest-neighbour site, the total energy of the ground state can thus be written as:

$$U = -2J \sum_{n=1}^{N} \boldsymbol{S}_n \cdot \boldsymbol{S}_{n+1} \tag{1.7}$$

where $\boldsymbol{J}$ is the exchange integral. For the unperturbed ground state, the scalar form of the total exchange energy is $U_0 = -2NJS^2$ when all site spins S are parallel. The effective field acting on site n can be derived from the exchange energy $-2J\boldsymbol{S}_n \cdot (\boldsymbol{S}_{n-1} + \boldsymbol{S}_{n+1})$ as:

$$\boldsymbol{B}_n = -\frac{2J}{g\mu_B}(\boldsymbol{S}_{n-1} + \boldsymbol{S}_{n+1}) \tag{1.8}$$

where the magnetic moment for site n is $\boldsymbol{\mu_n} = -g\mu_B\boldsymbol{S}_n$, μ_B is the Bohr magneton.

The angular momentum dynamics of the spin under the external B field is driven by the torque $\boldsymbol{\mu}_n \times \boldsymbol{B}_n$, which evolves into:

$$\frac{d\boldsymbol{S}_n}{dt} = \frac{2J}{\hbar}\boldsymbol{S}_n \times \boldsymbol{B}_n = \frac{2J}{\hbar}(\boldsymbol{S}_n \times \boldsymbol{S}_{n-1} + \boldsymbol{S}_n \times \boldsymbol{S}_{n+1}) \tag{1.9}$$

Assuming the spin is perturbed with small excitation, the scalar equations expressed by Cartesian coordination are, therefore

$$\begin{aligned} \frac{dS_n^x}{dt} &= \frac{2JS}{\hbar}(2S_n^y - S_{n-1}^y - S_{n+1}^y) \\ \frac{dS_n^y}{dt} &= -\frac{2JS}{\hbar}(2S_n^x - S_{n-1}^x - S_{n+1}^x) \\ \frac{dS_n^z}{dt} &= 0 \end{aligned} \tag{1.10}$$

where S_n^x, S_n^y are in-plane projections of spin S when triggering spin wave oscillation, and $S_n^z \approx S$ is assumed in the third equation. If trying with travelling wave solution for both S_n^x, S_n^y with the form:

$$S_n^x = \boldsymbol{u} \cdot exp[i(nka - \omega t)];\ S_n^y = \boldsymbol{v} \cdot exp[i(nka - \omega t)] \tag{1.11}$$

where $\boldsymbol{u}$ and $\boldsymbol{v}$ are unit vectors in the x and y directions. We may derive the dispersion relationship by diagonalising the eigen-equation matrix by replacing Equation 1.11 with Equation 1.10

$$\hbar\omega = 4JS(1 - \cos ka) \tag{1.12}$$

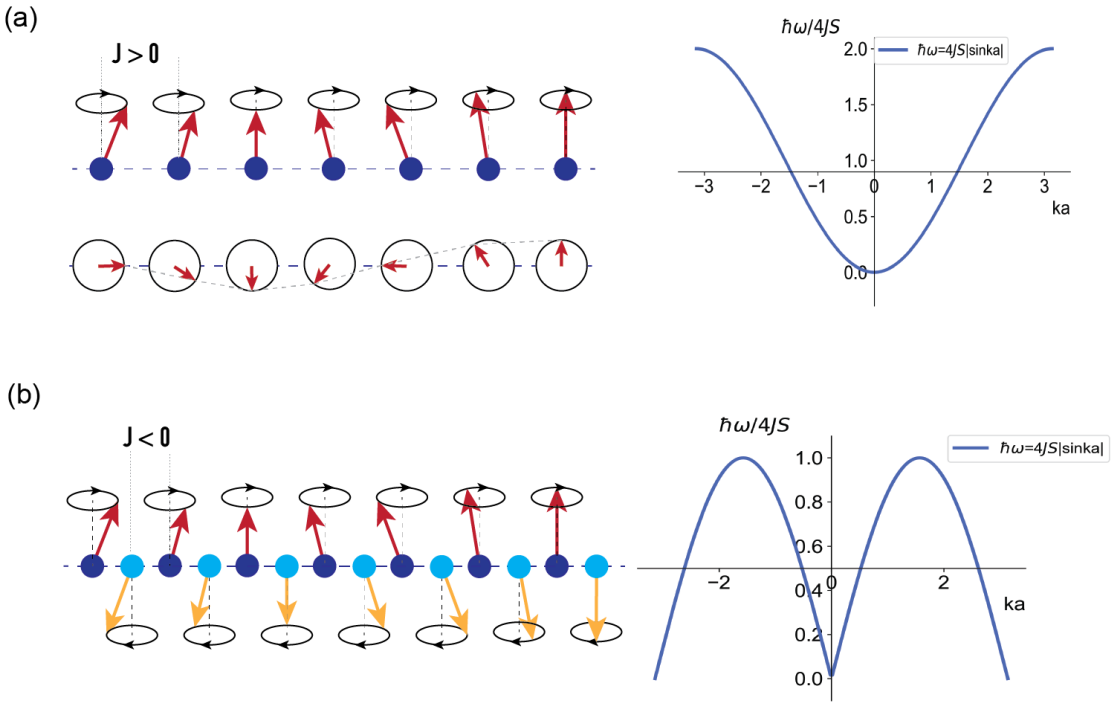


Figure 1.6: Semiclassical depiction of the spin wave excitation in ferromagnetic spin chain (a) and antiferromagnetic spin chain (b). Only the nearest exchange interactions are taken into account.

For long wavelength approximation $ka \ll 1$, the dispersion relation for FM spin wave excitation gives rise to quadratic dependence on reciprocal wave vector k:

$$\hbar\omega = (2JSa^2)k^2 \tag{1.13}$$

However, the energy dependence on reciprocal space vector k differs in the antiferromagnetic case. Considering an antiferromagnetic spin chain consisting of two FM spin chains with opposite spin coupling, as shown in the diagram in Figure 1.6 (b), the total periodicity is reduced by half, and the even index spins are aligned up while the odd spins are pointing down for the ground state. When considering the nearest exchange coupling constant J to be negative between sublattice A (blue, $S^z_{2n} = S$) and A′ (cyan, $S^z_{2n+1} = -S$), the AFM version of Equation 1.10 for A sublattice can be written as:

$$\frac{dS^x_{2n}}{dt} = \frac{2JS}{\hbar}(-2S^y_{2n} - S^y_{2n-1} - S^y_{2n+1}) \tag{1.14}$$

$$\frac{dS^y_{2n}}{dt} = -\frac{2JS}{\hbar}(2S^x_{2n} - S^x_{2n-1} - S^x_{2n+1}) \tag{1.15}$$

and for B sublattice:

$$\frac{dS^x_{2n+1}}{dt} = \frac{2JS}{\hbar}(2S^y_{2n+1} + S^y_{2n} + S^y_{2n+2}) \tag{1.16}$$

$$\frac{dS^y_{2n+1}}{dt} = -\frac{2JS}{\hbar}(2S^x_{2n+1} - S^x_{2n} - S^x_{2n+2}) \tag{1.17}$$

The ladder operator $S^+ = S^x + iS^y$ can be used to combine the above two sets of equations for A and A′ lattice:

$$\frac{dS^+_{2n}}{dt} = \frac{2iJS}{\hbar}(2S^+_{2n} - S^+_{2n-1} - S^+_{2n+1}) \tag{1.18}$$

$$\frac{dS^+_{2n+1}}{dt} = -\frac{2iJS}{\hbar}(2S^+_{2n+1} - S^+_{2n} - S^+_{2n+2}) \tag{1.19}$$

When replacing a trial solution in the form of :

$$S^+_{2n} = \boldsymbol{u} \cdot exp[i(2nka - \omega t)];\ S^+_{2n+1} = \boldsymbol{v} \cdot exp[i((2n+1)ka - \omega t)]$$

The solution of the eigen-equation leads to the dispersion relation of the AFM chain:

$$\hbar\omega = 4|J|S \cdot |\sin ka| \tag{1.20}$$

The figure for plotting the AFM dispersion relations can be found in Figure 1.6. Noticeably, the long wavelength approximation for the AFM chain gives rise to the linear dependence between energy and reciprocal space vector $\hbar\omega = 4|J|S \cdot |ka|$, distinct from the quadratic dependence in the FM chain. Analogous to the phonon dispersion, the magnon dispersion derived in this way is the acoustic mode, not the optical mode, since we describe the wave propagation in collective spin rotation instead of relative displacement between the spins. This classical derivation is adopted widely by many textbooks on solid-state physics. By recalling the spin chain model dispersion, we can get the gist of the intrinsic relations for describing magnetic excitations for the antiferromagnetic system, which is far more complicated than AFM chain description in natural AFM systems, such as NiO, $YMnO_3$ and so on. The hematite α-Fe_2O_3 has six superexchange interactions through metal-oxygen-metal bondings, which is much more complicated than the 1D spin chain model. Nevertheless, we can still establish the dispersion relations by projecting the 1D chain method into a 3D lattice coupling.

1.3 Magnetic topology

The term 'topological quantum state' was first encountered by discovering the quantum hall effect (QHE), especially the integer and fractional quantum hall phenomena in two-dimensional electron gas systems [4, 48]. This pioneering work discovers a 'topological nontrivial' entangled state of matter, totally different from the conventional 'topological trivial' entanglement with continuous surfaces without 'holes' such as soccer or rugby. The 'topological nontrivial' surfaces, however, describe those surfaces with one or more 'holes' that exist in a closed path that cannot be smoothly shrunk into a tiny circle around a point. 'Topological equivalence' refers to the geometric equivalence between a doughnut and a coffee cup, which have a hole throughout the surface regardless of what kind of continuous evolution. This 'topological equivalence' can be indexed mathematically by an integer number called 'topological invariant' or 'topological charge number', the Berry curvature over the surface [49]. In nonmetallic magnetic systems, a group of small swirling magnetisation textures exhibit topological properties; the so-called 'magnetic skyrmions' are such magnetic structures with integer topological numbers demonstrating topological invariance while experiencing continuous deformation.

1.3.1 Topological textures in magnetic materials

Skyrmion is a celebrated family of magnetic topological structures, a circular disk-like spin-whirling structure with a two-dimensional limit. Two types of skyrmions are of interest, *Néel* (Figure 1.7 (a)) or *Bloch* type (Figure 1.7 (b)), which can usually be generated under different symmetry environments between spins. The typical characteristic of both Bloch and Néel-type skyrmions are symmetric rotation of the azimuthal spin and 180° of rotation for spins from the centre to the exterior. The main difference lies in the helical direction of the rotation along the diameter, which is perpendicular (parallel) to the spin propagation for Néel (Bloch) type skyrmion.

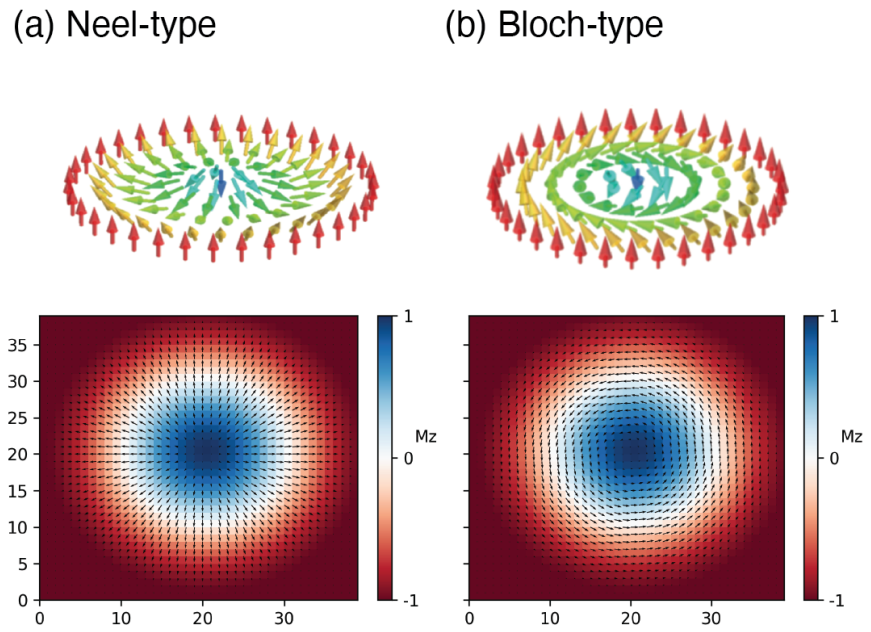


Figure 1.7: Demonstrations of Néel type (a) and Bloch type (b) skyrmion structure. The top two schematics are reproduced with permission from [50], while the bottom two plots are generated with Equation 1.21 under parameter set (Q, Q_h, Q_v) = (1,0,1) for (a) Néel type and (Q, Q_h, Q_v) = (1,π/2,1) for (b) Bloch type. The arrows represent the in-plane spin orientation.

The mathematical form of magnetisation for skyrmion is determined by several critical parameters expressed by polar coordination:

$$\boldsymbol{m}(\theta, \phi) = (\sin\theta\cos\theta, \sin\theta\sin\phi, \cos\theta) \tag{1.21}$$

where ϕ and θ are in-plane projection angles with respect to the x-axis and out-of-plane angles with respect to the z-axis, while the total spin magnitude is normalised to one. The skyrmion requires the condition $\theta|_{r=0} = 0$ and $\theta|_{r=\infty} = \pi$, while the helicity number Q_h and vorticity number Q_v determine the type of skyrmion:

$$\phi = Q_v\varphi + Q_h$$

where φ refers to the in-plane rotation angle ranging from 0 to 2π. Once the skyrmion mapping is generated by the (Q_h, Q_v) parameter set, the topological charge (or topological number) can be obtained accordingly by:

$$Q = \frac{1}{4\pi}\int_{\pi}^{0}\sin\theta d\theta\int_{0}^{2\pi}d\phi \tag{1.22}$$

As shown in Figure 1.7, two types of skyrmions are demonstrated with schematic diagrams (on top row), which can be plotted according to the mathematical expression in Equation 1.21 with parameters $(Q_h,Q_v) = (0,1)$ for Néel type skyrmion and $(Q_h,Q_v) = (\pi/2,1)$ for Bloch type skyrmion. Both structures hold the same topological charge $Q = 1$.

As a special type of magnetic soliton, skyrmion has an integer topological charge with intrinsic topological protection from thermal fluctuations, therefore, is regarded as a promising candidate for information carriers in memory devices. More and more topological structures are discovered following the skyrmion. Suppose the vorticity number reverses the sign, in which case, the in-plane projection exhibits anti-vortex; one can obtain a structure with an opposite topological charge called *anti-skyrmion*, This anti-particle of the skyrmion has been extensively reported theoretically and experimentally [51–56]. In addition to the anti-skyrmion, the higher-order topological structure and its anti-particles expand the topological family, such as *skyrmionium*, which shows the more complicated structure in real space [57–61]. By transforming under topological equivalence, the *bimeron* structure is reported to exhibit the same integer topological charge as its prototype skyrmion. This bimeron can further be fractionalised by splitting into *merons*, which have half-integer topological charges. Meron and its anti-particle called *anti-meron* have another name *half-skyrmion* [62–65].

1.3.2 Domains and domain walls

Another type of topological defect ubiquitously seen in magnetic materials is the magnetic domain wall, which bridges two ferroic domains through a continuous moment rotation. The domain wall's generation has been studied for a long time [66–68]. From the point of view of symmetry, the symmetry breaking from a high-symmetric parent phase to a low-symmetry phase characterized by a new order parameter will spontaneously generate regions of uniform order called domains. Due to the self-energy reduction that a single large domain is always energetically

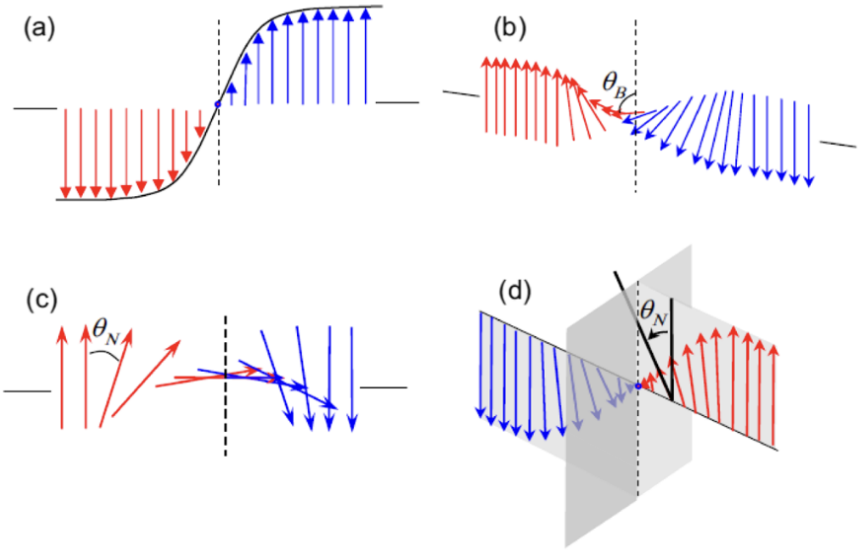


Figure 1.8: (a) Ising wall, (b) Bloch wall, (c) Néel wall, and (d) mixed Ising-Néel wall. Recent calculations show that domain walls in perovskite ferroelectrics tend to be of mixed character. The figures are adapted from [74].

unfavourable, small fragments broken from the single domain with opposite order parameter directions can solve the problem of depolarisation.

As a new type of interface, domain wall is referred to as homo-interfaces to distinguish them from conventional boundaries, such as p-n junctions or the interface between heterostructures, which is expected to be made into functional devices, especially in the field of spintronics [69–71]. Prevailing applications for magnetic domain walls can be found in producing functional non-trivial topological spin texture [50, 68] and wall control in memory devices [72, 73].

A common form of domain wall in ferromagnetic domains is an Ising wall, as indicated by Figure 1.8 (a). The order parameter for magnetic domains is the magnetisation M. When M evolves continuously by 180° connecting the two domains, there exist either Bloch (Figure 1.8 (b)) or Néel (Figure 1.8 (c)) type walls; sometimes, the superposition of both cases can be found(in Figure 1.8 (d)). The difference between the Bloch and Néel types is the moment (or spin) rotation plane orienting either perpendicular or within the domain wall. The chiral structure in Bloch or Néel type generally results from Heisenberg energy reduction between the spins within an Ising chain model. The chirality of the spin orientation found

within the domain wall provides the opportunity for discovering the domain wall's polarisation property, which is extensively studied in multiferroics [29, 30], where ME coupling may be significant profiting from the chirality.

1.4 Thesis outline

This thesis presents a set of experimental and simulation studies of the magnetic order in two functional iron oxides. Chapter 2 introduces the experimental techniques centralising X-ray diffraction and X-ray absorption-based dichroism for analysing the magnetic structure and magnetic domain/structure imaging. In chapter 3, we perform experimental studies on a single crystal $Ba_{0.5}Sr_{1.5}Mg_2Fe_{12}O_{22}$ (BSMFO), a magnetic material exhibiting a significant magnetoelectric coefficient. Magnetometry, magneto-current measurements and magnetic diffraction experiments investigate its magnetic phases and switching mechanisms under external magnetic fields. In chapter 4, we exploit the circular dichroism of resonant X-ray diffraction to perform multiferroic phase imaging. These domains are switched by the external electric field and a customised THz pulse.

Chapter 5 introduces the X-ray photo-emission electron microscopy (X-PEEM) study on an antiferromagnetic α-Fe_2O_3 thin film. We develop a novel vector-mapping technique based on polarised X-PEEM images. Aid with the ability to resolve both in-plane and out-of-plane Néel vectors, we unravel a series of topological structures, such as merons, anti-merons and possible bimerons in antiferromagnetic analogue. Further studies on the dynamics of these topological structures are performed by large-scale atomistic micromagnetic simulations in chapter 6. The simulation results reveal the annihilation patterns from different topological bimerons, leading to the THz spin wave generation and topological charge transition in an ultra-short time scale. Finally, we address the significance of this topology-based AFM spin wave studies by analysing the THz wave behaviours.

2
Experiment methods

Contents

2.1 Introduction 21
2.2 Theory backgrounds of magnetic phenomena 22
2.2.1 Basis of magnetic diffraction 22
2.2.2 Basis of magnetic absorption 31
2.3 Experiment instruments 37
2.3.1 X-ray tube 37
2.3.2 Synchrotron facility 38
2.4 Micromagnetic simulation 40
2.4.1 Introduction of atomistic micromagnetics 41
2.5 Conclusion 45

2.1 Introduction

The investigation of dynamics in magnetic materials is a rather complicated project which requires synthetical experimental techniques. The key to investigating magnetism is to invent powerful tools for characterising magnetic structures and obtaining effective magnetic signals. In this chapter, we will introduce the standard instruments and facilities used for investigating the physics of magnetism. We will focus on the magnetic diffraction technique and its theoretical background in X-ray and neutron applications, which is helpful for essential magnetic structure

determination. During our experiments, the temperature, magnetic field, electric field, light pulses, and so on compose the primary external factors that can influence the dynamical behaviours of the magnetic structures. Among all these practical electromagnetic radiation tools, more emphasis will be put on techniques relevant to ultrafast laser, which can generate a picosecond pulse electric field called Terahertz radiation through a non-linear optical process. This powerful radiation exhibits growing popularity in phase transition studies. In the last section, we introduce a novel micromagnetic simulation tool complementary to the experiment, a prevailing practice in the studies of magnetic dynamics. This new micromagnetic simulation software features atomic scale, enabling multiple functions in contrast to previous micromagnetic tools.

2.2 Theory backgrounds of magnetic phenomena

2.2.1 Basis of magnetic diffraction

The last few decades have witnessed a surge of research on applying X-ray beams to investigate the magnetic properties of materials, driven by the improved performance of synchrotron facilities. In general, the magnetic contribution to the interaction between X-ray and material is weak, e.g. the magnetic diffraction intensity is five orders smaller than Thomson scattering. Consequently, the discrimination between charge and magnetic contributions observed in elastic scattering is necessary. For specific magnetic orders, the charge and magnetic peaks are not overlapped. Therefore, magnetic contributions can easily be distinguished by the characteristic magnetic diffraction position. Another vital phenomenon called *resonant elastic diffraction*, which can often be observed for $L_{2,3}$ absorption edges for rare earth and transition metal elements, enables the significant enhancement of magnetic elastic scattering intensity. Lastly, the interference between charge and magnetic distributions can be generated in ferromagnetic material during the scattering of circularly polarised photons, which can contribute to magnetic circular dichroism. These methods are only part of the applications in that X-ray plays a role in magnetic detection. Aiding with the modern electron microscope, some variant

methods can be invented, such as an X-ray the photoemission microscope with circular/linear dichroism (XMCD/XMLD-PEEM).

Although X-ray scattering is widely applied in experiments, one cannot avoid the basic theory of the interaction between the X-ray photons and macroscopic materials, some of which are quantum phenomena. A semiclassical approximation partially solved the primary form of interaction, e.g. photon scattering, by defining the scattering cross-section, usually called the *Kramers-Heisenberg relation* proposed by Kramers and Heisenberg in 1925 [75]. The energy level in the atom is quantised, while the electromagnetic (EM) field is treated classically as waves. The full quantum interpretation of the light scattering cross-section was gradually established by the pioneers of quantum mechanics [76–79]. The quantum electrodynamical results of the scattering cross section were first derived by Dirac using minimal-coupling Hamiltonian, which contains only electric-dipole transition moment without considering higher order multipolar transition moment, giving rise to the quantum form of Kramers-Heisenberg relation. For magnetic materials, the quantum version Kramers-Heisenberg relation must be generalised to include events arising from the spins of unpaired electrons in magnetic materials.

We start with the full quantum mechanical description based on the atomic picture in the magnetic system to understand the fundamental physics of X-ray scattering. Equation 2.1 demonstrates the interaction Hamiltonian for electrons in a quantised electromagnetic field with spin freedom.

$$\begin{aligned} H = & \frac{1}{2m}\sum_j [\boldsymbol{p}_j - \frac{e}{c}\boldsymbol{A}(r_j)]^2 + \sum_{i>j} V(|\boldsymbol{r}_i - \boldsymbol{r}_j|) - \frac{e\hbar}{2mc}\sum_j \boldsymbol{s}_j \cdot [\nabla \times \boldsymbol{A}(r_j)] \\ & + \frac{e\hbar}{2(mc)^2}\sum_j \boldsymbol{s}_j \cdot [\boldsymbol{E}(r_j) \times (\boldsymbol{p}_j - \frac{e}{c}\boldsymbol{A}(r_j))] + H_R \end{aligned} \tag{2.1}$$

where $\boldsymbol{p}_j$, $\boldsymbol{A}(\boldsymbol{r})_j$, $\boldsymbol{s}_j$ are momentum operator, vector potential and spin vector at site j, respectively. The vector potential $\boldsymbol{A}$ is utilised to describe the photon field, which is linear in the summation of creation and annihilation operators. H_R is the quantisation form of the electromagnetic field, which is irrelevant to electrons. From a general point of view, the first three terms are assigned as kinetic energy, Columb energy and Zeeman energy. And the fourth term describes the

spin-orbital coupling term. Further expansion of the Hamiltonian according to the vector potential order $\boldsymbol{A}$ can be written as:

$$\begin{aligned} H = & \underbrace{\sum_j \frac{e^2}{2mc^2}\boldsymbol{A}(\boldsymbol{r})_j^2 - \frac{e\hbar}{2(mc)^2}\frac{e^2}{c^2}\sum_j \boldsymbol{s}_j \cdot [\boldsymbol{A}(\boldsymbol{r})_j \times \boldsymbol{A}(\boldsymbol{r})_j]}_{\boldsymbol{H}_1'(\propto \boldsymbol{A}^2)} \\ & \underbrace{- \frac{e}{mc}\boldsymbol{p}_j \cdot \boldsymbol{A}(\boldsymbol{r})_j - \frac{e\hbar}{2mc}\sum_j \boldsymbol{s}_j \cdot \nabla \times \boldsymbol{A}(\boldsymbol{r})_j}_{\boldsymbol{H}_2'(\propto \boldsymbol{A})} \\ & \underbrace{+ \sum_j \frac{p_j^2}{2m} + \sum_{i>j} V\left(|\boldsymbol{r}_i - \boldsymbol{r}_j|\right) + \frac{e\hbar}{2m^2c^2}\sum_j \boldsymbol{s}_j \cdot \left[\nabla\phi\left(\boldsymbol{r}_j\right) \times \boldsymbol{p}_j\right] + H_R}_{\boldsymbol{H}_0} \end{aligned} \tag{2.2}$$

Here, we use the quantisation expression of the electric field $\boldsymbol{E}(\boldsymbol{r_j}) = -\nabla\phi - \frac{\dot{A}}{c}$. It is still not clear at this stage which term contributes to the charge scattering or magnetic scattering in Equation 2.2, until we apply the perturbation theory to the scattering amplitude from the transition probability. However, we can discover the physical process by orders of $\boldsymbol{A}$ occurred in such a complicated scattering Hamiltonian. First of all, the quadratic terms of $\boldsymbol{A}$ in $\boldsymbol{H_1'}$ usually are treated with first-order perturbation, representing the absorption of a primary photon and the simultaneous emission of a secondary photon. The terms with linear dependence of $\boldsymbol{A}$, as indicated by $\boldsymbol{H_2'}$, are treated with the second order perturbation, which entails the transition of intermediate virtual states commonly occurring in magnetic dichroism and resonant scattering phenomena. To derive the mathematical form of scattering amplitude (or the square root of cross-section), which measures the probability of transition between states, it is necessary to briefly introduce the *Fermi Golden Rule* to describe the full picture of scattering between photon and matter.

The quantum mechanical interpretation of the scattering can be simplified into a transition from ground state $|\varphi_i\rangle = |a, \boldsymbol{k}, \boldsymbol{\epsilon}\rangle$ to the final state $|\varphi_f\rangle = |b, \boldsymbol{k'}, \boldsymbol{\epsilon'}\rangle$ under the interaction Hamiltonian described above. The initial (final) ground state contains the part of the electron state $|a\rangle$ ($|b\rangle$) and the part of the photonic state with propagation vector $\boldsymbol{k}$ ($\boldsymbol{k'}$) and polarisation vector $\boldsymbol{\epsilon}$ ($\boldsymbol{\epsilon'}$). Under the perturbation part of the interaction Hamilton $\boldsymbol{H_{per}}$ (which is consisted of $\boldsymbol{H_1'}$ and

$\boldsymbol{H_2'}$ corresponding to the first and second-order perturbation assumption), the transition probability is demonstrated mathematically as:

$$w_{i\to f} = \frac{2\pi}{\hbar}\left|\langle\varphi_f|H_{per}|\varphi_i\rangle + \sum_n \frac{\langle\varphi_f|H_{per}|\varphi_n\rangle\langle\varphi_n|H_{per}|\varphi_i\rangle}{E_i - E_n}\right|^2 \times \delta(E_i - E_f) \quad (2.3)$$

The Fermi Golden Rule describes the basic transition probability between the initial and final state under perturbation. The transition rate $w_{i\to f}$ not only describes the hopping of bounded electrons between initial state $|a\rangle$ and final state $|b\rangle$ through the interaction with the matter, but also gives the explicit state of the scattered photon$|\boldsymbol{k'}, \boldsymbol{\epsilon'}\rangle$ evolved from the initial state $|\boldsymbol{k}, \boldsymbol{\epsilon}\rangle$. When substituting the full description of the state into Equation 2.3, then the decomposition of the transition probability can be obtained according to the perturbation orders:

$$w^{(1)} = \frac{2\pi}{\hbar}\left|\langle b, \boldsymbol{k'}, \boldsymbol{\epsilon'}|H_1'|a, \boldsymbol{k}, \boldsymbol{\epsilon}\rangle\right|^2 \times \delta(E_a - E_b + \hbar\omega - \hbar\omega') \quad (2.4)$$

This is the proportion contributed by first-order perturbation $\boldsymbol{H_1'}$. And the second-order perturbation scattering can be analogously given by $\boldsymbol{H_2'}$ terms:

$$w^{(2)} = \frac{2\pi}{\hbar}\left|\sum_n \frac{\langle b, \boldsymbol{k'}, \boldsymbol{\epsilon'}|H_2'|\varphi_n\rangle\langle\varphi_n|H_2'|a, \boldsymbol{k}, \boldsymbol{\epsilon}\rangle}{E_i + \hbar\omega_i - E_n}\right|^2 \times \delta(E_a - E_b + \hbar\omega - \hbar\omega') \quad (2.5)$$

Both transition rates involve the coupling term between $\boldsymbol{s}_j$ and vector potential $\boldsymbol{A_j(r)}$. Thus the magnetic contribution emerges at every stage of perturbation, showing the intrinsic complexity of magnetic scattering.

Non-resonant magnetic scattering

The non-resonant scattering is often observed for hard X-ray diffraction experiments, where the photon energy is typically tuned within 5-10 keV far away from atomic levels in transition metals. The short wavelength wave probes the electrons within the shell; the energy is high enough to ionise them to a continuous state. During this process, the first-order perturbation dominates the transition rate because the denominators in $w^{(2)}$ are far away from zero because of the high energy. Therefore the second order perturbation term is negligible. Since two vector potential terms appear in $\boldsymbol{H_1'}$, which correspond to scatterings with different origins. From Born

approximation that plane waves can describe the incident and scattered photons in the form of $e^{i\boldsymbol{k}\cdot\boldsymbol{r}}$, the photon part of the initial and final states can be rewritten to obtain the transition rate under first-order perturbation:

$$w^{(1)} = \frac{2\pi}{\hbar}\left|\frac{2\pi\hbar c^2}{V\omega}\frac{e^2}{mc^2}\times\left[\left\langle b\right|\sum_j e^{i\boldsymbol{K}\cdot\boldsymbol{r_j}}\left|a\right\rangle\boldsymbol{\epsilon'}\cdot\boldsymbol{\epsilon} - i\frac{\hbar\omega}{mc^2}\left\langle b\right|\sum_j e^{i\boldsymbol{K}\cdot\boldsymbol{r_j}}\boldsymbol{s}_j\left|a\right\rangle\cdot\boldsymbol{\epsilon'}\times\boldsymbol{\epsilon}\right]\right|^2 \tag{2.6}$$

where $\boldsymbol{K} = \boldsymbol{k} - \boldsymbol{k'}$ is the moment transfer vector of the photon scattering. Following the convention by Blume [80], the cross-section can be obtained from transition probability by multiplying ω_f by the density of final state $g(\omega_f)$ and dividing by the incident flux I_0. The final cross-section of the scattering is expressed as:

$$\left(\frac{d^2\sigma}{d\Omega dE}\right) = w^{(1)}\cdot g(\omega_f)/I_0 \tag{2.7}$$

$$= r_0^2\left|\left[\left\langle b\right|\sum_j e^{i\boldsymbol{K}\cdot\boldsymbol{r_j}}\left|a\right\rangle\boldsymbol{\epsilon'}\cdot\boldsymbol{\epsilon} - i\frac{\hbar\omega}{mc^2}\left\langle b\right|\sum_j e^{i\boldsymbol{K}\cdot\boldsymbol{r_j}}\boldsymbol{s}_j\left|a\right\rangle\cdot\boldsymbol{\epsilon'}\times\boldsymbol{\epsilon}\right]\right|^2 \tag{2.8}$$

where $g(\omega_f) = \frac{V\omega_f^2}{(2\pi)^3\hbar c^3}$, $I_0 = \frac{c}{V}$. $r_0 = \frac{e^2}{mc^2}$ is the Thomson scattering length.

The first term is *Thomson scattering*, which is dependent on the Fourier transform of the electron density $\sum_j e^{i\boldsymbol{K}\cdot\boldsymbol{r_j}}$ when $|a\rangle = |b\rangle$, representing the classical radiation from the charge of the electrons. The scattering ability from this term is proportional to the atomic number Z_n contained in the $\sum_j e^{i\boldsymbol{K}\cdot\boldsymbol{r_j}}$ term [1]. The polarisation factor $\boldsymbol{\epsilon'}\cdot\boldsymbol{\epsilon}$ describes the polarisation change of the photon induced by the charge scattering. We explain this factor bit further by taking the example of a standarded diffraction setup, as shown in the cartoon Figure 2.1. The linear polarisation of the beam is defined as σ or π according to the orientations perpendicular or parallel to the scattering plane, composing a set of the basis for the matrix of the polarisation factor, as shown by:

$$\begin{bmatrix}\boldsymbol{\epsilon}_{\sigma\to\sigma} & \boldsymbol{\epsilon}_{\sigma\to\pi}\\ \boldsymbol{\epsilon}_{\pi\to\sigma} & \boldsymbol{\epsilon}_{\pi\to\pi}\end{bmatrix}$$

where $\boldsymbol{\epsilon}_{\sigma\to\pi}$ represents the polarisation state of the incident beam to be σ, and the scattered beam to be π. For the Thomson scattering where the polarisation state

[1] $\sum_j e^{i\boldsymbol{K}\cdot\boldsymbol{r_j}} \propto \sum_n^{cell} f_n^0(\boldsymbol{K})e^{i\boldsymbol{K}\cdot\boldsymbol{x_n}}\delta(\boldsymbol{G}-\boldsymbol{K})$, where the Thomson form factor is $f_n^0(\boldsymbol{K}) = \int d\boldsymbol{x}e^{i\boldsymbol{k}\cdot\boldsymbol{x}}n(\boldsymbol{x}) \propto Z_n$

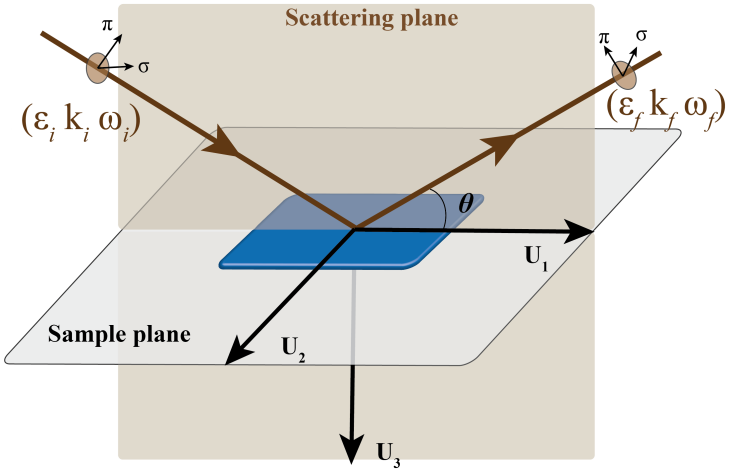


Figure 2.1: Scattering geometry diagram. The coordinate system (U_1, U_2, U_3) follows the convention from Hill and McMorrow [81] on polarisation-dependent resonant X-ray scattering. The photon scattering angle θ halves the angle between the incident and the scattered beam. The π (σ) polarisation is defined within (perpendicular to) the scattering plane.

is given by $\boldsymbol{\epsilon}' \cdot \boldsymbol{\epsilon}$, the matrix form of the polarisation factor

$$\boldsymbol{\epsilon}' \cdot \boldsymbol{\epsilon} = \begin{bmatrix} 1 & 0 \\ 0 & cos2\theta \end{bmatrix} \tag{2.9}$$

indicates that the $\sigma \rightarrow \pi$ or $\pi \rightarrow \sigma$ channel is prohibited because charge scattering will not induce the linear polarisation rotation, noticeably, the σ or π polarised beam will maintain its polarisation after the scattering. Furthermore, the $\cos2\theta$ dependence of the $\pi \rightarrow \pi$ channel means that the π polarisation component of the scattered beam can be reduced to zero if the π polarised beam incomes with angle $2\theta = 90°$. This effect has been applied to filter out the π polarisation light, acting as the linear polarisation analyser in synchrotron beamline.

The second term with the dependence of $\sum_j e^{\boldsymbol{K}\cdot\boldsymbol{r}_j}\boldsymbol{s}_j$ indicates the magnetic scattering arising from the spin density. This term is imaginary in contrast to the Thomson scattering term, which means that only circular polarised light can be utilised to detect this effect in a centrosymmetric system. Additional contributions from second-order perturbation terms have to be considered to scope the pure magnetic scattering at a high energy limit. Combing the magnetic contribution of the second-order perturbation into the total cross-section, we can derive the

total magnetic scattering at a high energy limit as:

$$\left(\frac{d^2\sigma}{d\Omega dE}\right)_{magnetic} = r_0^2\left|\frac{i\hbar\omega}{mc^2}\left\langle b\right|\sum_j e^{i\boldsymbol{K}\cdot\boldsymbol{r}_j}\left[\frac{i\boldsymbol{K}\times\boldsymbol{p}_j}{\hbar k^2}\cdot\boldsymbol{A'}+\boldsymbol{s}_j\cdot\boldsymbol{B'}\right]\left|a\right\rangle\right|^2 \tag{2.10}$$

where $\boldsymbol{p}_j$ is the electronic momentum, $\boldsymbol{A'}=\boldsymbol{\epsilon}\times\boldsymbol{\epsilon'}$ and $\boldsymbol{B'}=\boldsymbol{\epsilon}\times\boldsymbol{\epsilon'}+(\boldsymbol{k'}\times\boldsymbol{\epsilon'})(\boldsymbol{k'}\cdot\boldsymbol{\epsilon})-(\boldsymbol{k}\times\boldsymbol{\epsilon})(\boldsymbol{k}\cdot\boldsymbol{\epsilon'})-(\boldsymbol{k'}\times\boldsymbol{\epsilon'})\times(\boldsymbol{k}\times\boldsymbol{\epsilon})$. The additional coefficient $\frac{\hbar\omega}{mc^2}$ for 10 keV X-ray is about 0.02 ($mc^2\sim 0.511$ MeV), meaning that the magnetic scattering is much weaker than charge scattering. The practical comparison can be estimated from the cross sections σ between charge and pure magnetic scatterings as the example of Fe element:

$$\frac{\sigma_{mag}}{\sigma_{charge}}\approx\left(\frac{\hbar\omega}{mc^2}\right)^2\frac{N_m^2}{N^2}\frac{f_m^2}{f^2}\sim 10^{-6} \tag{2.11}$$

where N_m is the number of magnetic electrons/atom, N is the number of electrons/atom, and f_m and f are magnetic and charge form factors. From the intensity estimation, we can conclude that the scattering from the magnetic component is much less significant in contrast to the charge scattering. However, it is still possible to employ the magnetic scattering effect for some unique magnetic structures, such as antiferromagnetic or spiral structures where magnetic diffractions are not coincident with charge Bragg peak in reciprocal space.

Resonant magnetic scattering

The previous section discusses the scattering process at a high energy limit by considering the scattering from charge and magnetic contributions. When tuning the photon excitation energy to the resonant edge, where the denominators in Equation 2.5 approach zero, the significant enhancement of transition probability from second-order perturbation will dominate the total scattering cross-section. In other words, the cross-section of magnetic scattering due to this resonant effect will be primarily amplified. During that process, the electrons hop to a virtual state by photon absorption and coherently drop back to the ground state with photon emission. This element-dependent Soft X-ray resonant absorptions are widely applied in modern synchrotron beamlines, especially useful in magnetic

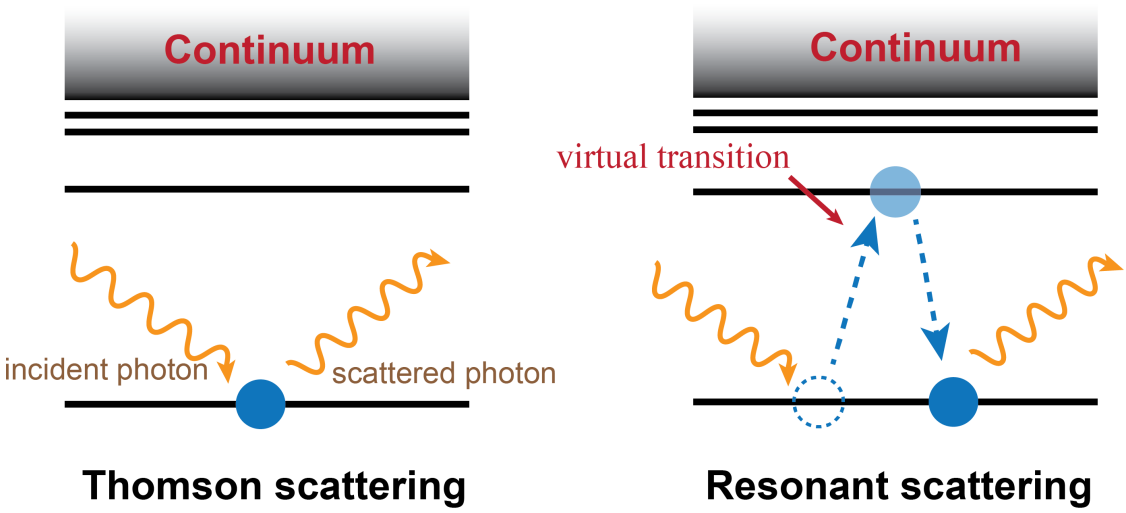


Figure 2.2: The diagram of the scattering process. The left subplot indicates Thomson scattering in which incident beam energy is tuned off-resonant, and no electronic excitation is involved. The resonant scattering requires the photonic energy to be adjusted precisely to realise the electronic virtual transition, which enhances the cross-section of magnetic scattering.

scattering at resonant edges when studying transition metals and heavy rare-earth elements (two main groups with strong magnetism).

Multipole transitions also contribute to the resonant scattering behaviours. Taking the example of rare-earth elements, the enhanced magnetic resonances are observed occurring at L_2, L_3, M_2 and M_3 absorption edges, where L edge corresponds to electric quatropole (E_2) transition to the tightly bound $4f$ shell, and M edge corresponds to the electric dipole (E_1) transition to the $5d$ shell. For the transition metal element Fe, the corresponding E_1 transitions occur at the L_2 absorption edge from $2p$ core states to $3d$ valence states. Here we mainly talk about the case of electric dipole transition for the magnetic structures since only iron oxides are discussed throughout the thesis.

Following the convention by Hill and McMorrow [81], the scattering amplitude f from a specific magnetic structure can ideally be reformatted into real and imaginary parts as:

$$f = f_0 + f' + if'' \tag{2.12}$$

The $f_0 \propto Zr_0$ is Thomson scattering arising from charge distribution. The f'

and f'' are dispersive and absorptive factors for the resonant case. Following the electric dipole approximation, the vector spherical harmonics $Y_{LM}(\theta, \varphi)$ in this transition are $L = 1, M = -1, 0, 1$. Therefore, the resonant scattering amplitude can be expressed as:

$$f_{E_1}^{res} \propto \sum_{M=-1,0,1} \left[\boldsymbol{\epsilon'} \cdot \boldsymbol{Y}_{1M}(\boldsymbol{k'}) \cdot \boldsymbol{\epsilon} \cdot \boldsymbol{Y^*}_{1M}(\boldsymbol{k}) \right] \tag{2.13}$$

for $L = 1, M = \pm 1$, the equation above can be reduced into:

$$\left[\boldsymbol{\epsilon'} \cdot \boldsymbol{Y}_{1\pm1}(\boldsymbol{k'}) \boldsymbol{\epsilon} \cdot \boldsymbol{Y^*}_{1\pm1}(\boldsymbol{k}) \right] = \frac{3}{16\pi} [\boldsymbol{\epsilon'} \cdot \boldsymbol{\epsilon} \mp i(\boldsymbol{\epsilon'} \times \boldsymbol{\epsilon}) \cdot \boldsymbol{z}_j - (\boldsymbol{\epsilon'} \cdot \boldsymbol{z}_j)(\boldsymbol{\epsilon} \cdot \boldsymbol{z}_j)] \tag{2.14}$$

whereas for $L = 1, M = 0$, the vector harmonic summation comes to:

$$\left[\boldsymbol{\epsilon'} \cdot \boldsymbol{Y}_{10}(\boldsymbol{k'}) \cdot \boldsymbol{\epsilon} \cdot \boldsymbol{Y^*}_{10}(\boldsymbol{k}) \right] = \frac{3}{8\pi} [(\boldsymbol{\epsilon'} \cdot \boldsymbol{z}_j)(\boldsymbol{\epsilon} \cdot \boldsymbol{z}_j)] \tag{2.15}$$

Thus, the total contribution of E_1 transition in Equation 2.13 from the j^{th} magnetic ion can be written as:

$$f_{res}^{j} = (\boldsymbol{\epsilon'} \cdot \boldsymbol{\epsilon}) F^{(0)} - i(\boldsymbol{\epsilon'} \times \boldsymbol{\epsilon}) \cdot \boldsymbol{z}_j F^{(1)} + (\boldsymbol{\epsilon'} \cdot \boldsymbol{z}_j)(\boldsymbol{\epsilon} \cdot \boldsymbol{z}_j) F^{(2)} \tag{2.16}$$

with

$$F^{(0)} = (3/4k)[F_{11} + F_{1-1}] \tag{2.17}$$

$$F^{(1)} = (3/4k)[F_{11} - F_{1-1}] \tag{2.18}$$

$$F^{(2)} = (3/4k)[2F_{10} - F_{11} - F_{1-1}] \tag{2.19}$$

The first term of Equation 2.16 without magnetic contributions is Thomson scattering, where the polarisation factor matrix $\boldsymbol{\epsilon'} \cdot \boldsymbol{\epsilon}$ has already been analysed. The second and third terms represent the first and second harmonic magnetic scattering, often observed away from charge scattering peaks as magnetic satellites due to a specific magnetic structure with a non-zero propagation vector. As stated above, the coefficients in front of each term $F^{(i)}$ depend on the overlapping integrals of the magnetic transitions, which are primarily enhanced at the resonant absorption edge.

For the magnetic scattering terms in Equation 2.16, the magnetic moments are coupled with polarisation vectors, which could result in the non-zero contribution

to the off-diagonal terms if the scattering amplitude was written into the matrix form. Further reducing the tensor form of Equation 2.16 based on the scattering geometry in Figure 2.1, we can generate an empirical formula for the analysis of the polarised X-ray scattering experiments:

$$f_{res}^{j} = F^{(0)} \begin{bmatrix} 1 & 0 \\ 0 & \cos 2\theta \end{bmatrix} - iF^{(1)} \begin{bmatrix} 0 & z_1 \cos\theta + z_3 \sin\theta \\ z_3 \sin\theta - z_1 \cos\theta & -z_2 \sin 2\theta \end{bmatrix}$$

$$+ F^{(2)} \begin{bmatrix} z_2^2 & -z_2(z_1 \sin\theta - z_3 \cos\theta) \\ z_2(z_1 \sin\theta + z_3 \cos\theta) & -\cos^2\theta((z_1)^2 \tan^2\theta + (z_3)^2) \end{bmatrix}$$

where θ is the scattering angle and the jth magnetic moment $\boldsymbol{z}^j = (z_1^j, z_2^j, z_3^j)$. Given that the second harmonics $F^{(2)}$ is significantly weak, we usually consider the first two terms when performing polarisation analysis. The first term (or charge scattering) will not generate the off-diagonal in the matrix. Therefore, no polarisation shift occurs. However, in the polarisation channel of $\sigma - \pi$ and $\pi - \sigma$, the structure factor has the contribution from the magnetic moments along the x or z direction. This pure magnetic effect is feasible for detection using a polarisation analyser crystal. Another feature worthy of notice is the diagonal contributions from the magnetic components. On the one hand, there is no contribution from the magnetic moment in $\sigma - \sigma$ channel. On the other hand, the $\pi - \pi$ channel consists of a non-magnetic contribution from charge and a sinusoidal harmonic term associated with y component of magnetic moment. In the following chapters, we will apply this empirical scattering formula for analysing respective magnetic structures.

2.2.2 Basis of magnetic absorption

X-ray photoelectron spectroscopy (XPS) and X-ray absorption spectroscopy (XAS) are prevailing techniques for beamline experiments since these two methods complement each other. The former investigates the occupied electronic states, and the latter focuses on the unoccupied states. Employing sum rule analysis on the magnetic circular dichroism (MCD) spectra of X-ray absorption, one can distinguish the moment contribution from spin or orbital in the absorption spectrum. The precision of applying XAS for moment measurements can be compared with the established

methods, such as vibrating sample measurement (VSM) or superconducting quantum interference device (SQUID) magnetometry. The X-ray method features the direct measurements of electronic spin states that are quantum mechanical, whilst the high precision magnetometry responds to the magnetic moment, which is the quantum phenomena in the macroscopic regime.

As demonstrated in the previous section, the scattering cross section is directly coupled with the transition probability described by Fermi Golden Rule. Analogously the absorption coefficient μ can be characterised by the absorption cross section, the underpinning of which is still the probability of electronic state transition upon excitement:

$$\mu \propto \frac{P_{i\to f}}{I_{ph}} = \frac{1}{I_{ph}} \sum_{f,i} M_{E_n}^2 \cdot (1 - n(E_f)) \cdot \delta(\hbar\omega - (E_f - E_i)) \tag{2.20}$$

Here, I is the total X-ray flux intensity, M_{E_n} represents the transition matrix element by n^{th} order electric approximation, such as E_1 for electric dipole approximation, $1 - n(E_f)$ refers to the density of unoccupied final state. According to the E_1 dipole approximation, the selection rules: $\Delta m_s = 0, \Delta m_l = \pm 1$ describe the transitions such as $2p$ to d states at $L_{2,3}$ absorption edges or transitions from $1s$ to p at the K edge. In contrast, quadrupole (E_2) contribution follows a different selection rule $\Delta m_l = 2$. The interference between E_1 and E_2 may simultaneously contribute to the absorption spectra.

The vital selection rules for electron hoppings suggest that the absorption intensity may reflect the density of the spin states; in other words, the difference between spin-up or spin-down states (e.g. magnetic moment) may lead to the contrast of absorption intensity while probing with the different polarised photons under the same orientation.The common practice for such an effect can be found using a circularly polarised X-ray beam called *X-ray Magnetic Circular Dichroism (XMCD)*. The schematic of the XMCD effect in Fe metal for the L edge spectrum is shown in Figure 2.3 with valence states exhibiting a Stoner splitting. In contrast, the density of states for spin-up (blue filling) and spin-down (green filling) states is inequivalent. The probability of transitions from $2p$ core-shell to $3d$ empty states

are different when excited by photons with positive or negative angular momentum. Since the opposite spin-orbital coupling for $p_{3/2}$ and $p_{1/2}$, the spin polarisation states are opposite at two absorption edges, resulting in the swiching of sign for circular dichroism signal, as shown in Figure 2.5 (c). As the result of spin-flips forbidden in E_1 transitions, the excited photoelectrons can only reside in the d-hole state with the same spin polarisation. Hence the transition intensity is simply proportional to the density of empty d states whilst the spin-split valence $2p$ shell serves as the 'detector' for photon spin polarisation.

This way, the magnetic circular dichorim intensity exhibits an angular dependence between light polarisation $\boldsymbol{L_{ph}}$ and magnetisation $\boldsymbol{M}$. The maximum XMCD effect is found at collinear arrangement between the light polarisation state $\boldsymbol{L_{ph}}$ and magnetisation state $\boldsymbol{M}$, whereas the minimum XMCD effect is found for antiparallel alignment.

$$I_{XMCD} \propto P_{circ}\boldsymbol{M} \cdot \boldsymbol{L_{ph}} \propto P_{circ}\langle \boldsymbol{M} \rangle cos\theta \tag{2.21}$$

where P_{circ} is the degree of circular polarisation, which is defined as 1 for fully circular polarisation, θ is the relative angle between spin polarisation of photon and magnetisation direction, and $\langle M \rangle$ represents the expected value of the magnetic moment of the $3d$ shell.

Analogously, linear dichroism can be easily understood by replacing the circular polarisation state of a photon with linear polarisation when performing absorption spectroscopy. Noticeably, the angle dependence effect between the incident E field and sample axis can also be found in the system absence of spin, where the contribution is only attributed to the anisotropic charge distribution caused by bonding, which is termed a 'natural' linear dichroism. The precise definition of magnetic linear dichroism refers to the linear dichroism arising from the magnetic origin, whereby the anisotropic charge order is preferentially modified relative to the spin directions by magnetic order and spin-orbital coupling effects. To exclude the 'natural' linear dichroism, the magnetic system with cubic symmetry is ideal for searching for magnetic linear dichroism since the spherical charge distribution (for

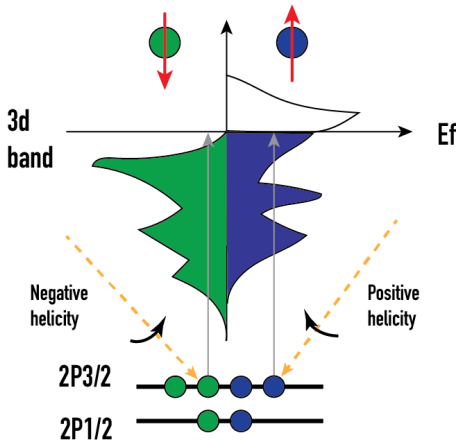


Figure 2.3: Electronic transition diagram for XMCD in L-edge absorption for Fe element, illustrated by one-atom model. The transitions occur from the spin-orbital splitting of the $2p$ core shell to $3d$ empty states. The electrons are selectively excited by circular polarised X-rays with different helicity, thus resulting in the so-called dichroism effect that the X-ray absorption difference can carry the information of spin moment.

cubic symmetry, p or d orbitals are spatially spherical due to the degeneracy) around the atom due to chemical bonding can always be suppressed in such symmetric environment while only magnetic linear dichroism counts. However, for magnetic atoms without a cubic symmetry environment, the linear dichroism effect due to magnetic origin can also be revealed by tuning the magnetic order with an external magnetic field or temperature cycling when 'natural' linear dichroism maintains under an external field.

X-ray magnetic linear dichroism (XMLD) from X-ray absorption (XAS) can be identified in both ferro- and anti-ferromagnetic systems. Because the electric field (E) of linear polarisation X-ray acts as a search light for the number of valence holes in different orientations of atomic orbitals, the axial alignment between the X-ray E field and magnetisation M of the sample weighs huge for the XAS. The XMLD signal can usually be obtained from axial-parallel or axial-normal orientations between light polarisation and magnetisation axis by $I_{XMLD} = I_{\parallel} - I_{\perp}$, while the angular dependence can thus be described by :

$$I_{XMLD} \propto P_{lin}|\boldsymbol{M} \cdot \boldsymbol{E}|^2 \propto P_{lin}\langle \boldsymbol{M}^2 \rangle \cos^2\theta \tag{2.22}$$

the θ angle refers to the relative orientation between E field polarisation and M

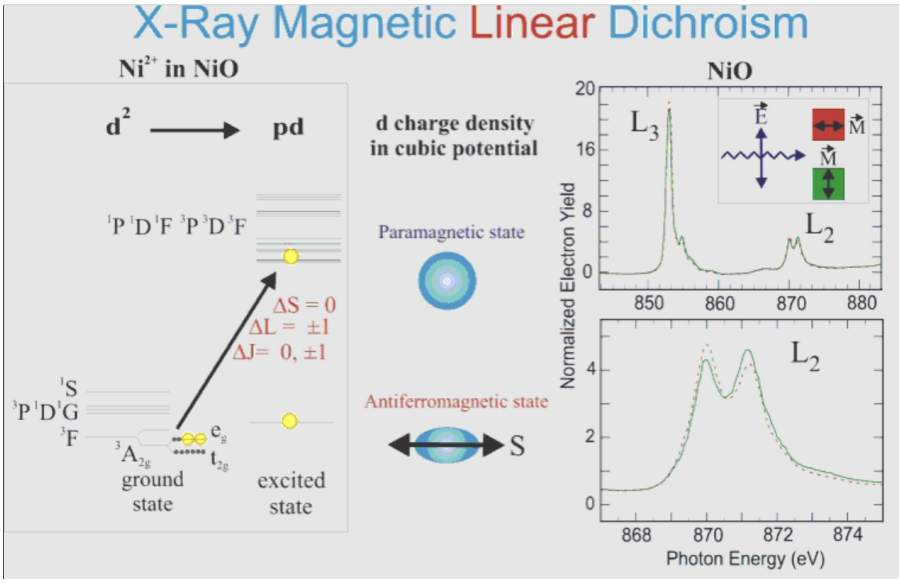


Figure 2.4: The electronic configuration of Ni^{2+} in NiO (left) and the XMLD effect for L-edge X-ray absorption (right). The $p-d$ hole picture describes the L-edge absorption for Ni^{2+}, and the complicated selection rules are responsible for the linear dichroism effect. The spin-orbital coupling twists the d orbital charge distribution along the magnetisation axis in the antiferromagnetic phase. Figure is adapted from permission [82].

direction, while P_{lin} represents the degree of linear polarisation of E field and $\langle M \rangle$ is the expectation of magnetic moment.

A typical example of XMLD application can be found in a cubic antiferromagnetic NiO, which is paramagnetic above 520K and orders antiferromagnetically at room temperature with Ni^{2+} spins aligned antiparallelly within the (1,1,1) plane along three possible directions in the fcc lattice. As shown by Figure 2.4, the maximum XMLD signal for the antiferromagnetic phase is visible at the Ni L_2 edge, contributed by the contrast from the signals obtained with geometries of $E_{\parallel}$ and $E_{\perp}$. The left subplot shows the electronic configuration of room temperature Ni^{3+} upon linear polarised absorption. Due to multiplet and crystal field effects, the ground state consists of two d holes ($3d^{8+}$ in electronic configuration), while the excited state is formed by $2p$-$3d$ hole configuration, while one electron is hopping from $2p$ by X-ray absorption. The spin-orbital couplings lead to the distortion of charge distribution along the magnetic axis, thus forming the magnetic linear dichroism.

Both XMCD and XMLD effects can be applied to determining the density of spin state and magnetic domain imaging. When an absorbed X-ray photon excites

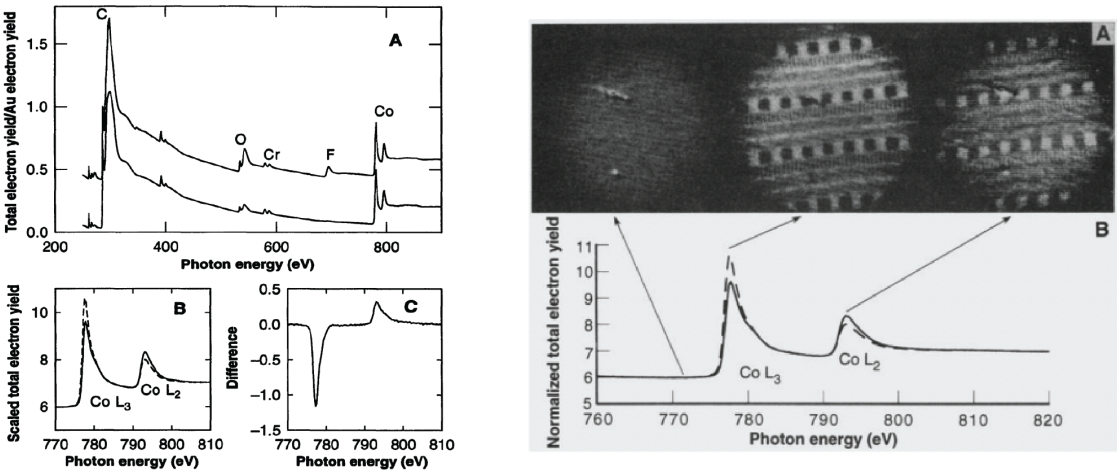


Figure 2.5: Left. X-ray absorption spectra of CoPtCr magnetic recording disk. (a) total electron yield (TEY) mode from linear polarised X-ray beam; (b) Spectra for near L edge of Co with left circular (solid line) or right circular (dashed line) polarised X-ray photons; (c) Circular dichroism obtained from (b). **Right.** Magnetic domain images obtained by XMCD at L_3, L_2 Co edge. Reprinted with permission from J. Stöhr *et al.* [83].

a core electron, higher energy level electrons will hop to occupy the hole position accompanied by the emission of either a photon or an Auger electron; these two processes can usually be adopted to obtain the XMCD/XMLD signal. Therefore, the absorption coefficient of X-ray can be measured by the fluorescence yield (FY) or the Auger electron along with the cascade secondary electrons, called total electron yield (TEY). The TEY mode requires an external bias electric field to obtain the drain current by releasing the secondary electrons from bulk to the sample surface, while the FY mode does not. Circular dichroism of the Co element for the $L_{2,3}$ edge can be seen in Figure 2.5 (B, C) obtained by the TEY mode, the sign of which are opposite due to the reversal of spin polarisation state between $2p_{3/2}$ and $2p_{1/2}$. The early work done by J.Stöhr in CoPtCr reveals the high potential of XMCD application in imaging by introducing the PEEM (Photo-Emission Electron Microscope) into the Co L edge spectra, as shown in Figure 2.5, right panel.

In contrast with other electron microscope techniques with spin polarisation freedom for magnetic imaging, such as Lorentz microscopy, scanning electron microscopy with polarisation analysis (SEMPA), spin-polarised low-energy electron microscopy (SPLEEM), XMCD-PEEM excels in elemental and chemical state

specificity as well as variable probing depth, with relatively generous constraints to sample quality. This XMCD-PEEM combination is advantageous for magnetic heterostructures with multiple magnetic layers, such as Pt/Co/Fe or alloys like CoFeB. In the later chapter, I will utilise this technique to investigate the magnetic domains and their topological structures in α-Fe_2O_3 thin films by XMLD-PEEM, with similar methodology but features in revealing antiferromagnetic domains and other novel textures.

2.3 Experiment instruments

2.3.1 X-ray tube

The history of X-ray traces back to a photograph Röntegen took accidentally in the lab in 1895 by a mysterious radiation that had never been discovered before. This novel radiation was named 'X-ray' due to the lack of information at that time. It was found to be able to penetrate through almost everything. This peculiar radiation was generated from the discharge tube which finally became the prototype of the first-generation X-ray source. Following researchers revealed that X-ray is nothing but electromagnetic radiation with a short wavelength located to the order of Angstroms (Å), comparable to the length of atoms. After knowing the wave behaviour of this particular radiation, several fundamental phenomena, such as *absorption*, *emission* and *diffraction* process, were successively investigated, leading to a series of advanced techniques widely applied in modern industry. These descendant techniques associated with X-rays are now widely used in the fields of medicine, physics, and chemistry.

The tube-type X-ray source is widely applied in commercial equipment like diffractometers, as shown in Figure 2.6. The electrons emitted from heating Tungsten filaments by high voltage are accelerated within a finite potential range, bombarding the target material. The rapid deceleration of electrons causes a series of reactions including the emission of X-ray radiation. Some of the collisions between the thermal electrons and the target result in the emission of a continuous X-ray spectrum, which is called white radiation or *Bremsstrahlung*. By contrast, several

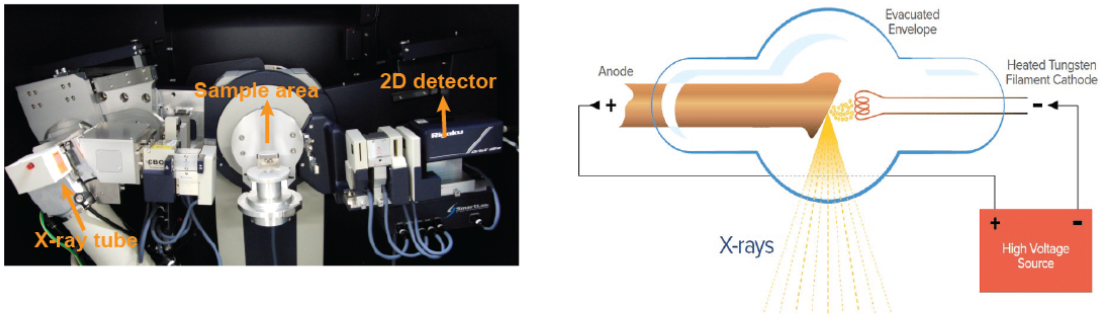


Figure 2.6: The lab-based X-ray diffractometer from Smartlab Rigaku. (a) The lab-based X-ray diffractometer, and (b) the X-ray tube diagram[84]. The X-ray photons were emitted from the copper target by thermal electron bombarding.

characteristic radiation peaks may arise on top of the *Bremsstrahlung* background due to the kick-off and re-filling of the core-shell electrons arranged in the atomic levels. The characteristic lines in the absorption or emission spectra are labelled as K, L, M, ... corresponding to the principle quantum number n = 1, 2, 3, ... of the core-shell electrons. A more specific classification of characteristic lines can be made according to the energy level difference, e.g. if the two atomic energy levels differ by only one quantum number (n=2 to n=1 or n=3 to n=2) then the transitions are called α lines. Whereas the spectra lines with an energy level difference exceeding more than one quantum number are often called β lines. A Copper (Cu) K_α line of energy 8.04 keV is typically used for a lab-based diffractometer. In contrast, the fluence from K_β lines is much less intense than the K_α, which can be filtered when performing diffraction experiments.

2.3.2 Synchrotron facility

Another dominant X-ray source is generated from a cyclic accelerator, descended from the cyclotron proposed by Lawrence [88] at Berkeley. When a linear accelerator boosts the electrons to relativistic speed, they are entered into the circle orbitals called storage rings. Bending by a series of magnetic poles, the electrons stored in the rings can continuously emit broad spectrum radiation from infrared to hard X-ray range; this physical process is called *synchrotron radiation*. The modern

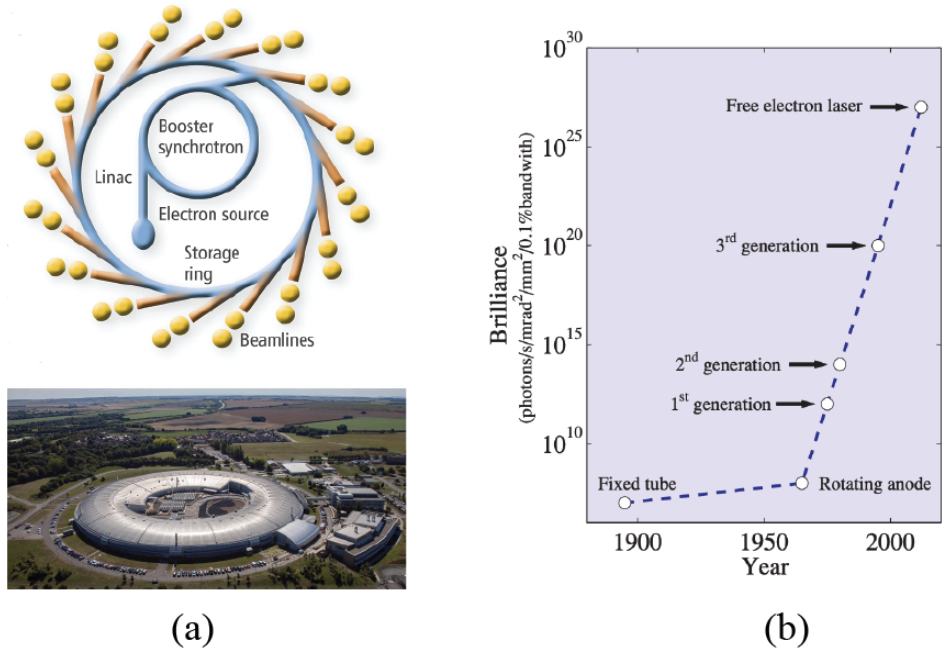


Figure 2.7: (a) Synchrotron facility and accelerator based X-ray radiation[85, 86]. (b) Brilliance of X-ray growth as a function of time[87]. A cliffy brilliance increase after the 3rd generation synchrotron facility emerged. The most advanced 4th light source is the free-electron laser (FEL), whose peak brilliance has exceeded 10^{30}.

synchrotron facility is also called a synchrotron light source, consisting of four main components as indicated in 2.7(a): the *linac* and *booster* are accelerator part that boosting electrons to the speed of relativity. These relativistic electrons are stored within the *storage ring* with a constant energy that can provide stable synchrotron radiation output. The experimental stations built along the tangent lines of the electron trajectory are called *beamlines*, where most of the experiments occur. The second-generation synchrotron facility deflects the electrons by bending magnets, limiting the radiation's focusing and polarisation.The third generation facility upgrades the magnetic structures with an array of magnet components called *undulators*, making the electrons wiggle, creating a more focused beam of radiation with higher polarisation quality.

A typical 3rd generation synchrotron facility is the Diamond Light Source (DLS), shown by Figure 2.7 (b), where 3 Gev energy electrons provide high brilliant, coherent, broad spectrum X-ray radiation that can satisfy the requirements in many scientific areas. Due to the fast development of the acceleration technique, the

brilliance (an index for measuring the quality of X-ray beams) of X-ray radiation has surged tens of orders in contrast to the rotation anode tube. The latest 4th generation synchrotron is also called free electron laser (FEL), which can provide high flux, broad spectrum, and extremely short pulse beams.

2.4 Micromagnetic simulation

With the aid of rapid-growing computing ability in recent decades, multiscale modelling is drawing significant attention in interdisciplinary subjects, especially in the large-scale simulation of a complex system like strong correlation electron system. The material properties or system behaviours from different levels of information are investigated by particular simulation approaches, which makes an excellent complement to tackle the problems that are unsolvable by current experiment tools. The magnetic properties of a system are studied by different methods in different scalings, given the available computing resources. The Ab-initio calculation involves the quantum mechanical solution of the interacting electrons. The standard formalism is the Density Functional Theory (DFT) which is highly consuming in computing resources due to solving many-body problems and thus often limited to a few hundred atoms. The atomistic spin dynamics calculation makes the adiabatic approximation of a classical atomic spin with fixed length and complete rotation freedom under the classical Heisenberg regime. This method can calculate systems of 10^6 to 10^8 spins and timescales of up to $\sim$ 100 ns. The *micromagnetic* calculation is based on the continuum approximation, which ignores the material's atomic structure to extend several orders' lengthscale and timescale of the system. The mechanical equations for the micromagnetic method are the same as the spin dynamics described by Landau-Lifshitz-Gilbert (LLG) atomistic spin models. Most magnetic modelling is performed in a micromagnetic way using finite difference and finite element flavours [89, 90]. Two prevailing software that is widely used is Object Oriented MicroMagnetic Framework (OOMMF) [91] and Mumax3 [92].

Micromagnetics has proven to be an essential tool for investigating various dynamic spin phenomena. However, more and more problems propose challenges

to the continuum approximation where structural symmetry has to be considered, such as exchange bias and anisotropy between interfaces in the heterostructure. Meanwhile, the ultrafast time scale of magnetic dynamics is increasingly significant in up-to-date research fields like ultrafast laser-induced demagnetisation. Traditional micromagnetics is insufficient to study the atomistic problems in an ultrafast time regime. Furthermore, micromagnetics is unfavourable for studying antiferromagnetic systems, which forbids the existence of net moment, the core of the dynamic model in micromagnetics.

Here we will introduce a new version of micromagnetics, VAMPIRE, an open-source package that is naturally advantageous in dealing with antiferromagnetic systems by providing customised lattice structure. This atomistic scale micromagnetic software bridges the gap between the computing cost *ab initio* method and the over-simplified continuum-based micromagnetic method. It can give a sub-nm spatial resolution and ultrafast time scale in studying a wide range of magnetic dynamical problems, including laser-induced magnetic dynamics, exchange bias in core-shell nanoparticles and multilayers, surface anisotropy, spin valve and spin torque, and temperature effects.

The VAMPIRE uses classical language to describe the atomic moment in a continuous 3D space, allowing for finite anisotropies and dynamic calculations. In some sense, this classical spin model is analogous to molecular dynamics (MD), where the energetics of the system are determined primarily from quantum mechanics. Still, the time evolution and thermodynamic properties are treated classically. We introduce the basic principles of VAMPIRE software and its extended functions in studying magnetic dynamics.

2.4.1 Introduction of atomistic micromagnetics

Definition of Energy terms

The atomistic spin dynamics usually are based on the adiabatic approximation with an effective local moment (mainly approximated by spin moment **S**) bonded

to the atomic sites, and Heisenberg approach on magnetic exchange term. The spin Hamiltonian $\mathcal{H}$ is typically formulated as:

$$\mathcal{H} = \mathcal{H}_{exc} + \mathcal{H}_{ani} + \mathcal{H}_{ext} \tag{2.23}$$

composing by the exchange interaction, magnetic anisotropy and external magnetic field.

The dominant term in spin Hamiltonian is the Heisenberg exchange, which is given by

$$\mathcal{H}_{exc} = -\sum_{i \neq j} J_{ij} \boldsymbol{S}_i \cdot \boldsymbol{S}_j \tag{2.24}$$

where J_{ij} is the exchange integral constant between adjacent unit spin vectors $\boldsymbol{S}_i, \boldsymbol{S}_j$. The unit spin vectors are taken from the actual atomic moment $\boldsymbol{\mu}_s$ by $\boldsymbol{S}_i = \boldsymbol{\mu}_s / |\boldsymbol{\mu}_s|$.

For ferromagnetic materials where neighbouring spins align in parallel, $J_{ij} > 0$, and for antiferromagnetic materials where the spins prefer to align anti-parallel $J_{ij} < 0$. Due to the strong distance dependence of the exchange interaction, the sum in Equation 2.24 is often truncated to include nearest neighbours only. This significantly reduces the computational effort while being a good approximation for many materials of interest. Usually, the exchange interaction can be extended to several atomic spacing by including second or higher-order nearest neighbour atoms when treating superexchange or double-exchange interactions. The simplest case of exchange interaction matrix $\boldsymbol{J}_{ij}$ is isotropic, meaning the exchange energy depends only on the magnitude of the spins. However, in more general cases the exchange interaction forms as a tensor with non-diagonal terms which describe anisotropic exchange interactions, e.g. Dzyaloshinskii-Moriya interaction,

$$\boldsymbol{J}_{ij} = \begin{pmatrix} J_{xx} & J_{xy} & J_{xz} \\ J_{yx} & J_{yy} & J_{yz} \\ J_{zx} & J_{zy} & J_{zz} \end{pmatrix} \tag{2.25}$$

therefore, the exchange summation in Equation 2.24 can be written in the tensor product

$$\mathcal{H}_{exc} = -\sum_{i \neq j} (S_x^i, S_y^i, S_z^i) \begin{pmatrix} J_{xx} & J_{xy} & J_{xz} \\ J_{yx} & J_{yy} & J_{yz} \\ J_{zx} & J_{zy} & J_{zz} \end{pmatrix} \begin{pmatrix} S_x^j \\ S_y^j \\ S_z^j \end{pmatrix} \tag{2.26}$$

The generic form of anisotropy is the single-ion uniaxial type, if not specified, where the magnetic moments prefer to align along a single axis which is often called the easy axis. It is an interaction confined to the local moment, the energy of which is given by the expression:

$$\mathcal{H}_{ani}^{uni} = -k_u \sum_i (\boldsymbol{S}_i \cdot \boldsymbol{e})^2 \tag{2.27}$$

where k_u is the anisotropy energy per atom. Uniaxial anisotropy is most commonly found in particles with elongated shape (shape anisotropy), or where the crystal lattice is distorted along a single axis as in materials such as hexagonal Co and FePt. For materials with a cubic crystal structure, such as iron and nickel, a different form of anisotropy known as cubic anisotropy is identified. Cubic anisotropy is generally much weaker than uniaxial anisotropy and has three principal directions: easy, challenging and tough magnetisation. The expression describes cubic anisotropy:

$$\mathcal{H}_{ani}^{cub} = \frac{k_c}{2} \sum_i (S_x^4 + S_y^4 + S_z^4) \tag{2.28}$$

where k_c is the cubic anisotropy energy per atom.

The Zeeman energy from the interaction between magnetic moment and external magnetic field composes the $\mathcal{H}_{app}$ term,

$$\mathcal{H}_{app} = -\sum_i \mu_s \boldsymbol{S}_i \cdot \boldsymbol{H}_{app} \tag{2.29}$$

where atomic moment $\boldsymbol{\mu}_s$ is involved. External areas can arise in many ways, such as a nearby magnetic material or an effective field from an electric current.

Dynamical equations

Although the spin Hamiltonian describes the energetics of the magnetic system, it provides no information regarding its time evolution, thermal fluctuations, or ability to determine the system's ground state. Suppose the system is evolved at 0 K where no thermal fluctuations are considered on the spin moment; the Landau-Lifshitz-Gilbert equation can describe the time-dependent dynamical equation for a macroscopic moment,

$$\frac{\partial \boldsymbol{m}}{\partial t} = \gamma[\boldsymbol{m} \times \boldsymbol{H} + \alpha \boldsymbol{m} \times (\boldsymbol{m} \times \boldsymbol{H})] \tag{2.30}$$

where $\boldsymbol{m}$ is a unit vector representing the direction of the sample magnetisation, $\boldsymbol{H}$ is the effective applied field acting on the sample, γ is the gyromagnetic ratio, and α is the material's phenomenological damping constant property. This equation describes two basic motions of the moment: the first term in Equation 2.30 is the precession rotation under an external magnetic field; the second term represents the relaxation of the moment arising from the intrinsic couplings such as spin-lattice and spin-electron interactions, and extrinsic couplings, e.g. demagnetisation fields, field defects, doping and temperature. The atomic moment is represented by unit spin vector $\boldsymbol{S}_i$ and only intrinsic damping λ for the local moment is considered; the macroscopic LLG equation can be reformed into:

$$\frac{\partial \boldsymbol{S}_i}{\partial t} = -\frac{\gamma}{(1+\lambda^2)}\left[\boldsymbol{S}_i \times \boldsymbol{H}^i_{eff} + \lambda \boldsymbol{S}_i \times \left(\boldsymbol{S}_i \times \boldsymbol{H}^i_{eff}\right)\right] \tag{2.31}$$

where $\boldsymbol{H}^i_{eff}$ is the effective magnetic field at the site i, which can be obtained from spin Hamiltonian by

$$\boldsymbol{H}^i_{eff} = -\frac{1}{\mu_s}\frac{\partial \mathcal{H}}{\partial \boldsymbol{S}_i}$$

Given the typical energies in the Hamiltonian of 10 μeV - 100 meV range, the effective field derived from the first derivative yields 0.1-1000 T when the spin moment is set to the same order as Bohr magneton. The units of effective physical variables used in the dynamical simulation of VAMPIRE are listed in Table 2.33 below.

Table of key values and their units in VAMPIRE simulation (2.32)

Variable	Symbol	Unit	
Atomic magnetic moment	μ_{S}	Joules/Tesla	(J T^{-1})
Unit cell size	a	Angstroms	(Å)
Exchange energy	J_{ij}	Joules/link	(J)
Anisotropy energy	k_{u}	Joules/atom	(J)
Applied field	$\mathbf{H}$	Tesla	(T)
Temperature	T	Kelvin	(K)
Time	t	Seconds	(s)

(2.33)

2.5 Conclusion

This chapter reviews several experimental techniques for probing magnetic properties in a general magnetic system. First, we introduced two categories of the interaction process between magnetic materials and X-ray photons, which paved the foundation for other proliferated experiment techniques that are commonly used nowadays. In the third section, we introduce several experimental instruments that can be accessible from built-in laboratories and large facilities. These are popular approaches for crystallographic and magnetic characterisations and for probing non-equilibrium magnetic dynamics. In the last section, we introduce new software that emerged recently for micromagnetics. A brief introduction to the physical background of this tool could help to discover the atomic scale feature that is significant for the simulations of the antiferromagnetic system. Subsequent chapters will present experimental results using techniques mentioned above for many interesting magnetic phenomena.

3

Switching of multiferroic Y-type hexaferrite

Contents

3.1 Introduction 48
3.1.1 Structures of Y-type hexaferrite 48
3.1.2 Block model for magnetic structure 50
3.1.3 Magnetic phase diagram 51
3.2 Electric control of the multiferroic phase 55
3.2.1 Ferroelectricity switched by the electric field 55
3.2.2 Ferroelectricity switched by the magnetic field 57
3.2.3 Ferroelectric polarity switched by the electric field . . . 60
3.3 Identification of the intermediate phase 63
3.3.1 Transport evidence 64
3.3.2 X-ray diffraction evidence 65
3.3.3 Intermediate phase diagram 68
3.4 Models of phase switching 69
3.4.1 Cone rotation model 70
3.4.2 Rotation model with phase coexistence 77
3.5 Conclusions 83

Multiferroics refer to the compounds in which magnetic and ferroelectric orders are coexisted, which are believed to be a promising material system to achieve cross-control between ferromagnetism and ferroelectricity. To realise highly efficient manipulation of electric-controlled magnetism, multiferroics are the most suitable platform to study with. Although Maxwell equations elegantly describe the

relations between $\boldsymbol{E}$ and $\boldsymbol{H}$ fields, the coupling between the order parameters $\boldsymbol{P}$ for ferroelectrics and $\boldsymbol{M}$ for available magnetic materials is highly nontrivial. From the point of view of symmetry, the former is related to the inversion symmetry operation I, while the latter is related to the time-reversal symmetry T. As magnetism is a macroscopic quantum mechanical phenomenon contributed by occupied bands or lone pairs of electrons, ferroelectricity is usually described by a classical charge dipole model where partially filled d or f orbitals are required. Distinct as they are, the coupling between the electric polarisation and magnetic moment is usually very weak because the electrons that arise from these scenarios are independent and less correlated. Suppose the electronic structure simultaneously satisfies electric polarisation and magnetic moment contribution; the magnetoelectric (ME) property can vastly be enhanced, especially in a long-range order system. Multiferroics is an ideal system to study the strong ME coupling in a phase where inversion symmetry and time-reversal symmetry are simultaneously broken. In this chapter, we will explore the multiferroicity in ferrite with a hexagonal crystalline structure called *hexaferrite*. A systematic investigation of magnetic phases and magnetic properties will be discussed. On this basis, we propose a new model for describing the switching between the anti-polarised domains, which gives a satisfying explanation for understanding the complicated switching process in hexaferrite.

3.1 Introduction

3.1.1 Structures of Y-type hexaferrite

The discovery of a rare-earth perovskite type magnetite $TbMnO_3$, which demonstrates a new mechanism for ferroelectricity arising from a cycloidal magnetic order [27, 28] has attracted extensive interest in type-II multiferroics. However, this perovskite candidate is disadvantageous at slight electric polarisation and low working temperature, making it unfavourable for practical usage. Another large group of ferroic oxides crystalising in a hexagonal structure (which is called hexaferrite) sheds light on the practical ME material. $Sr_3Co_2Fe_{24}O_{41}$ and $Ba_{0.8}Sr_{1.2}Co_2Fe_{12-x}Al_xO_{22}$ are reported to exhibit ferroelectricity near room temperature [35, 93], given that the

Hexaferrite types				
type	Chemical formula	Stacking sequence	c(A)	Space group
M	(Ba,Sr)Fe_12O_{19}	RSR*S*	23	$P6_3/mmc$
W	(Ba,Sr)$Me_2Fe_{16}O_{27}$	$RS_2R^*S_2^*$	33	$P6_3/mmc$
Y	$(Ba,Sr)_2Me_2Fe_{12}O_{22}$	TST'S'T"S"	43	$R\bar{3}m$
Z	$(Ba,Sr)_3Me_2Fe_24O_{41}$	RSTSR*S*T*S*	52	$P6_3/mmc$
X	$(Ba,Sr)_2Me_2Fe_{28}O_{46}$	$(RSR^*S_2^*)_3$	84	$R\bar{3}m$
U	$(Ba,Sr)_4Me_2Fe_{36}O_{60}$	$(RSR^*S^*TS^*)_3$	113	$R\bar{3}m$

Table 3.1: Different types of hexaferrite classified by the stacking manners of chemical blocks. The Me represents the divalent ions such as Mg^{2+}. The * in block symbol represents a 180-degree rotation around the c axis. And the apostrophe means the corresponding block is rotated by 120 degrees. The longer the sequence stacking, the more extended the c axis lattice parameter.

induced polarisation is relatively small because of the intrinsic limitation of type-II multierroics. Although few amounts of polarisation exist in type-II multiferroics in contrast with type-I such as $BiFeO_3$, the linear magnetoelectric coefficient is much higher ($\alpha_H = \frac{dE}{dH} \sim 1000$). The giant ME coupling enables the polarisation to be switched at a fragile magnetic field, making the type-II multiferroics outstanding in erasable memory devices.

Hexaferrite has long been applied for microwave devices and permanent magnets due to their room-temperature ferromagnetism and insulating properties. Most of the hexaferrite is ferrimagnetic at ground state, but there are exceptions for some types. The table shows six main classes in the hexaferrite family according to the stacking difference. The chemical formulas define three basic blocks: R $[(Ba,Sr)Fe_6O_{11}]^{2-}$, S $[Me^{2+}Fe_4O_8]$ and T $[(Ba,Sr)_2Fe_8O_{14}]$. As indicated in the table, the sequence stacking blocks for different types of hexaferrite affect the length of the c axial lattice parameter and the crystalline symmetries. Three out of the six types exhibit noncollinear magnetic orders as the ground state; they are M-type $Ba(Fe,Sc)_{12}O_{19}$ [94], W-type $BaNi_2Sc_2Fe_{16}O_{27}$ [95] and Y-type $(Ba,Sr)_2Zn_2Fe_{22}O_{22}$

[96, 97]. All these types hold the possibility for ME effects predicted by the spin-current model (as mentioned in Chapter 1). This chapter focuses on the Y-type hexaferrite in which the ME effect is first reported [98].

3.1.2 Block model for magnetic structure

The crystalline structure of the Y-type hexaferrite $Ba_2Mg_2Fe_{12}O_{22}$ (BMFO) belongs to space group $R\bar{3}m$, which does not allow spontaneous polarisation. To understand the magnetic structures within this rather complicated crystalline structure, it is convenient to divide the lattice into two block types according to the spin accumulation, distinct from the TS block, which is a classification from the crystal structure. One spin block is named the L block with significant overall spin moments (μ_L), and the other is the S block with smaller spin moments (μ_S). The moments from each magnetic ion tend to align antiparallelly to reduce the exchange energy of the block. By summing over the moments from the magnetic ions within the block, a simplification of a 'super-spin' can be established for representing the whole spin moment for each block, as illustrated in Figure 3.1. These super-spins lie within the *ab* plane to form a helical structure at room temperature or antiparallelly aligned between L and S blocks to form a ferrimagnetic structure at a higher magnetic field, which will be discussed in detail in the next paragraph. The boundary of the L and S block is located between two Fe ions (Wycoff position 6*c*) connected by Fe-O bonds, as highlighted by orange circles in Figure 3.1. The superexchange interactions across the boundary of these blocks are reinforced by replacing Ba with Sr [99], because the Fe-O-Fe bond angle can be tuned by substituting smaller Sr for larger Ba. As Sr doping increases, the Fe-O-Fe bonding angle is further reduced, which enhances the magnetic frustration at the boundary between blocks, leading to the non-zero tilting angle between the moments of the two Fe ions [100]. Thus, the noncollinear twisting between the super-spins is formed within the *ab* plane and propagates along the *c* axis, which composes proper-screw magnetic structure as reported in $Ba_{2-x}Sr_xZn_2Fe_{12}O_{22}$ compound [101, 102]. A similar doping

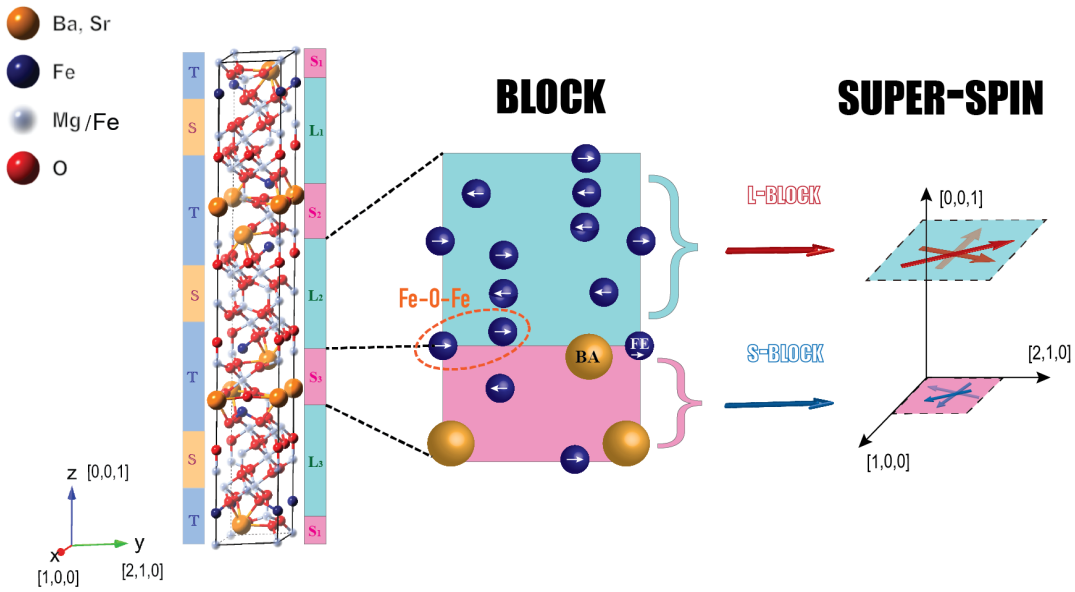


Figure 3.1: Schematics of the crystal structure and magnetic structure of Y-type hexaferrite $Ba_2Mg_2Fe_{12}O_{22}$. The crystal structure block is labelled by TS stacking on the left, while the magnetic structure block is denoted by the LS sequence on the right of the rhombohedral lattice structure. The magnetic blocking is divided according to the superexchange bonds between Fe ions, as shown in the middle diagram. These blocks stacking along the c axis are simplified into the super-spins model by summing over all the single ion magnetic moments within each block.

strategy can be applied to tune the magnetic phases in the candidate compound studied throughout the thesis.

3.1.3 Magnetic phase diagram

The ground state of Y-type hexaferrite $Ba_2Mg_2Fe_{12}O_{22}$ at room temperature free of the external field is ferrimagnetic. The twisting of the μ_S and μ_L develops as cooling down to 200 K and forms the incommensurate helical phase. However, this magnetic frustration-induced helical structure can be converted into ferrimagnetic phase under strong enough magnetic field [36, 103]. The BMFO undergoes a phase transition from helical to longitudinal cone structure (LC) at zero magnetic fields since 50 K [98]. This effect with a spontaneous out-of-plane moment can be explained by reducing the in-plane anisotropy at low temperatures. However, when applying a weak in-plane magnetic field, the longitudinal cone can be flipped into an *ab* plane, forming a transversal cone structure (TC). The LC phase exhibits

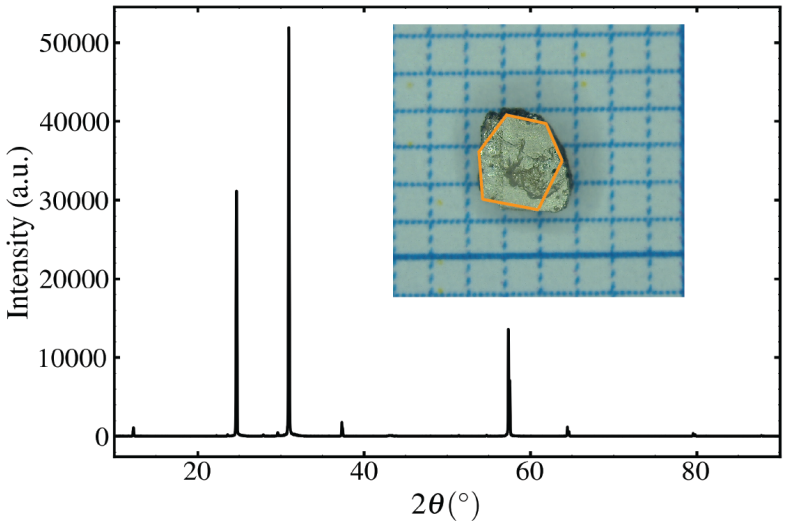


Figure 3.2: Crystalline characterisation of Y-type hexaferrite $Ba_2Mg_2Fe_{12}O_{22}$ by X-ray diffractometer. The high-quality XRD data is measured along the c axis by $\theta - 2\theta$ scan, showing a series of diffraction peaks in $(0, 0, 3n)$ direction that $R\bar{3}m$ space group allows.

various symmetries with different folds, such as two, four and six, depending on the field intensity [36, 98, 104]. Both the LC and helix phase are not polar since the inversion symmetry breaking is not allowed in the respective magnetic space group. The TC phase, however, can give rise to finite polarisation due to the non-centrosymmetric inverse Dzyloshinskii-Moria interaction (i-DMI). Nevertheless, the TC phase has many variants in different Y-type compounds, just like the LC phase. It is widely accepted that a two fan structure (one of the structures in the TC phase) is responsible for generating weak polarisation in the BMFO compound.

We study a high Sr-doped Y-type system $Ba_{0.5}Sr_{1.5}Mg_2Fe_{12}O_{22}$ (BSMFO), in which the phase diagram is dramatically modified by doping. The helical order temperature is tuned to above room temperature and the LC phase is developed since 150 K (as shown in Figure 3.3) when cooling down. The TC phase is derived from the LC phase by applying the IP magnetic field. As discussed later, the TC phase can be identified by magnetic diffractions with characteristic magnetic satellites due to commensurate magnetic sublattice. Our sample is grown by flux method with good hexagonal quality, as shown in Figure 3.2. An X-ray diffractometer characterises the fingerprints of $(0, 0, 3n)$ peaks on Rigaku Smartlab2000 under Cu k_α edge. The characteristic peaks indicate that the lattice parameter is approximately 43.3

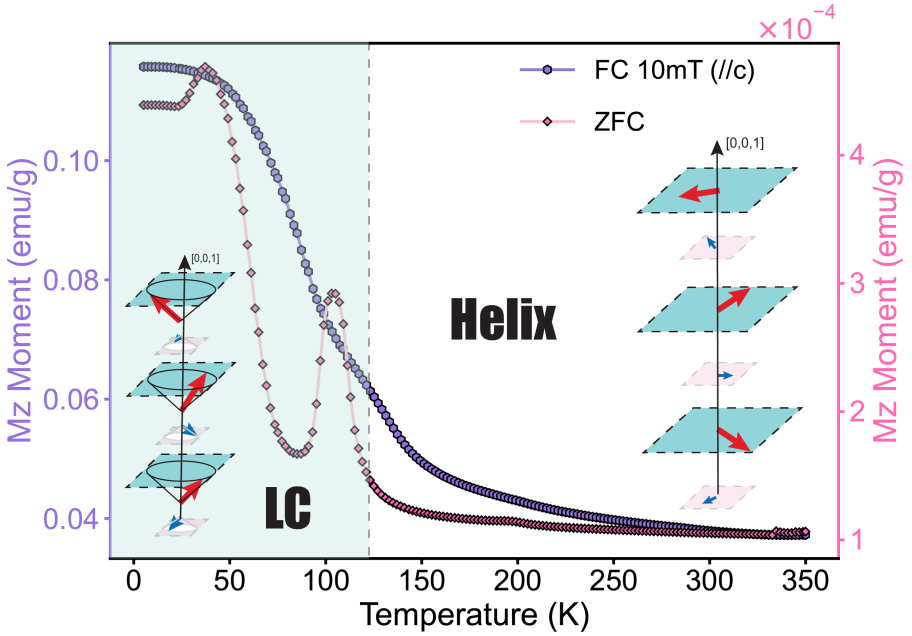


Figure 3.3: Magnetometry and magnetic phase transition of $Ba_{0.5}Sr_{1.5}Mg_2Fe_{12}O_{22}$. The helical phase is developed at room temperature with the finite out-of-plane moment. The longitudinal cone phase is developed when cooling down to 120 K. Both field cooling and zero field cooling strategies demonstrate the growth of the moments along the c axis due to the decrease in planar anisotropy at low temperatures.

Å for the c axis. The sample is annealed in an oxygen atmosphere to enhance the electrical resistivity because the Y-type hexaferrite is more conducting at a higher temperature, which is a hazard for switching experiments. The pre-annealing procedure can assist in maintaining electrical polarisation, which is significant for switching experiments at higher temperatures.

We performed the magnetometry measurements for identifying the magnetic phases by zero field cooling (ZFC) and field cooling (FC) procedures, as shown in Figure 3.3. The sample is mounted with a 2D rotational sample holder compatible with MPMS3 (Quantum Design) magnetic measurement system. The out-of-plane (OOP) magnetic moments in zero field cooling witness a peak occurred at 105 K following the rise since 120 K and finally saturate at 10 K. The OOP moment is significantly increased in field cooling conditions when the magnetic field is applied along the c axis, which is three orders larger than the ZFC case. From the magnet current measurements (which will be introduced in the next section) on the induced polarisation at the TC phase, we find the polarisation is lost when warming up

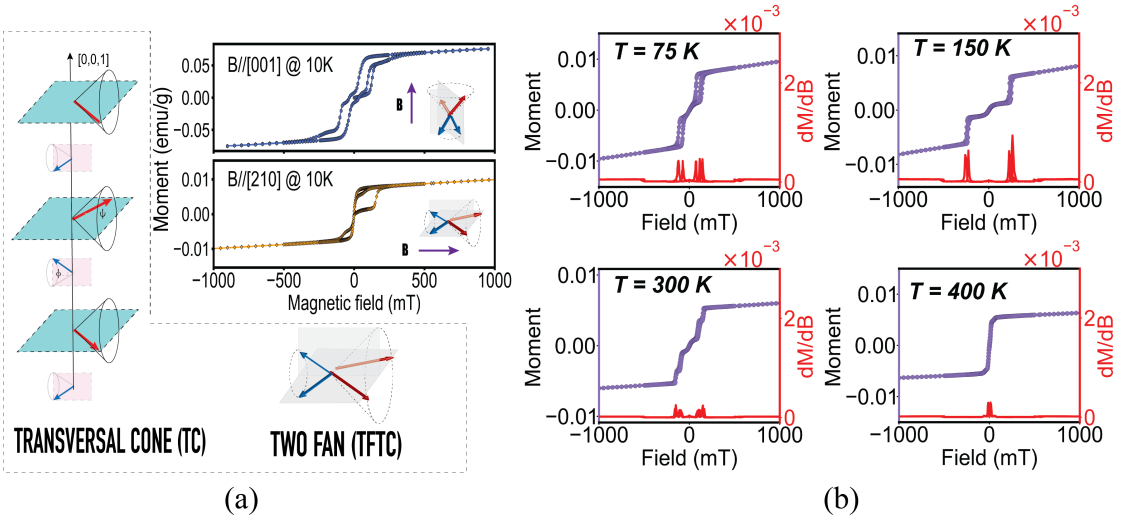


Figure 3.4: Magnetometry on the two fan transversal phase. (a) The SQUID measurements along the c and a^* directions. (b) In-plane moments are measured at different temperatures. The red curve is obtained from the derivative of the purple SQUID curve, which highlights the phase transition positions.

to 120 K. Thus; we conclude the phase boundary between LC and helical phase is 120 K as indicated by the dashed lines.

Then we move on to study the properties of TC phase through magnetometry while applying IP magnetic field. From the magnetometry data shown in Figure 3.4 (a), we find the hysteresis curves by sweeping the magnetic field either within the ab plane (bottom) or along the c axis (top) are primarily different. The magnetometry curve scanning along the c axis is more hysteretic (the top panel), which is largely attributed to the features of the LC structure. While a smaller hysteretic signal is found when applying the field within the ab plane (the bottom panel). The initial step-like half cycle occurring at 200 mT describes the flipping of the cone structure from the LC phase to the TC phase. However, a small remnant moment is observed within the plane when switching the field back and forth across zero. A rotational cone picture around the c axis can be described as triggered by IP magnetic field. A prevailing model for describing such TC structure is a two fan transversal cone structure (TFTC) [97, 98, 100], as shown by the inset diagram from many neutron and X-ray diffraction experiments. More IP scannings are performed in a series of temperatures, as shown in Figure 3.4 (b). Multiple phase transitions are observed

below room temperature. However, these features disappear at 400 K, which is ferrimagnetic according to previous literature [35, 100, 101]. These multiple-phase transitions indicate loads of details for the switching incidence and a simple cone rotation model. As discussed in later content, we show that a modified model can further understand the complexity of such phase transitions.

3.2 Electric control of the multiferroic phase

3.2.1 Ferroelectricity switched by the electric field

The ferroelectric polarisation in type-II multiferroics is relatively small, in contrast to proper ferroelectrics such as $BaTiO_3$ or type-I multiferroic $BiFeO_3$. It is pretty challenging to perform direct measurements on ferroelectrics with slight polarisation. Unfortunately, BSMFO is a system with weak polarisation due to the type-II multiferroic at low temperatures. We attempt to measure the weak ferroelectric polarisation at the TFTC phase from the P–E hysteresis loop, which is a straightforward demonstration of electric polarisation. The prevailing method of modern hysteresis loop measurement is based on the Sawyer-Tower method [105], which can estimate the charge through the variation of the voltage on a large capacitor plate during charging and discharging process when all the components are in series connection. Further modifications can be made to convert the voltage and current measurements through protection circuitry. However, this traditional method for measuring ferroelectric polarisation fails in magneto-electric systems where the size of polarisation usually is two to three orders of magnitude smaller. Moreover, weak polarisation is often masked with significant leakage and contributions from non-ferroelectric polarisation. Together with the domain switching kinetics and broader relaxation effects associated with depolarising fields [106–108], it makes the direct measurement of the P–E hysteresis loop in improper ME coupling materials very difficult. Therefore, new approaches are developed based on the Sawyer-Tower method to eliminate the non-hysteretic and leakage components.

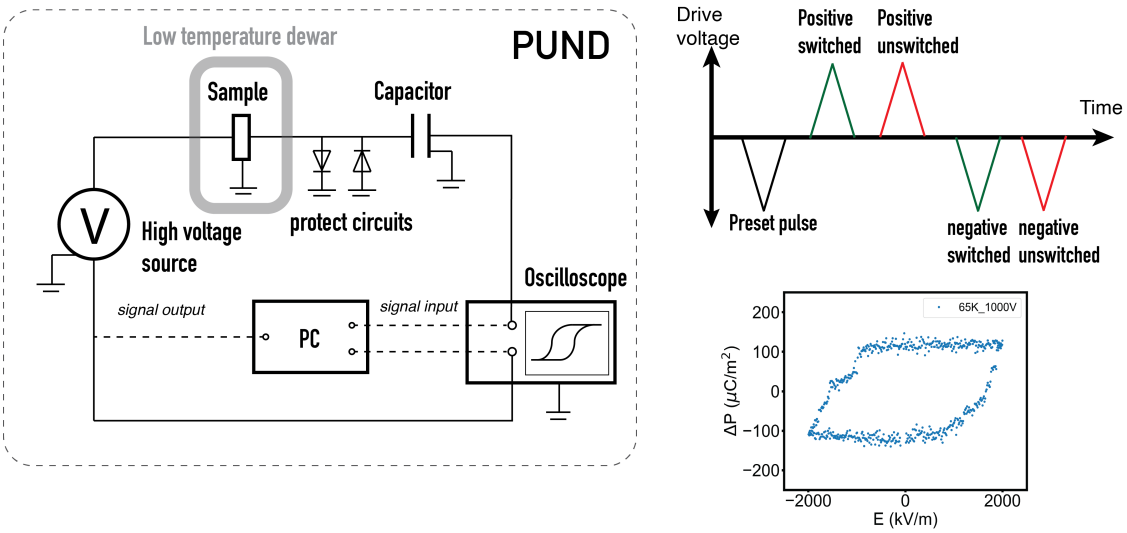


Figure 3.5: Experimental demonstration of ferroelectricity in multiferroic BSMFO. The left frame is the layout for the Positive-Up-Negative-Down (PUND) method for measuring ferroelectric polarisation. The hysteresis loop in the right corner is obtained from the above electric pulse train.

We adopt the Positive-Up-Negative-Down (PUND) method to measure the weak polarisation in multiferroic BSMFO. The experiment layout of the PUND setup, similar to the Sawyer-Tower strategy, is shown in Figure 3.5 on the left. The choice of the shunt capacitor is essential for obtaining a reliable dataset since too large a capacitance would reduce the voltage applied on the sample, which results in the failure of switching, whilst too small a capacitance would bring considerable leakage of charge. We prepared a set of shunt capacitances ranging from 10 nF to 5 μF for different sample properties. High voltage output goes from 100 V to 1200 V. To obtain a large enough electric field to realise the switching, we reduce the sample thickness instead of further increasing the voltage to protect the sample from breaking down. The PUND method features applying a train of five pulses, as shown in the diagram on the top right. A preset pulse is necessary for any ferroelectric measurement since the memory effect is present in any permanent ferroelectrics. The first preset pulse is sent for polarising the sample with a finite size of polarisation. Then, the ferroelectric polarisation can be switched by applying the pulse in the other direction (here is a positive sign). A successive pulse in the same direction is applied later to get rid of this dielectric response, which will

not switch the ferroelectric polarisation. The actual polarisation response in the positive half cycle can be obtained by subtracting the charge current signal from these two pulses. The other half cycle in the negative direction can be derived by applying two pulses in the opposite direction. Then the whole P–E loop can be composed of such procedures contained by five pulses, as shown in the diagram.

We performed the PUND experiment when the sample was cooled down into a multiferroic phase. The sample was firstly quenched to 10 K. However, the switching of ferroelectric polarisation went through multiple failures at such low temperatures due to the high coercivity of the polarisation, and the thin sample flake was somewhat fragile under such high voltage and easily broken down. A compromised strategy is slightly increasing the sample thickness and lifting the switching temperature. The final successful PUND result was obtained from a 0.5 mm thick flake under 1000 V, which could generate an electric field up to 20 kV/cm while keeping at 65 K from a lower temperature. The successful result is shown in the bottom-right panel in Figure 3.5, where a sizable 100 μ C/m^2 polarisation is measured under this improvement. This switching evidence supports the possibility of direct electric field switching by high voltage field, which paves the way for further developments of THz setup in chapter 4.

3.2.2 Ferroelectricity switched by the magnetic field

The direct switching of the polarisation is quite challenging due to three reasons as mentioned above: the electrical signal is faint because of the weak polarisation; the strong coercive field for the polarisation is enhanced at low temperature; the BSMFO sample is a poor insulator, and also an improper capacitor, which can be easily broken down by high voltage when adopting PUND method. Due to the mentioned reasons, we adopt the strategy of obtaining the polarisation from the displacement current by magnetic field switching. This magnetic field switching method can not only get a sizable current without the risk of breaking down the sample but can realise an effective polarisation switching by the weak magnetic field because of the high magnetoelectric coefficient.

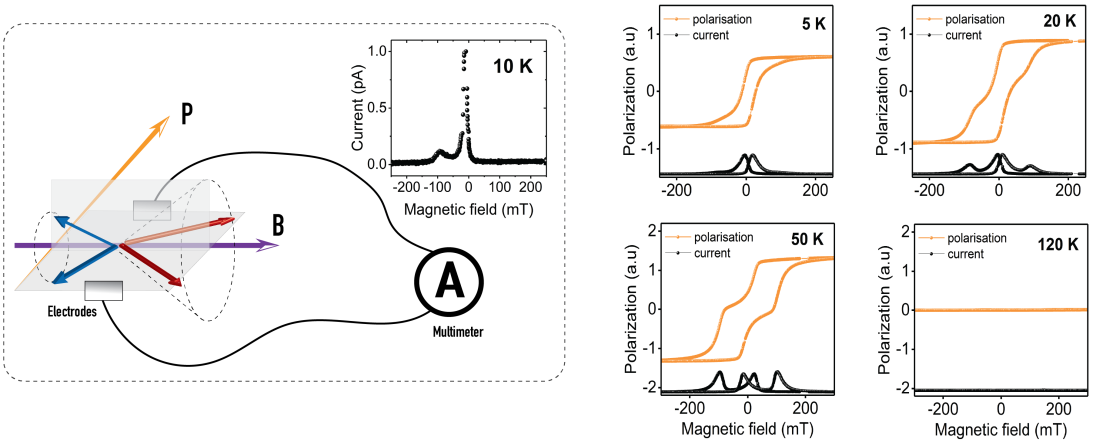


Figure 3.6: The ferroelectric polarisation is measured by magnetocurrent scheme. The left dashed box illustrates the magnetocurrent method designed for detecting the orthogonal polarisation. Switching polarisation by the magnetic field can generate a substantial magnetocurrent, labelled by a black curve. The polarisation is calculated by current integrals indicated by the orange curve. The temperature-dependent magnetocurrents are shown in right arrays, which implies that the ferroelectricity is lost at the cone/helical phase boundary near 120 K.

The spin twisting induces the polarisation according to the inverse Dzyaloshinskii-Moria interaction (i-DMi) as the cone structure is flipped into the *ab* plane. Therefore, the measurement geometry requires the current to be detected orthogonal to the applied magnetic field, as illustrated in Figure 3.6 left dash box. The sample is mounted on the bespoke probe with four channel electrodes. Two channels are used for collecting the current, mounted on the sample surface and elongated out of the fridge to the multimeter. The probe is suitable for the Quantum Design company's physical property measurement system (PPMS), which can provide low temperature and magnetic field of up to 7 Tesla. Only a weak field up to 0.5 T is required in our experiments. When cooling the sample straightforwardly to 4 K, and then applying a weak magnetic field to 250 mT, the TFTC phase can be well established. However, to obtain a considerable macroscopic polarisation, we must apply a biased electric voltage since 100 K when the sample becomes insulating. The voltage poling helps to establish a single polarised domain. Once triggering the magnetic field to the opposite direction, we can observe a substantial current generated by sweeping the field, as shown in the corner subplot within the

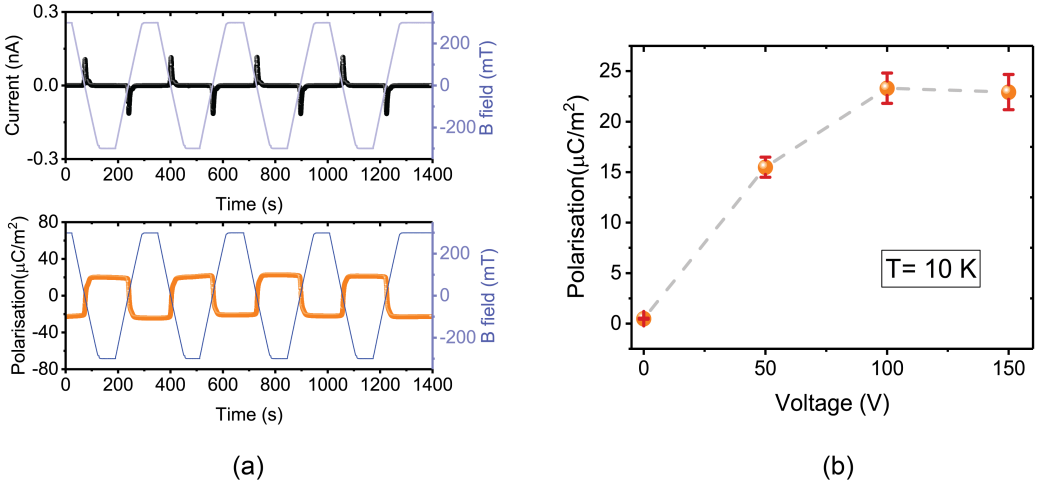


Figure 3.7: Magnetic switching of electrical polarisation at low temperatures. (a) Sequence switchings of the magnetocurrent (top) and polarisation (bottom) by magnetic field sweeping. The purple curve indicates that the field is applied between -250 mT to 250 mT. (b) The polarisation is scaling dependent on the applied bias voltage. Multiple cooling cycles to 10 K under different voltage magnitudes are performed after warming at room temperature for more than 1 hour.

dashed box. A step-like current peak is induced when the field crosses the zero point, the sharpness of which is dependent on the rate of magnetic field scanning, which was set as 15 Oe/s during all the measurements for the consideration of balancing the peak sharpness and amplifier threshold.

The size of polarisation is calculated from the current intensity by integration, as shown in Figure 3.6 orange curve. We can switch the polarisation direction repeatedly, almost without any loss from the polarisation hysteresis. The size of polarisation is slightly increased as warming up, mainly because the sample is becoming more conducting that some charges can be trapped between domain walls or contacts. However, the measured polarisation dropped significantly when warming up to 120 K. The poled single domain becomes much less polarised when the TFTC phase approaches the phase boundary, and the remaining polarisation is negligible. From the perspective of ferroelectric properties, we can estimate that the 120 K is approaching the phase transition boundary between cone phase (polar) and the helical phase (non-polar).

Once the sample is fully polarised, the measured polarisation can be maintained

after multiple times of switchings, as shown in the Figure 3.7 (a). The polarisation curve in the bottom subplot demonstrates step-like switchings following the driving magnetic field pulses (indicated by the purple line). In addition, the bias voltage applied orthogonally for poling the multi-domain is shown in Figure 3.7 (b), where the scale of the polarisation changes as different sizes of bias voltages. The voltage-free case exhibits a negligible amount of polarisation because of the cancelling of the multi-polarised domains. However, very small polarisation can be detected due to the uneven distribution of these domains from memory effects. The total polarisation soars up as voltage increases, and the final saturated polarisation is obtained when cooling with the bias voltage of 100 V. Higher bias voltage at 150 V cannot generate more polarisation, in contrast, less polarisation is obtained since the whole sample is fully polarised and higher voltage will increase the risk of leakage. The gap between voltage electrodes is about 2 mm. Therefore, the electric field under 100 V approaches 50 kV/m, which is believed to be close to the damage threshold of the sample flake. The error bar at each point indicates that the polarisation may be lost after multiple times of switching at fixed voltage due to the fatigue damage in the sample.

3.2.3 Ferroelectric polarity switched by the electric field

The giant electric polarisation demonstrated in Figure 3.6 is purely a domain effect. From the point of view of the associated magnetic structure, external fields such as electric bias and magnetic field may give rise to different polarity characters of the magnetic structure.The poling electric field should guide the induced polarisation; however, due to the i-DMi interaction from the TFTC structure, this microscopic magnetic sublattice may have a two-fold degenerate structure with opposite helicities. This naturally leads to the concept of polarity in the TFTC phase, as shown in Figure 3.8, in which the polarity of the TFTC structure is reflected in the cycloidal structure with different handedness.

To understand the polarity freedom of the multiferroic phase, one has to decompose the TFTC structure into two periodic sections from a reciprocal point

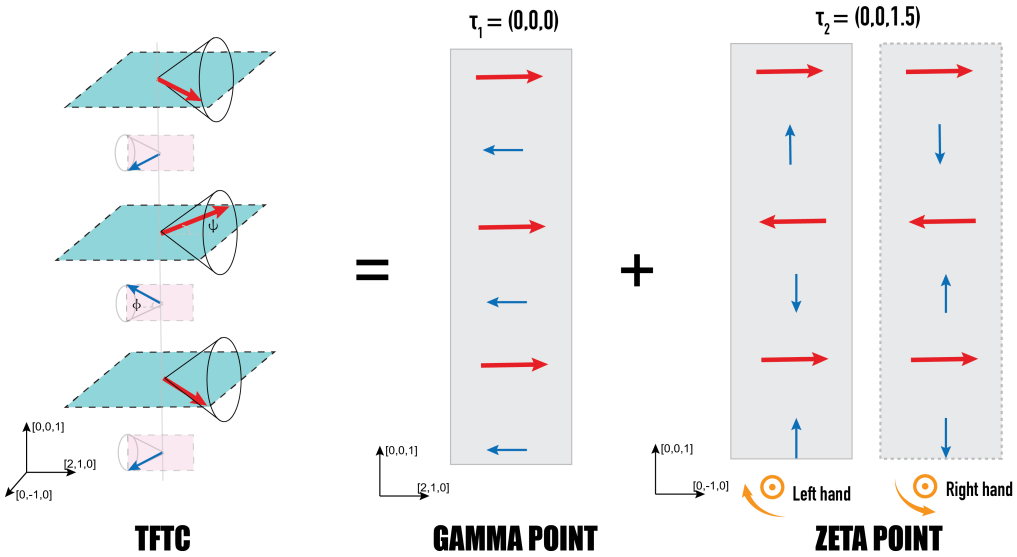


Figure 3.8: TFTC structure is depicted in magnetic reciprocal space. The transversal cone structure with two fan folds can be decomposed into the ferrimagnetic Γ point and cycloidal Z points. Both reciprocal positions demonstrate two different magnetic propagation vectors. The Z point structure has two degenerate structures with opposite helicity, which is naturally indistinguishable if applying the in-plane magnetic field.

of view, shown in Figure 3.8. One is a ferrimagnetic component in a^*c plane which is composed of antiparallel alignment of μ_S and μ_L when observing along [0, -1, 0] direction; the other part is the cycloidal component in the b^*c plane consisting of the out-of-plane part of μ_S and rotational part of μ_L when looking along [2, -1, 0] direction. The ferrimagnetic component is commensurate with atomic positions. Thus, the propagation vector of the magnetic component is zero. At the same time, the cycloidal component is repeated by half of the lattice length (repeated every three blocks in total six blocks), which results in the magnetic propagation vector $\tau_2 = (0, 0, 1.5)$. In magnetic diffraction, these fractions are assigned as Γ point and Z point in reciprocal space.

By right-hand convention, the cycloidal nature at Z point can be distinguished by observing the super-spins from bottom to top, clockwise or anti-clockwise. In other words, if fixing the rotation axis along the $[2, -1, 0]$ direction, the structure can be described by a parameter $\lambda = 1(-1)$ representing left (right) chirality. The chirality is directly coupled with the polarisation vector $\boldsymbol{P}$ from the perspective

of inverse DM interaction:

$$\boldsymbol{P} \sim \lambda \hat{\boldsymbol{e}}_{ij} \times (\boldsymbol{S}_i \times \boldsymbol{S}_j)$$

where $\hat{\boldsymbol{e}}_{ij}$ refers to the unit vector between two adjacent spins and $\boldsymbol{S}_{i,j}$ are the spin moment vectors. In this sense, the induced polarisation direction is either inward pointing into the paper plane for left chirality, or outward for right chirality. The cycloidal TFTC structures are indistinguishable under a small magnetic field since both types degenerate with external magnetic fields. However, when applying a biased voltage in the $[2, 1, 0]$ direction, the two cycloids become nondegenerate since polarity preference is selected in the bias field. During the magnetocurrent experiments, we discovered that the distinction of the two polarities could be achieved by changing the bias field direction while the magnetic field is unchanged.

In order to discover the polarity of the TFTC structure, the bias voltage and in-plane magnetic field are applied at 100 V and 250 mT, respectively, and then the sample is cooled down to 4 K. The results are shown in Figure 3.9. The magnetocurrent is shown in the black curve, while the polarisation hysteresis is depicted in the blue curve. Arrows and crossings highlight sweeping directions and starting points. Comparing subplot (a) and (d), in which the only change is the bias voltage direction, we find the current sign is switched while the main profile remains the same. The effect of bias voltage takes place similarly in Figures (b) and (c). This result indicates that the cycloidal TFTC structure with a certain polarity can be selectively chosen by external bias voltage direction when the magnetic field direction is kept the same. However, by comparing subfigures (b) and (d) (or (a) and (c)), almost identical hysteresis loops can be identified, which means the effects of simultaneous changing the signs of both bias and the magnetic field cancel with each other. This equivalence can be understood by the subplots at the corner, where the initial states are indicated. This effect can ideally be described by a new order parameter called *Ferrotoroidal moment* (or *toroidal moment* labelled as $\boldsymbol{T}$), which has been postulated and argued quite often in twisted magnetic structures:

$$\boldsymbol{T} \sim \boldsymbol{P} \times \boldsymbol{M}$$

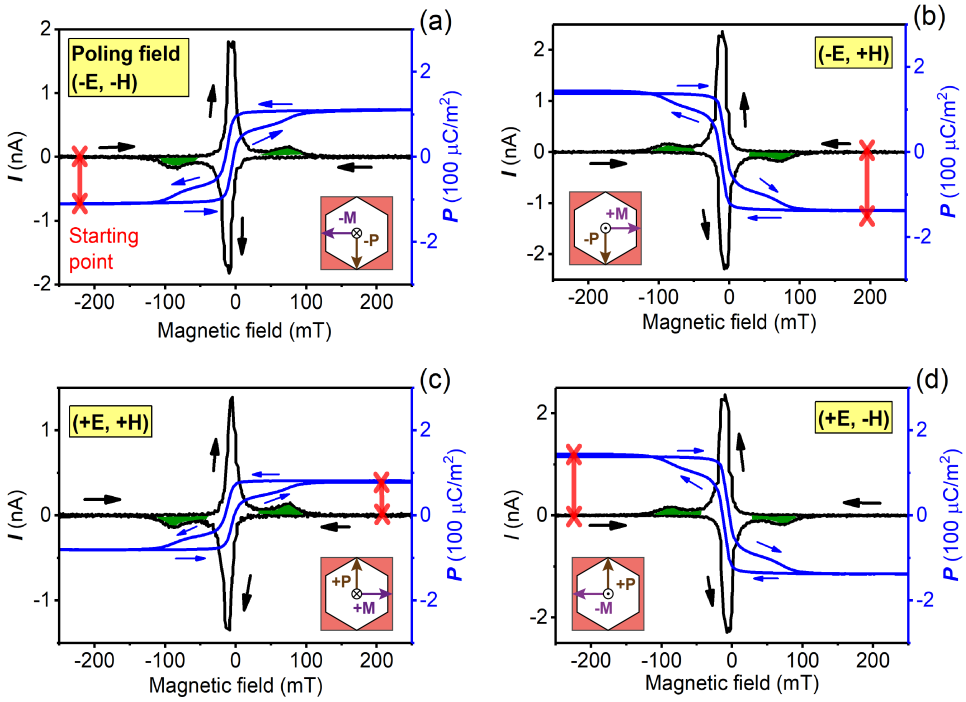


Figure 3.9: Magneto-current measurements on the electrical polarisation at 10 K under different bias field combinations. Current-field (I–H) and polarisation-field (P–H) hysteresis loops are obtained after cooling with poling fields of different orientations (a) (-E, -H) field; (b) (-E, +H) field; (c) (+E, +H) field; (d) (+E, -H) field. Blue curves represent P–H dependence by the sweeping magnetic field; the red cross indicates the starting point. Green filling circulates the small peak associated with the second switching stage. The corner hexagonal cubic demonstrates the direction of $\boldsymbol{P}$ and $\boldsymbol{M}$ at the starting point after poling, which determines the signs of the toroidal moment along the c axis.

This toroidal moment is either parallel or antiparallel to the c axis. The sign of this moment will not be changed by magnetic field sweeping due to the coupling between $\boldsymbol{E}$ and $\boldsymbol{M}$ Thus, the sign of $\boldsymbol{P}$ follows the change sign of $\boldsymbol{M}$, and $\boldsymbol{T}$ remains unchanged while sweeping the magnetic field. However, the realisation of the toroidal direction is demonstrated in the experiment by tuning the bias voltage to be opposite, which is the only solution effective in adjusting the domain polarity.

3.3 Identification of the intermediate phase

During the back-and-forth scanning of the magnetocurrent, we found a strange anomaly that occurred after the first sharp peak, as highlighted in Figure 3.9 by the area with green filling. A second peak always follows the first large peak when

sweeping a magnetic field across zero, regardless of which direction the field is heading. The double peaks in the magneto-current indicate that the multiferroic phase switching is far more complicated than the magnetic cone structure rotating under the magnetic field. As discussed later, more experimental evidence suggests that an intermediate phase occurs between the two polarised single domains.

3.3.1 Transport evidence

The small tails in the magneto-current was initially discovered in *P–H* measurement in Figure 3.9 at 10 K. Having preliminarily established a good correspondence between features in magneto-current and magnetometry data at low temperatures, then I decided to employ SQUID magnetometry to study this feature, hoping to find the reason from the perspective of magnetic structure in the broader temperature range. This approach is justified because both measurements are only sensitive to the TFTC phase, which is polar and carries a non-zero magnetic moment. A comparison between the *P–H* and *M–H* data for results at 10 K and 50 K is shown in Figure 3.10 (panels (a) and (b) for 10 K and panels (c) and (f) for 50 K). The SQUID data is obtained in AC mode, and the data derivative is labelled by a red curve. While the *P–H* loop data is different, the current is directly measured, but the polarisation is obtained from integrating the current. The comparisons between these two methods on the same phase under magnetic field switching are presented in Figure 3.10 for 10 K and 50 K cases. The features observed in the two data sets at the same temperature are very similar. However, the *M–H* curves are sharper as expected because of the direct measurement for M, whereas the broader loop in *P–H* arises from the indirect measurement of P. Akin to the *P–H* data, the *M–H* data collected at 10 K shows fast switching of the magnetization around zero fields, followed by a smaller and flatter step around 100 mT. Substantial similarities are found between *P–H* and *M–H* data at 50 K, but both of which are rather different when comparing the counterparties in 10 K. The remaining panels in Figure 3.10 show the *M–H* data for an intermediate temperature (25 K) and a higher temperature (125 K, where *P–H* data cannot be collected). A zero-field step

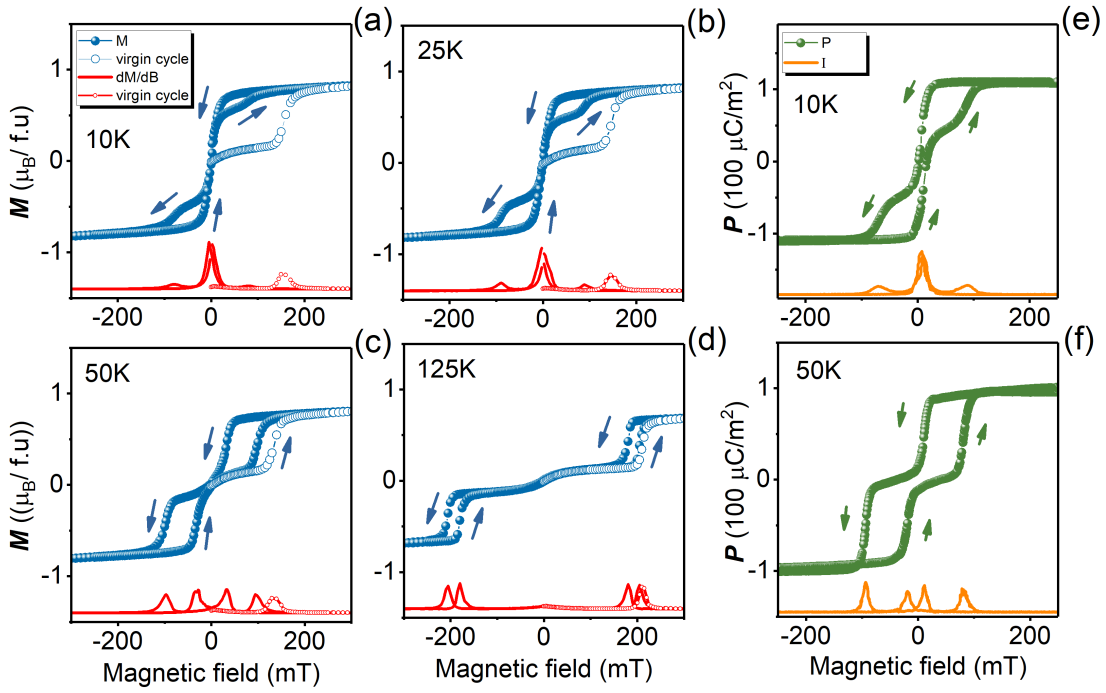


Figure 3.10: Temperature dependence of the switching measured by M–H and P–H along the a axis and b^* direction. The blue dot curves represent the raw data of the in-plane magnetisation, and the red curves show the derivatives which highlight the switching positions. The red empty circle lines are initial virgin scans. Similar patterns are found in magneto-current data at 10 K and 50 K as a reference, which shares identical switching behaviours in each temperature case. The raw data of the magneto-current are labelled by yellow curves, which contribute to the P-H loops by integrating the currents.

is observed in all data sets except for 50 K, where a negligible small step hides within the extensive overlapping of the two successive peaks.

Since two aspects of the multiferroic TFTC structure (M and P sides) show many similarities in magnetic field switching within a wide temperature range, we have enough reason to postulate that the TFTC structure experience some phase transition during the magnetic field switching, the details of which are still unknown and waiting to be answered.

3.3.2 X-ray diffraction evidence

We then employed the magnetic resonant X-ray diffraction (RXMS) technique to study the switching cases and transport methods. The resonant magnetic scattering

theory introduced in chapter 2 shows that the cross-section from magnetic moments is dramatically improved when X-ray energy reaches the absorption edge (here is the L edge). Therefore, we can always find two satellites sitting on the two sides of the charge diffraction peak for a specific magnetic order commensurate to the lattice structure. We monitor the magnetic satellite peak when applying a series of magnetic field intensities.

The experiment is performed at Beamline I10 RASOR diffractometer, Diamond Light Source, which equips with a pair of in-situ electromagnets that are required for switching experiments. In contrast to the transport measurements mentioned earlier at various temperatures, the sample is studied at low temperature onlys, a weak magnetic field of up to 250 mT is applied for the initial cycle. For soft X-ray at L edge energy 707.8 eV, the reciprocal lattice vector along the c axis is found to be $(0, 0, 3)$ for 2θ at 74.3°. Meanwhile, the magnetic satellites are found at $2\theta = 130.4°$ and $2\theta = 18.2°$, corresponding to reciprocal vector $(0, 0, 4.5)$ and $(0, 0, 1.5)$ respectively. Due to the TFTC propagation vector to be $(0, 0, 1.5)$, the pure magnetic contribution is found at high angle diffraction, and a small contribution from Γ point is located at $(0, 0, 3)$, which sits overlapping the charge diffraction peak.

Figure 3.11 shows the evolution of diffraction pattern as a function of magnetic field. As the magnetic field is swept towards zero and back to the opposite direction, the pure magnetic peak $(0, 0, 4.5)$ starts to descend when approaching the vicinity of zero fields, while a broad incommensurate peak at $(0, 0, 3.9)$ emerges, roughly corresponding to the propagation vector of the helical phase previously found at room temperature. The large width of the $(0, 0, 3.9)$ peak suggests that the incommensurate phase is poorly coherent. As highlighted by the red dashed curve, the $(0, 0, 4.5)$ peak intensity remains low at the field range between -6 mT and 100 mT, then quickly recovers after 100 mT. The incommensurate structure exists at the same field range.

Meanwhile, the $(0, 0, 3)$ peak displays a minor change, suggesting that charge scattering dominates the diffraction intensity at this angle while the contribution from Γ point diffraction is negligible. We can therefore predict that the low-field

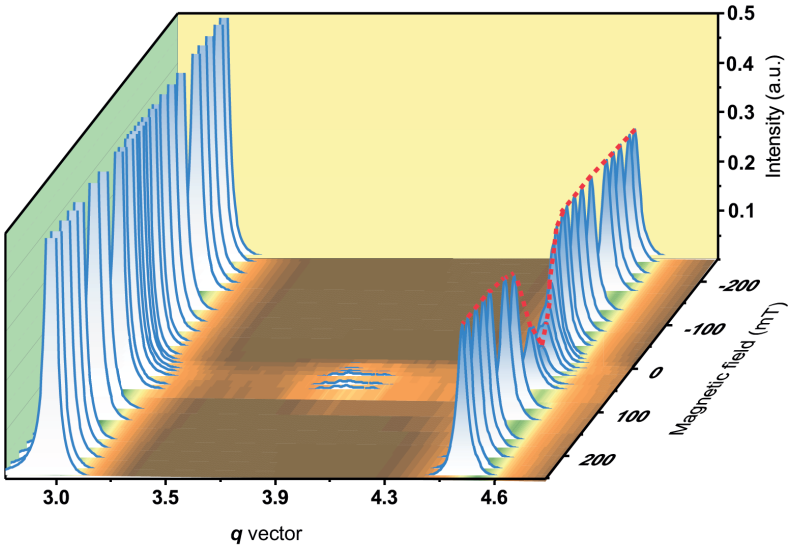


Figure 3.11: The signature of phase coexistence during the switching of the TFTC phase. The intensity of the Z point diffraction reflected by the pure magnetic peak at $(0, 0, 4.5)$ descends at a low field range between -6 mT and 100 mT, which is depicted by the red guided line. Within the same region, an intermediate helical phase can be found by a broad and weak incommensurate peak at $(0, 0, 3.9)$ with worse coherency than a pure TFTC peak. To clarify the broadened weak incommensurate peak, the logarithm of the intensity is inserted at the bottom, characterised as brown-green 2D plot.

switching process involves more than a simple rotation of the magnetic cone structure, justified by the fact that the external magnetic field modulates the $(0, 0, 4.5)$ pure magnetic peak amplitude because the cone rotation will not change diffraction intensity as will be modelled later. Together with the unambiguous demonstration of the incommensurate peak at $(0, 0, 3.9)$, we assume that a mixed helical/TFTC state is formed in the field range between -6 mT and 100 mT.

In light of the two-step magneto-current peak from P–H data, we can propose the following scenario: as the field passes through zero, the TFTC phase rotates rapidly. Still, it is also partially converted to the non-polar incommensurate phase (IC phase). When the IC phase disappears, the mixed phase remains up to 100 mT, until a pure TFTC state is fully recovered. This further contributes another polarisation jump, consistent with the second 'step' observed in the magneto-current measurement.

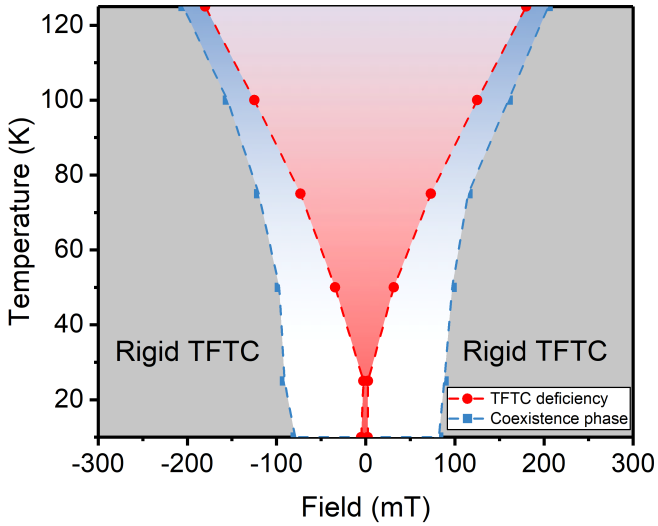


Figure 3.12: Phase diagram of the switching dynamics. The blue and red dots connected by dash lines are depicted from the first and second peak positions in switching *M–H* loops. The area shaded in red demonstrates the phase boundary of the broken TFTC structure, which follows the conventional rotation switching pattern. At the same time, the blue enclosure represents the boundary of phase coexistence. The mixed state recovers to the uniform TFTC state at the high field, labelled by grey filling.

3.3.3 Intermediate phase diagram

An explicit phase diagram for such mixed phase can be inferred from the magnetometry data since there is a temperature-dependent evolution for the step-like features in Figure 3.10 switching loops: the relative size of the non-hysteretic zero-field step progressively decreases when warming, while the hysteretic second step increases and is pushed to higher fields as warming up. Noticeably, the secondary loops also become narrower at higher temperatures, indicating a reduced coercivity which is believed to be a thermal effect. Correlating the manifold information between RXMS, *P–H* and *M–H* data, we can propose an interpretation of the various processes taking place as a function of temperature and field. First, the central non-hysteretic step is contributed by the rotational behaviour of the cone. This prominent peak is tiny at 50 K and 125 K, but it is still clearly visible. Second, the hysteretic high-field switchings are manifested by the inter-exchange between the mixed phase, when reconstructing the TFTC structure at the higher field.

This switching picture can be explicitly understood by a phase diagram based on the SQUID magnetometry data, where a T–H map depicts the temperature-dependent evolution of the intermediate phase. As shown in Figure 3.12, the dashed lines represent the position of the peaks in the first derivative of the magnetisation. The red and blue dash lines depict the boundaries of the cone rotation region and phase mixture area. Meanwhile, the grey filling represents the TFTC structure, which is always fully restored at a high field. The remaining TFTC cones and the range of phase coexistence are obviously temperature dependent, supported by the step height from magnetometry and the red 'funnel' structure in the phase diagram.

In conclusion, the data demonstrate that the switching process cannot be described as a simple 'magnetic cone rotation', as previously proposed in other works [98, 109, 110]. However, it is still acknowledged that the magnetic cone rotation is the dominant process at low temperatures, with a relatively small incommensurate phase when leaving the zero field. A similar effect is found for the compound $Ba_{0.5}Sr_{1.5}Mg_{1.6}Co_{0.4}Fe_{12}O_{22}$ where cone rotation model is valid until 150 K [111]. The following section will establish a mathematical description of the TFTC structure from RXMS theory. By utilising the linear polarisation diffraction theory to fit the RXMS data quantitatively, we propose a new model based on the fact of the intermediate phase by supplementing the contribution from the incommensurate phase.

3.4 Models of phase switching

Before considering the full picture of the switching where phase coexistence emerges, we review the development of the rotation model, which can phenomenologically describe the non-hysteretic switching. We extend the rotation model by adding only two parameters for quantitatively describing the TFTC distortion effects and the IC/TFTC phase coexistence degrees. We prove that the new modified model fits the RXMS data with good agreement, in which the postulated parameters are independently derived from transport measurements.

3.4.1 Cone rotation model

Description of the block TFTC structure

As reiterated by previous sections, the block model is widely utilised to describe the magnetic structure of BSMFO. This basic model divides the structure into a periodic series of magnetic blocks: L (large moment) and S (small moment) blocks. Within each block, Fe moments are assumed to be antiferromagnetically aligned in a collinear or non-collinear manner. The stacking of the magnetic blocks is found along the $[0, 0, 1]$ direction. Further simplification of the single ion magnetic moments goes into super-spin (L_i or S_j), which is the summation of the moments within the block and is assumed to sit at the block centre. As shown in Figure 3.13 (I), the coordinates of the super-spins in each block are $\vec{r} = [0, 0, r_z]$, where $r_z = [0, \frac{1}{6}, \frac{2}{6}, \frac{3}{6}, \frac{4}{6}, \frac{5}{6}]$. The total magnetic moments in L block are three times larger than the S block, as implied by neutron diffraction studies [100, 101].

The TFTC structure can be considered a superposition of a ferrimagnetic structure and a commensurate cycloidal structure described by propagation vectors $\tau_1 = (0, 0, 0)$ and $\tau_2 =(0, 0, 1.5)$, respectively. Considering a magnetic field applied parallel to the $[2, 1, 0]$ direction, L blocks lie exclusively in the *ab* plane normal to the $[0, 0, 1]$ featuring a ferromagnetic alignment parallel to the $[2, 1, 0]$, and an antiferromagnetic alignment parallel to the $[0, 1, 0]$. Meanwhile, S block moments have a ferromagnetic section along the $[-2, -1, 0]$, and an anti-ferromagnetic section along the $[0, 0, 1]$.

The mathematic description of the TFTC structure in real space can be expressed

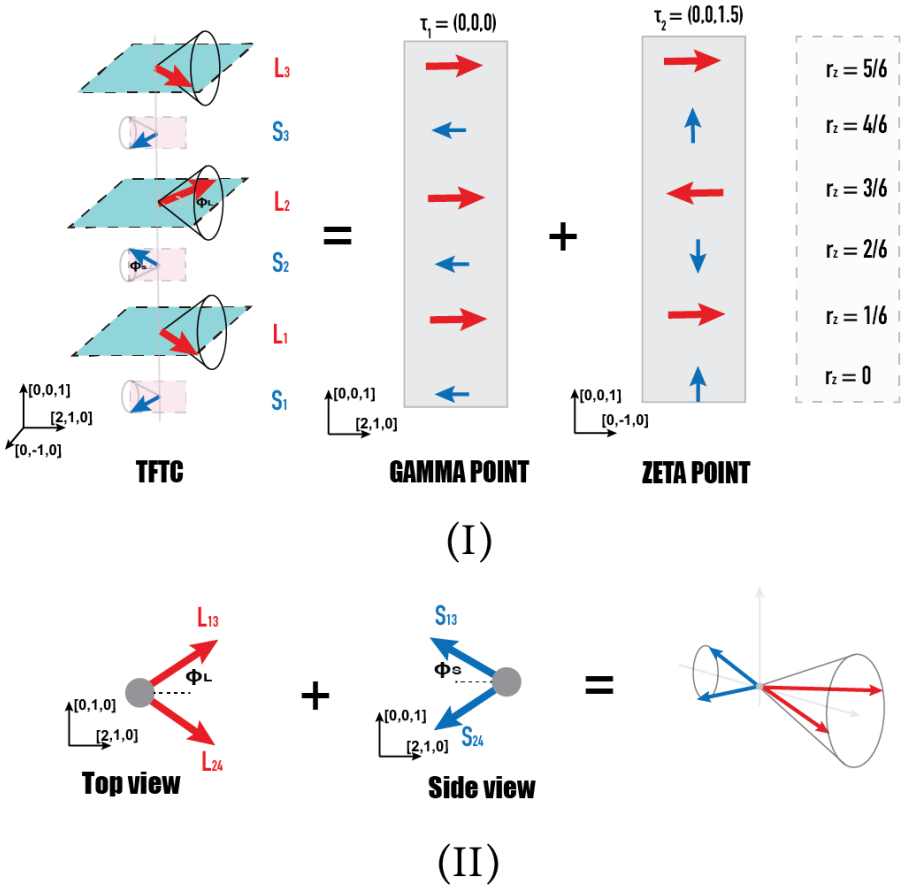


Figure 3.13: Illustration of TFTC magnetic components. (I). Two-fan transversal cone magnetic structure in the block model. *Left.* The cones locate in different blocks, where S spin blocks (blue) are enumerated by S_i and L spin blocks (red) are listed by L_j. *Right.* The construction of the TFTC structure from Γ point and Z point peroidic order. (II). The construction of TFTC structure from double cones. The left and centre panels shows the projections of the TFTC structure in two planes so that ϕ_L and ϕ_S can be observed.

by:

Ferrimagnetic component:

$$L\ blocks : \boldsymbol{m_{n,\tau_1}} = m_{Fe}\cos(\phi_L)\cos(\boldsymbol{\tau_1}\cdot\boldsymbol{r_n} + \phi_{n,0})\hat{\boldsymbol{x}} \tag{3.1}$$

$$S\ blocks : \boldsymbol{m_{n,\tau_1}} = m_{Fe}\cos(\phi_S)\cos(\boldsymbol{\tau_1}\cdot\boldsymbol{r_n} + \phi_{n,\pi})\hat{\boldsymbol{x}} \tag{3.2}$$

Cycloidal component:

$$L\ blocks : \boldsymbol{m_{n,\tau_2}} = m_{Fe}\sin(\phi_L)\cos(\boldsymbol{\tau_2}\cdot\boldsymbol{r_n} + \phi_{n,L})\hat{\boldsymbol{y}} \tag{3.3}$$

$$S\ blocks : \boldsymbol{m_{n,\tau_2}} = m_{Fe}\sin(\phi_S)\cos(\boldsymbol{\tau_2}\cdot\boldsymbol{r_n} + \phi_{n,S})\hat{\boldsymbol{z}} \tag{3.4}$$

The $\phi_{n,i}$ angles are the initial phase angles for each super-spin block. For ferrimagnetic structure in Γ point section, the phase angle of the moments between L and S blocks differ by π due to antiparallel alignment. In the case of the cycloidal Z point section, initial phases between adjacent L and S blocks differ by $\frac{\pi}{2}$, corresponding to the 90° of rotation.

In the propagation vector formalism, the ferrimagnetic component exhibits $\boldsymbol{\tau}_1$= $(0,0,0)$ propagation vector, whereas the cycloidal part exhibits $\boldsymbol{\tau}_2 = (0,0,1.5)$ propagation vector. A collection of moments describing a universal magnetic structure can be decomposed into Fourier components concerning each different propagation vector $\boldsymbol{\tau}_j$,

$$\boldsymbol{m}_n = \sum_j (\boldsymbol{S_{j,n}} e^{-i\boldsymbol{\tau_j}\cdot\boldsymbol{r_n} - i\phi_n} + \boldsymbol{S^*_{j,n}} e^{i\boldsymbol{\tau_j}\cdot\boldsymbol{r_n} + i\phi_n}) \tag{3.5}$$

where $\boldsymbol{r}_n$ is the position vector of the n^{th} spin, $S^*_{j,n}$ is the Fourier coefficient of the j^{th} propagation vector $\boldsymbol{\tau_j}$ for the n^{th} spin, ϕ_n is the site-specific phase for $\boldsymbol{r}_n$. The sum runs over each propagation vector of the structure. According to this formulism, we can describe the magnetic structure vector of the TFTC phase with respect to the propagation vectors $\boldsymbol{\tau}_1 = (0,0,0)$ and $\boldsymbol{\tau}_2 = (0,0,1.5)$, respectively:

L Blocks:

$$\boldsymbol{S}_{1,L} = \frac{3m_{Fe}}{2}\cos(\phi_L)[1,0,0] \tag{3.6}$$

$$\boldsymbol{S}_{2,L} = \frac{3m_{Fe}}{2}\sin(\phi_L)[0,i,0] \tag{3.7}$$

S Blocks:

$$\boldsymbol{S}_{1,S} = \frac{m_{Fe}}{2}\cos(\phi_S)[-1,0,0] \tag{3.8}$$

$$\boldsymbol{S}_{2,S} = \frac{m_{Fe}}{2}\sin(\phi_S)[0,0,-1] \tag{3.9}$$

TFTC structure factor

The structure factor plays a central role in the scattering of crystalline structures. The theory of resonant magnetic scattering can refer to in the appendix A. The magnetic structure vector is based on the assumption of a symmetric cone structure

for both small and large blocks. Therefore, the ϕ_L and ϕ_S are critical parameters for TFTC phase. Following the convention in Equation A.5, we rewrite the magnetic structure vector $\boldsymbol{S}$ into magnetic structure factor matrix $\hat{\boldsymbol{M}}(K)$:

$$\begin{aligned} \boldsymbol{M}_{\Gamma}^{S} &= \begin{bmatrix} -\frac{1}{2}m_S\cos(\phi_S) \\ 0 \\ 0 \end{bmatrix}, \ \boldsymbol{M}_{\Gamma}^{L} = \begin{bmatrix} \frac{1}{2}m_L\cos(\phi_L) \\ 0 \\ 0 \end{bmatrix} \\ \boldsymbol{M}_{Z}^{S} &= \begin{bmatrix} 0 \\ 0 \\ -\frac{1}{2}m_S\sin(\phi_S) \end{bmatrix}, \ \boldsymbol{M}_{Z}^{L} = \begin{bmatrix} 0 \\ \frac{i}{2}m_L\sin(\phi_L) \\ 0 \end{bmatrix} \end{aligned} \tag{3.10}$$

where m_S and m_L keep the relationship of $m_L = 3m_S$, M_K^{Block} represents the magnetic vector contribution from L or S block at K diffraction point, and Γ is the τ_1 vector while Z is the τ_2 vector. The total magnetic vector is summed over all block sites from the two components, which is expressed by:

$$\begin{aligned} \boldsymbol{M}_{\Gamma} &= \boldsymbol{M}_{\Gamma}^{S} + \boldsymbol{M}_{\Gamma}^{L} = \begin{bmatrix} M_{\Gamma}^{1} \\ M_{\Gamma}^{2} \\ M_{\Gamma}^{3} \end{bmatrix} \\ \boldsymbol{M}_{Z} &= \boldsymbol{M}_{Z}^{S} + \boldsymbol{M}_{Z}^{L} = \begin{bmatrix} M_{Z}^{1} \\ M_{Z}^{2} \\ M_{Z}^{3} \end{bmatrix} \end{aligned} \tag{3.11}$$

By substituting the magnetic vectors into Equation A.5 for Γ and Z point fractions, we can derive the diffraction intensity for four channels according to Equation A.2. Since only the first-order approximation of the atomic form factor is taken, the matrix elements from the $F^{(2)}$ term is not considered. While the $\sigma - \sigma'$ element in the $F^{(1)}$ term is zero, thus the remaining channels give rise to the non-zero diffraction intensity as follows:

$$\begin{aligned} I_{\Gamma}^{\sigma-\pi} &\propto (iF^{(1)})^2 \left| M_{\Gamma}^{1}\cos\theta + M_{\Gamma}^{3}\sin\theta \right|^2 \\ I_{\Gamma}^{\pi-\sigma} &\propto (iF^{(1)})^2 \left| -M_{\Gamma}^{1}\cos\theta + M_{\Gamma}^{3}\sin\theta \right|^2 \\ I_{\Gamma}^{\pi-\pi} &\propto (iF^{(1)})^2 \left| -M_{\Gamma}^{2}\sin 2\theta \right|^2 \end{aligned} \tag{3.12}$$

for diffraction at Γ point; while

$$\begin{aligned} I_{Z}^{\sigma-\pi} &\propto (iF^{(1)})^2 \left| M_{Z}^{1}\cos\theta + M_{Z}^{3}\sin\theta \right|^2 \\ I_{Z}^{\pi-\sigma} &\propto (iF^{(1)})^2 \left| -M_{Z}^{1}\cos\theta + M_{Z}^{3}\sin\theta \right|^2 \\ I_{Z}^{\pi-\pi} &\propto (iF^{(1)})^2 \left| -M_{Z}^{2}\sin 2\theta \right|^2 \end{aligned} \tag{3.13}$$

are derived for diffraction at the Z point. θ is the Bragg angle at the diffraction condition. We can see from the Equations in 3.12 and 3.13 that the diffraction intensities in different channels are associated with the vector components of the magnetic structure factor.

A simple model describing the response to the magnetic field sweeping is the cone structure rotating within the ab plane [109]. In other words, the principal axis for rotation is along the c-axis once the external magnetic field triggers the cone to move. Reflecting on diffraction intensity from linear channels, the cone rotation along the magnetic field is modulated by sinusoidal patterns, as shown in Figure 3.14 for Γ and Z sections separately. For the ferrimagnetic component on Γ point (corresponding to the right panel), the $\pi - \pi$ channel exhibits sinusoidal while the other two channels change with a phase shift of $\frac{\pi}{2}$. For the Z point component, the rotation of 180° gives a sinusoidal pattern for $\pi - \pi$ channel while keeping the other two channels with a phase shift of $\frac{\pi}{2}$.

TFTC structure factor with modification

We know that simple cone rotation is insufficient to describe the actual case of switching. The diffraction intensity at $+H$ or $-H$ is not symmetric, as indicated in Figure 3.16. From the neutron experiments performed (not published yet) on BSMFO at low temperatures, we are known that the phase under the influence of small field finds the smaller cone S is distorted toward the c axis, which results in the expansion of ϕ_L under the conservation of superexchange energy between blocks. Therefore, a reasonable postulation is that the cone structure is slightly distorted after 180° rotation. An additional factor is considered to describe this distortion effect on the cone structure. The shifted angle ψ_S for small cone is defined, and the following constraint of the dot product between the blocks determines the expansion angle for the larger cone structure ψ_L

$$\cos(\phi_S - \psi_S)\cos(\phi_L + \psi_L) = \cos(\phi_S + \psi_S)\cos(\phi_L - \psi_L) \tag{3.14}$$

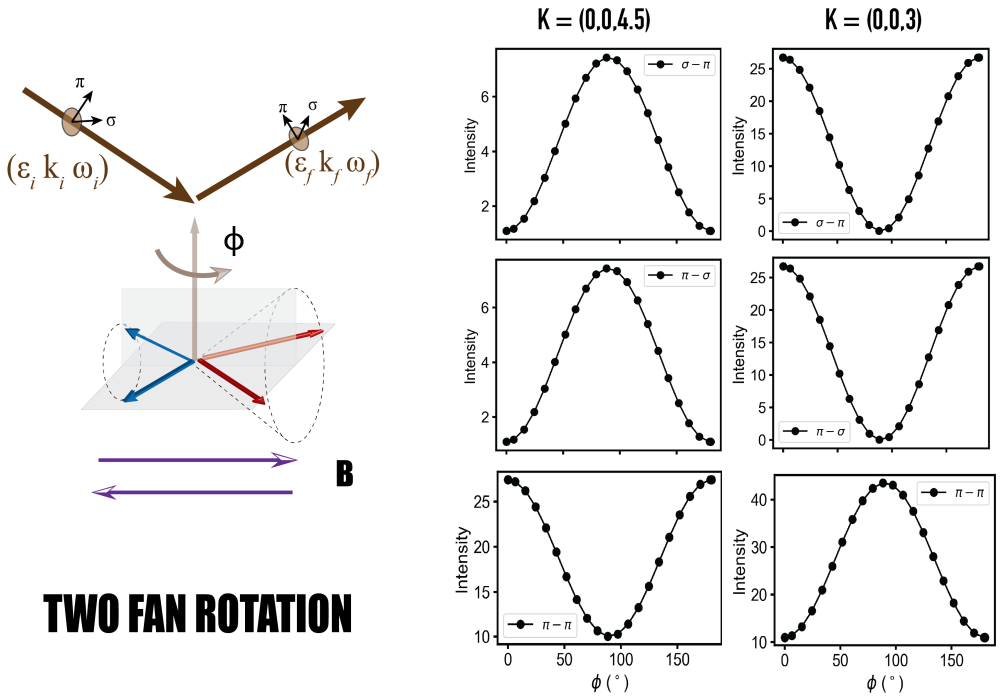


Figure 3.14: The rotational model for TFTC structure switching. Left is the diagram of the cone structure rotation under the influence of a magnetic field sweeping within the *ab* plane. Right is the intensity evolution by 180° rotation of the cone structure on the magnetic diffraction point at Γ and Z. Symmetric sinusoidal curves depict symmetric magnetic vector components after two-fold rotation.

The magnetic vector described on the basis of symmetric cone are accordingly modified as follows:

$$\begin{aligned} \boldsymbol{M}_{\Gamma}^{S} &= \begin{bmatrix} -\frac{1}{2}m_S \cos\phi_S & \cos\psi_S \\ 0 \\ \frac{1}{2}m_S \cos\phi_S & \sin\psi_S \end{bmatrix}, \quad \boldsymbol{M}_{\Gamma}^{L} = \begin{bmatrix} \frac{1}{2}m_L \cos(\phi_L + \psi_L) \\ 0 \\ 0 \end{bmatrix} \\ \boldsymbol{M}_{Z}^{S} &= \begin{bmatrix} \frac{i}{2}m_S \sin\phi_S & \sin\psi_S \\ 0 \\ -\frac{i}{2}m_S \sin\phi_S & \cos\psi_S \end{bmatrix}, \quad \boldsymbol{M}_{Z}^{L} = \begin{bmatrix} 0 \\ \frac{1}{2}m_L \sin(\phi_L + \psi_L) \\ 0 \end{bmatrix} \end{aligned} \tag{3.15}$$

As shown in Figure 3.15, the implemented factors in both cone angles bring the asymmetry effect in magnetic diffraction intensities in $\sigma - \pi$ and $\pi - \sigma$ channels. In contrast, the $\pi - \pi$ channel remains symmetric. We choose the ψ_L factor to be 27.3° by fitting the experimental data to obtain the optimised percentage of asymmetry.

Advantage of distortion factor in linear polarisation diffraction

From the experimental data shown in the top panel in Figure 3.16, we can find a good improvement by considering the cone structure distortion factor in the rotation

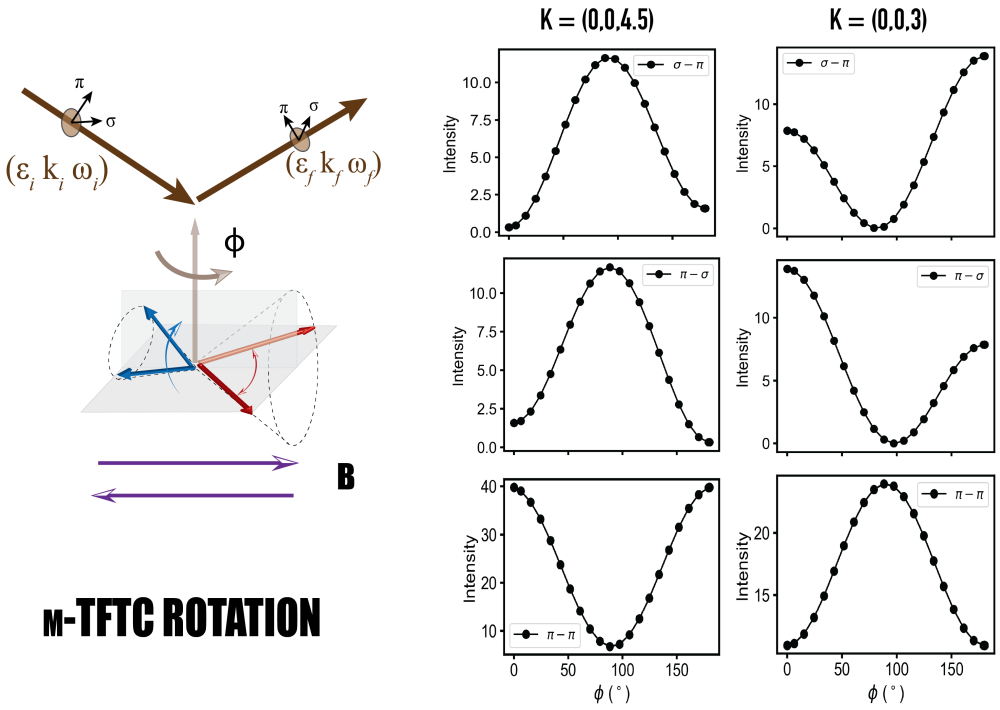


Figure 3.15: The modified model for TFTC structure rotation. Left is the diagram of the distorted cone structure rotation under the influence of magnetic field sweep. Right is the modulated magnetic diffraction intensity when 180° rotation occurred on the cone structure. Giant asymmetric characters are observed for $\sigma - \pi$ or $\pi - \sigma$ channel channels for ferrimagnetic or cycloidal components. The symmetric $\pi - \pi$ channels demonstrate that the y- direction moment remains symmetric in the distorted cone structure.

picture. The **a**, **b**, **c** panels in Figure 3.16 (I) and (II) are diffraction intensity from three linear channels concerning magnetic field intensity. The mathematical form of the *I*–*H* curve is based on Equations 3.12 and 3.13 with the modified magnetic form factor components from Equation 3.15. The top panels in both I and II are taken from experiments. The intensities of diffraction for both $\sigma - \pi$ and $\pi - \sigma$ channels exhibit an asymmetric feature at $+H$ and $-H$ edges, while for the $\pi - \pi$ channel, the diffraction intensity remains symmetric. As shown in the middle panels with dashed lines, the cone rotation model cannot explain such asymmetry in diffraction intensity if we don't consider the cone distortion factor. The bottom panels of **g**, **h**, **i** are the simulation results with cone distortion factor. By carefully tuning the rotation range and moment size on the basis of empirical formula from Equation 3.13 and 3.15, the features for all channels in both diffraction points can be fitted with good agreement, except for specific details on the rising edge across

the switching point near zero. In this regard, it can be concluded that the conical structure (in TFTC phase) is not robust upon switching, which may arise from magnetic striction effect induced by an external field.

3.4.2 Rotation model with phase coexistence

Recalling the discovery of the phase coexistence presented in Figure 3.12, some further modifications of this effect can be implemented into the modified rotation model, given that the switching behaviour in Figure 3.16 still leaves some puzzling details of the curve which may arise from the phase coexistence. We demonstrate here that a 'minimal' model based on the phase coexistence picture is capable of fitting some of the fine details of our RXMS data in all channels, which cannot be fully explained in cone distortion model. In order to achieve this, our model must necessarily include the relative fractions of the TFTC and LC phases, since their contributions to the RXMS are clearly different: The scattering at commensurate reciprocal points are dominantly contributed by TFTC phase, while incommensurate LC phase are negligible at given scattering condition.

We do this by introducing the parameter $\delta = 1 - \frac{f_{LC}}{f_{TFTC}}$ where f_{LC} and f_{TFTC} are the two-phase fractions and $\delta = 1(0)$ for pure TFTC (LC) phases, respectively. The parameter δ is both fields- and temperature dependent, and it is strongly hysteretic as a function of field — in other words, the up-sweep(represented by $+$) and down-sweep(represented by $-$) functions $\delta^{+}(H,T)$ and $\delta^{-}(H,T)$ are mirror image of each other through $H = 0$. Nevertheless, these functions can be readily deduced from the M–H data for each temperature and field sweep direction. We assumed that the actual magnetic signal for both SQUID and RXMS is a linear combination of the signals from TFTC and LC structures throughout the whole coexistence range. Given that the TFTC phase is the ground state phase at the high field, the function of $\delta(B)$ is segmented and starts (or ends) at 1, representing the total magnetic signal contributed by the TFTC phase only. This field-dependent

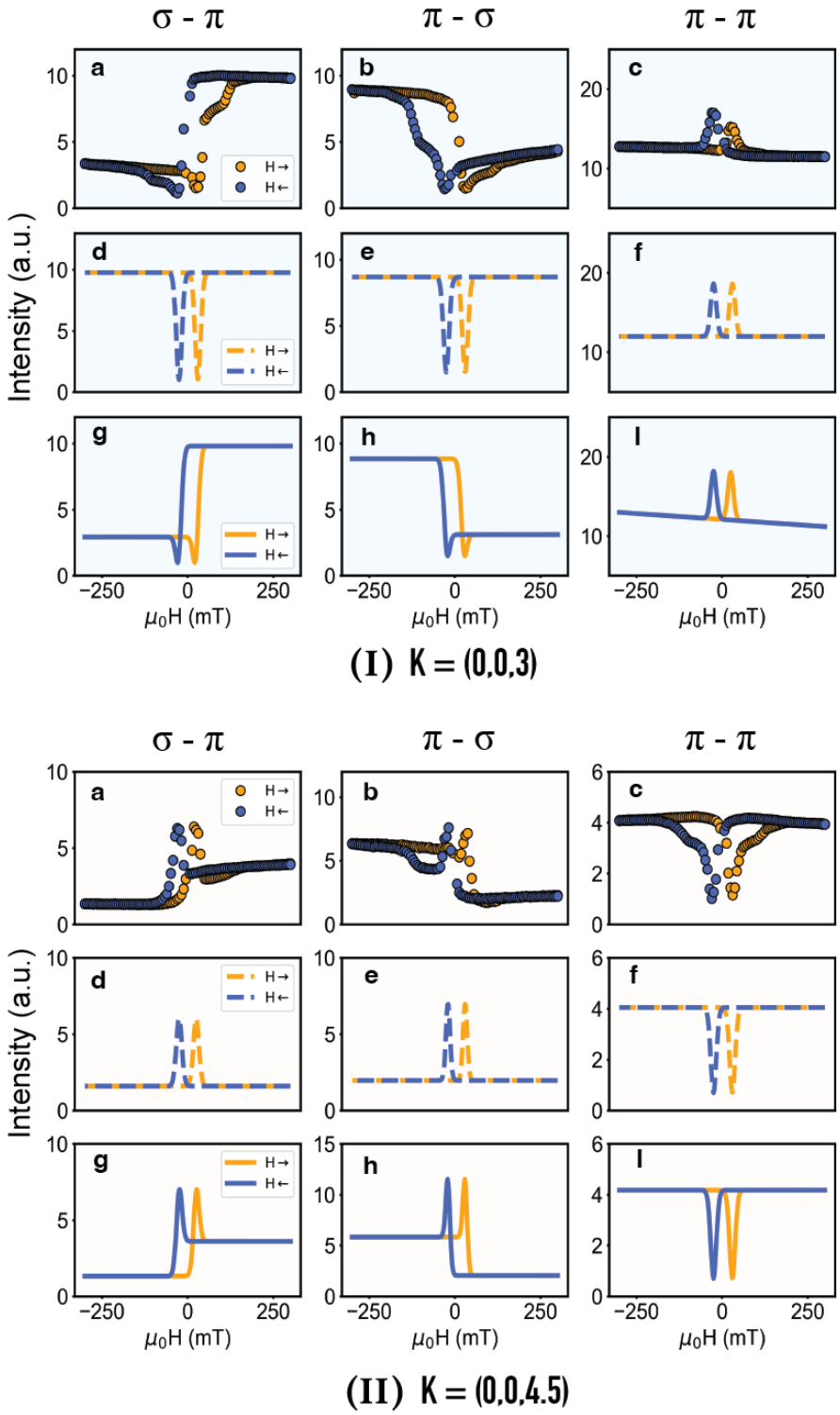


Figure 3.16: Experiment results of the linear polarisation diffraction. (I) Γ point diffraction and (II) Z point diffraction (top panels), in contrast with the applicaiton of the standard cone model (middle panels) and cone distortion model (bottom panels). **a**, **b**, **c** are experimental data in three different channels. The dashed curves in **d**, **e**, **f** are derived from the standard rotation model. While the **g**, **h** and **i** are derived from a modified rotation model.

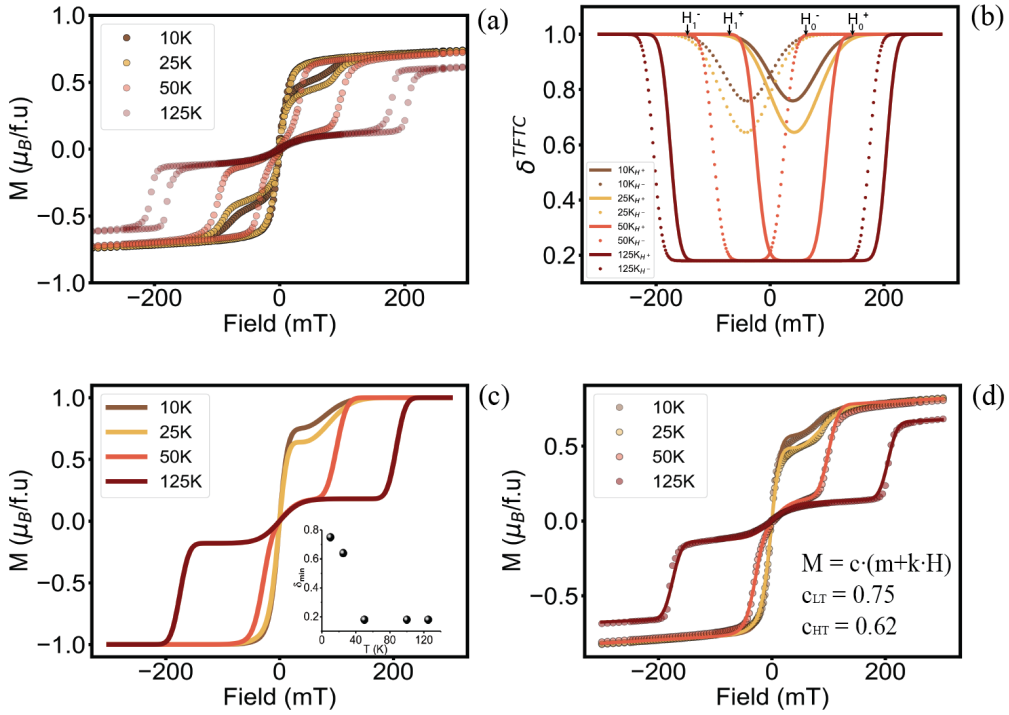


Figure 3.17: Magnetometry and coexisted model fitting. (a) The magnetometry data for low field switching in different temperatures. (b) $\delta(H,T)$ function describing the proportion change of TFTC structure while sweeping the magnetic field. Solid (dot) curves depict the fraction values change by increasing (decreasing) the field. (c) The models of magnetisation change by considering the $\delta(H,T)$ function at different temperatures. Inset shows the minimum proportion of TFTC structure surviving in the intermediate phases. (d) The fitting of half the SQUID data at different temperatures.

function can thus be expressed as:

$$\delta(H,T) = \begin{cases} 1 & H > H_0(T) \\ g(H,T) & H_1(T) < H < H_0(T) \\ 1 & H < H_1(T) \end{cases} \tag{3.16}$$

where the H_0 and H_1 are critical fields of the phase coexistence. The hysteresis is expressed by the fact that $H_0^- \simeq -H_1^+ \ll H_0^+ \simeq -H_1^-$ (see Figure 3.17 (b)) consistent with the symmetric shape of the 'funnel' in Figure 3.12. The function $g(H,T)$ describes the inter-conversion between the two phases and can be phenomenologically constructed by a series of continuous functions. We describe the $\delta(H,T)$ function through linear combination of error functions by properly defining several parameters which can be estimated from the 'funnel'-like phase diagram.

Temperature (K)	δ_{min}	H_c^1(mT)	H_c^2(mT)	w_c(mT)
10	0.75	70	10	50
25	0.64	80	5	50
50	0.18	100	-25	20
125	0.18	205	-175	18

Table 3.2: Parameters for the TFTC fraction function $\delta(H,T)$.

The mathematical expression of the $\delta(H,T)$ is written as:

$$\delta(H,T) = 1-(1-\delta_{min}(T))\cdot\left(erfc\left[\frac{H-H_c^1(T)}{w_c(T)}\right]-erfc\left[\frac{H-H_c^2(T)}{w_c(T)}\right]\right) \quad (3.17)$$

where $\delta_{min}(T)$ is the minimum value of the remaining TFTC phase while sweeping the magnetic field; $H_c^1(T)$ and $H_c^2(T)$ are the critical field positions for the breaking and recovery of the TFTC phase, respectively; $w_c(T)$ representing the speed of the inter-conversion of the phases. The $\delta_{min}(T)$ can be estimated from the measurements by SQUID while the other three parameters can be obtained from the 'funnel'-phase diagram from Figure 3.12. In this way, the $\delta^{TFTC}(H,T)$, shown in Figure 3.17 (b), describes the dynamical evolution of the fraction of the TFTC phase while switching the field in either an up-sweeping direction (solid curve) or down-sweeping direction (dot curve) at series of temperature conditions. The parameters used at different temperatures are indicated in Table 3.2 (only the values for solid curves are listed).

In light of the $\delta(H,T)$ function, the ascending branch of the hysteretic curve $M(T)$ can also be phenomenologically modelled by a simple continuous function. Since the x component of the TFTC magnetisation is reflected directly by SQUID data, the non-hysteretic switching near zero field can be described by an odd sinusoidal function as:

$$m(H,T) = \sin(\frac{\pi}{2}\tanh(\frac{H}{v_c(T)}))$$

where the $v_c(T)$ is the switching velocity and temperature-dependent. By considering the fraction information $\delta(H,T)$, the SQUID data can thus be depicted by a continuous model:

$$m(H,T) = \sin(\frac{\pi}{2}\tanh(\frac{H}{v_c(T)}))\cdot\delta(H,T) \quad (3.18)$$

Temperature (K)	10	25	50	125
$v_c(T)$ (mT/μ_B)	25	25	50	55

Table 3.3: Temperature-dependent switching velocity for SQUID switching model.

As demonstrated in Figure 3.17 (c), this single-cycle switching reflects the ratio of TFTC fraction with apparent temperature dependency. The parameters for fitting the SQUID data are shown in Table 3.3. Additional scaling parameter c and a background factor k are considered for better fitting, $M = c \cdot (m(H,T) + k \cdot H)$ describes the experimental SQUID data with reasonable precision when $k = 0.0003$. The scaling factors are chosen for high and low temperatures, respectively, as shown in Figure 3.17 (d), due to the total magnetic moment from Curie-Weiss law.

After exhaustingly exploiting the SQUID magnetometry data, we derived the phase coexistence function $\delta(H,T)$ which is temperature dependent and can elegantly describe the TFTC structure behaviour across the whole switching field range. However, other experimental techniques require further verification of the model derived from magnetometry. Herein, we have already obtained a modified cone rotation model from RXMS, which could be an ideal platform to justify the phase coexistence model further. The straightforward idea is to alter the channel intensities from Equation 3.12 and 3.13 with the multiplication of $\delta(H,T)$:

$$
\begin{aligned}
I_{\sigma-\pi}(H) &= \delta(H,T)\left|F^{(1)}(M_1(H)\cos\theta + M_3(H)\sin\theta)\right|^2 \\
I_{\pi-\sigma}(H) &= \delta(H,T)\left|F^{(1)}(M_1(H)\cos\theta - M_3(H)\sin\theta)\right|^2 \\
I_{\pi-\pi}(H) &= \delta(H,T)\left|F^{(0)}\cos 2\theta + iF^{(1)}M_2(H)\sin 2\theta\right|^2
\end{aligned}
\tag{3.19}
$$

The TFTC part should remains unchanged since $\delta(H,T) = 1$ at two ends of a large field, while the switching edge in the middle should be improved by TFTC reduction. The RXMS experiment was taken at 34 K, thus, the $\delta(H,T)$ curve should be accordingly constructed by the given temperature. Because of the intermediate state between 25 K and 50 K, the $\delta(H,34K)$ is tuned between $\delta(H,25K)$ and $\delta(H,50K)$. The goodness of the fitting on RXMS data is explicitly demonstrated in Figure 3.18 I (for Γ point) and II (for Z point).

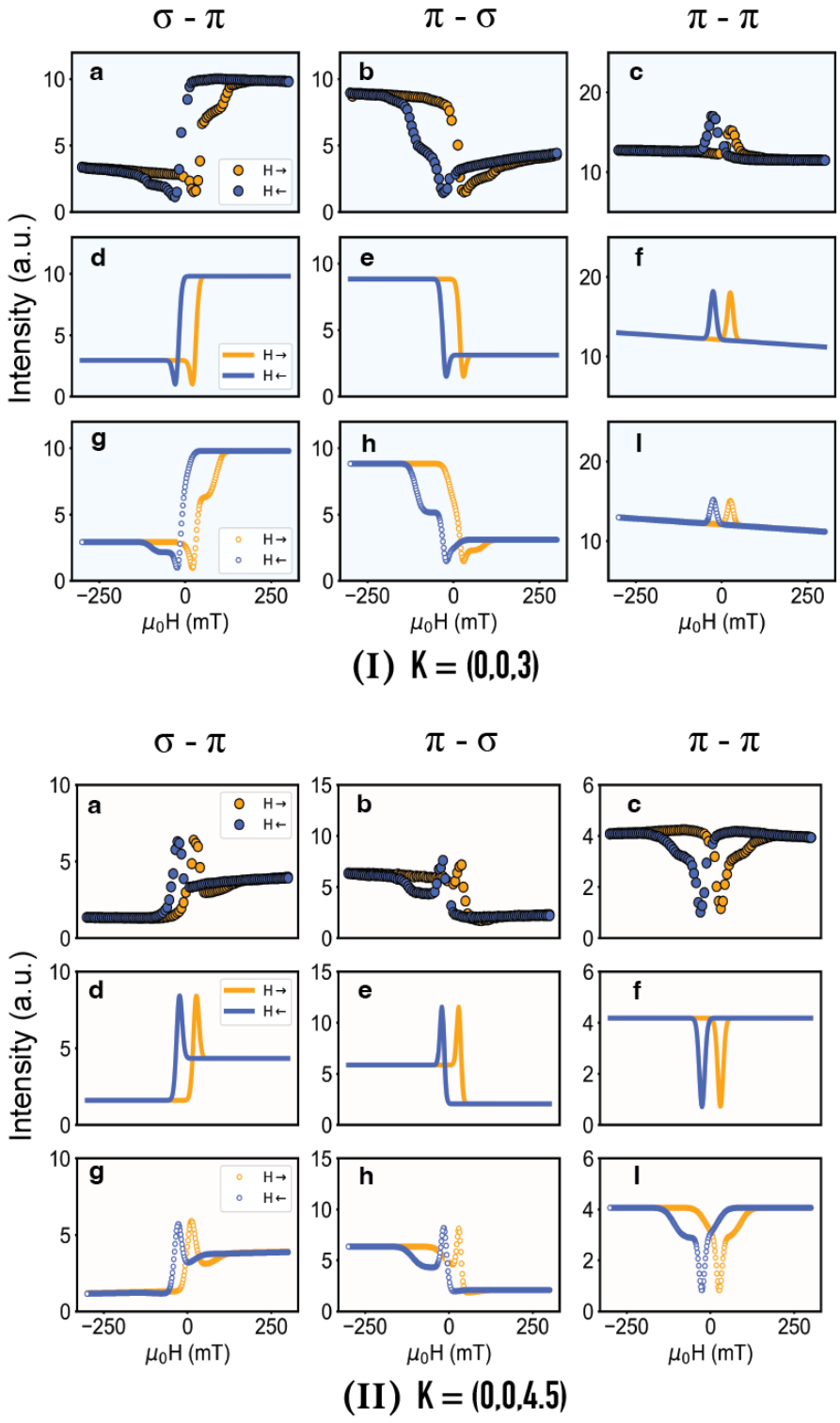


Figure 3.18: Linear polarisation diffraction channels at Γ point (top row) and Z point (bottom row). The dotted curve are obtained by RXMS at 40 K, while the solid fitted curve are made as described by the corrected block model. The trim features at the low field can be successfully described with the new model, which further supports the evidence of the phase coexistence in a small field range.

Analogously presented as Figure 3.16, the top rows of Figure 3.18 in I and II are experimental RXMS results (solid dots). In contrast, as stated before, the middle rows (solid curve) are modified rotation models, and the bottom rows (empty beads) are further fittings from the model, taking into account the phase coexistence effect. The salient difference between modified rotation and coexisted phase model is observed for $\sigma - \pi$ and $\pi - \sigma$ channels in both Γ and Z diffraction and $\pi - \pi$ channel in Z diffraction. The symmetric steps in the modified model near $H = 0$ switching position are replaced by winding curves in the coexistence model, which is much bettter fitting the experiment data. The improvement of the fitting is mainly due to the $\delta(H, T)$ fixing parameters which consider the broadening of the phase coexistence range and a large proportion of TFTC phase loss and reconstruction. Furthermore, as clearly seen on $\sigma - \pi$ and $\pi - \sigma$ channels in Z diffraction from II, the double sharp peaks in the modified model are largely suppressed if considering $\delta(H, T)$, as shown by coexistence model. This can be attributed to the fact that a large proportion of TFTC is lost within the coexistence phase range, resulting in the weaker contribution to the diffraction.

Overall, the quality of applying the coexistence phase model to fit the linear polarisation RXMS experiment data is improved. Loads of details of switchings are found in linear polarisation diffraction by taking into account the TFTC fraction function $\delta(H, T)$. This is, so far, the most accurate interpretation of switching dynamics for the Y-type hexaferrite magnetic cone structure.

3.5 Conclusions

In this chapter, we report the study on one of the multiferroics candidates, Y-type hexaferrite $Ba_{0.5}Sr_{1.5}Mg_2Fe_{12}O_{22}$. We introduce this crystal's crystallographic and magnetic structures and report the experimental characterisation of the multiferroicity from magnetometry and ferroelectricity aspects. We also report the latest progress studying the multiferroic phase switching in Y-type hexaferrite. We propose a more precise model to describe the magnetic field switching based on the TFTC rotation model earlier. When the external magnetic field is sweeping

on the single domain generated by cross-field poling, we find a two-step transition pattern in magneto-current and magnetometry measurements that was not fully understood before. Further evidence from RXMS diffraction and temperature-dependent magnetometry demonstrates that a mixed state between TFTC and intermediate LC phase is formed once the system is triggered by a small magnetic field crossing the zero point. The switching details are found in all linear polarisation diffraction curves, which can be well described by introducing a new block model with a proportional factor $\delta(H, T)$ considered. This work promotes the understanding of the polarity switching process of the multiferroic domains in Y-type hexaferrite. The phase diagram is rather complicated at low temperatures, especially in the dynamic switching process.

4

Magnetic domain imaging and ultrafast switching

Contents

4.1 Introduction 85
4.2 Domain size controlled by electric bias fields 86
4.2.1 XMCD imaging on magnetic domain 86
4.2.2 Electric field control of the single domain 89
4.3 Domain switching by THz pulse train 91
4.3.1 Development of the experiment setup 91
4.3.2 Results and discussion 96
4.4 Conclusion 98

4.1 Introduction

The magnetic polarity exhibited by the TFTC structure is linked to the handiness of the cycloidal structure. Almost every non-collinear magnetic order could demonstrate a certain sense of rotation, which could be utilised for imaging by magnetic circular dichroism. As explained in chapter 2 on the circular dichroism effect, the selection rules lead to the transition probability for excited electrons being different for opposite circular polarised X-rays. In chapter 3, we report the linear polarisation effect of resonant diffraction for the TFTC order, where the behaviour of

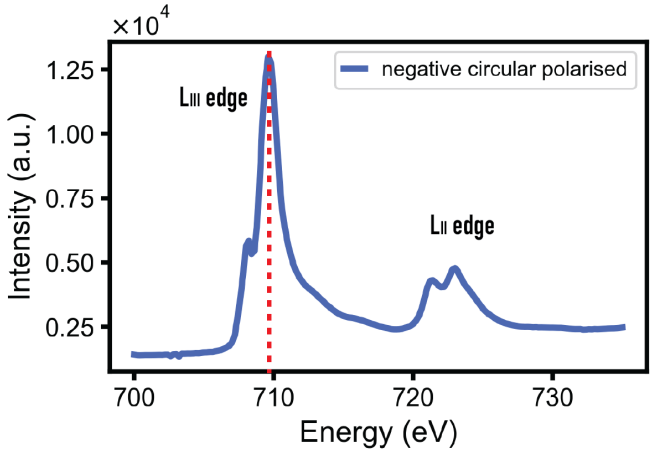


Figure 4.1: Fe *L*-edge from BSMFO by FY mode probed with negative circular polarised X-rays. The peak position at 708 eV is the energy we chose for imaging where circular dichroism is maximum.

the diffraction intensity demonstrates the polarity. Here, we will exploit the circular dichroism effect brought by the helical/cycloidal nature of the BSMFO phases (RT-helical/LT-TFTC) for domain imaging. I will demonstrate that the domain size can be manipulated due to the polarisation properties of the multiferroics. Furthermore, a challenging experimental setup is established for switching the magnetic domains by THz pump-probe, aiming at realising the switching at the ultrashort time scale.

4.2 Domain size controlled by electric bias fields

4.2.1 XMCD imaging on magnetic domain

Although a relatively comprehensive understanding of the magnetic phases for Y-type hexaferrite BSMFO is introduced in the last chapter, the image of the magnetic domains still needs to be explored. This is quite important and challenging since the domain size and speed of response to voltage are significant indices for assessing a memory device. This chapter will utilise the XMCD effect from the polar TFTC structure for domain imaging at Fe L_3 resonant energy, performed at Beamline I10 at Diamond Light Source (DLS).

As introduced in the previous chapter about the Y-type hexaferrite phase, the BSFMO is ordered at the helical phase at room temperature, exhibiting an

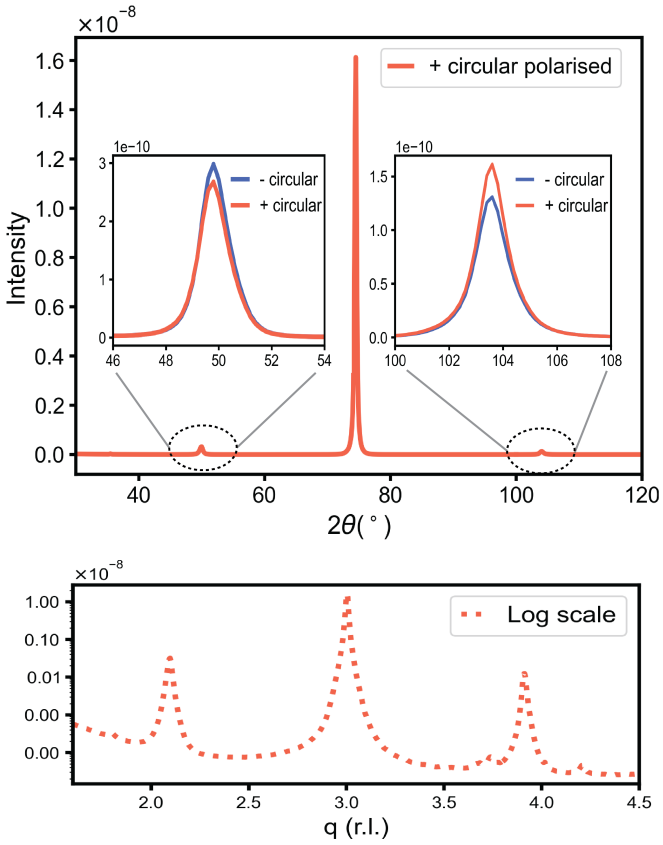


Figure 4.2: Circular dichroism of resonant magnetic diffraction on room temperature helical phase for BSMFO single crystal. Top: $\theta/2\theta$ scan around $(0, 0, 3)$ peak, where circular dichroism is observed for both magnetic peaks. Bottom: Log scale of the $\theta/2\theta$ scan in reciprocal lattice unit.

incommensurate propagation vector at $(0, 0, 0.9)$. By tuning the X-ray energy at the peak position in Fe L_3 edge, as shown in Figure 4.1, double magnetic diffraction satellites exist at both sides of the charge diffraction peak $(0, 0, 3)$. As clearly demonstrated by Figure 4.2, the orange curve in the background is the $\theta/2\theta$ scanning centralised around $(0, 0, 3)$ charge peak with the positive circular polarised beam. The zoomed subplots on the two magnetic diffraction peaks highlight the circular dichroism (CD) compared with negative circular polarised light shown by the blue curve. The sign of CD is reversed at the two magnetic diffraction positions.

Similar procedures are performed for the low-temperature TFTC phase, which exhibits a propagation vector of $(0, 0, 1.5)$, as shown by the log scaling scan in Figure 4.3 bottom. The unequal intensity of $(0, 0, 1.5)$ and $(0, 0, 4.5)$ peaks is

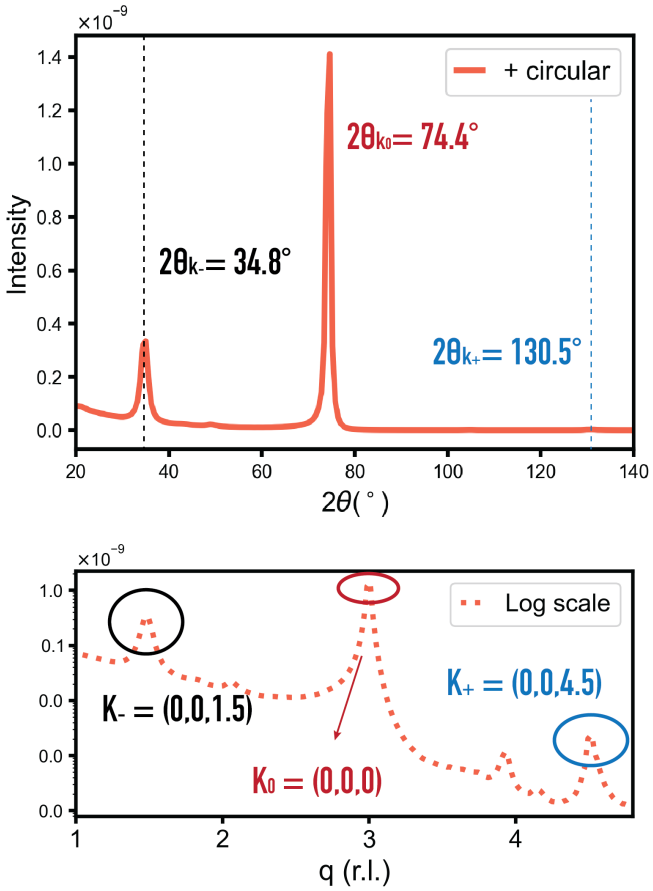


Figure 4.3: The magnetic characterisation for TFTC phase at low temperature by resonant magnetic diffraction.

due to the imperfect cleaving surface, broken into two sections that result in the beam deviation when rotating the sample. Therefore, the detector misses the maximum intensity position for $(0, 0, 4.5)$ diffraction for high-angle scanning. After successfully characterising the sample at different temperatures with correct circular dichroism, this CD effect can be exploited to obtain the domain pattern by scanning the surface. The resolution of the pattern is defined by the beam diameter, the minimum of which is 50 μm, enough for the millimetre-size magnetic domains. In the following scanning experiments, a small angle peak at $(0, 0, 1.5)$ is strong enough and is utilised to consider the diffraction intensity of magnetism. However, the problem of beam expansion due to the grazing incidence is introduced into the experiment. Although the imaging resolution is reduced by this projection effect, the error is within an acceptable range.

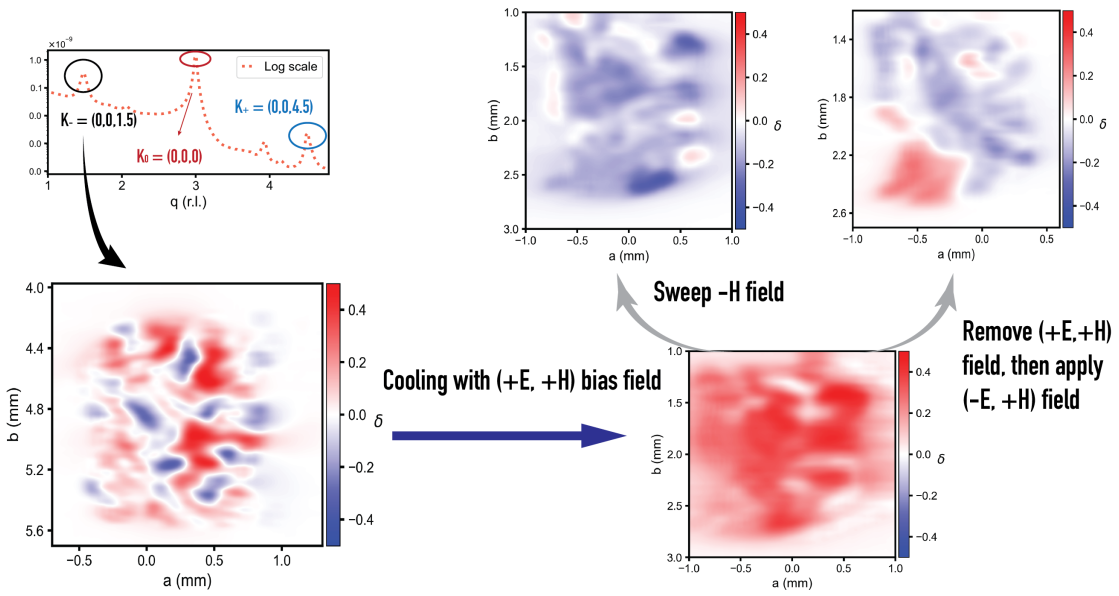


Figure 4.4: The procedures of the domain manipulation on multiferroic TFTC structure. The multi-domain pattern was obtained by scanning the sample surface via magnetic dichroism effect of the $(0, 0, 2.1)$ satellite. The single red domain was generated by applying the $+E$ bias poling field. On that basis, the reversed single blue domain and partially switched large blue domain were obtained by sweeping the $-H$ field and applying $-E$ bias voltage, respectively, as indicated by the top two panels.

4.2.2 Electric field control of the single domain

The challenge of imaging the TFTC phase with electric field control resides in the high coercivity of the magnetic domains at low temperatures, which means high voltage poling is necessary. Meanwhile, it requires the protection of the sample to avoid breaking down. As it has already been known from the previous chapter, the voltage contact is applied perpendicular to the electromagnets, complying with the polarisation and magnetisation geometry of this special multiferroics.

To experiment safely, the sample is mounted with insulating glue and cleaved the sample *ex-situ* before transferring to the vacuum chamber. Therefore, the TEY mode scanning for the L edge absorption spectrum is unable to use. First, it is necessary to obtain the FY mode spectrum and then characterise the circular dichroism of the helical phase at room temperature. Next is to cool the sample down without an electric field, and only a magnetic field is applied to generate the TFTC phase. As shown in Figure 4.4, the multi-domain state of the TFTC structure is re-examined

by directly cooling down to 34 K. It is clear that the multi-domains are randomly distributed, shown by the circular dichroic regions, where large-size domain walls (white lines where $\delta = 0$) are found between the domains. As discussed in the previous chapter, the dichroic property is relevant to the cycloidal spin components aligning along the a axis, which is perpendicular to the TFTC conical axis. The blue or red dichroic signal represents the $\pm a$ alignment for the cycloidal part.

Taking a similar strategy for poling the sample as in Figure 3.9, high voltage is applied since 150 K when sample is less conducting, and the orthogonal (E, H) field is on throughout the cooling process until 34 K, then removing the E field when temperature equilibrium is achieved. The single domain is constructed by the homogeneous red dichroic signal across the whole sample, which is attributed by the high poling voltage during the generation process of TFTC structure.

The domain polarity switchings are performed in two strategies. First, the magnetic field is swept in the opposite direction, resulting the single domain polarity being reversed, as shown by a negative dichroic signal. This single blue domain is found at the Figure 3.9 top panel when sweeping the magnetic field to the opposite. The second method is slightly complicated with polarity switching by an electric field. When switching the magnetic field back to $+H$, the sample recover to a homogeneous red domain state, and then removing the magnetic field. A tentative negative bias voltage with -100 V is successively applied, then followed by $+H$ again to 300 mT. Under the influence of $(-E, +H)$ set of external fields, the magnetic domain image is shown on the top right panel in Figure 4.4 with switched blue domain. Although the red domain is switched to blue, the $-E$ field results into the partial switching, leaving almost a quarter of the sample area to remain red.

By applying electric and magnetic fields simultaneously, the intrinsic multi-domain state of the multiferroic phase can be manipulated into a single homogeneous domain. Another significant feature is that both E and H fields can switch the magnetic polarity to the opposite. Furthermore, the E field switching is more difficult to change the whole domain. This coercivity, or memory effect from electric field switching, is common in many multiferroic systems [22, 28].

4.3 Domain switching by THz pulse train

4.3.1 Development of the experiment setup

Although not flawlessly switched, a static electric field has verified the possibility of electrical switching on a single magnetic domain. In this section, I will employ THz pulses, one of the most powerful electric field pulses so far available in the laboratory, to realise the non-contact switching on the magnetic domains.

First, I will discuss a few physical backgrounds of the THz generation, a prevalent subject, before starting to introduce the development of the experiment setup. There are two main strategies for THz generation on the basis of near-IR femtosecond laser facility: optical rectification (OR) and difference frequency generation (DFG). Here in our experiment, I adopt one of the mainstream methods utilising OR for high power THz generation, using the titled-pump-pulse-front technique in nonlinear crystal $LiNbO_3$ (LNO).

THz source from LNO

The tilted-pump-pulse-front scheme for efficient phase-matched THz pulse generation has been rapidly developing since Hebling *et al.* proposed it in 2002 for the first time for $LiNbO_3$, a trigonal $3m$ structure with a high electro-optical coefficient. The basis of THz generation in LNO is optical rectification process, which is intimately relevant to the linear electro-optical effect (or Pockel's effect). Pockel's effect implies that the refractive index of a nonlinear crystal can be modified by applying a *dc* electric field E_0, which is useful for THz pulse detection. However, the OR process is the reversal process from Pockel's effect. In non-linear media with non-zero second order dielectric susceptibilities $\chi^{(2)} \neq 0$, a polarisation is induced within the non-linear material proportional to the electric field intensity E_0^2:

$$P^{(2)} \propto \chi^{(2)} E_0^2 \cos^2(\omega t) = \chi^{(2)} E_0^2 [1 - \cos(2\omega t)]/2 \tag{4.1}$$

The 'zero-frequency' gives a *dc* polarisation for monochromatic frequency. However, for an ultrashort pulse with broadband frequency, this time-dependent *dc* polarisa-

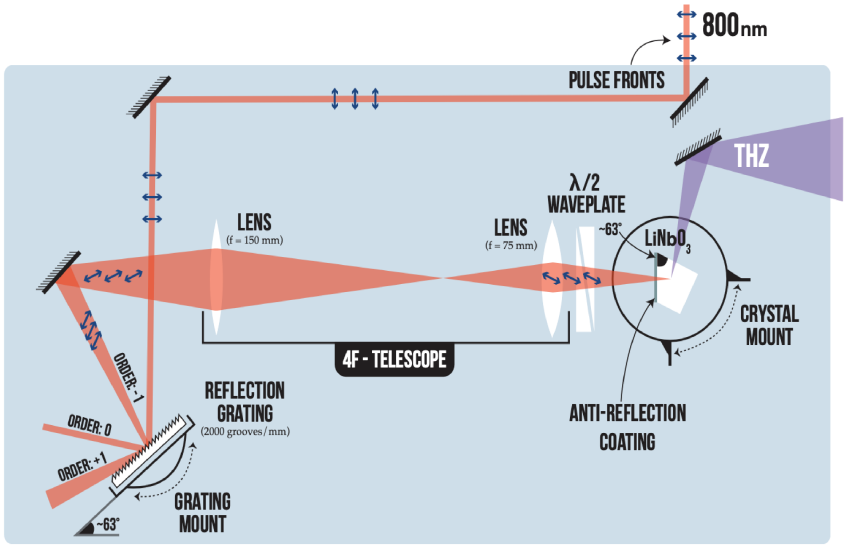


Figure 4.5: Illustration of tilted pulse front scheme for THz generation from LNO nonlinear crystal. The grating system turns the pulse front to a certain degree before leading to the 4–f telescope system, which focuses the beam into the target crystal.

tion is modulated by the pulse envelope function, resulting in THz radiation with $E_{THz} \propto \frac{\partial^2 P_0}{\partial t^2}$

To obtain optimal THz beam quality and pump-to-THz conversion efficiency, the noncollinear velocity of pump v_p^{gr} and THz pulses v_{THz} requires the peculiar phase match condition: $v_p^{gr} \cos\gamma = v_{THz}$, the pump-pulse front angle γ is tuned by a reflective holographic grating (groove of 1200 mm^{-1}) and a 4–f telescope system, as shown in Figure 4.5. For efficient generation around 1 THz, the pulse front angle is tuned $\gamma = 62°$ [112]. To improve the THz emission efficiency, an anti-reflection coating is mounted on the normal incidence surface by a piece of Kapton tape (DuPont Electronics).

Free space THz pulse characterisation

Once the THz pulse is generated from the crystal, a golden reflection mirror is placed close enough to the LNO crystal to collect the THz radiation into the collimation system. To enhance the THz intensity, a pair of large diameter off-axis parabolic mirror (OAPs) with RFL(radial focal length) = 50.8 mm and another RFL = 25.4 mm to used to expand the beam size by twice and then propagates along

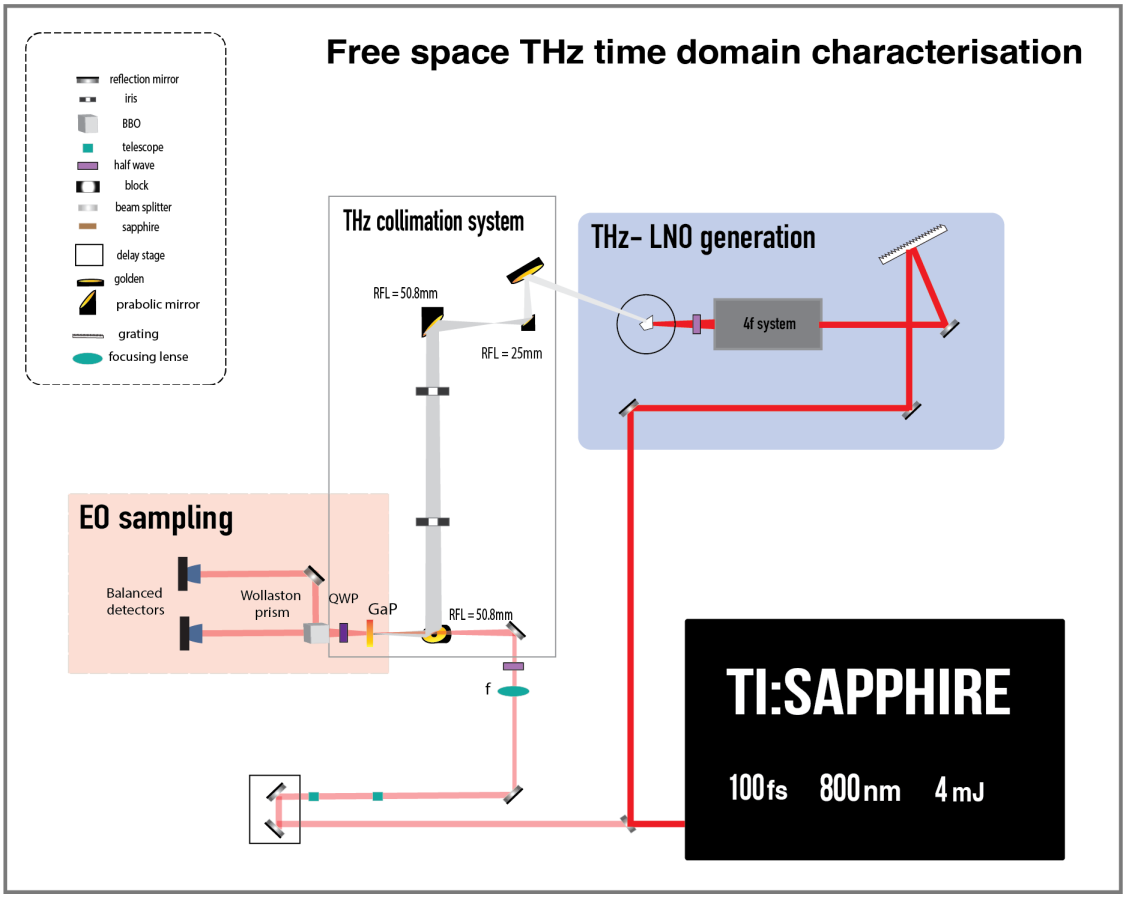


Figure 4.6: Schematic of THz pulse characterisation via time-domain spectroscopy in free space. A golden mirror guides the THz pulse into the collimation system composed of off-axis parabolic mirrors (OAPs). In contrast, the detection 800 nm pulse goes through the second OAP within the drilled hole and is focused on the detection crystal GaP. The birefringence change of the GaP is modulated by the THz electric field, which results in the polarisation signal of the detection beam changes along with E_{THz}.

the collimated path, as shown in Figure 4.6 gray line. The collimation system is placed within a vaccum box for the purpose of reducing water vapor absorption, since the water molecular has characteristic absorption lines between 2 meV and 20 meV from molecular rotations and bonding oscillations [113].

Electro-optic (EO) sampling aims to convert the THz electric field signal into a light signal that a photodiode can detect by utilising the Pockels effect. The electro-optic crystal used in the experiment is $\langle 110 \rangle$ cut GaP (TO phonon cutoff is 11.1 THz), which only works under the constraint of the complete overlapping of THz beam and IR detection beam after focusing. The instantaneous THz electric field induces a change in the birefringence of the crystal, which rotates the plane

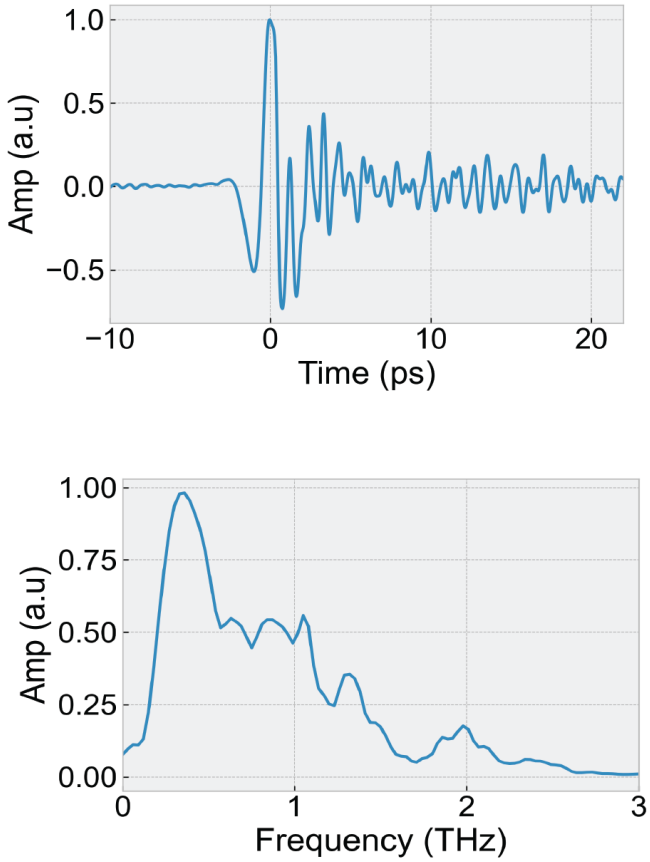


Figure 4.7: Time domain characterisation of the free space THz pulse from LNO. Top: time domain signal of THz electric field in 30 ps range; Bottom: THz spectrum by Fourier transform of $E(t)$.

of polarisation of the IR detection pulse. Then the quarter-wave plate (QWP) turns the linear polarisation of the IR light into circular polarisation, which is then decomposed into the horizontal and vertical components by the Wollaston prism and detected by a pair of photodiodes. The spatially separated s and p IR components may not remain balanced when the THz electric field tunes the birefringence of GaP for the IR pulse. Since the THz pulse is picosecond while the detection IR pulse is in the femtosecond range, the entire THz electric field can be mapped by tuning the relative time delay between THz and IR pulses through the mirrors mounted on the delay line. In this way, the THz electric field intensity with respect to the delay time depicts the THz pulse amplitude and phase information simultaneously, which is the most accurate characterisation of the THz pulse. This powerful method is called THz time-domain spectroscopy (THz-TDS).

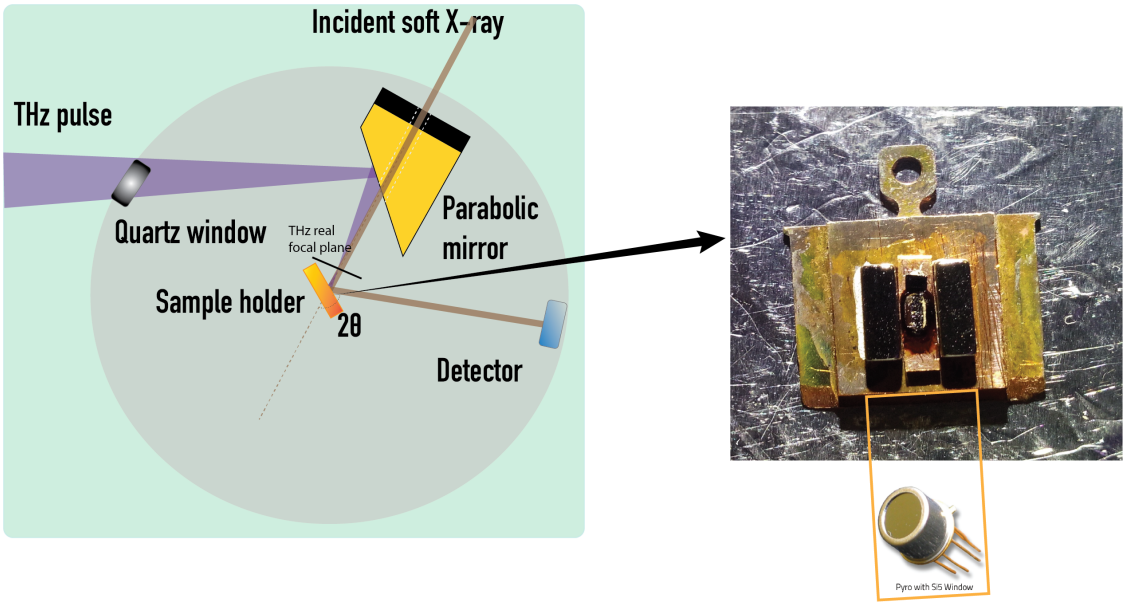


Figure 4.8: THz pump-Xray probe experimental setup at beamline I06, Diamond Light Source (DLS). The self-developed THz source is combined with a high vacuum diffraction chamber. The sample holder is mounted with a pyrodetector to find the THz focal plane within the high vacuum.

Figure 4.7 shows the time domain spectroscopy of the reference THz pulse propagating in free space (Top panel). The spectrum of THz pulse is obtained by Fourier transform on the $E(t)$ (Bottom panel). Without purging the water vapour, there are some clear vapour absorption lines at 0.5 and 1.2 THz, and the spectrum is not smooth due to broadband absorption. The THz-TDS used in measuring the dielectric response requires the reference and sample signal. Thus it is necessary to exclude the absorptions by placing them into the vacuum.

Assembling the THz with a high vacuum system

To reduce the THz beam expansion after long-distance propagation, an f =250 mm Teflon focal lens is used outside the chamber. The THz beam is re-focused by another parabolic mirror (RFL=25.4 mm) within the chamber close to the sample position. The onsite THz energy is measured at room temperature before pumping the vacuum chamber by a thermo-detector. The pulse energy is estimated to be 5 μJ equivalents to 500 kV/cm at the peak electric field.

The green section of Figure 4.8 describes the inner geometry of X-ray and THz beam, which are tuned and overlapped on the sample holder through a hole-drilled parabolic mirror when the chamber is open. The sample holder is shown on the right, on which a pair of permanent magnets are mounted at both sides of the sample. The most challenging part is the alignment of the THz beam and soft X-ray within the chamber at low temperatures. First of all, the overlapping of the beam with focused THz changes when pumping the vacuum down due to the unexpected movement of OAP mirror. Secondly, the THz focal plane is in front of the sample plane, which means the X-ray beam misses the THz focal point on the sample surface. Although a pyro-detector is mounted beneath the sample holder, as shown in the figure, to find the THz focal point before placing the holder, it brings much trouble when performing experiments with different temperature conditions because of the thermal expansion and contraction. The THz beam projected on the sample surface can roughly be depicted by the dashed areas, as shown in Figure 4.9. Here we cannot perform the magnetic field scanning due to the permanent magnets since the vacuum chamber is not equipped with an additional channel for voltage output.

4.3.2 Results and discussion

After all the preparation was ready, I took the experiment with an ongoing strategy. Firstly, a single THz pulse was applied as a tentative switching, and no sign of switching was found. Then the strategy is changed to use a series of pulse trains for 30 seconds, acting as a *dc* electric field pulse, to try to observe the signal. As shown in the Figure 4.9 second panel, the same range of scanning was performed and a significant switching sign was observed within the circled area, in other words, the change in the dichroic signal was detected. One pulse switching was not convincible to induce the change since the mechanical scanning over the sample surface may bring huge noise in the dichroic signal. The sample exposure under the THz radiation for a certain of time is taken as the strategy for switchings in the following experiments.

The low-temperature switching signal was not very obvious from the signature of a confined range of domain reversing, highly due to the resistance from the domain

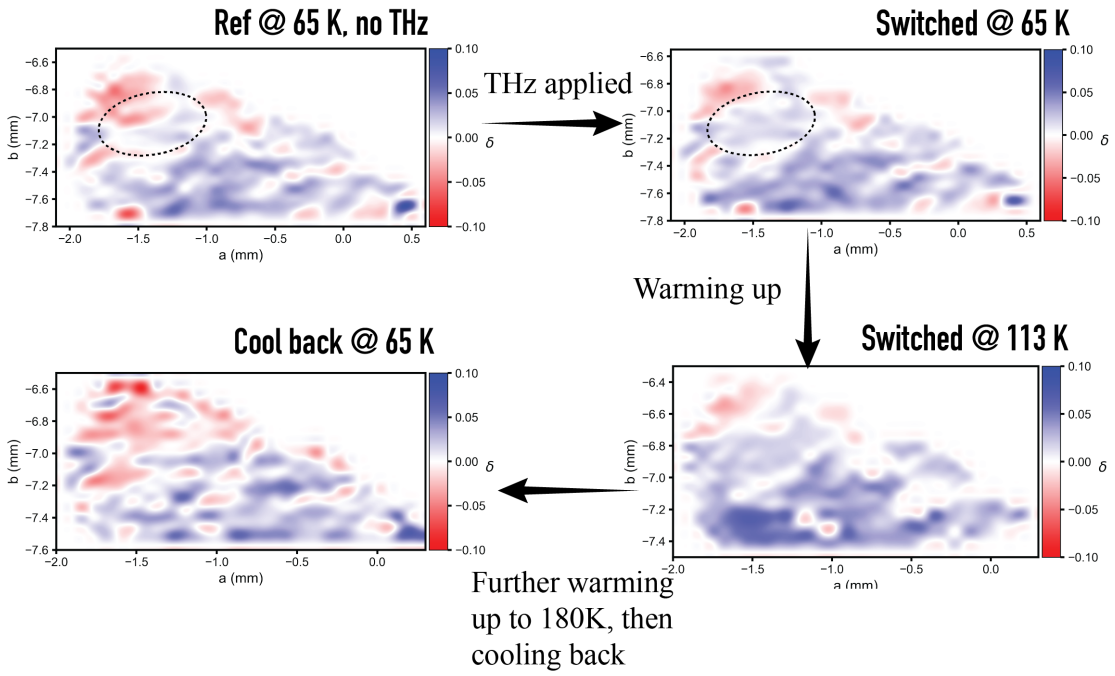


Figure 4.9: The evidence of direct THz switching on the TFTC magnetic domains at different temperatures.

at low temperature. Then the THz pulse is kept applied during the warming cycle and removed not until performing the scanning is done. More area was found to be reversed, including small island domains with red and blue dichroism, as shown in Figure 4.9. This indicates that both polarised TFTC domains can be switched in another direction. This is counter-intuitive because the THz time-dependent electric field has a preferred direction due to the pulse asymmetry. Here, the temperature was an important factor since the magnetic domain energy would be homogeneously reduced upon warming up, and the domains would become less resistant to switching. This explains the random switching for specific domains.

With THz consistently applied, we warmed up the sample across the TFTC–LC (longitudinal cone phase) transition temperature (150 K) up to 180 K, then cooled down back to the TFTC phase at 65 K. Surprisingly, more reversed domains (blue to red) were identified around the THz beam profile area, indicating that THz was unable to stabilise a few 'blue' domains, at least for this temperature cycling.

4.4 Conclusion

In this chapter, the study on the switching of magnetic domains in the BSMFO multiferroic TFTC phase is continued by THz radiation. First, we introduce the magnetic domain imaging technique methodology based on the magnetic dichroism of the magnetic diffraction peak. We utilised this technique for TFTC domain imaging, extrapolating the toroidal nature of the TFTC structure, which an external electric bias field can manipulate. By selecting the (E, H) bias fields, the polarities of the TFTC single domain can be achieved and switched. Last but not least, we attempted to switch the domain by a non-contact method using THz radiation generated separately outside the chamber. The experiment was challenging due to the invisible THz radiation that brought much uncertainty in optical alignment when combining the high vacuum and low-temperature environment together. Although complicated, we still obtain tentative results on the magnetic domain manipulation by THz pulse train illumination, justifying the possibility of realising non-thermal magnetic domain switching via picosecond light pulses. This achievement can guide the design of further experiments in an ultrafast time scale on the platform of the FEL facility, where the ultrafast X-ray can catch up with the dynamical process induced by the picosecond THz pulse when the magnetic structure reverses.

5

Imaging of antiferromagnetic structures in hematite

Contents

5.1 Introduction–Magnetic structure of hematite 100
5.2 Anisotropic XMLD effect in hematite 102
5.2.1 Angular dependence of XMLD for In-Plane order 102
5.2.2 Angular dependence of XMLD for Out-Of-Plane order . 105
5.2.3 Images constructed by anisotropic XMLD effect 107
5.3 Results and discussion 112
5.3.1 Domain wall analysis 112
5.3.2 Intermediate state at Morin transition 113
5.3.3 AFM topological structures 114

Magnetic materials offer a versatile platform for exploring exotic information carriers. Except for multiferroics, the topological spin solitons in real space are attracting unprecedented focus from researchers interested in fundamental questions. Magnetic skyrmions are one of the categories with topological features, which show great promise as solitonic information carriers in device applications [114–116]. Most of the studies on skyrmions are based on ferromagnetic systems [52, 117–121], in which the dipolar and inverse-Dzyaloshinskii Moriya interactions tend to stabilise the winding of spins. However, the ferromagnetic spin textures are intrinsically hazardous in generating small textures because of long range dipolar fields, and has

side-way deflection effects when driven by spin-orbital torque due to the skyrmion Hall effect (SkHE) [115, 122]. The antiferromagnetic analogues for skyrmions are now gaining increasing attention since the mentioned drawbacks because of the net moment can largely be overcome by the spin cancelling from antiparallelly aligned magnetic sublattices [114, 123, 124]. In this chapter, we report the discovery of a family of topological antiferromagnetic spin textures in α-Fe_2O_3 – an Earth-abundant oxide insulator. We introduce the technique of imaging these topological structures with a soft X-ray-based photon emission microscope (X-PEEM) by utilising the XMLD effect. We apply the XMLD-PEEM techniques in two methods, which enables the difference between in-plane (IP) AFM moment and out-of-plane (OOP) moment, as well as the relative orientation of the AFM moment within the plane. Based on imaging with a high resolution of 50 nm, we demonstrate the evolution of the AFM textures under a series of temperature conditions. We reveal various kinds of AFM spin structures, such as AFM domain walls (both Néel and Bloch types), AFM spin vortices, and AFM half-skyrmions, by developing an advanced technique of XMLD data analysis for resolving orientational AFM moments. This work is mainly derived from the work published in Nature 590, 74–79 (2021).

5.1 Introduction–Magnetic structure of hematite

α-Fe_2O_3 crystallises in the trigonal corundum structure (space group $R\bar{3}c$, point group D_{3d}), with lattice parameters (in the hexagonal setting) $a = 5.038(2)$ Å and $c = 13.772(12)$ Å. It orders antiferromagnetically at T_N (946 K) with the Fe^{3+} spins being ferromagnetically coupled in the basal (0001) plane and antiferromagnetically stacked along the c axis. The spin orientation is governed by the axial magneto-crystalline anisotropy $K_u(T)$, which changes with temperature owing to the interplay between magnetic dipolar and single-ion interaction. Most noteworthy is that α-Fe_2O_3 is one of the few systems that holds $K_u(T)$ sign reversal, leading to the spin-flop while keeping antiferromagnetic alignment. This so-called 'Morin transition' is usually located at 260 K [125] but can be tuned by chemical substitutions even close to room temperature [126–128]. This character enables the α-Fe_2O_3, an ideal

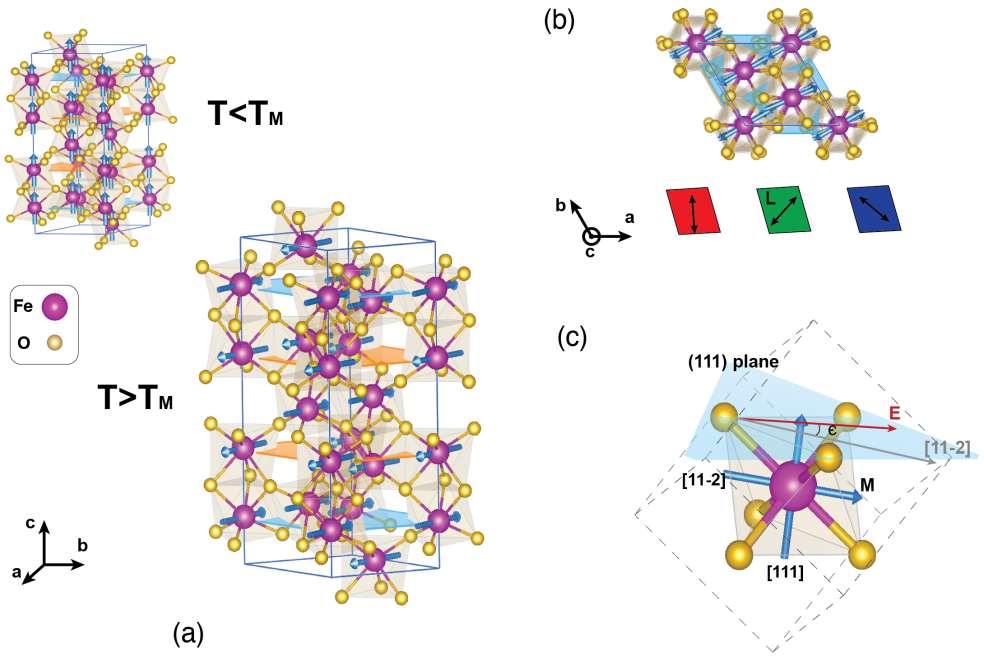


Figure 5.1: Commensurate antiferromagnetic structure of α-Fe_2O_3. (a) The antiferromagnetic alignment of spins flip between in-plane (IP) to out-of-plane (OOP) when crossing the critical Morin temperature T_M. (b) In-plane AFM spins order in three directions with Néel vector L rotating by 120° each, forming RBG-colored domains. (c) Fe^{3+} octahedral is represented in O_h point group symmetry, with [111] direction parallel to the c axis of the α-Fe_2O_3 lattice.

system, to be customised for applications on weak magnetisation devices. The diagram of Morin transition in α-Fe_2O_3 is shown in Figure 5.1 (a), where the phase transition of spin reorientation belongs to the first order type. Instead of using magnetisation **M** for ferromagnetism, the Néel vector, $\mathbf{L} = \mathbf{M}_1$ - $\mathbf{M}_2$ (from two adjacent layers), can describe the spin-flop between in-plane ($T > T_M$) and out-of-plane $T < T_M$ more precisely, giving 90° shift around one of the principle axis within the plane. As for the in-plane phase, the Néel vector **L** is typically rotated by a certain degree from the principle axis due to the competition of parallel/anti-parallel superexchange interaction, pointing to three equivalent directions by 3-fold rotational symmetry, forming three parent domains as indicated by Figure 5.1 (b) with RBG colours. Experiments find that in-plane phase has equally distributed three domains correlated by 120°, which will be analysed further in later sections.

5.2 Anisotropic XMLD effect in hematite

To study the antiferromagnetic properties, we utilise X-ray absorption spectroscopy (XAS), a powerful tool to reveal abundant magnetic information, such as the spin moment size and bonding environments in antiferromagnetism. As introduced in chapter 2, XMLD effect is ubiquitous in antiferromagnetism from linear polarised X-ray absorption, when the polarisation of the incident X-ray photons can either be chosen with horizontal (LH) or vertical (LV) with respect to surface plane. Although the 'natural' linear dichroism (XNLD) arising from non-magnetic origin may exist in α-Fe_2O_3, we find the experimental signal for XNLD is relatively tiny compared with XMLD. The local symmetry environment of magntic ions is crucial for the angular dependent of XAS because of the highly anisotropic d^n electron configuration. The XAS change due to the structural or crystal field of the magnetic ions has been extensively explored [129–132]; however, the measuring geometry for the near-edge absorption spectra is also quite important, especially for obtaining the correct XMLD signal by two energy differences. The geometry influence on the Fe $L_{2,3}$ edge has been successfully illustrated by Arenholz and Gerrit van der Lann [133] on the magnetite Fe_3O_4, which is ferrimagnetic with $Fe^{2+(3+)}$ valence states and two types of Fe ions with O_h, T_d site symmetries.

In the specific case of hematite α-Fe_2O_3 with point group symmetry D_{3d}, each Fe^{3+} is located at 12c Wyckoff position surrounded by 6 O^{2-} forming octahedral, analogous to the Fe^{3+} octahedral in magnetite Fe_3O_4, as shown in Figure 5.1 (c). Given a slight distortion along the projection of [111] direction, the local environment of Fe^{3+} octahedral in hematite is analogous to that in cubic symmetry from magnetite. Furthermore, for XAS spectra, this lowing of symmetry has no significant influence for the XMLD signal concerning measuring geometry, which is mentioned in the supplimentary information from [134].

5.2.1 Angular dependence of XMLD for In-Plane order

Fe^{3+} octahedral with O_h site symmetry has body diagonal direction [111], pointing out-of-plane, as shown in Figure 5.1 (c); the dashed line cage represents the cubic

basis. The [111] direction of the octahedral is parallel to the c axis in a hexagonal lattice, which can be figured out by comparing it with the lattice structure in (a). Therefore, the IP spin moments are found to lay within the (111) plane in cubic basis, and the OOP spin moments are along [111] direction. This corresponds to the Morin transition in hematite.

For either IP or OOP moments, the XAS spectra obtained by a specific polarised X-ray can reflect the magnetic information with certain symmetry constraints. Following the methods introduced by Arenholz and Gerrit van der Lann [133], two standard spectra I_0 and I_{45} are sufficient to establish the XAS spectra set through a linear combination of the basic standard spectra. Both spectra can be obtained from the first principle calculation on octahedral site Fe^{3+} with electric dipole approximation.

$$I_0 = XAS(\boldsymbol{M} \parallel [001], \boldsymbol{E} \parallel [001]) - XAS(\boldsymbol{M} \parallel [001], \boldsymbol{E} \parallel [010]) \tag{5.1}$$

$$I_{45} = XAS(\boldsymbol{M} \parallel [011], \boldsymbol{E} \parallel [011]) - XAS(\boldsymbol{M} \parallel [011], \boldsymbol{E} \parallel [01\bar{1}]) \tag{5.2}$$

The basic XAS spectra curves are shown in Figure 5.2. The difference of $L_{2,3}$ edge between I_0 and I_{45} shows the strong effect of anisotropy when probing in a different geometry.

For IP phase where spin moments are laid within the (111) plane, the relative angle between polarisation (ϵ) and spin moment direction (μ) can be accordingly defined with respect to $[11\bar{2}]$ direction. As shown in the right part of Figure 5.2, the experimental geometry can be designed by rotating the incident beam polarisation within the horizontal plane (which is denoted as LH polarisation) or fixing the incident X-ray while rotating the sample around the c axis. The later geometry is more practical since the polarisation rotation for horizontal X-ray within the plane is quite tricky at the synchrotron.

Akin to ref [133], the XAS spectra at given (μ,ϵ) angle pairs can be obtained by standard spectra as:

$$XAS(\mu, \epsilon) = F_{\parallel} + \frac{1}{6}[-4I_0 + I_{45} + (I_0 + 2I_{45})\cos(2\mu - 2\epsilon)] \tag{5.3}$$

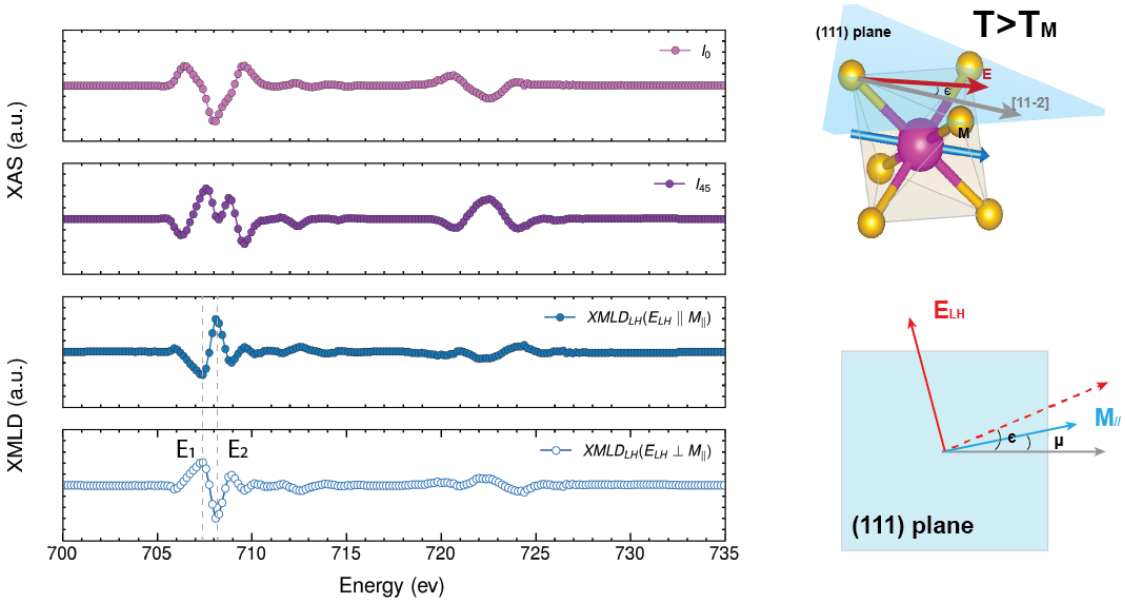


Figure 5.2: The standard XAS and XMLD spectra on IP moments probed by horizontal polarised X-rays. The diagram shows the experimental geometry in cubic octahedral coordination, ϵ, μ angles refer to the polarisation and spin moment directions with respect to the $[11\bar{2}]$ axis.

where $F_{\parallel} = XAS(\mathbf{M} \parallel [001], \mathbf{E} \parallel [001])$ is the constant term irrelevant to the two angles. If the ϵ is shifted by 90° within the plane by measuring at a normal E field, the angular dependence of XAS(μ,ϵ) is π shifted, and the linear dichroism signal can be derived by subtracting the two XAS spectra:

$$XMLD_{LH}(\mu, \epsilon) = XAS(\mu, \epsilon) - XAS(\mu, \epsilon + 90^{\circ}) \tag{5.4}$$

$$= -\frac{1}{3}(I_0 + 2I_{45}) \cos(2\mu - 2\epsilon) \tag{5.5}$$

The total XMLD signal is proportional to $(I_0 + I_{45})$ profile which has maximum or minimum at $E \perp M$ and $E \parallel M$ geometry, as plotted in Figure 5.2. Suppose we carefully choose two energy sites corresponding to the peak and bottom at the L_3 edge in XMLD spectra, as indicated by the grey dashed lines, we can tell the difference between $E_{LH} \parallel M_{\parallel}$ and $E_{LH} \perp M_{\parallel}$ at a given horizontal polarised E field by sign change of the XMLD difference:

$$\delta^{2E}_{LH}(\mu, \epsilon) = I^{E_1}_{XMLD}(\mu, \epsilon) - I^{E_2}_{XMLD}(\mu, \epsilon) \tag{5.6}$$

which decides the contrast of the signal: for $M_{\parallel}$ parallel to E_{LH} to be positive while for $M_{\parallel}$ perpendicular to E_{LH} to be negative. The sensitivity of the relative angle dependence of XMLD signal at two energy differences is significant in constructing the in-plane distribution of antiferromagnetic moment, which will be discussed further.

5.2.2 Angular dependence of XMLD for Out-Of-Plane order

For phases below the Morin transition, the out-of-plane spin order that hematite exhibits can also be revealed by XMLD, however, in a slightly different manner. As shown by Figure 5.3 (a), the measuring geometry is different from IP order since the spin moment flops into the normal plane, here is shown along [111] direction by the blue arrow. Here the polarisation direction along the surface normal is denoted as LV polarisation while the polarisation direction within the plane is labelled as LH polarisation. Experimental geometry can be set with E_{LH} or E_{LV} incidence by shifting the beam polarisation to out-of-plane through the crystal polariser. The XAS spectra of $M_{\perp}$ moments in such two polarisation cases are different:

$$XAS(M_{\perp}, E_{LV}) = -(\frac{2I_0}{3} - \frac{2I_{45}}{3}) + F \tag{5.7}$$

$$XAS(M_{\perp}, E_{LH}) = -(\frac{2I_0}{3} + \frac{I_{45}}{3}) + F \tag{5.8}$$

The XMLD signal can accordingly be defined by the difference of (LH, LV) spectra on $M_{\perp}$ moments as:

$$XMLD_{LH-LV}(M_{\perp}) = XAS(M_{\perp}, E_{LH}) - XAS(M_{\perp}, E_{LV}) = -I_{45} \tag{5.9}$$

which is shown in the black curve of Figure 5.3 (b). However, when encountering in-plane moments, the XAS spectra of $M_{\parallel}$ probed by E_{LV} are defined as:

$$XAS(M_{\parallel}, E_{LV}) = -(\frac{2I_0}{3} + \frac{I_{45}}{3}) + F$$

which is in the same format as $XAS(M_{\perp}, E_{LH})$ from Equation 5.8. The XMLD signals from $M \parallel 0°$ and $M \parallel 90°$ alignment defined by two polarisation methods

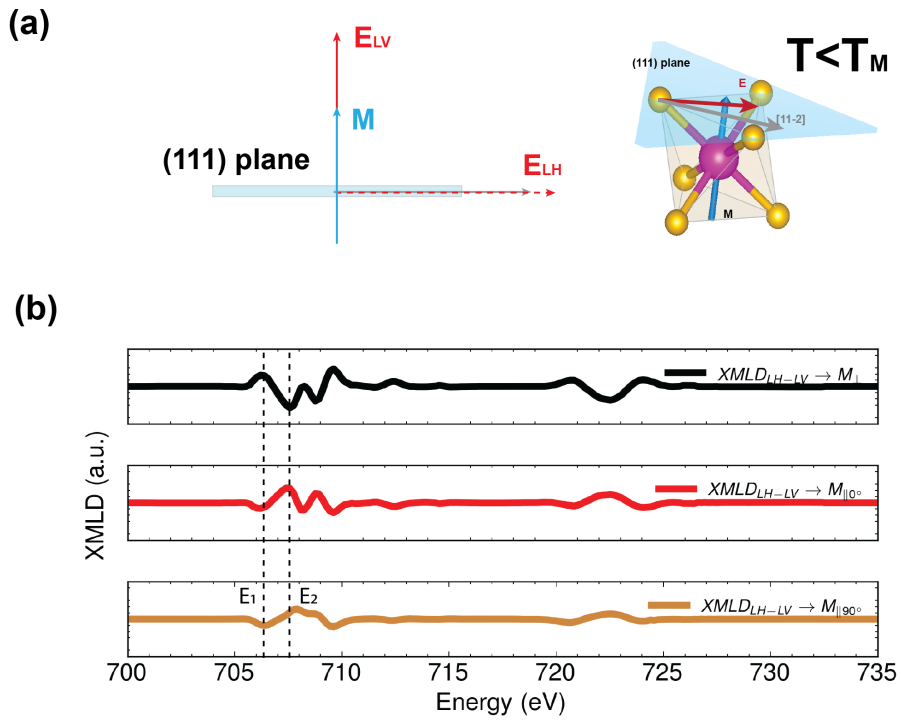


Figure 5.3: The XMLD spectra for OOP and IP moments revealed by (LH, LV) polarised X-ray. (a) Diagram of spin moment direction and X-ray polarisation direction with respect to the crystallographic axis. (b) XMLD spectra for different moment orientations have an opposite signal of contrast at (E_1, E_2) energies for OOP and IP moments.

are expressed by:

$$XMLD_{LH-LV}(M_{\parallel 0^\circ}) = XAS(M_{\parallel 0^\circ}, E_{LH}) - XAS(M_{\parallel 0^\circ}, E_{LV}) \tag{5.10}$$

$$= \frac{I_0}{6} + \frac{5I_{45}}{6} \tag{5.11}$$

$$XMLD_{LH-LV}(M_{\parallel 90^\circ}) = XAS(M_{\parallel 90^\circ}, E_{LH}) - XAS(M_{\parallel 90^\circ}, E_{LV}) \tag{5.12}$$

$$= \frac{-I_0}{6} + \frac{I_{45}}{6} \tag{5.13}$$

This simplified analysis indicates the XMLD signal follows the same rules of the analysis in the geometry of $M_\parallel$ and E_{LH}, as discussed in the previous section from Equation 5.3. The plots of the above equations can be found in Figure 5.3 (b) with red (for $M_{\parallel 0^\circ}$) and brown (for $M_{\parallel 90^\circ}$) curves.

Analogous to the method for probing (E_{LH}, $M_\parallel$), by selecting the first two opposite peaks of the XMLD curve at E_1 and E_2 energies, the sign of the XMLD difference (δ^{2E}_{LH-LV}) can reflect the spin moment orientation for the case of low

temperature OOP phase where $M_{\parallel}$ is distributing at the domain boundaries or small domains, meanwhile, the $M_{\perp}$ exists in most of the OOP domains.

$$\delta^{2E}_{LH-LV}(M_{\perp}) = I^{E_1}_{XMLD}(M_{\perp}) - I^{E_2}_{XMLD}(M_{\perp}) \tag{5.14}$$

$$\delta^{2E}_{LH-LV}(M_{\parallel}) = I^{E_1}_{XMLD}(M_{\parallel}) - I^{E_2}_{XMLD}(M_{\parallel}) \tag{5.15}$$

From the curves of Figure 5.3 (b), the OOP moments exhibit negative results for $\delta^{2E}_{LH-LV}(M_{\perp})$, while the $\delta^{2E}_{LH-LV}(M_{\parallel})$ at two orthogonal IP basis show positive, consistent with the previous analysis for $(M_{\parallel}, E_{LH})$ case. Thus the OOP and IP moments can be distinguished following the XMLD results from energy difference, by reasonably choosing the (LH, LV) modes at the appropriate two energies.

5.2.3 Images constructed by anisotropic XMLD effect

We utilise the secondary electrons emitted from the inner shell by X-ray absorption to produce the images with magnetic information. A large-scale CCD array equipped with a photoemission electron microscope (PEEM) enables us to image the sample surface by a range of 10μm $\times$ 10μm with resolution of approximate 50 nm. The X-ray light is accessible in beamline I06, Diamond Light Source, which can be tuned by energy range from 80 eV to 2100 eV with polarisation modulation ability by APPLE II undulators. The sample surface is required to be electrically grounded within the ultra-high vacuum chamber to replenish the photoemitted electrons. The experimental geometry is designed with 16° of grazing incidence for X-ray beam while the sample is mounted with [111] as surface normal (which is $c \parallel$ [001] axis in crystalline coordinate), which does not affect the results with LH polarisation. However, the grazing projection of LV polarisation can affect the results for IP moment since a slight signal contrast is found at different azimuthal angles by sample rotation. Nevertheless, the IP/OOP moments can still be unambiguously identified for LV polarisation light and, the grazing projection influence is negligible in this circumstance.

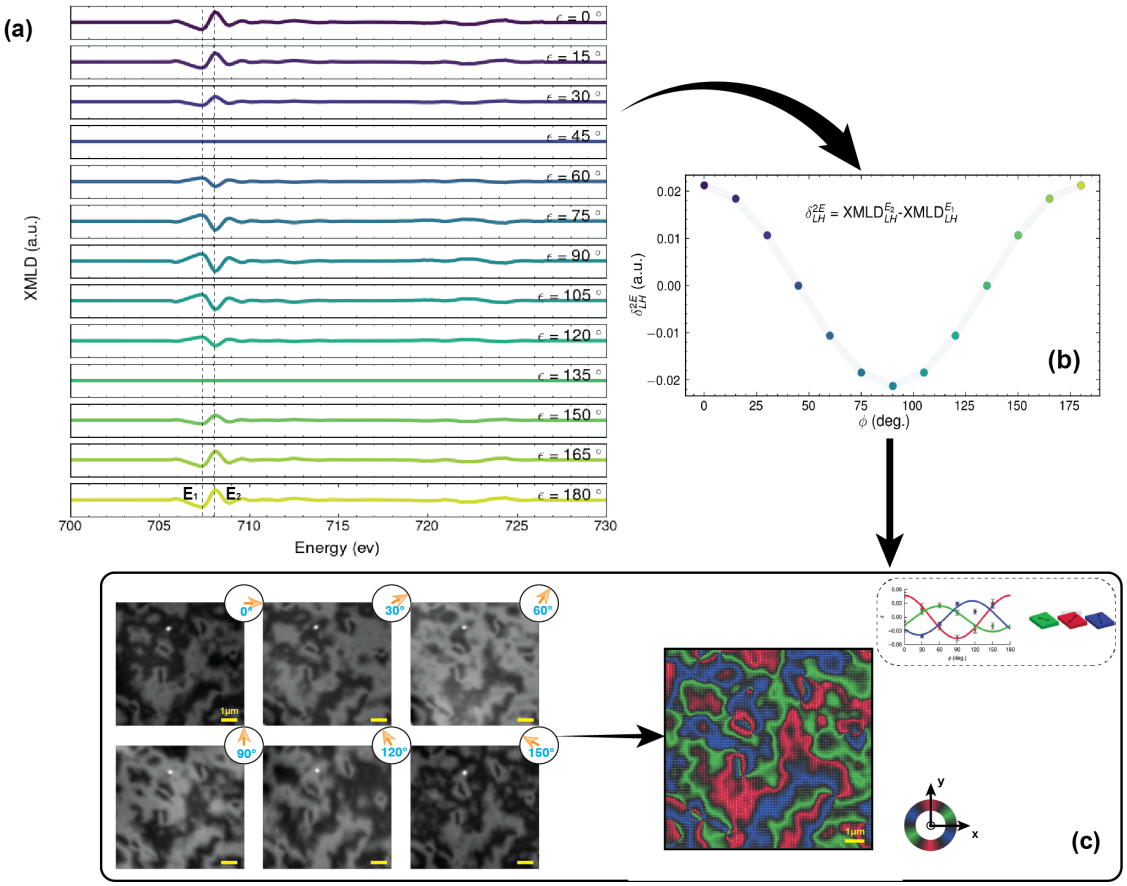


Figure 5.4: Construction of IP domain vector image. (a) The XMLD spectra change with relative angular rotation between LH polarisation and IP spin moment. (b) The signal of difference taking at E_1 and E_2 energies with respect to the relative angle ϕ, defined by (ϵ, μ). (c) Indicated by the sinusoidal dependence of XMLD with relative angle ϕ, the IP moments with three different initial angles give rise to three types of sinusoidal curves with different initial phases, which can be replicated by PEEM data taken at six sampling points between [0°,180°]. The information of phase reflects the relative orientation of IP moment, which can generally be classified by three sections labelled with (R, G, B) colours. The total (R, G, B) domains (labelled by the end of the arrow) are thus constructed on a pixel-by-pixel basis, from the phases revolved by six images measured at different rotation angles, as shown by the raw images in black and white.

IP domain vector image

Recalling the XMLD effects for IP moment distribution in Equation 5.5, the relative angle between LH polarisation ϵ and spin moment direction μ is the key to enhancing the contrast signal obtained by Equation 5.6. The XMLD from Equation 5.5 at different angles are plotted in Figure 5.4 (a), obtained by fixing μ to be zero while rotating the LH polarisation angles from [0°, 180°]. For simplicity, we reduce the (ϵ, μ) set into a single ϕ angle, representing the relative angle between LH polarisation and IP moment direction within the (111) plane. The signal of contrast from XMLD at(E_1, E_2) energies with respect to ϕ is plotted in (b), demonstrating a sinusoidal pattern with maximum value at 0° and minimum at 90°, following the conclusions of Equation 5.5 for $E_{LH} \parallel M_{\parallel}$ and $E_{LH} \perp M_{\parallel}$ scenarios. We perform the IP moment detection by fixing the X-ray polarisation with horizontal LH, while the relative angle ϕ is realised by rotating the sample along the c axis. The image at a particular angle is generated by subtrating raw PEEM images measured at two energies, as shown in Figure 5.4 (c). The contrast of black and white for the same position will change along with ϕ angle when rotating the sample. In this experimental geometry, the contrast of the PEEM signal (I_{LH}^{2E}) as the result of the in-plane anisotropy of the XMLD can be expressed by:

$$I_{LH}^{2E}(\phi) = I_c + I_M(cos2\phi) = I_c + I_M(2\cos^2\phi - 1) \tag{5.16}$$

where I_c is the constant term associated with absorption edge and is irrelevant to XMLD, while the $I_M \propto \langle \vec{M}^2 \rangle$ is the magnetic coefficient scaling with spin moment size. Due to the intrinsic antiferromagnetic XAS spectra, the XMLD for antiferromagnetic moments is incapable of resolving directions, only sensitive to moment modulus.

This empirical formula 5.16 implies that the information of IP moment orientation is associated with the phase from $I_{LH}^{2E}(\phi)$ function. Hints are also provided in Figure 5.4 (b) from the sinusoidal dependence of the XMLD signal of contrast. The profiles of angular dependence for IP spins with different orientations are shown in the inset plot (c) by RGB curves, varying by the initial phases. Six

angles are taken to estimate the phase of the sinusoidal curve gapped by 30°, as shown in the array of raw images in (c). Each contrast image is constructed by performing two PEEM images at (E_1, E_2) energies while the E_{LH} X-ray is fixed with the same grazing incidence. The information on Néel moment orientation is constructed on a pixel-by-pixel basis, following the principle of phase fitting. Three colours are assigned to plot the calculated phase across the field of view, corresponding to three types of IP domains due to weak anisotropy. The color wheel is set with (R$\|$ $[210]_h$, B$\|$ $[120]_h$, G$\|$ $[\bar{2}10]_h$)[1] colours in clock-wise gapped with 120° while a conjugated version of (R*, B*, G*) represent the 0° and 180° directions are indistinguishable from XMLD. Therefore, a colour wheel with (R, B, G, R*, B*, G*) colours shaded with black representing the intermediate angles is established for the IP vector maps, as shown in Figure 5.4.

Three types of IP domains are irregular and exhibits the feature of stripes, forming exceptional points where three domains emerge. These extraordinary characteristics will be discussed in further from the perspective of topological magnetic textures in an antiferromagnetic system.

OOP domain image

In contrast to IP domains, there is no signal contrast for the single OOP domain since the direction of OOP moments can not be resolved due to the limit of the imaging technique, but that does not mean we cannot distinguish the OOP domains. In previous sections, we introduced the origin of XMLD signal from IP and OOP moments using LH or LV polarised X-ray from theoretical analysis. Furthermore, we demonstrate the possibility of generating IP domains by XMLD-PEEM via sample rotation. We took a similar strategy to obtain the raw images for OOP domains by subtracting two images taken at (E_1, E_2) while keeping the incident beam with fixed polarisation. For LV polarisation, as shown in the diagram on the top left, the E_{LV} is parallel to the OOP moment. The OOP component exhibits both island-like and block-wise domains in dark contrast, while the domain walls

[1] here the footnote h represent the hexagonal basis

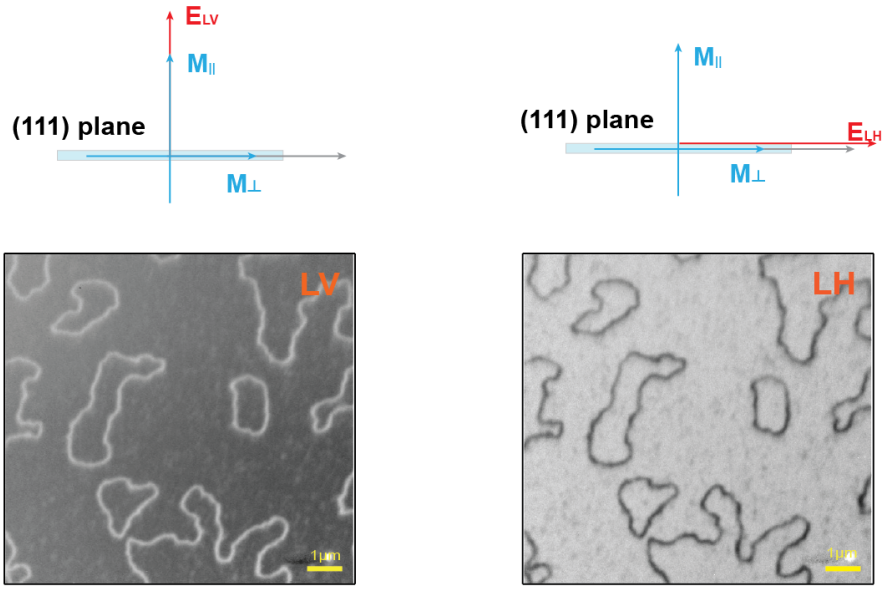


Figure 5.5: The OOP domains and domain walls at low temperature below Morin transition, by E_{LV} polarised (left) and E_{LH} polarised (right) light.

composed predominantly of IP moments are highlighted by bright contrast. The difference between OOP and IP moment by 2E modes can clearly be distinguished without additional raw images from different polarisation states of X-rays. In other words, the $(2E, 2P)$ method introduced in Section 5.2.2 can be replaced by only applying 2E, which proved to resolve the OOP/IP difference without ambiguity.

The same domain/domain wall structures can be obtained by adopting LH polarisation, as shown in Figure 5.5, where the E_{LH} polarised beam completely reverses the signal. This makes sense because the dark contrast corresponds to $E \parallel M$ sites while bright contrast occurs at $E \perp M$ positions, consistent with the results by E_{LV} polarisation. The sign reversal of image signal for the same moment direction by E_{LV} or E_{LH} is not surprising since the discussion on XMLD effects in previous sections tends to support the conclusion that $E \parallel M$ and $E \perp M$ geometries can always generate the maximum and minimum intensity of XMLD effect.

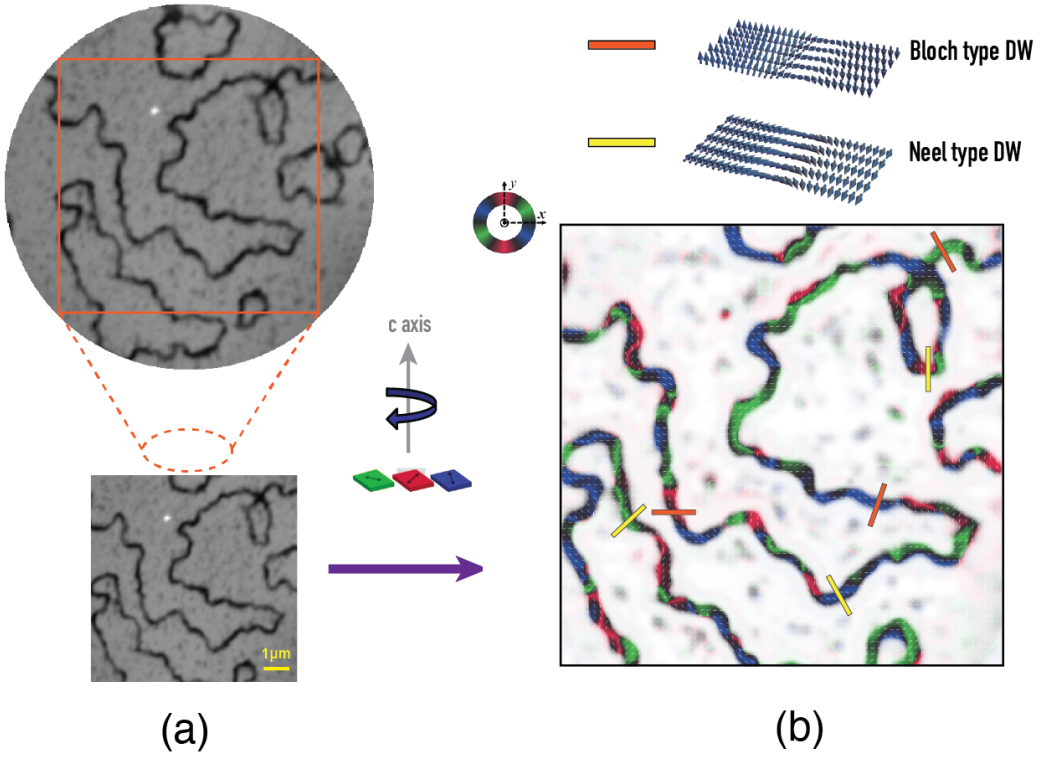


Figure 5.6: Illustration of anti-phase domain wall (ADW) at 194 K for α-Fe_2O_3. (a). Raw image at a specific angle by LH-PEEM in 2E modes. The region within the orange frame is the overlapped area between the rotated images. (b). Vector map of the IP component within the ADW, following the same strategy of IP domain image. The OOP domains are covered with a white mask for clarity. The bars on the top demonstrate two types of DWs, estimated from the colour wheel indication on IP moments.

5.3 Results and discussion

5.3.1 Domain wall analysis

Previous images at OOP phase in Figure 5.5 taken by both E_{LV} and E_{LH} polarisation X-ray exhibits clear domain boundaries, with opposite sign of intensity from 2E mode PEEM. Inspired by constructing a vector map on IP domains through six image compositions, we applied the same strategy on the IP domain wall components at the OOP domain by rotating the sample when performing the PEEM measurement. The merit of performing such measures is that the IP domain wall acts as a bridge to connect the OOP domains with anti-phase; in other words, two OOP domains (although indistinguishable from X-PEEM) have characteristic initial directions and change homogeneously to the opposite when crossing the IP domain wall.

The sample was cooled at 194K, and the incident beam polarisation was tuned to be horizontal. One of the raw images through LH-PEEM is presented in Figure 5.6 (a). The bright colour represents the OOP domains, and the dark boundary between the domains are twisted domain walls connecting the anti-phase AFM domains, as shown by the colourful representations on domain walls. The overlapped region within the orange frame is taken from a series of rotated images; each inherits a circular field of view from the PEEM detector. The RGB colour wheel logic is consistent with the one for IP domains, indicating the three-fold Néel vector within the plane. Some nuclei textures with the shape of islands containing IP information are observed within the OOP domains, which are processed with white mist for clarity, as shown in subplot (b).

When examining the Néel vector rotations from anti-phase domains, roughly two types of domain walls can be identified across the extended swirling boundaries, as shown by orange and yellow bars. The orange bar labels Bloch type DW, and the yellow bar marks Néel type DW, demonstrated by the cartoon on the top. The difference between the Bloch type and Néel type resides in whether the spin (here is Néel vector $\boldsymbol{L}$) rotation axis is parallel (Bloch type) or normal (Néel type) to the propagation direction. Both domain walls are found with equal probability within the sample range. However, due to the DW twisting and the confinement of the microscope resolution, some part of the DW connecting the anti-phase OOP domains is twisted by a random phase, which can be regarded as decomposing into Bloch and Néel type DWs.

5.3.2 Intermediate state at Morin transition

During the experiment, we find that the OOP domains shrink smaller while IP domain walls expand when warming across the Morin transition. When the temperature approaches the Morin transition, the IP part of the ADW gradually grows, and the small nucleations that emerge inside the OOP domain start to diffuse across the sample, leading to the expansion of the IP part and shrinking of the OOP part. As indicated in Figure 5.7 (a), the raw image is taken at zero

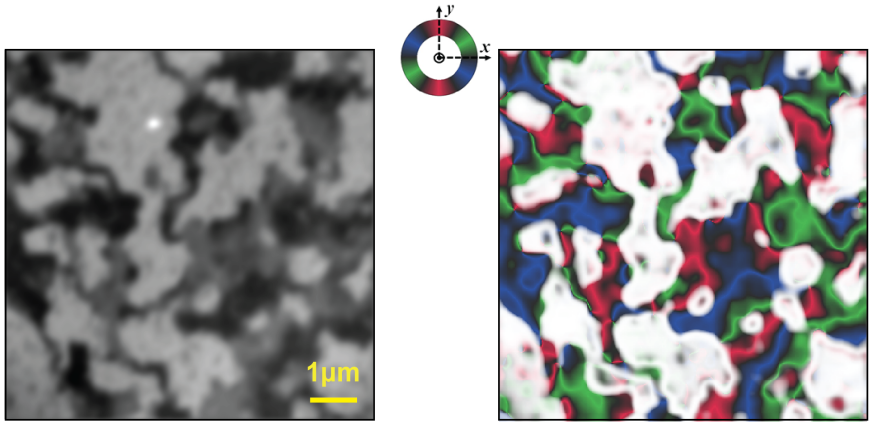


Figure 5.7: Illustration of IP and OOP coexisted domain at Morin temperature. (a) Raw data from LH-PEEM with grazing incident at 0 °. (b) Vector maps of the IP domains are constructed following the procedures of six rotational images. The OOP domains are vaguely processed in order to highlight the IP nucleation islands.

rotation angle at a slightly higher temperature at T_M = 240 K. The expanded domain walls and IP islands merge at some point, exhibiting bright, dark and grey colours. Probed at a grazing angle and fixed the sample at 0°, the IP domains are highlighted by dark or grey regions while OOP is indicated by bright colour. Thus, we construct the vector map similarly by rotating the sample continuously at six angles and derive the map, as shown in Figure 5.7 (b).

The OOP domains are filled by white mist for clarity, as shown in Figure 5.7 (b). The grey and black IP domains are constructed by the vector map method in the (R,B,G,R*,B*,G*) colour wheel. As the IP domain grows, some vortex-like defects are identified along the IP and OOP domain boundaries, some located within the domain wall analogous to the ADWs in Figure 5.6 (b). This phenomenon of the vortices proliferation recalls the formation of topological defects such as vortices through the Kibble mechanism when going through a phase transition.

5.3.3 AFM topological structures

Now we come to the IP domain with a vector map constructed for scoping all IP moments across the sample, expecting to look in detail at the antiferromagnetic textures at the edges of domains. When the sample is warmed to room temperature,

the growth of IP components prevails over the OOP components, which are finally shrunk into small textures, forming pinch points between three types of IP domains as singularities. This is extremely interesting since we find that these defects emerge in pair-wise combination (statistically from a picture on a larger scale which is not shown here), as shown in Figure 5.8 by white and black symbols. These pairwise dots survive after several temperature cyclings with robustness, exhibiting specific protection from fully unwinding from OOP to IP.

At pinch points, the domains merge to form two six-fold pinwheels: R-G*-B-R*-G-B* and R-B*-G-R*-B-G*, where the asterisk corresponds to the time reversal of $\boldsymbol{L}$ indicated by the color wheel. The side subplots show the zoom-out plots in Figure 5.8. The white lines on top of the coloured domain map indicate the Néel vector surrounding the pinch point, which assists to clarify the winding types.

We now examine the details of the structures formed around the pinch points in Figure 5.8. The first and third types of AFM textures (label one and label three) are twisting in anti-vortex and vortex patterns, judging only from the IP Néel vectors. While the textures in label one and label two form a pair of anti-vortex/vortex, extracting from the same half-moon structure position from the sample. The vortex structure in label two exhibits a different winding in contrast to label three. Recalling the description of magnetic skyrmions in chapter 1, we define the order parameter in Néel vector $\boldsymbol{L}$ for the antiferromagnetic counterpart, replacing the magnetisation $\boldsymbol{M}$, when describing the topological charge:

$$Q = \frac{1}{4\pi} \int \boldsymbol{L}(\boldsymbol{r}) \cdot \left(\frac{\partial \boldsymbol{L}(\boldsymbol{r})}{\partial x} \times \frac{\partial \boldsymbol{L}(\boldsymbol{r})}{\partial y} \right) d^2\boldsymbol{r} \tag{5.17}$$

In the case of hematite, the Néel vector can approximately be defined by the ferromagnetic sublattices in the adjacent two layers, as indicated by the cartoon besides the structures. The calculation of the topological charge Q from Equation 5.17 can be found in Appendix II, where a discretisation method on continuous spin space is introduced.

If focusing on a single half-moon structure, the vortex and anti-vortex pair can always be found at two ends of the half-moon, which correspond to the winding

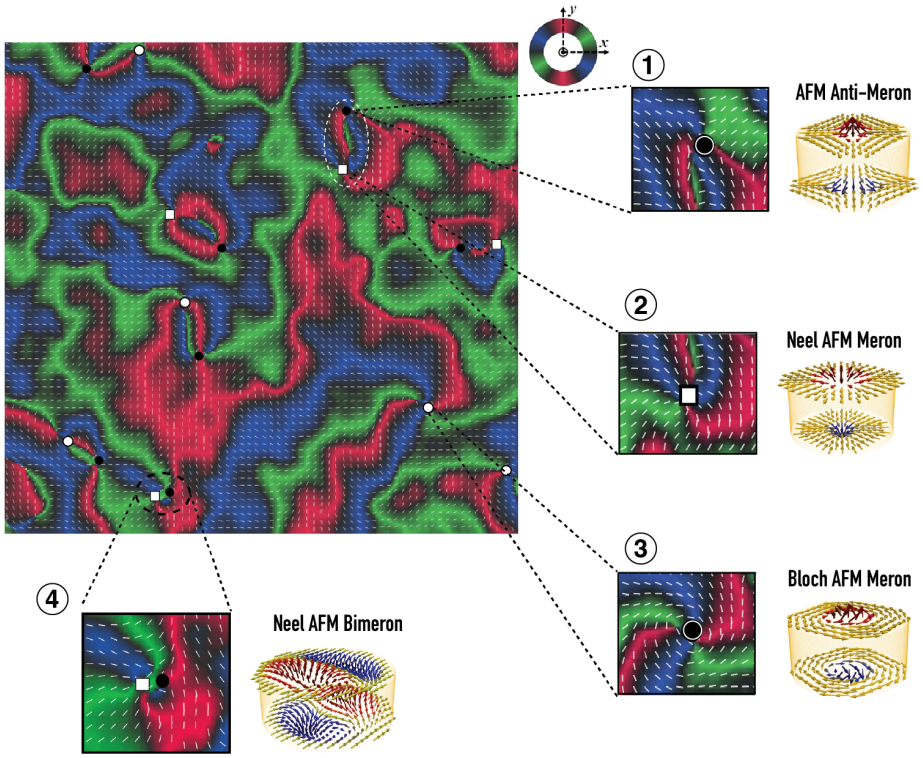


Figure 5.8: Topological properties of the IP AFM textures at T>T$_M$. The pinch points connecting the stripe IP domains demonstrate abundant topological features, most of them pair in a half-moon structure indicated by a white dashed circle. White and black dots represent merons and anti-meron structures, with vortex and anti-vortex IP moments. The labels from one to four are four possible topological structures estimated from the Néel vector geometries around the pinch points, attached with a cartoon showing the three-dimensional spin orientation in the lattice.

number of $\omega = +1$ (for vortex) and $\omega =$ -1 (for anti-vortex). In addition to the IP information, the OOP cores assist in depicting the complete profile of these half-moon structures. The three-dimensional topological charge Q for the entire half-moon structure is found to be either an integer number or zero. The structure is topologically equivalent to the magnetic skyrmion structure for the integer case. This makes sense because the magnetic skyrmions and half-moon structures with opposite OOP cores can be mutually transformed by each other by rotating the overall spins of antiferromagnetic skyrmions homogeneously by 90° along one of the axes within the plane. Assuming the total $Q = 1$, when the vortex and anti-vortex are close enough, with a meron and an opposite polarised anti-meron pairing, the entire structure can be regarded as *bimeron*, in which case, each half is assigned

with a fictionalised topological charge $Q = \frac{1}{2}$.

The topological properties of these meron structures are intriguing. Taking the example of merons from label two and label three, both are merons with OOP centre and IP exteriors, however, exhibit different helicity features. If a series of lines cut through the meron centres, a Néel-type domain wall from label two meron is found, while the label three meron exhibit a Bloch-type domain wall. Therefore, Néel-type and Bloch-type meron are assigned to these two types of merons. These features may indicate the merons' formation history when the sample experiences the Morin phase transition. In the bimeron structure, we still need more information since the spin direction is hardly to be determined from the current experimental technique. As shown in label four, the total winding is 0 due to the coexistence of vortex and anti-vortex. However, the middle information between cores is hard to identify due to the limit of instrument resolution. Therefore, an imaginary Néel-type AFM bimeron cartoon is presented based on the behaviours of the exterior spins. The topological characters of the bimeron structure revealed from the vector map are still insufficient due to the lack of Néel vector orientation, more variants are waiting to be discovered.

6

Spin wave dynamics in AFM topological structures

Contents

6.1 The hematite model for micromagnetics 120
6.2 Spin dynamics in bimeron annihilation 130
6.2.1 Trivial bimeron annihilation 130
6.2.2 Non-trivial bimeron annihilation 131
6.3 Analysis of annihilation 135
6.3.1 Spin wave spectrum 135
6.3.2 Dispersion model 139
6.3.3 Topological charge transition 143
6.4 Conclusion 145

The research of spin texture engineering in magnetic systems has portrayed a great picture with a family of topologically interesting spin structures, the representatives of which are skyrmions, merons (or half-skyrmions), bimerons and their anti-particles with opposite topological charge [121, 135–137]. The topological protection due to integral topological number leads to many intriguing phenomena, such as the quantum hall effect [138] and spin-momentum lockings in topological insulators [139–142]. Together with the ultra-small size and high mobility, these properties make the spin texture outstanding topology candidates for designing high-density and low-energy consumption memory devices [50].

After discovering the topological structures by X-PEEM demonstration, as reported in the previous chapters, the feasibility of designing the antiferromagnetic topological structures in a time-honoured hematite system through advanced PLD growth technique has been proved. However, due to the limitations of the instrumental techniques, it is impossible to resolve the Néel vector direction, as well as not fast enough to capture the annihilations of the meron structures (which is still a big challenge in AFM imaging). In this chapter, these antiferromagnetic topological structures are simulated by a new micromagnetic tool called VAMPIRE, which can reproduce the collective spin dynamics with atomic resolution. These non-equilibrium structures originated by single-ion anisotropy change are found to be unstable and annihilated in all cases, which is in contrast to our experimental results. The annihilations are accompanied by many exotic phenomena, such as the generation of spin waves in a surprisingly broadband THz range, fast propagation velocity of the acoustic magnons and a quick topological charge transition.

6.1 The hematite model for micromagnetics

α-Fe_2O_3 is one of the iron oxides with a high spin state that existed in nature. Hematite crystallises in trigonal corundum structure with space group $R\bar{3}c$. The spins from each of the two Fe^{3+} sublattices are antiparallelly aligned and alternately stacked along the c axis, making α-Fe_2O_3 a 'classic' antiferromagnetic (AFM) system. We will construct an atomistic model of the antiferromagnetic system for micromagnetic simulations and test the model's validity by LLG-Heun simulations of the Néel phase transition from a paramagnetic state to an antiferromagnetic state.

Exchange matrix definition

As introduced in chapter 2 on the workflow of VAMPIRE software, the total Hamiltonian requires the exchange and anisotropy terms to be defined on the unit cell basis, which means the site symmetries of magnetic ions need to be considered. Four types of super-exchange interactions via Fe^{3+}–O^{2-}–Fe^{3+} linkage can be defined for the hematite corundum structure, as shown in Figure 6.1. The

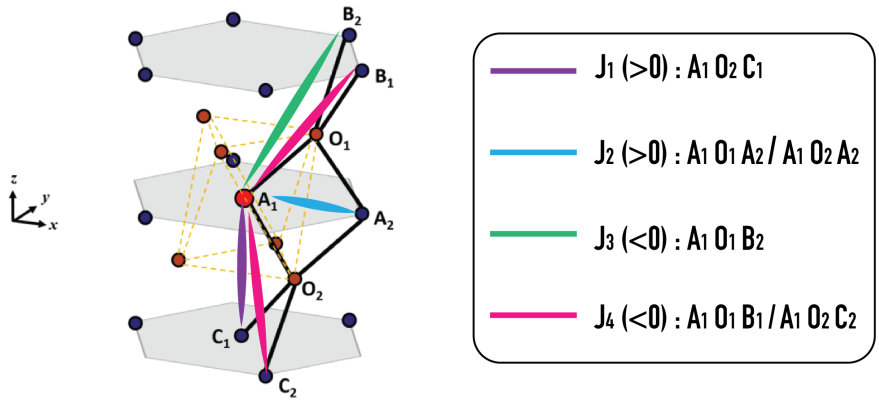


Figure 6.1: Superexchange bondings in corundum structure α-Fe_2O_3. Fill circles are Fe^{3+} ions in Wycoff position 12*c*. As indicated by the black line path, superexchange bondings are formed by two Fe cations through an intermediate oxygen anion. Four types of superexchange interactions are labelled in different colours. Purple and light blue bondings are ferromagnetically aligned, while the green and pink colour bondings are antiferromagnetic aligned.

antiferromagnetism mainly arises from negative J_3 and J_4 interactions representing AFM between out-of-plane (OOP) Fe^{3+} cations. Although both J_1 and J_2 are weak ferromagnetic interactions with a positive sign, the in-plane ferromagnetism is dominated by J_2 via 3 equivalent A_1–O_1–A_2 and A_1–O_2–A_2 paths, while the J_1 representing OOP interactions are much weaker[143] and not included in our model.

The metal ions Fe^{3+} in Wycoff position 12*c* of the corundum structure can be enumerated as 1, 2, 3, 4 along the rhombohedral [1,1,1] axis. The atomic sites are given by coordinates $\mathbf{r_1} = (\frac{1}{2} - v, \frac{1}{2} - v, \frac{1}{2} - v)$, $\mathbf{r_2} = (v, v, v)$, $\mathbf{r_3} = (1 - v, 1 - v, 1 - v)$, $\mathbf{r_4} = (\frac{1}{2} + v, \frac{1}{2} + v, \frac{1}{2} + v)$, where $v = 0.355$ for α-Fe_2O_3. The spin structure is denoted as 1^+, 2^-, 3^-, 4^+, where the $\pm$ refers to the parallel and antiparallel directions along the easy axis. The super-exchange interactions conveyed by M–O–M bonds are depicted in Figure 6.1 and re-defined by a set of parameters normalised to antiferromagnetic exchange J_4, as shown in Table 6.1.

Since VAMPIRE defines the exchange energy terms and the magnetic structure in separated files, the magnetic ions are categorised by spin polarisation. These two types of Fe^{3+} are defined with position information listed in the structure file with the suffix *.ucf*. In the UCF files, the relative positions of a total of 24 Fe atoms (single unit cell has 12 Fe atoms) are considered by doubling the unit cell (which

Table 6.1: Parametrising exchange interactions by nearest neighbouring ion pairs for corundum structure α-Fe_2O_3.

Iron pair	M-O-M angle(°)	Interaction constant	Normalised parameters
$1^+ - 2^-$ $3^- - 4^+$	87.4	J_1	r
$1^+ - 2^-$ $3^- - 4^+$	94.1	J_2	s
$1^+ - 2^-$ $3^- - 4^+$	118.2	J_3	p
$1^+ - 2^-$ $3^- - 4^+$	132.1	J_4	1

is required by the orthogonal coordination from the VAMPIRE code), and the exchange energy J_i between different types of atoms are also specified in the UCF file, representing the anisotropic exchange bondings of Fe atoms. However, all the relative J_i values given in the UCF file are normalised to J_4, as shown in Table 6.1, giving rise to the r, s, p relative coefficients. From previous works by E. Samuelsen [143], we know the relationship between AFM and FM energies as $s = 0.276r$, $p = 1.28$, and from experimental reports we deduce the $p = -4.39 \times 10^{-21} J(/bond)$ and $r = 2.17 \times 10^{-22} J(/bond)$. These energy values are defined in another file specifying energy parameters in all types of atoms (from two sublattices) ending with the suffix *.mat* file. The MAT file also defines the atomic spin moment size, damping constant, uniaxial anisotropy and initial spin directions. The atomic spin moment is five μB for the Fe^{3+} valence state. It keeps the value in all simulations introduced in this chapter. The initial state is defined in MAT file, which can be either random for describing paramagnetic state or along $[0, 0, 1]$ ($[1, 0, 0]$) for describing OOP (IP) antiferromagnetic state. In addition, the damping term is tuned to be much smaller than critical damping $\lambda = 1$ since magnetic transport experiment has revealed that rather weak damping is observed in hematite [144].

Néel temperature simulation

The spin dynamics require a high-efficient integration of the LLG equations with good precision. Considering the nature of stochastic LLG equations, the Heun

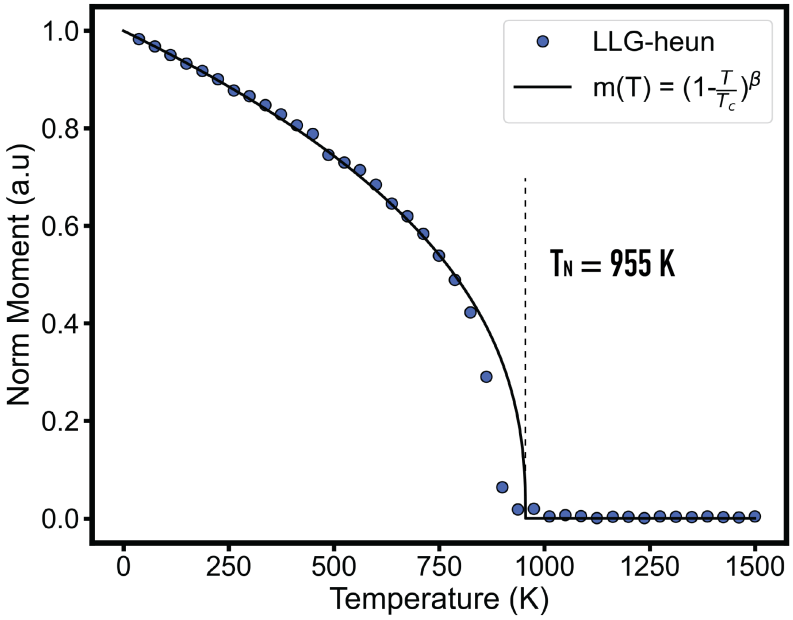


Figure 6.2: Néel order simulation by LLG-heun method (blue dots). The Curie-Weiss law fits the simulation data with $\beta = 0.4$ (black line). The Néel temperature is around 955 K, indicating the exchange parameters are set within the reasonable range.

method is adopted as the solver to the numerical integration considering the balance between the computational cost and precision. The Heun method takes the *predictor-corrector* strategy by calculating the new spin direction $\boldsymbol{S_i'}$ for a given effective field H_{eff}^i in a standard Euler integration step as: $\boldsymbol{S'}_i = \boldsymbol{S}_i + \Delta\boldsymbol{S}\Delta t$, where $\Delta\boldsymbol{S}$ are given by the stochastic LLG equation with effective field H_{eff}^i. During this *predictor* step the spin length will not be preserved and the new effective field must be re-evaluated. The second *corrector* step uses the predicted spin position and revised effective field to calculate the final spin position with a re-normalised spin vector length. The predictor step of the integration is performed on every spin in the system before proceeding to evaluate the corrector step for every spin. For micromagnetic simulations at zero temperature, the minimum time step is a well defined quantity since the largest field (usually the exchange term) essentially defines the precession frequency. However, for atomistic simulations using the stochastic LLG equation with Langevin dynamics, the effective field becomes temperature dependent. The consequence of this is that for atomistic models the most difficult region to integrate

is in the immediate vicinity of the Curie point. From the test examples provided by the manual, we are known that a reasonably large time step of 1 fs can describe the low-temperature case quite well. However, for temperatures close to the Curie point, the time step with 0.1 fs precision is required to find the ideal agreement.

In order to verify the exchange constants as well as the Heun integration validity, we take the simulation example of Néel temperature. We create the system size to be 50 nm × 50 nm × 14 nm multi-layer thin film. The initial spin state is set to be random for all ions. The temperature is set by starting from 1500 K and ending at 0 K in total 0.1 ns relaxation time with 0.1 fs time step. The spontaneous moment from single sublattice emerged from paramagnetic phase transition is an excellent variable for testing exchange parameters since the critical temperature T_c of a magnetic system is primarily determined by the strength of the exchange interaction between spins. In our model, antiferromagnetic ordering emerges at the Néel temperature due to the predominately antiferromagnetic exchange coupling. Figure 6.2 demonstrates the temperature dependence of normalised magnetic moment, indicating the spontaneous generation of moment from one Fe^{3+} sublattice. The Néel temperature appears near 960 K when cooling from high-T paramagnetic state, while the magnetisation emerged in the other sublattice is opposite and cancels the moment to be zero (not shown here). As indicated by the black curve in Figure 6.2, the fitting curve is used by the equations from Curie-Weiss law, where the critical exponent is found to be β= 0.4, showing the LLG-heun simulation with acceptable precision at the critical point of the Néel temperature.

Morin transition simulation

In the previous section, we investigated in detail the ADWs and topological structures generated by temperature cycling across the Morin transition, where the shift of the moment orientation between in-plane and out-of-plane in antiferromagnetic order occurs at the critical temperature near 260 K. The first-order phase transition of the spin orientation occurs in hematite due to the change of anisotropy between uniaxial and easy-plane, which corresponds to the sign change of the anisotropy

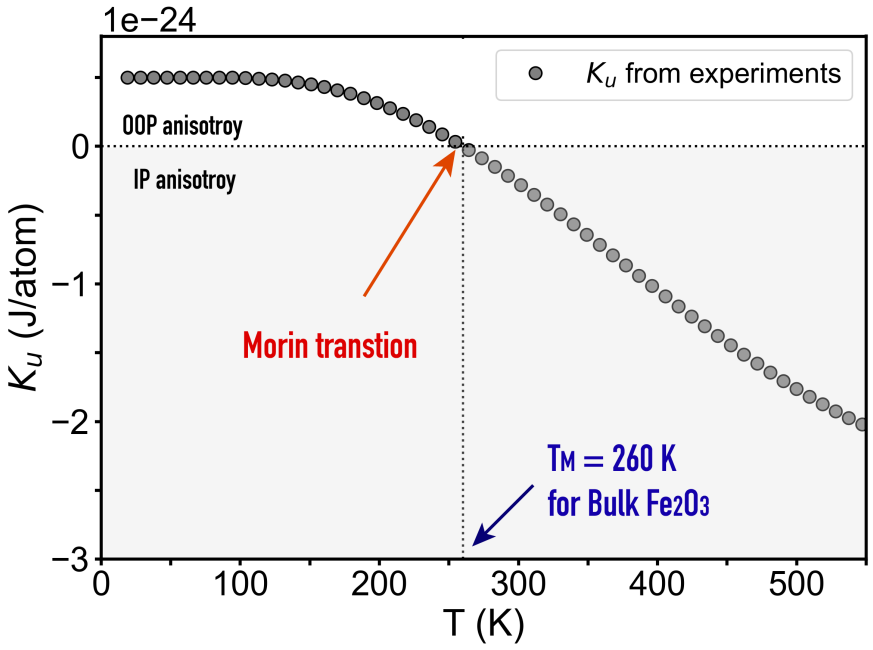


Figure 6.3: Anisotropy parameter change with temperature.

energy. Here, in Figure 6.3, we exhibit the reported anisotropy energy values from experiments in literature [127] (labelled by gray dots), the units of which are transformed into the unit sets in VAMPIRE. The zero point of the curve finds the Morin transition temperature. The OOP uniaxial anisotropy is set to be positive and saturates at $5 \times 10^{-25}(J/atom)$. At the same time, the IP anisotropy energy is negative and increases upon warming up.

The anisotropy energy we used in our simulations follows the curve in Figure 6.3. More specifically, the maximum values for the OOP and IP anisotropies describe the phases below and above the Morin transition[145]. More precisely, the LLG dynamics are based on an adiabatic approximation corresponding to the 0 K situations. However, the thermal effects on classical spin dynamics usually deal with Langevin dynamics. One of the prevailing methods is the Landau-Lifshitz Bloch equation, where the thermal bath described by Langevin fields is simplified by mean-field approximation proposed by D.Garanin in 1997 [146], provides a partial solution to the classical ferromagnetic dynamics in the thermal bath without considering the coupling between spin and lattice.

Here in our case, we try to avoid the complicated processings on the finite temperature stochastic LLG equation with Langevin dynamic terms. For the case of the Morin transition, the 'temperature effect' is represented by the thermal behaviour of the uniaxial anisotropy energy K_u. By setting up the system with an initial state of spin direction and a final state of anisotropy energy K_u, the zero temperature LLG-Heun method can achieve the same effect of Morin transition. This is an extraordinary case for Morin transition only since the thermal fluctuation on each spin is less important than the spin-floppings induced by the anisotropy change due to the fact that the K_u variable includes the 'thermal effect'. Therefore, it is reasonable to simplify that the LLG equation can still describe the antiferromagnetic spin dynamics in the adiabatic approximation.

Although the Dzyaloshinskii-Moriya (DM) interaction has been reported in hematite for a long time by Dzyaloshinskii and Moriya [45, 46] based on symmetry analysis, the experimental determination of the DM vector remains challenging until a recent group unravelled the origin of such weak DM interaction [147]. In the X-PEEM experiment of imaging AFM topological structures, we found the DM interaction is negligible since the Bloch or Néel type of domain walls were generated with equal probability. Therefore, we set the initial ground state to be collinearly antiferromagnetic by excluding the DM interaction. It should be noted that the magnetic dipole interaction in hematite is relatively weak because of its AFM nature and thus not included within the total Hamiltonian.

On this basis, the total Hamiltonian in equation 2.23 is reduced to considering only the exchange and anisotropy terms. At the same time, the warming (cooling) process is simulated by setting up the initial state and the anisotropy energy value. For Morin transition warming-up cycles, we adopt the strategy of defining the initial state as OOP (corresponding to a low temperature below Morin temperature) and the anisotropy energy as negative, representing the final state stabilising at the IP state. For the cooling cycle, we can simulate this process by defining the initial state as IP and the anisotropy as positive. As indicated by Figure 6.4, the evolution of spins by LLG dynamics describes the Morin phase transitions close

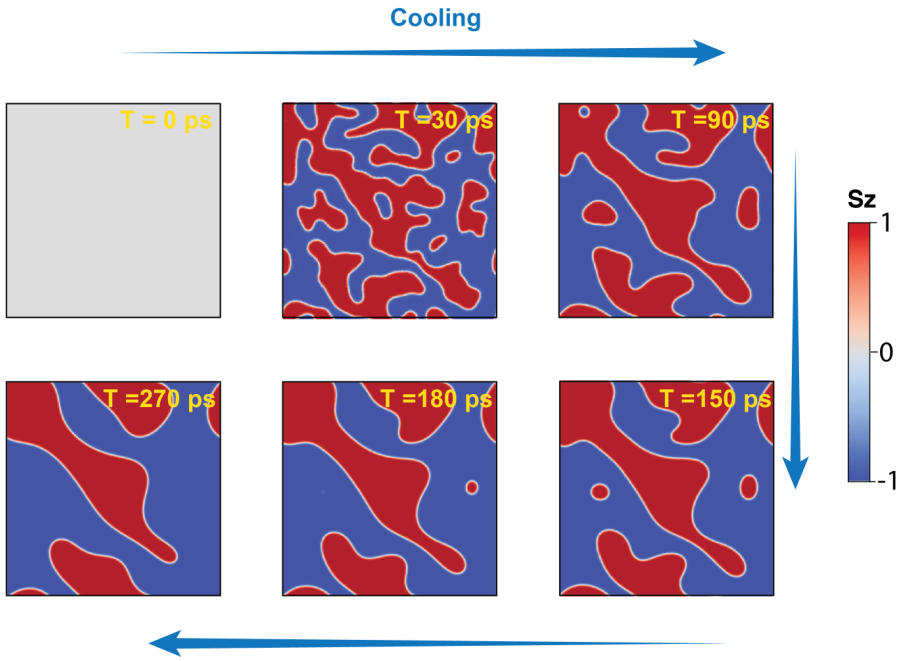


Figure 6.4: Simulation of Morin transition in the cooling process.The simulation scale is set by $300\mu m \times 300\mu m$ with periodic conditions in the XY plane, and $1\mu m$ thick without periodic confinments in the z-direction. The time resolution of the simulations is set to 0.1 fs. The initial state is set to be IP, while the final state arrives at OOP, consisting of domains with equal-sized opposite directions. Analogous to the experiment results, magnetic bubbles or small-size domains are also discovered in the middle process.

to the experimental results. In Figure 6.4, the z component of the spin, which is zero in the homogenous IP (the initial state) and finally reaches the OOP direction, constitutes two types of opposite domains separated by domain walls with almost equal sizes. Noticeably, the spin direction is plotted according to the 1^+ or 4^+ atom layer, as shown in Figure 6.6. The adjacent layer consisting of 2^- or 3^- atoms have identical domain structures with opposite spin directions. Distinct from experiments, where spin moment directions are degenerated due to the limitations of the X-PEEM technique, we can reveal the spin vectors directly in the simulation.

The cooling cycle simulation is plot in Figure 6.4. The second picture exhibits a large number of small-size multi-domains, reflecting the trend by the Kibble-Zurek mechanism that faster quenching results in denser domains and topological defects (here the defects refer to domain walls). When the domains start to form, the small domains in Figure 6.4 evolve and merge into larger domains, as shown in the following snapshots. In the middle of the relaxation, we find the generation

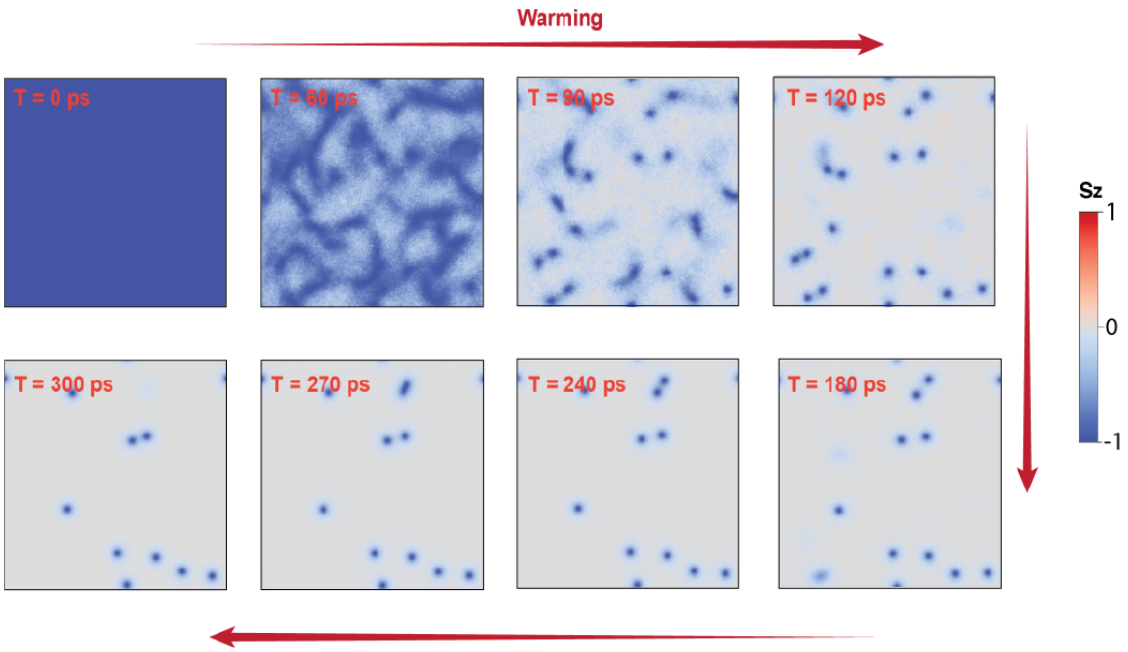


Figure 6.5: Simulation of Morin transition in warming process. The initial OOP domain is collapsed into IP, with many OOP circular structures forming in pairs. Some pairs are annihilated in hundreds of picoseconds, and the nuclearisation will be erased in enough relaxation time.

of small domain islands inside the opposite domain, which are unstable and very similar to the magnetic bubbles found in the experiments [144].

The warming-up cycle is simulated similarly but with a reversed initial state and sign of anisotropy energy. The initial state is set to be OOP while the anisotropy energy is negative 2×10^{-24}, representing transient heating from low temperature to 500 K across the Morin transition. The dynamical process is shown in Figure 6.5 for a total of 300 ps simulation time. We find that the homogenous OOP domain transforms to in-plane by firstly forming OOP 'chains' and then breaking into isolated circular structures. The circular dots are stabilised pairwisely within a short time gap, resembling the topological structure identified in the experiments. These structures are finally annihilated into homogenous IP domains given a long enough relaxation time, indicating that these isolated structures are not metastable states.

The spin vector configuration of the typical circular pairs is presented in Figure 6.6. Two arrays of atoms with opposite spin directions are shown in each layer, while the black arrows represent the IP spin moments, exhibiting a vortices-

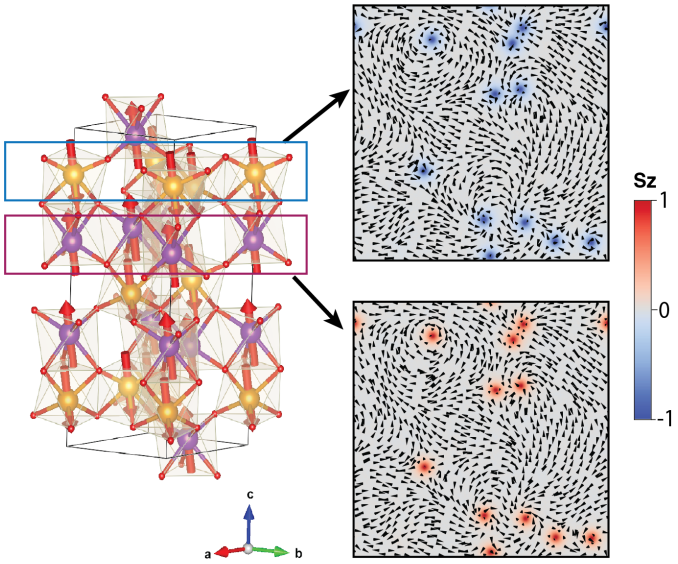


Figure 6.6: Illustration of the plotting layers of atoms within the crystalline structure. The top picture with negative OOP spin direction shows the atomic arrays at the 4^- position. The image demonstrates the number of atoms at the 3^+ site at the bottom, which exhibits the opposite direction of spin. Except for the OOP directions, the IP windings are also found reversed between the spin arrays from different layers.

like structure. The pairs of circular textures which are close enough feature the in-plane moments with 'vortex-antivortex'. The pair has a total winding number of 0, contributing by a +1 for vortex and -1 for anti-vortex. Meanwhile, some vortex structures demonstrate Bloch-type merons, which have a sizable area with OOP and clockwise (or anti-clockwise) IP components surrounding the core. Similarly, Néel-type merons can also be identified, in which the spins circulate cycloidal from the OOP core to IP exteriors. Since no DM interaction is included in the simulation, there is no sign of preference of Bloch or Néel type for these meron (anti-meron) structures. The global spin configuration within the lattice shows zero net moments, as the antiferromagnetic alignment requires. The net moment direction of these spin textures indicates a specific inheritance from the OOP direction in the single domain.

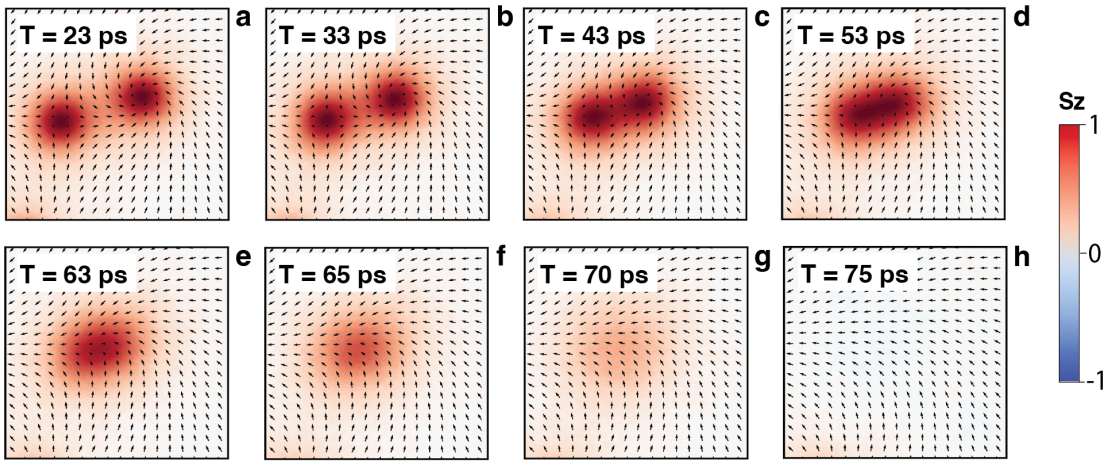


Figure 6.7: The dynamical process of $Q = 0$ bimeron structure annihilation. **a-h** describes the evolution of the meron/antimeron structures through attraction, merging and collapsing steps. The region's total topological charge is conserved during the whole evolution time.

6.2 Spin dynamics in bimeron annihilation

6.2.1 Trivial bimeron annihilation

The intermediate dynamics of the annihilation in Figure 6.5 is intriguing. The meron/anti-meron pairs resemble the structures we found in the experiment, but here we have the additional information on core moment directions. When the vortex and anti-vortex come close enough, they should form the so-called *bimeron* structure as we use this terminology for structures reported in experiments. However, the 'real' bimeron can be continuously transformed from skyrmion by adding a global phase, therefore, the topological charge number, according to the topology invariance, should remain the same (± 1). In contrast to the conventional bimeron definition, the compact meron/antimeron pairs we observed have zero topological charges, according to the method introduced in Appendix B. The meron can be regarded as half-skyrmion due to the $-\frac{1}{2}$ topological charge (obtained from Figure 6.7), while the anti-vortex part contributes $\frac{1}{2}$ topological charges due to the anti-winding with the same polarisation. Thus the total topological charge in this configuration is zero, corresponding to the $Q = 0$ bimeron.

Figure 6.7 reflects the evolution of the $Q = 0$ structure identified in Figure 6.5 from the 180 fs frame to the 270 fs frame. The core polarisation sign is reversed because we plot the next adjacent layer. The **a-b** finds that the meron/antimeron structures attract with each other while keeping the size and shape unperturbed. In **c-d**, the two objects merge into a single cluster with the same OOP component. Then the elliptical collection gradually fades, representing the OOP component continuously collapsing to IP, as shown in **e-h**. Surprisingly, the oval structure in **d** is unique since the IP arrows do not exhibit a complete vortex or anti-vortex pattern. Therefore no windings are found throughout the region of the texture. The total topological charge and winding number are kept at zero during the whole time of evolution.

6.2.2 Non-trivial bimeron annihilation

The simulation of the Morin transition demonstrates the annihilation of topological structure, which corresponds to similar results found in experiments, providing the missing information for understanding the dynamics of topological defects that experimental investigation can not answer. Inspired by the $Q = 0$ bimeron found in warming cycles in Figure 6.7, we investigate whether generating non-trivial topological structures from the simulation through Néel phase transition is possible. Based on the Morin transition simulation, the moment centre's polarisation direction can primarily affect the winding configurations. Although the final state remains IP due to the negative anisotropy energy term, we can generate different topological spin configurations with various spin orientation centres by controlling the starting configuration. For Néel transition simulations, we define the initial state as random, analogous to the paramagnetic state at a high temperature above the Néel transition. We also relax the system in sudden quenching to the IP plane state. The total simulation time is enough to arrive at the final state of being IP, and the other parameters in the equation are set to be the same as in the Morin transition.

Figure 6.8 shows the evolution from the paramagnetic state to the IP state, during which several intermediate structures emerge and dynamical activities occur.

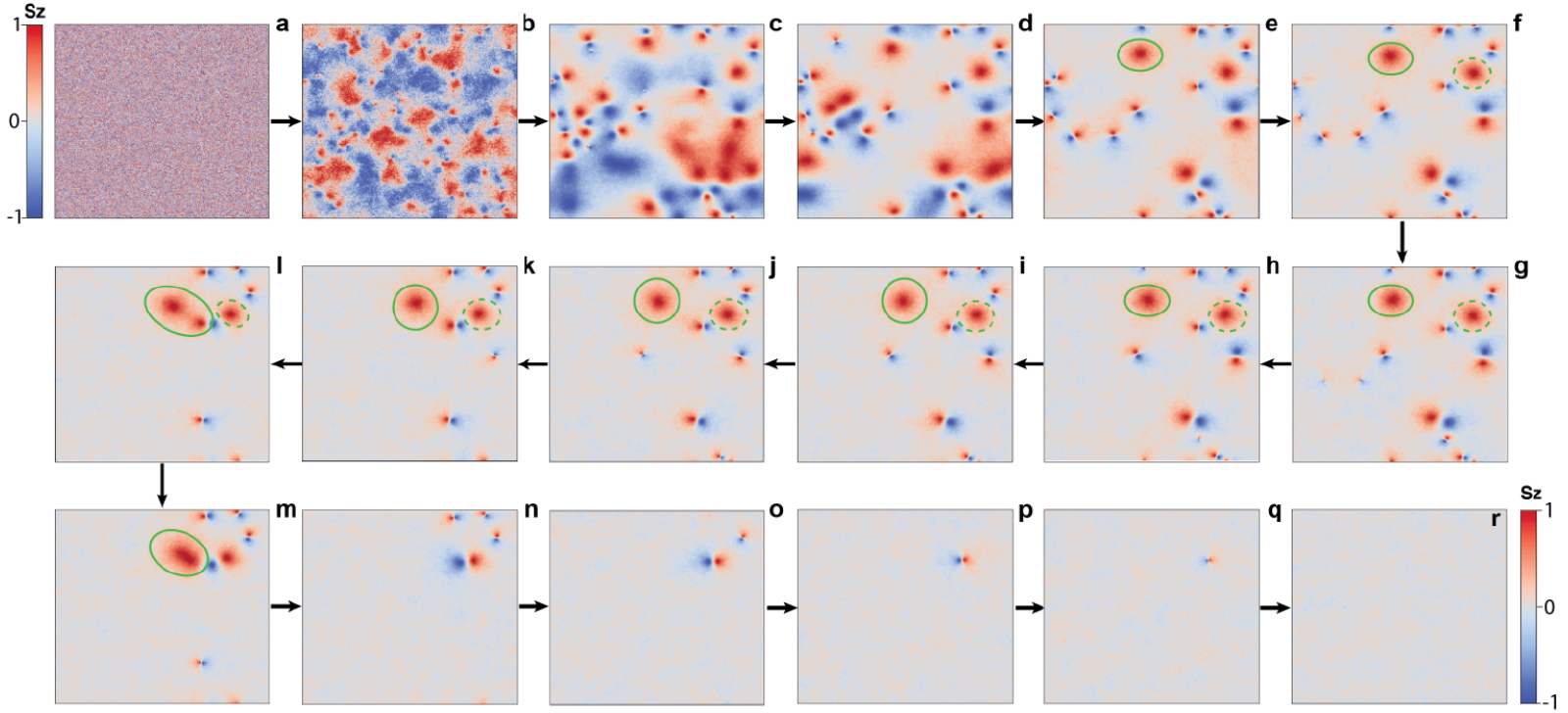


Figure 6.8: The modelling of Néel phase transition from paramagnetic phase to IP antiferromagnetic phase. The initial state is random, while the ultimate state is homogenous IP. Among the intermediate time shots, many structures emerge by pairs, characterising textures with OOP moment circulated by IP components. All these structure pairs annihilate at the end of the simulation.

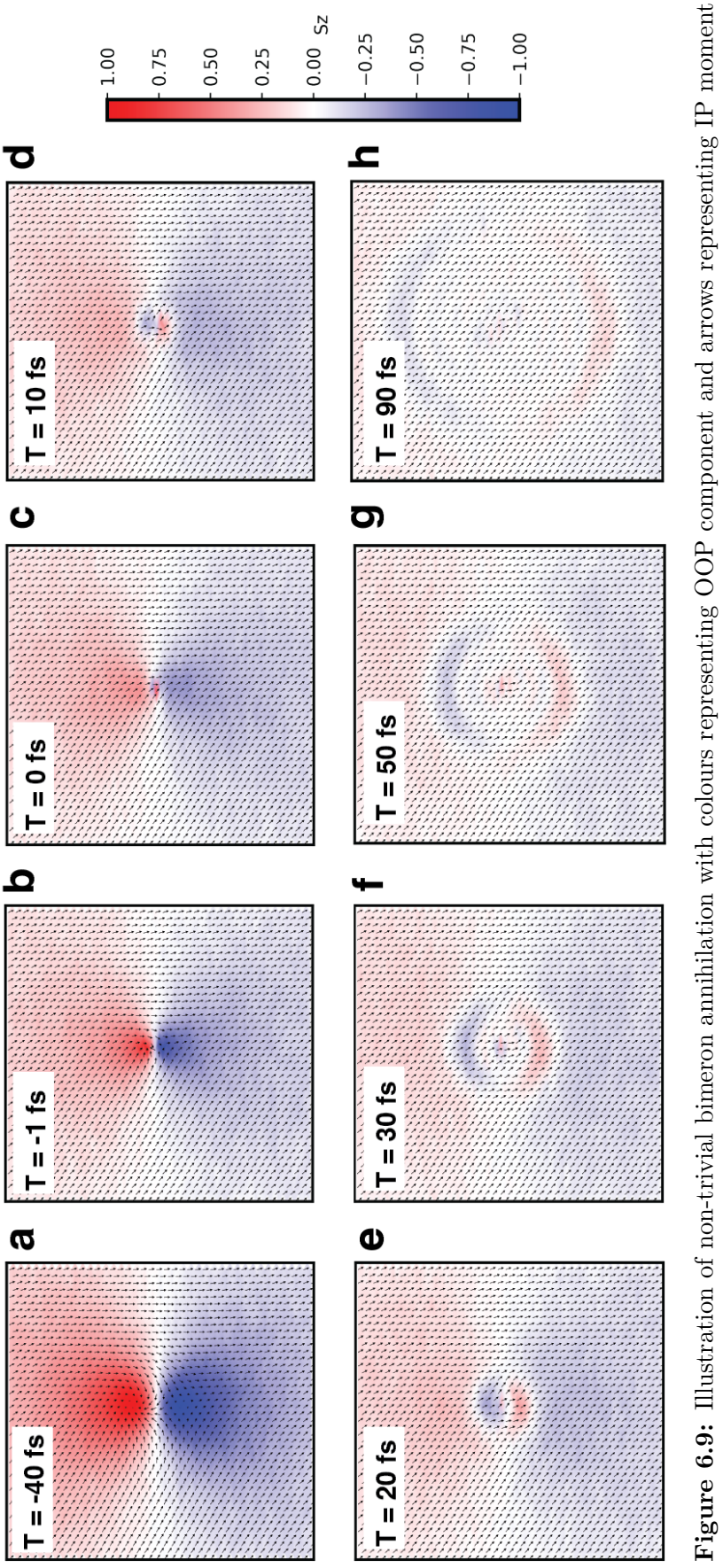


Figure 6.9: Illustration of non-trivial bimeron annihilation with colours representing OOP component and arrows representing IP moment direction. The annihilation can be described as shrinking, bursting and wave propagation stages.

The paramagnetic state is firstly reduced into domain structure soon after the simulation starts. Then the domains evolve further into pair-wise structures, as indicated in **c,d**. The pair-wise structures exhibit half blue and half red with different sizes, the IP 'vortex' part is similar to the bimerons in the previous section but with opposite OOP cores. Several such structures emerge and annihilate as the simulation continues; meanwhile, these bimeron structures are also identified and destroyed, as illustrated by Figure 6.7. They are labelled by solid and dashed green circles across the middle panels in Figure 6.8. Such $Q = 0$ bimeron dynamics have been illustrated previously; we focus on the annhilating the other type of structure with a 'red/blue' pairing.

In topological space, this structure is the non-trivial bimeron which exhibits non-zero topological charge and can be continuously transformed from skyrmion(regardless of Néel or Bloch type). The in-plane component of this structure is depicted in Figure 6.9 **a,b**. Within the confined view area, the core polarisation is opposite in two sections and mediated by IP spins, forming an IP domain wall line. If taking the two sections as a whole, we obtain the $Q = -1$ bimeron composed by $Q = -\frac{1}{2}$ meron and $Q = -\frac{1}{2}$ 'anti-meron'. Noticeably, the topological charge for this type 'anti-meron' is not the reversal of meron since the winding number and core polarisation here are reversed at the same time.

This non-trivial bimeron demonstrates a different evolution pattern than the trivial bimeron annihilation, as shown by Figure 6.9. The initial behaviour for non-trivial bimeron is shrinking instead of attraction; see panels **a-c**. Secondly, the OOP components are not vanishing but transmitting through each other and bursting into collective waves, as indicated by **c-d**. Meanwhile, the cores are observed oscillating in the z direction and swinging within the plane, which provides the source of spin wave outward propagation.

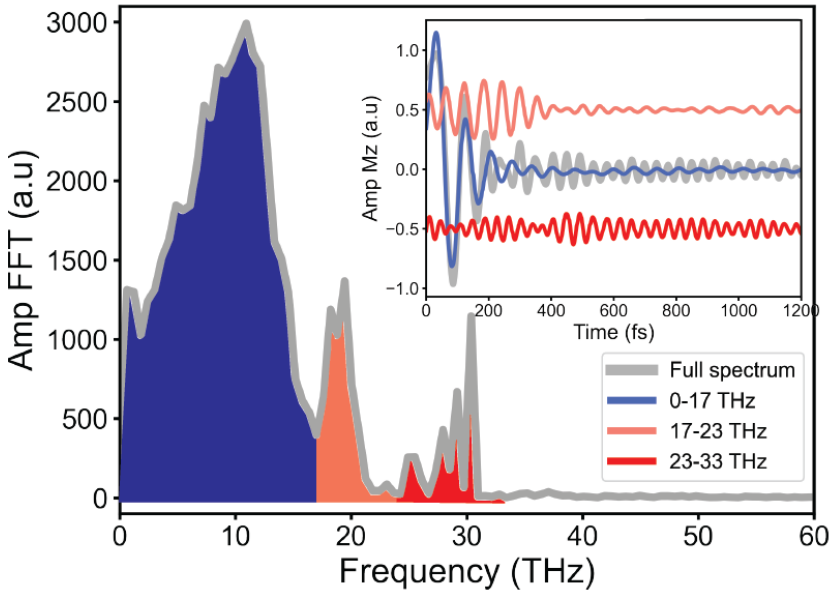


Figure 6.10: The spectrum of the spin wave oscillation at the bimeron core centre.

6.3 Analysis of annihilation

6.3.1 Spin wave spectrum

The annihilation of non-trivial bimeron is exotic because of the collective spin-wave emission, which is not found in the trivial case. With the aid of our simulation tools, we elucidate the dynamic behaviour of the topological structures with time and three-dimensional spin information.

Supposing a tiny detector is placed at the centre of the bimeron structure, all three-dimensional spin vectors can be recorded as time evolves. From a series of 'movie' pictures in Figure 6.9, we can find that the small cluster of spins at the centre oscillates in all directions. Here we only plot the oscillation in the z direction and analyse the spectrum based on the time-dependent spin oscillation in the z direction, since the other two trends show similar behavior, except for finally damping into the XY plane. The grey curve describes the M_z oscillation of the atom located at the bimeron centre in Figure 6.10. The temporal oscillation of $M_z(t)$ is shown in the inset plot and the spectrum is obtained by Fourier Transform on $M_z(t)$, offering a wide spectrum in the Terahertz frequency range up to 33 THz.

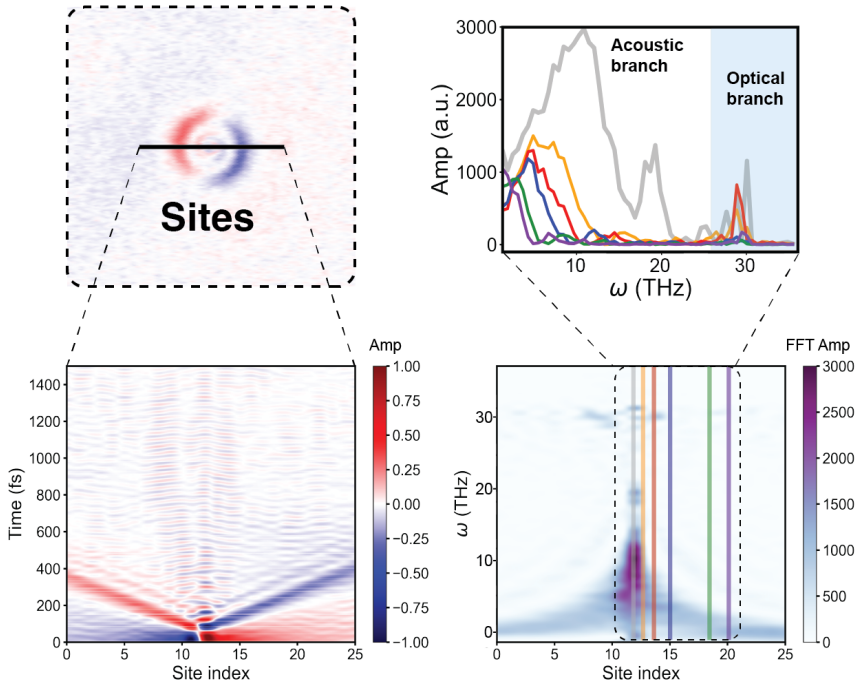


Figure 6.11: Real and reciprocal space analysis of spin waves at different atomic positions. The sites for research are chosen along the symmetric axis of the spin wave propagation direction. The heat map on the right demonstrates in-situ Fourier analysis. The spectrums' redshift is observed at these selected positions when moving away from the centre, as indicated by the zoomed line curves.

The full spectrum can be classified into three sections, shown in different colours. By applying a bandpass filter on the natural oscillation, we can replicate the temporal change for each frequency band, as indicated by Figure 6.10. The first two bands with blue and orange fillings correspond to the 0–17 THz and 17–23 THz frequencies, which can be converted to temporal curve through the inverse Fourier Transform. The amplitudes for these two bands have strong oscillation amplitudes in the initial 400 fs, then damped to zero. However, the temporal amplitude for higher band at 23–33 THz remains oscillating with no sign of decaying at first 1.2 ps. From the analysis of the inelastic neutron experiment [143], we are known that the first two subbands should be the acoustic branch and the last band should reside on the optical branch, judging by their frequency range only. Further evidence will be provided from the dispersion relations of these three bands (as discussed later in Figure6.12) that the higher frequency optical branch spin wave has a characteristic low group velocity.

Spatial dispersion effect

More sampling positions were chosen along the symmetric axis of the ring structures when the spin wave propagates, as shown in Figure 6.11. The heat map on the left indicates the temporal oscillations found at these positions, and the Fourier Transform of the temporal map are demonstrated on the right. The temporal map shows that the annihilation occurs around 100 fs (time zero is set earlier), and the bimeron structure is identified before destruction happens. The wave packet propagation is the direct evidence of acoustic magnon which ranges within 0–23 THz, as shown by Figure 6.10. The ripples identified in the temporal map are residual oscillations brought by the spin wave packet, which is contributed by the high-frequency part near 30 THz. The ripple-like oscillations consist of magnons from the optical branch, which have much smaller effective velocities than acoustic branch magnons, and thus exhibit stationary oscillations.

The frequency spectra are shown in by the right panel of Figure 6.11 and Figure 6.12 (b), with x coordinates in real space positions and reciprocal units ($k \cdot a$ is the product of wave vector k and lattice parameter a), respectively. Both frequency maps find the difference in propagation features for magnons from acoustic or optical modes.

From the frequency map for real space positions in Figure 6.11, the acoustic bands below 30 THz exhibit red-shift as moving the detection positions away from the centre. The zoom-out plot shows that the curves obtained at different positions exhibit a sizeable red shift from the low-frequency bands while the high-frequency band remains more or less unchanged. This red shift effect on the frequency band is only observed for low energy bands, indicating the modes from the acoustic branch has large group velocity.

On the other hand, the frequency map in reciprocal space, as shown in Figure 6.12 (b), depicts the behaviour of magnon dispersion relations. The white and blue solid lines are guidelines of acoustic and optical magnons from the analytical antiferromagnetic spin wave dispersion relations (will discuss later). By performing the 2D-Fourier transform for the (x, t) variable simultaneously, we can obtain the

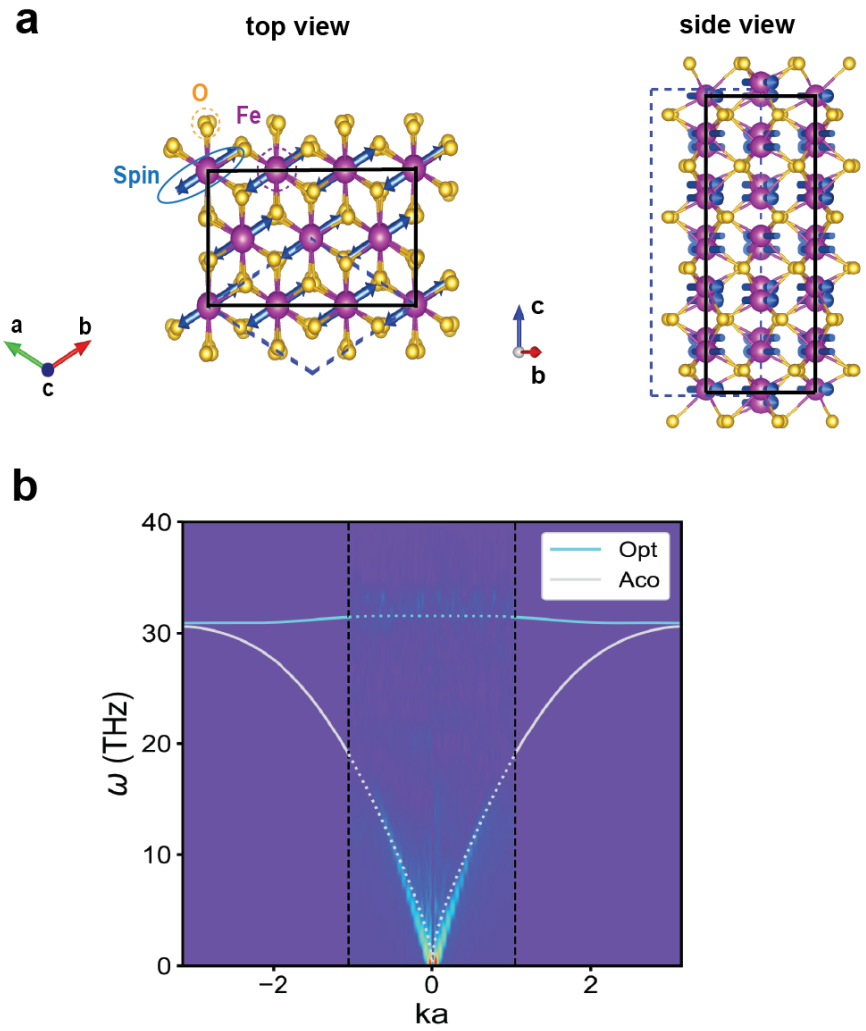


Figure 6.12: (a) The construction of the simulation unit cell by doubling the size of the unit cell on an orthogonal basis. (b) The Fourier transform of the temporal oscillations in reciprocal space is shown by a heat map guided by the dashed curve from the theoretical model.

reciprocal variables in (k, ω) space, which is the magnon dispersion relation. Here the x-tick is written in $k \cdot a$ (a is lattice parameter) for the purpose of indicating the Brillouin zone range of [-π, π]. The amplitudes of acoustic magnons are stronger when k is closer to 0, as guided by the white dashed lines, while the amplitudes of optical magnons are weak but average throughout $[-\frac{\pi}{3a}, \frac{\pi}{3a}]$ (shown by blue dashed line). As the data set of the spins for analysing consist of the spins from the same layer, which repeats three times longer than the nearest neighbours, thus the 'actual spin lattice' is $3a$ and the $k \cdot a$ truncates at $[-\frac{\pi}{3}, \frac{\pi}{3}]$, as shown in Figure 6.12 black

line region. As the higher k region is so weak and folded into the Brillouin zone, they are no longer considered for simplicity.

The high intensity of the spin wave oscillation around Γ point indicates that the wave packet of the THz spectrum consists of many acoustic magnons, where large v_g means fast propagation. When k approaches the boundary at $-\frac{\pi}{3a}, \frac{\pi}{3a}$, strong nonlinearity of the v_g for the acoustic branch emerges, which is responsible for the spatial dispersion effect evidenced by the redshift of the low-frequency band.

6.3.2 Dispersion model

Dispersion relation for magnons in hematite

To prove that the spatial dispersion effect is induced by the nonlinearity of the acoustic magnon dispersion, we need to determine the magnon dispersion relationship for further discussion. First, we have to derive the dispersion relationship of spin waves in terms of normal modes associated with the isotropic Heisenberg spin Hamiltonian. The Heisenberg spin Hamiltonian for collinear spins in two sub-systems with antiferromagnetic alignment is constructed as [148]

$$\mathcal{H} = -\sum_{nn'jj'} J_{nn'jj'} \boldsymbol{S}_{n,j} \boldsymbol{S}_{n'j'} - \mu_B \sum_{nj} g_{nj} \cdot H_{A_{nj}} \cdot S^z_{nj} \tag{6.1}$$

The sum runs over the unit cells n, n' and the sublattices j, j'. $J_{nn'jj'}$ denotes the exchange interaction constant between spins $\boldsymbol{S}_{nj}$ and $\boldsymbol{S}_{n'j'}$ at sites nj and $n'j'$. The g_{nj} refers to the spectroscopic splitting factor for the spins at site nj. $H_{A_{nj}}$ is the effective anisotropy field at the site nj assumed to be directed along the z-axis of the local magnetic moment. The anisotropy term here differs from the phenomenological anisotropy $-k \cdot S_z^2$, which highlights the spin orientation to the crystal lattice; it is based on the mean-field approximation of the internal magnetic field, analogous to the form of Zeeman energy.

The excited states of Hamiltonian described above are expressed in terms of normal modes, which follow the procedures provided by Saenz and Wallace[149, 150]. A matrix T is derived from the Fourier transform of the exchange constants

in the Hamiltonian, and the eigenvalues of this matrix determine the energy of the normal modes.

Here, we only give the expressions of the energy dispersion, and the procedures of diagonalisation of the Hamiltonian in equation 6.1 is not shown in detail:

$$E(k) = \sqrt{P \pm \sqrt{R}} \tag{6.2}$$

where $\pm$ represents the optical and acoustic branch, and P and R consist of four types of exchange density constants A, B, C and D,

$$P = A^2 + DD^* - BB^* - C^2$$
$$R = 4(AD - BC)(AD^* - B^*C) + (BD^* - B^*D)^2$$

where the A, B, C and D are derived from elements of matrix $T_{kjj'}$, as given by the equation (A 2b) in [148], which are composed of a series of travelling waves

$$A = -2SJ_4(-h_A + (r + 3p - (3s - 6)))$$
$$B = -2SJ_4(r + p(e^{-i\mathbf{k}\cdot\mathbf{t_1}} + e^{-i\mathbf{k}\cdot\mathbf{t_2}} + e^{-i\mathbf{k}\cdot\mathbf{t_3}})) \cdot e^{-i\mathbf{k}\cdot(\mathbf{r_1}-\mathbf{r_2})}$$
$$C = -2SJ_4(e^{i\mathbf{k}\cdot\mathbf{t_1}} + e^{i\mathbf{k}\cdot\mathbf{t_2}} + e^{i\mathbf{k}\cdot\mathbf{t_3}} + e^{i\mathbf{k}\cdot(\mathbf{t_1}+\mathbf{t_2})} + e^{i\mathbf{k}\cdot(\mathbf{t_2}+\mathbf{t_3})} + e^{i\mathbf{k}\cdot(\mathbf{t_3}+\mathbf{t_1})}) \cdot e^{-i\mathbf{k}(\mathbf{r_1}-\mathbf{r_3})}$$
$$D = -2SJ_4s(e^{i\mathbf{k}\cdot\mathbf{t_1}} + e^{i\mathbf{k}\cdot\mathbf{t_2}} + e^{i\mathbf{k}\cdot\mathbf{t_3}}) \cdot e^{-i\mathbf{k}\cdot(\mathbf{r_3}-\mathbf{r_2})}$$

$h_A = \mu_B g H_A / 2SJ_4$, J_4, r, p, s are defined in Table 6.1, $\boldsymbol{t}_1, \boldsymbol{t}_2, \boldsymbol{t}_3$ are translation vectors of rhombohedral lattice and $\boldsymbol{r}_1, \boldsymbol{r}_2, \boldsymbol{r}_3, \boldsymbol{r}_4$ are positions of magnetic ions defined in Table 6.1, with constraint of $\boldsymbol{r}_1 - \boldsymbol{r}_2 = \boldsymbol{r}_3 - \boldsymbol{r}_4$ and $\boldsymbol{r}_1 - \boldsymbol{r}_3 = \boldsymbol{r}_2 - \boldsymbol{r}_4$.

Here we constrained the wave vector in 1-dimension along the $\boldsymbol{t_1}$ direction, regarded as the wavefront propagation direction. The $\omega(k) = \frac{E(k)}{\hbar}$ dispersion curves depicted from eq 6.2 is shown in Figure 6.13 (a), in which the energy unit is transformed into frequency, and only the first Brillouin Zone (BZ) is indicated. The acoustic and optical branches are labelled by blue and red curves. The excitation frequency for the optical branch is around 29 THz. At the same time, the acoustic branch modes cover the frequency range from zero to the maximum at the Brillouin zone boundary, where the two branches coincide.

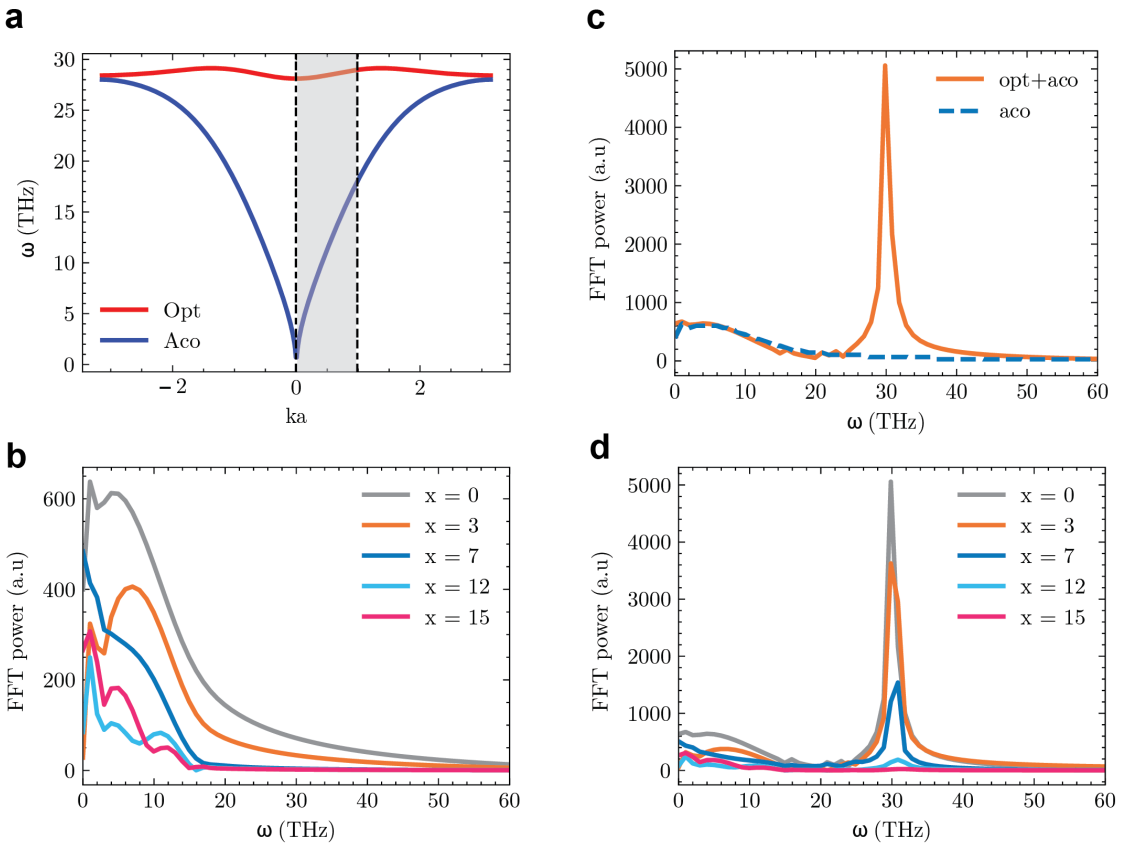


Figure 6.13: The magnon dispersion in antiferromagnetic hematite. **a**. Magnon dispersion relations established from neighbouring exchange interactions. The grey filling region highlights the plane waves consisting of the wave packet. **b**. The spectra of the wave packet composed of only acoustic modes in different positions away from the centre. **c**. The spectrum power contributed by acoustic magnons (blue dash curve) and entire branch magnons (solid orange curve) within $K = [0,1]$. **d**. The spectrum evolution of the modes contributed from acoustic and optical branches in different positions.

Spatial dispersion effect on plane wave packet

From the information in Figure 6.12 (b), the spin waves with significant amplitudes are those near the Γ point, where k covers from $[-\frac{\pi}{3a}, \frac{\pi}{3a}]$. Considering the propagation in one direction with positive k vector only, we assume that there is a wave packet consisting of a group of plane waves with k vectors within the grey-filled area in Figure 6.13 (a). The contribution from the acoustic or optical branch should behave differently since each branch's group velocities are not the same.

First, the wave packet is constructed based on a group of normalised Gaussian pulses at the same wave vector k_0 centralised at x_0. The expression in real space

and its reciprocal version can be written as:

$$f(x) = e^{-\frac{1}{2}(\frac{x-x_0}{\sigma_x})^2} e^{ik_0 x} \Longleftrightarrow \widetilde{f}(k) = \frac{1}{\sqrt{2\pi}\sigma_k} e^{-\frac{1}{2}(\frac{k-k_0}{\sigma_k})^2} e^{-ix_0(k-k_0)}$$

where $\sigma_k = \frac{1}{\sigma_x}$ and σ_x is the spatial width of the pulse. When the wave packet moves in a simple non-dispersive medium, the new position of the Gaussian wavefront x can be found at $x - vt$, where $\omega(k) = vk$ leading to the wavefront $A_{k_0}(x,t)$ expressed as:

$$\begin{aligned} A_{k_0}(x,t) &= \int e^{ik(x-vt)} \widetilde{f}(k) dk = \int e^{i(kx-\omega(k)t)} \widetilde{f}(k) dk \\ &= f(x-vt) = e^{-\frac{1}{2}(\frac{x-(x_0+vt)}{\sigma_x})^2} e^{ik_0(x-vt)} \end{aligned}$$

By including wave packets with a series of wave vectors k_n within the range $[-K, K]$, under the same assumption of non-dispersion, the wavefront can be extended into:

$$A(x,t) = \sum_n A_{k_n}(x,t) = \sum_n e^{-\frac{1}{2}(\frac{x-(x_0+v^n t)}{\sigma_x})^2} e^{ik_n(x-v^n t)} \tag{6.3}$$

A more general scenario requires the travelling wave propagating in dispersive media, where $\omega(k)$ is modulated by high dispersion into $\omega(k) = v_p k_0 + v_g(k-k_0) + \frac{1}{2}\Gamma(k-k_0)^2$. The $v_p = \frac{\omega(k)}{k}|_{k=k_0}$, $v_g = \omega'(k)|_{k=k_0}$ and $\Gamma = \omega''(k)|_{k=k_0}$ are phase velocity, group velocity and high order dispersion, respectively. Wave packet in eq 6.3 can thus be re-written by considering high-order dispersion in $\omega(k)$:

$$A(x,t) = \sum_{k_n} A_n(x,t) = \sum_{k_n} e^{-\frac{1}{2}\left(\frac{x-(x_0+\omega'(k_n)t)}{\sigma_x^2 - i\omega''(k_n)t}\right)^2} e^{ik_n x} e^{-ik_n t(\frac{\omega(k_n)}{k_n} - \omega'(k_n))} \tag{6.4}$$

This equation gives the mathematical form of wave packets composed of Gaussian plane waves within a specific range of reciprocal space $[-K, K]$ under the magnon dispersion $\omega(k)$. By uniformly distributing the wave vectors in the acoustic/optical branch indicated by the grey-filling area in Figure 6.13 (a), we can replicate the spin waves found in the bimeron annihilation in Figure 6.11, as shown by Figure 6.13 (c). In particular, the first two bands in 0–23 THz range can be recreated by plane waves in the acoustic branch, while the last high-frequency band around 30 THz is from the optical branch. The trial wave packet comprises 100 magnon modes evenly distributed within $ka = [0, 1]$. The obtained spectrum is indicated in the

blue dashed line in Figure 6.13 (c) if they are acoustic only. However, if additional magnon modes are chosen at the optical branch, another peak emerges around 30 THz, as shown in the orange curve in panel (c). The spectra amplitudes in Figure 6.13 (c) are determined by the density of modes included in the wave packet, which can further be optimised for an improved fitting of the simulation result.

Furthermore, the spatial dispersion effect in Figure 6.11 can also be explained by eq 6.4. The redshift of the spectra in Figure 6.11 at different positions away from the bimeron centre is recreated by Figure 6.13 (b). This indicates the significant dispersion effect in acoustic magnons. As for the modes from an optical branch, the resulting high-frequency spectra around 30 THz do not exhibit an apparent frequency shift, which matches the simulation result in Figure 6.11.

This simple phenomenological model based on magnon dispersion can describe the non-trivial bimeron annihilation process with good agreement, again emphasising the significance of magnon dispersion relation in describing the spin wave.

6.3.3 Topological charge transition

The magnon dispersive model has analysed the non-trivial bimeron annihilation behaviours in reciprocal space. However, this phenomenon has not been studied in topological space yet. Before examining the topological charge change versus time, it is necessary to establish the mathematical process of the topological charge in the discretised spin-lattice. We take the discretisation method of the lattice spin field proposed by Berg *et al.* [151] to calculate the topological charge value within the simulation box. The discretisation version of continuous topological charge definition in eq1.22 is shown as:

$$Q = \sum_{x^*} q(x^*) = \sum_{x^*} \frac{1}{4\pi} (\sigma A(s_x^*, s_i, s_j) + \sigma A(s_x^*, s_j, s_k)) \tag{6.5}$$

where $\sigma A(s_i, s_j, s_k)$ denotes the signed area of the spherical triangle with corners s_i, s_j, s_k , which definition can be found in Appendix II. By applying the eq6.5 on the sampling area when iterating all the vertices of the lattice grids, the global charge can be obtained by dividing the total signed area of a surface by 4π.

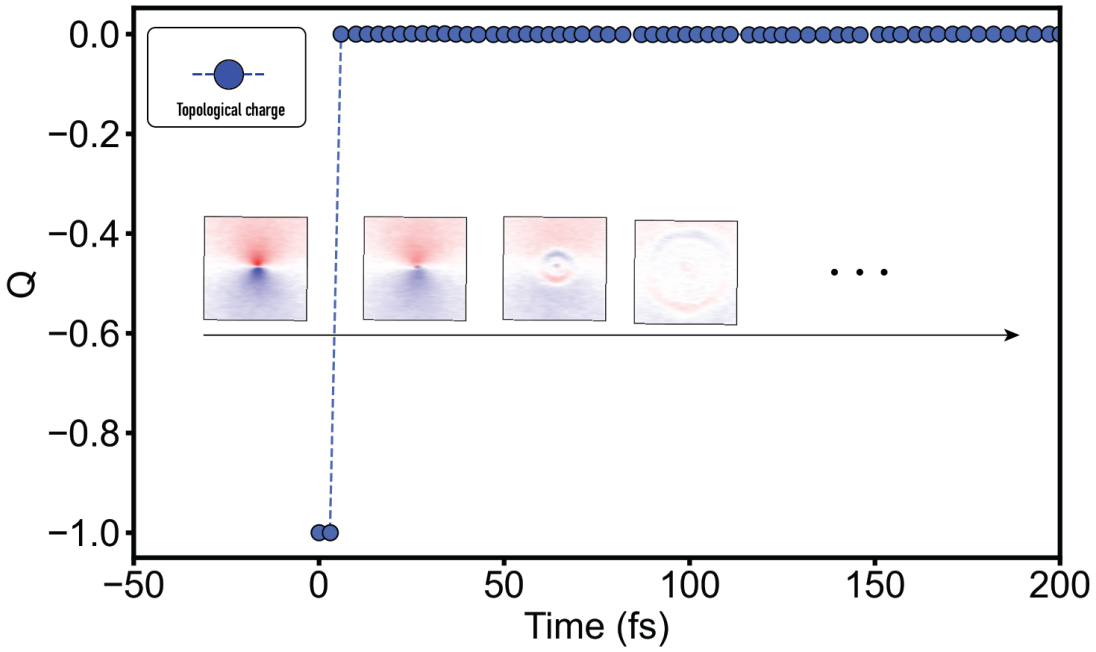


Figure 6.14: Time evolution of topological charge. The Q charge change from -1 to zero by a cliffy step in the initial 50 fs and remains at 0 as the spin wave propagates. The subplots of spin textures plotted by M_z shows the bimeron destruction and the spin wave propagation within the same time range.

A short time ranging up to 200 fs is chosen for describing the annihilation case. When calculating the charge across the surface by fully covering the bimeron area and the spin wave packet region, as the dynamics continue, we can obtain the Q-t plot, as shown in Figure 6.14. The blue dashed line shows a step-wise transition from -1 to 0 occurs in less than 10 fs. From the M_z plot above the arrow (indicating the timeline), an insignificant change occurs within a small area located at the bimeron centre, destroying the charge. Once the transition happens, the global zero charge is maintained during the spin wave propagation period and is irreversible.

This topological charge transition is intriguing and scarce reports have been found for antiferromagnetic spin textures. The time for such transition is less than 10 fs, as a result of the data export parameters when the time step for LLG dynamics is 0.1 fs. As Hertel and Schneider [152] reported in vortex/anti-vortex annihilation, the vortex and antivortex pair with opposite polarisation centres, giving burst-like emission of spin waves, which matches the bimeron case in our model. Nevertheless, the argument of the formation of Bloch point (BP) acting as the spin wave bursting

is not found in bimeron annihilation. Furthermore, the disappearance of topological charge remains puzzling in the two-dimensional spin-lattice. It is highly possible that the charge may be transferred to the longitudinal direction of the lattice, where a three-dimensional topological structure can be constructed.

6.4 Conclusion

In this chapter, we introduce the atomistic micromagnetic simulation tool named VAMPIRE and its basic parametrisation principles. We construct a micromagnetic model from emperical parameters that is verified suitable for antiferromagnetic simulation. Various physical properties, such as Néel and Morin transitions, are simulated with good agreement on experiment results. On that basis, we find two topological structure annihilation modes generated from different mechanisms. In the Morin transition, we find that the meron/antimeron pair demonstrates zero topological charges and annihilates without the emission of waves. On the other hand, in the Néel quenching scenario, we find the emergence of bimeron, which is finally destructed by emitting spin waves. We analyse this spin wave emission from various dimensions, for instance, in time, frequency and topology degrees. The spin wave spectrum generated from non-trivial bimeron annihilation covers the 'window' of the Terahertz range to tens of THz. This could be extremely useful to be developed into next-generation spintronic THz source. A phenomenological model based on the antiferromagnetic magnon dispersion is established, which describes the dynamical behaviour of the spin wave with good agreement. Finally, we investigate the topological relationships between bimerons and spin waves. An irreversible topological charge transition from integer to zero is observed in a short time.

7
Conclusion and outlook

To conclude, I have presented my experimental studies on two functional magnetic iron oxide systems, single crystals of $Ba_{0.5}Sr_{1.5}Mg_2Fe_{12}O_{22}$ (BSMFO) and an α-Fe_2O_3 thin film incorporated into a magnetic heterostructure. The overarching theme of this work is to understand the magnetic orders and structures at length scales of nanometers, as well as the dynamical behaviours of these magnetic objects under external fields. The long-term motivation is that the understanding developed in this work will eventually lead to the development of novel magnetic memory devices utilising the magnetic orders of these systems.

In chapter 3, I systematically study the Y-type hexaferrite compound through multiple techniques. Magnetometry was used to construct the most detailed magnetic phase diagram of a Y-type hexaferrite studied to date and enabled us to identify the metamagnetic phases of BSMFO during switching. Magnetocurrent measurements were performed to confirm that BSMFO was indeed magnetoelectric at low temperatures. However, the poor insulating properties of our Y-type single crystal samples prevented us from directly establishing whether the high-temperature phases were polar. We found an incommensurate propagation vector characterised at the zero field phase. All field-induced phases were modulated commensurately with the crystallographic lattice, consistent with the known magnetic fan structures of the Y-type hexaferrite. Following phase identification, the switching model based on

the changing magnetic structure factor hypothesis is established. Taking advantage of the sensitivities to resonant X-ray diffraction from different magnetic orders, the intermediate phases can be distinguished from RXMS and SQUID magnetometry data when performing the switchings. Combining all these data, a new block model with modifications between intermediate phases proportion has been established.

Following the static switching studies on Y-type hexaferrite BSMFO, we move forward to the short-time scale switchings at the extreme condition in chapter 4. I developed a complicated experimental setup by combining a single-cycle THz source with soft X-ray radiation at the synchrotron beamline station. The difficulty of obtaining high-power THz output and the pump/probe beam alignment were overcome by two cycles of beam time. Although not in an ultrafast time scale, the preliminary results did prove that the THz field can switch the multiferroic magnetic domains. This preliminary results boost our confidence in finally achieving the ultrafast magnetic domain manipulation by ultra-short asymmetric THz light in the future when even-shorter probes, such as free-electron-based X-ray pulses, become feasible.

Chapter 5 develops the AFM imaging technique using XMLD-based X-ray photoemission electron microscopy, especially the vector map method for imaging in-plane Néel vectors. This technique allowed us to observe an unprecedented group of topological structures in the antiferromagnetic system, such as merons, anti-merons and bimerons, in antiferromagnetic α-Fe_2O_3 system. These topological textures can be potentially used for fabricating magnetic memory devices, profiting from the property of topological stability resistant to small external perturbations. Additionally, the vector-mapping technique demonstrated in this chapter could have a wide range of applications in the study of the magnetic domain structures of spintronic devices that feature an antiferromagnetic layer.

Finally, in the last chapter, I continue the study of topological structures in antiferromagnets further into microscopic and ultrafast scale by the atomistic micromagnetic simulation tool VAMPIRE. The Landau-Lifshitz-Gilbert dynamics

reveal the generation and annihilation of the topological meron and bimeron structures sharing the same theory background as experimentally discovered structures. Assisted with an atomistic spin resolution, the topological meron/antimeron into different groups by topological charge number can be readily classified. It is also found that the spin wave emission can only be generated from non-trivial topological structures. This ultrafast process could be highly insightful for application on antiferromagnetic spintronic devices and magnonic resonators.

Appendices

A

Theory of magnetic diffraction

Magnetic resonant diffraction is widely applied in probing magnetic signals in ferromagnetic or antiferromagnetic systems by different effects such as circular dichroism or linear dichroism. Magnetic diffraction is sensitive to the polarisation states of the X-ray photons. The scattering cross-section commonly describes the absorption of incident X-rays with a particular polarisation state. The magnetic contribution in the total cross-section, which results from the magnetic structure factor, can be utilised as a good description of the magnetic structures.

The enhancement of X-ray magnetic scattering intensity arising from electric multipole transition is called resonant magnetic scattering, which can be understood by the atomic picture that electrons are excited to a virtual energy level and fall back to the ground state along with significant absorption of incident photons. Following the conventions by Hannon *et al.* [81, 153], with electric dipole (E_1) approximation, the resonant scattering amplitude on a single n^{th} magnetic ion is formulated as

$$\begin{aligned} f_{nE_1}^{RXMS} =& [F^{(0)}(\boldsymbol{\epsilon}\cdot\boldsymbol{\epsilon'}) - iF^{(1)}(\boldsymbol{\epsilon}\times\boldsymbol{\epsilon'})\cdot\boldsymbol{m_n} \\ &+ F^{(2)}(\boldsymbol{\epsilon'}\cdot\boldsymbol{m_n})(\boldsymbol{\epsilon}\cdot\boldsymbol{m_n})] \end{aligned} \tag{A.1}$$

where $F^{(0)}$, $F^{(1)}$ and $F^{(2)}$ are factors obtained from the atomic structure of the magnetic ion, $\boldsymbol{\epsilon}$ and $\boldsymbol{\epsilon'}$ are polarisation vectors of the incident and scattered photons, $\boldsymbol{m_n}$ is the single ion magnetic structure factor which is proportional to the spin

density. The first term arises from the Thomson scattering, independent of the magnetic moment. In contrast, the second and third terms are sensitive to the magnetic component orthogonal to the scattering plane and the moments within the scattering plane. Expressing the cross-section of scattering into 2×2 matrix form in Poincaré representation, which is adopted convention experimentally, we can obtain the scattering intensity in four channels formed by linear polarisation combinations of the incident and scattered light:

$$I(\boldsymbol{K}, \boldsymbol{P}, \eta) \propto tr[\hat{\boldsymbol{D}}(\eta) \cdot \hat{\boldsymbol{M}}(\boldsymbol{K}) \cdot \hat{\boldsymbol{\rho}}(\boldsymbol{P}) \cdot \hat{\boldsymbol{M}}(\boldsymbol{K})^{\dagger}] \tag{A.2}$$

where the scattering intensity is the dot product of incident polarisation matrix $\hat{\boldsymbol{\rho}}$, magnetic structure factor $\hat{\boldsymbol{M}}$ and its Hermitian, and polarisation analyser matrix $\hat{\boldsymbol{D}}$ which is formed as

$$\hat{\boldsymbol{D}}(\eta) = \begin{bmatrix} \cos^2(\eta) & -\sin(\eta)\cos(\eta) \\ -\sin(\eta)\cos(\eta) & \sin^2(\eta) \end{bmatrix} \tag{A.3}$$

where η is the angle of the analyser. And the polarisation matrix is given as

$$\hat{\boldsymbol{\rho}} = \frac{1}{2}(\boldsymbol{I} + \boldsymbol{P} \cdot \boldsymbol{\sigma}) \tag{A.4}$$

where $\boldsymbol{I}$ is the identity matrix and $\boldsymbol{P} = (P_1, P_2, P_3)$ gives the Poincaré-Stokes representation of the polarisation and $\boldsymbol{\sigma}$ is the vector of the Pauli matrices.

Taking single spin ferromagnetic structure as an example, the magnetic structure vector $\boldsymbol{M} = (M_1, M_2, M_3)$ can be Fourier transformed into magnetic moment density $\boldsymbol{M}(\boldsymbol{K}) = \sum_n e^{i\boldsymbol{K}\cdot\boldsymbol{r_n}} m_n$ in K space by neglecting Thomson scattering, we can derive the magnetic structure factor matrix for single ferromagnetic moment vector, which can further be extended to a more general magnetic structure:

$$\begin{aligned} \hat{\boldsymbol{M}}(\boldsymbol{K}) &= \begin{bmatrix} M_{\sigma\sigma} & M_{\sigma\pi} \\ M_{\pi\sigma} & M_{\pi\pi} \end{bmatrix} = \\ -iF^{(1)} &\begin{bmatrix} 0 & M_1\cos\theta + M_3\sin\theta \\ M_3\sin\theta - M_1\cos\theta & -M_2\sin 2\theta \end{bmatrix} \\ +F^{(2)} &\begin{bmatrix} M_2^2 & -M_2(M_1\sin\theta - M_3\cos\theta) \\ M_2(M_1\sin\theta + M_3\cos\theta) & -\cos^2\theta(M_1^2\tan^2\theta + M_3^2) \end{bmatrix} \end{aligned} \tag{A.5}$$

where 2θ is the scattering angle for scattering vector $\boldsymbol{K}$. In this regard, the resonant magnetic scattering intensity concerning an arbitrary incident polarisation for a

general magnetic structure can be mathematically established in this frame by further considering the complex Fourier components of magnetic structure factors.

B

Calculation of topological number in lattice spin field

In the continuum condition, the topological charge Q of a three dimension normalised spin field $\boldsymbol{s}(x)$, is defined by the equation:

$$Q = \frac{1}{4\pi} \int d^2 x s \cdot (\partial_1 \boldsymbol{s} \times \partial_2 \boldsymbol{s}) \tag{B.1}$$

which is the number of times $\boldsymbol{s}(x)$ winds around the sphere S^2. On the other hand, a lattice spin field $\boldsymbol{s}(x)$ can be regarded as a net composed of vertices x encompassing S^2, the times of encircling are defined by Q.

To discretise the continuum spin field, a spin-lattice structure is established with spins ordering at lattice points. A simple diagram for describing a 2D lattice with random ordering is depicted by a plaquette model in Figure B.1: Therefore, a sublattice consisting of vertices x^* commensurated with the original spin-lattice reduces the continuum form of topological structure into:

$$Q = \sum_{x^*} q(x^*) \tag{B.2}$$

where the topological density $q(x^*)$ attached to the vertex x^* is a function of four spins at the corner $\boldsymbol{s}_i|_{i=1,2,3,4}$ circulating x^*:

$$q(x^*) = \frac{1}{4\pi} \{(\sigma A)(\boldsymbol{s}_1, \boldsymbol{s}_2, \boldsymbol{s}_3) + (\sigma A)(\boldsymbol{s}_1, \boldsymbol{s}_3, \boldsymbol{s}_4)\} \tag{B.3}$$

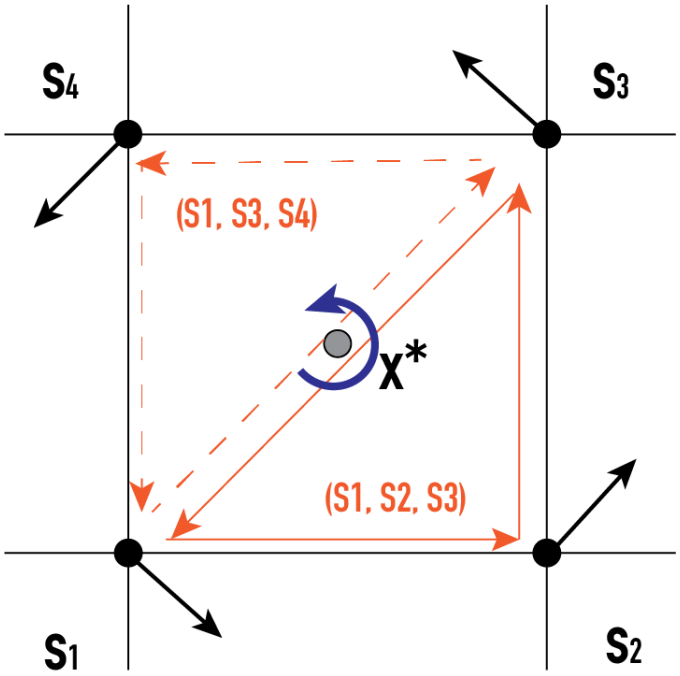


Figure B.1: A simplified model for 2D spin lattice in plaquette geometry centerlised at vertex x^* with corners labelled by $\boldsymbol{s}_i$. The spherical triangles composed by different paths are highlighted by orange color which areas are the elementary units for calculating topological charge.

Here, $(\sigma A)(\boldsymbol{s}_1, \boldsymbol{s}_2, \boldsymbol{s}_3)$ denotes the signed area of the spherical triangle with corner index $\boldsymbol{s}_i|_{i=1,2,3}$. The explicit expression for $(\sigma A)(\boldsymbol{s}_1, \boldsymbol{s}_2, \boldsymbol{s}_3)$ is obtained from the area of spherical triangle A plus a well-defined sign σ at non-exceptional points, following the convention defined by Berg [151]

$$A = \alpha_1 + \alpha_2 + \alpha_3 - \pi \tag{B.4}$$

where $\alpha_i|_{i=1,2,3}$ are angles of a spherical triangle, and

$$\sigma = sign[\boldsymbol{s}_1 \cdot (\boldsymbol{s}_2 \times \boldsymbol{s}_3)] = \pm 1 \tag{B.5}$$

when $A \neq 0, 2\pi$. The signed area of $\Omega = \sigma A$ can be calculated by expressing in polar coordinate by [154]:

$$exp(i\frac{\Omega(\boldsymbol{s}_1, \boldsymbol{s}_2, \boldsymbol{s}_3)}{2}) = \rho^{-1}[1 + \boldsymbol{s}_1 \cdot \boldsymbol{s}_2 + \boldsymbol{s}_2 \cdot \boldsymbol{s}_3 + \boldsymbol{s}_1 \cdot \boldsymbol{s}_3 + i\boldsymbol{s}_1 \cdot (\boldsymbol{s}_2 \times \boldsymbol{s}_3)] \tag{B.6}$$

where

$$\rho = [2(1 + \boldsymbol{s}_1 \cdot \boldsymbol{s}_2)(1 + \boldsymbol{s}_2 \cdot \boldsymbol{s}_3)(1 + \boldsymbol{s}_1 \cdot \boldsymbol{s}_3)]^{\frac{1}{2}}$$

The signed area Ω is, therefore, the phase in the imaginary part obtained from eq.B.6:

$$\tan\left(\frac{\Omega(\boldsymbol{s}_1, \boldsymbol{s}_2, \boldsymbol{s}_3)}{2}\right) = \frac{\boldsymbol{s}_1 \cdot (\boldsymbol{s}_2 \times \boldsymbol{s}_3)}{1 + \boldsymbol{s}_1 \cdot \boldsymbol{s}_2 + \boldsymbol{s}_2 \cdot \boldsymbol{s}_3 + \boldsymbol{s}_1 \cdot \boldsymbol{s}_3} \tag{B.7}$$

References

[1] Philip W Anderson. *Basic notions of condensed matter physics*. CRC Press, 2018.

[2] Steven M Girvin and Kun Yang. *Modern condensed matter physics*. Cambridge University Press, 2019.

[3] Paul M Chaikin, Tom C Lubensky, and Thomas A Witten. *Principles of condensed matter physics*. Vol. 10. Cambridge university press Cambridge, 1995.

[4] K. v. Klitzing, G. Dorda, and M. Pepper. "New Method for High-Accuracy Determination of the Fine-Structure Constant Based on Quantized Hall Resistance". In: *Physical Review Letters* 45 (6 Aug. 1980), pp. 494–497.

[5] Seongshik Oh. "The Complete Quantum Hall Trio". In: *Science* 340.6129 (2013), pp. 153–154.

[6] Xufeng Kou, Yabin Fan, and Kang L. Wang. "Review of Quantum Hall Trio". In: *Journal of Physics and Chemistry of Solids* 128 (2019). Spin-Orbit Coupled Materials, pp. 2–23.

[7] Philip W Anderson. "More is different: broken symmetry and the nature of the hierarchical structure of science." In: *Science* 177.4047 (1972), pp. 393–396.

[8] Harold Y Hwang et al. "Emergent phenomena at oxide interfaces". In: *Nature Materials* 11.2 (2012), pp. 103–113.

[9] Wilma Eerenstein, ND Mathur, and James F Scott. "Multiferroic and magnetoelectric materials". In: *nature* 442.7104 (2006), pp. 759–765.

[10] Nicola A Hill. "Why are there so few magnetic ferroelectrics?" In: *The journal of physical chemistry B* 104.29 (2000), pp. 6694–6709.

[11] BK Ponomarev et al. "Magnetoelectric properties of some rare earth molybdates". In: *Ferroelectrics* 161.1 (1994), pp. 43–48.

[12] Nicola A Spaldin. "Multiferroics: Past, present, and future". In: *MRS bulletin* 42.5 (2017), pp. 385–390.

[13] Nicola A Spaldin and Manfred Fiebig. "The renaissance of magnetoelectric multiferroics". In: *Science* 309.5733 (2005), pp. 391–392.

[14] JF Scott. "Multiferroic memories". In: *Nature Materials* 6.4 (2007), pp. 256–257.

[15] Manuel Bibes and Agnès Barthélémy. "Towards a magnetoelectric memory". In: *Nature Materials* 7.6 (2008), pp. 425–426.

[16] Fumihiro Matsukura, Yoshinori Tokura, and Hideo Ohno. "Control of magnetism by electric fields". In: *Nature nanotechnology* 10.3 (2015), pp. 209–220.

[17] Daniel Khomskii. "Trend: Classifying multiferroics: Mechanisms and effects". In: *Physics* 2 (2009), p. 20.

[18] DN Astrov. "The magnetoelectric effect in antiferromagnetics". In: *Sov. Phys. JETP* 11.3 (1960), pp. 708–709.

[19] VJ Folen, GT Rado, and EW Stalder. "Anisotropy of the magnetoelectric effect in Cr_2O_3". In: *Physical Review Letters* 6.11 (1961), p. 607.

[20] James R Teague, Robert Gerson, and William Joseph James. "Dielectric hysteresis in single crystal $BiFeO_3$". In: *Solid State Communications* 8.13 (1970), pp. 1073–1074.

[21] Izabela Sosnowska, T Peterlin Neumaier, and E Steichele. "Spiral magnetic ordering in bismuth ferrite". In: *Journal of Physics C: Solid State Physics* 15.23 (1982), p. 4835.

[22] T Zhao et al. "Electrical control of antiferromagnetic domains in multiferroic $BiFeO_3$ films at room temperature". In: *Nature Materials* 5.10 (2006), pp. 823–829.

[23] F Zavaliche et al. "Multiferroic $BiFeO_3$ films: domain structure and polarization dynamics". In: *Phase transitions* 79.12 (2006), pp. 991–1017.

[24] D. Lebeugle et al. "Electric-Field-Induced Spin Flop in $BiFeO_3$ Single Crystals at Room Temperature". In: *Physical Review Letters* 100 (22 June 2008), p. 227602.

[25] Claude Ederer and Nicola A Spaldin. "Weak ferromagnetism and magnetoelectric coupling in bismuth ferrite". In: *Physical Review B* 71.6 (2005), p. 060401.

[26] Nicola A Spaldin, Sang-Wook Cheong, and Ramamoorthy Ramesh. "Multiferroics: Past, present, and future". In: *Phys. Today* 63.10 (2010), pp. 38–43.

[27] T Kimura et al. "Magnetic control of ferroelectric polarization". In: *Nature* 426.6962 (2003), pp. 55–58.

[28] N Hur et al. "Electric polarization reversal and memory in a multiferroic material induced by magnetic fields". In: *Nature* 429.6990 (2004), pp. 392–395.

[29] Sang-Wook Cheong and Maxim Mostovoy. "Multiferroics: a magnetic twist for ferroelectricity". In: *Nature Materials* 6.1 (2007), pp. 13–20.

[30] Maxim Mostovoy. "Ferroelectricity in spiral magnets". In: *Physical Review Letters* 96.6 (2006), p. 067601.

[31] Hosho Katsura, Naoto Nagaosa, and Alexander V Balatsky. "Spin current and magnetoelectric effect in noncollinear magnets". In: *Physical Review Letters* 95.5 (2005), p. 057205.

[32] Tsuyoshi Kimura. "Magnetoelectric hexaferrites". In: *Annu. Rev. Condens. Matter Phys.* 3.1 (2012), pp. 93–110.

[33] IE Dzyaloshinskii. "Theory of helicoidal structures in antiferromagnets. I. Nonmetals". In: *Sov. Phys. JETP* 19.4 (1964), pp. 960–971.

[34] Tôru Moriya. "Anisotropic superexchange interaction and weak ferromagnetism". In: *Physical Review* 120.1 (1960), p. 91.

[35] Vilmos Kocsis et al. "Magnetization-polarization cross-control near room temperature in hexaferrite single crystals". In: *Nature Communications* 10.1 (2019), pp. 1–7.

[36] Hajime Sagayama et al. “Two distinct ferroelectric phases in the multiferroic Y-type hexaferrite $Ba_2Mg_2Fe_{12}O_{22}$”. In: *Physical Review B* 80.18 (2009), p. 180419.

[37] Jiangping Hu. “Microscopic origin of magnetoelectric coupling in noncollinear multiferroics”. In: *Physical Review Letters* 100.7 (2008), p. 077202.

[38] S. Picozzi et al. “Dual Nature of Improper Ferroelectricity in a Magnetoelectric Multiferroic”. In: *Physical Review Letters* 99 (22 Nov. 2007), p. 227201.

[39] Ivan A. Sergienko, Cengiz Şen, and Elbio Dagotto. “Ferroelectricity in the Magnetic E-Phase of Orthorhombic Perovskites”. In: *Physical Review Letters* 97 (22 Nov. 2006), p. 227204.

[40] T. Kimura, J. C. Lashley, and A. P. Ramirez. “Inversion-symmetry breaking in the noncollinear magnetic phase of the triangular-lattice antiferromagnet $CuFeO_2$”. In: *Physical Review B* 73 (22 June 2006), p. 220401.

[41] S. Seki, Y. Onose, and Y. Tokura. “Spin-Driven Ferroelectricity in Triangular Lattice Antiferromagnets $A\mathrm{CrO}_2$ (A = Cu, Ag, Li, or Na)”. In: *Physical Review Letters* 101 (6 Aug. 2008), p. 067204.

[42] A Kohn et al. “The antiferromagnetic structures of $IrMn_3$ and their influence on exchange-bias”. In: *Scientific Reports* 3.1 (2013), pp. 1–7.

[43] Louis Néel. “Some New Results on Antiferromagnetism and Ferromagnetism”. In: *Rev. Mod. Phys.* 25 (1 Jan. 1953), pp. 58–63.

[44] C. G. Shull, W. A. Strauser, and E. O. Wollan. “Neutron Diffraction by Paramagnetic and Antiferromagnetic Substances”. In: *Phys. Rev.* 83 (2 July 1951), pp. 333–345.

[45] I. Dzyaloshinsky. “A thermodynamic theory of “weak” ferromagnetism of antiferromagnetics”. In: *Journal of Physics and Chemistry of Solids* 4.4 (1958), pp. 241–255.

[46] Toru Moriya. “Anisotropic Superexchange Interaction and Weak Ferromagnetism”. In: *Phys. Rev.* 120 (1 Oct. 1960), pp. 91–98.

[47] John MD Coey. *Magnetism and magnetic materials*. Cambridge university press, 2010.

[48] D. C. Tsui, H. L. Stormer, and A. C. Gossard. “Two-Dimensional Magnetotransport in the Extreme Quantum Limit”. In: *Physical Review Letters* 48 (22 May 1982), pp. 1559–1562.

[49] Barry Simon. “Holonomy, the Quantum Adiabatic Theorem, and Berry’s Phase”. In: *Physical Review Letters* 51 (24 Dec. 1983), pp. 2167–2170.

[50] Christian Back et al. “The 2020 skyrmionics roadmap”. In: *Journal of Physics D: Applied Physics* 53.36 (2020), p. 363001.

[51] Wataru Koshibae and Naoto Nagaosa. “Theory of antiskyrmions in magnets”. In: *Nature Communications* 7.1 (2016), pp. 1–8.

[52] Ajaya K Nayak et al. “Magnetic antiskyrmions above room temperature in tetragonal Heusler materials”. In: *Nature* 548.7669 (2017), pp. 561–566.

[53] Wataru Koshibae and Naoto Nagaosa. “Creation of skyrmions and antiskyrmions by local heating”. In: *Nature Communications* 5.1 (2014), pp. 1–11.

[54] JJ Liang et al. “Magnetic field gradient driven dynamics of isolated skyrmions and antiskyrmions in frustrated magnets”. In: *New Journal of Physics* 20.5 (2018), p. 053037.

[55] Ulrike Ritzmann et al. “Trochoidal motion and pair generation in skyrmion and antiskyrmion dynamics under spin–orbit torques”. In: *Nature Electronics* 1.8 (2018), pp. 451–457.

[56] Lorenzo Camosi et al. “Micromagnetics of antiskyrmions in ultrathin films”. In: *Physical Review B* 97.13 (2018), p. 134404.

[57] Xichao Zhang et al. “Control and manipulation of a magnetic skyrmionium in nanostructures”. In: *Physical Review B* 94.9 (2016), p. 094420.

[58] Alexander G Kolesnikov et al. “Skyrmionium–high velocity without the skyrmion Hall effect”. In: *Scientific Reports* 8.1 (2018), pp. 1–8.

[59] Sai Li et al. “Dynamics of a magnetic skyrmionium driven by spin waves”. In: *Applied Physics Letters* 112.14 (2018), p. 142404.

[60] Marco Finazzi et al. “Laser-induced magnetic nanostructures with tunable topological properties”. In: *Physical Review Letters* 110.17 (2013), p. 177205.

[61] Shilei Zhang et al. “Real-space observation of skyrmionium in a ferromagnet-magnetic topological insulator heterostructure”. In: *Nano letters* 18.2 (2018), pp. 1057–1063.

[62] Shi-Zeng Lin, Avadh Saxena, and Cristian D Batista. “Skyrmion fractionalization and merons in chiral magnets with easy-plane anisotropy”. In: *Physical Review B* 91.22 (2015), p. 224407.

[63] YA Kharkov, OP Sushkov, and M Mostovoy. “Bound states of skyrmions and merons near the Lifshitz point”. In: *Physical Review Letters* 119.20 (2017), p. 207201.

[64] A Tan et al. “Topology of spin meron pairs in coupled Ni/Fe/Co/Cu (001) disks”. In: *Physical Review B* 94.1 (2016), p. 014433.

[65] Xichao Zhang, Motohiko Ezawa, and Yan Zhou. “Magnetic skyrmion logic gates: conversion, duplication and merging of skyrmions”. In: *Scientific Reports* 5.1 (2015), pp. 1–8.

[66] Kêitsiro Aizu. “Possible species of ferromagnetic, ferroelectric, and ferroelastic crystals”. In: *Physical Review B* 2.3 (1970), p. 754.

[67] VK Wadhawan. “Introduction to Ferroic Materials Gordon and Breach”. In: *Sci. Pub., Amsterdam* (2000).

[68] GF Nataf et al. “Domain-wall engineering and topological defects in ferroelectric and ferroelastic materials”. In: *Nature Reviews Physics* 2.11 (2020), pp. 634–648.

[69] Pankaj Sharma, Peggy Schoenherr, and Jan Seidel. “Functional ferroic domain walls for nanoelectronics”. In: *Materials* 12.18 (2019), p. 2927.

[70] Jan Seidel. “Domain walls as nanoscale functional elements”. In: *The Journal of Physical Chemistry Letters* 3.19 (2012), pp. 2905–2909.

[71] Gustau Catalan et al. “Domain wall nanoelectronics”. In: *Reviews of Modern Physics* 84.1 (2012), p. 119.

[72] Ekhard KH Salje. "Multiferroic domain boundaries as active memory devices: trajectories towards domain boundary engineering". In: *ChemPhysChem* 11.5 (2010), pp. 940–950.

[73] Stuart SP Parkin, Masamitsu Hayashi, and Luc Thomas. "Magnetic domain-wall racetrack memory". In: *Science* 320.5873 (2008), pp. 190–194.

[74] Donghwa Lee et al. "Mixed Bloch-Néel-Ising character of 180 ferroelectric domain walls". In: *Physical Review B* 80 (6 Aug. 2009), p. 060102.

[75] Hendrik A Kramers and Werner Heisenberg. "Über die streuung von strahlung durch atome". In: *Zeitschrift für Physik* 31.1 (1925), pp. 681–708.

[76] Paul Adrien Maurice Dirac. "The quantum theory of dispersion". In: *Proceedings of the Royal Society of London. Series A, Containing Papers of a Mathematical and Physical Character* 114.769 (1927), pp. 710–728.

[77] G. Breit. "Quantum Theory of Dispersion". In: *Reviews of Modern Physics* 4 (3 July 1932), pp. 504–576.

[78] WP Healy. "A generalization of the Kramers-Heisenberg dispersion formula". In: *Physical Review A* 16.4 (1977), p. 1568.

[79] WP Healy and RG Woolley. "On the derivation of the Kramers-Heisenberg dispersion formula from non-relativistic quantum electrodynamics". In: *Journal of Physics B: Atomic and Molecular Physics* 11.7 (1978), p. 1131.

[80] M Blume. "Magnetic scattering of x rays". In: *Journal of Applied Physics* 57.8 (1985), pp. 3615–3618.

[81] JP Hill and DF McMorrow. "Resonant exchange scattering: polarization dependence and correlation function". In: *Acta Crystallographica Section A: Foundations of Crystallography* 52.2 (1996), pp. 236–244.

[82] URL: `https://www-ssrl.slac.stanford.edu/dichroism/md.html`.

[83] J Stöhr et al. "Element-specific magnetic microscopy with circularly polarized X-rays". In: *Science* 259.5095 (1993), pp. 658–661.

[84] Raju Kumar. *Characterization of X-ray anode and absorption edges*. Mar. 2018.

[85] URL: `https://www.diamond.ac.uk/Home/About.html`.

[86] URL: `https://leaps-initiative.eu/synchrotrons/`.

[87] Jens Als-Nielsen and Des McMorrow. *Elements of modern X-ray physics*. John Wiley & Sons, 2011.

[88] O Ernest, M Lawrence, and S Livingston. *The Production of High Speed Light Ions without the Use of High Voltages II Phys*. 1932.

[89] Werner Scholz et al. "Scalable parallel micromagnetic solvers for magnetic nanostructures". In: *Computational Materials Science* 28.2 (2003), pp. 366–383.

[90] Thomas Fischbacher et al. "A systematic approach to multiphysics extensions of finite-element-based micromagnetic simulations: Nmag". In: *IEEE Transactions on Magnetics* 43.6 (2007), pp. 2896–2898.

[91] Sidi Fu et al. "Finite-difference micromagnetic solvers with the object-oriented micromagnetic framework on graphics processing units". In: *IEEE Transactions on Magnetics* 52.4 (2015), pp. 1–9.

[92] Arne Vansteenkiste et al. “The design and verification of MuMax3”. In: *AIP advances* 4.10 (2014), p. 107133.

[93] Yutaro Kitagawa et al. “Low-field magnetoelectric effect at room temperature”. In: *Nature Materials* 9.10 (2010), pp. 797–802.

[94] OP Aleshko-Ozhevskiĭ et al. “Helicoidal antiphase spin ordering in hexagonal ferrites of the $BaSc_xFe_{12-x}O_{19}$(M) system”. In: *Soviet Journal of Experimental and Theoretical Physics* 28 (1969), p. 425.

[95] R. A. Sizov and K. N. Zaĭtsev. “Noncollinear spin ordering in a hexagonal ferrite of type W”. In: *Soviet Journal of Experimental and Theoretical Physics* 39 (July 1974), p. 175.

[96] U. Enz. “Megnetization Process of a Helical Spin Configuration”. In: *Journal of Applied Physics* 32.3 (Mar. 1961), S22–S26.

[97] Nobuyuki Momozawa and Yasuo Yamaguchi. “Field-Induced Commensurate Intermediate Phases in Helimagnet $(Ba_{1-x}Sr_x)_2Zn_2Fe_{12}O_{22}$ (x=0.748)”. In: *Journal of the Physical Society of Japan* 62.4 (Apr. 1993), p. 1292.

[98] Shintaro Ishiwata et al. “Low-Magnetic-Field Control of Electric Polarization Vector in a Helimagnet”. In: *Science* 319.5870 (Mar. 2008), p. 1643.

[99] E. Pollert. “Crystal chemistry of magnetic oxides part 2: Hexagonal ferrites”. In: *Progress in Crystal Growth and Characterization* 11.3 (1985), pp. 155–205.

[100] Nobuyuki Momozawa, Yasuo Yamaguchi, and Masaru Mita. “Magnetic structure change in $Ba_2Mg_2Fe_{12}O_{22}$”. In: *Journal of the Physical Society of Japan* 55.4 (1986), pp. 1350–1358.

[101] Nobuyuki Momozawa et al. “Magnetic Structure of $(Ba_{1-x}Sr_x)_2Zn_2Fe_{12}O_{22}$ (x= 0–1.0)”. In: *Journal of the Physical Society of Japan* 54.2 (1985), pp. 771–780.

[102] Nobuyuki Momozawa et al. “Cation Distribution and Helimagnetic Structure of the $Ba_2(Zn_{1-x}Mg_x)_2Fe_{12}O_{22}$ System as Revealed by Magnetization Measurements and Neutron Diffraction”. In: *Journal of the Physical Society of Japan* 70.9 (2001), pp. 2724–2732.

[103] Kun Zhai et al. “Giant magnetoelectric effects achieved by tuning spin cone symmetry in Y-type hexaferrites”. In: *Nature Communications* 8.1 (2017), pp. 1–8.

[104] Kouji Taniguchi et al. “Ferroelectric polarization reversal by a magnetic field in multiferroic Y-type hexaferrite $Ba_2Mg_2Fe_{12}O_{22}$”. In: *Applied Physics Express* 1.3 (2008), p. 031301.

[105] Charles Baldwin Sawyer and CH Tower. “Rochelle salt as a dielectric”. In: *Physical Review* 35.3 (1930), p. 269.

[106] DJ Kim et al. “Polarization relaxation induced by a depolarization field in ultrathin ferroelectric $BaTiO_3$ capacitors”. In: *Physical Review Letters* 95.23 (2005), p. 237602.

[107] JY Jo et al. “Polarization switching dynamics governed by the thermodynamic nucleation process in ultrathin ferroelectric films”. In: *Physical Review Letters* 97.24 (2006), p. 247602.

[108] JY Jo et al. “Domain switching kinetics in disordered ferroelectric thin films”. In: *Physical Review Letters* 99.26 (2007), p. 267602.

[109] Francis P Chmiel et al. "Magnetoelectric domains and their switching mechanism in a Y-type hexaferrite". In: *Physical Review B* 100.10 (2019), p. 104411.

[110] Kun Zhai et al. "Electric control of exchange bias in multiferroic hexaferrite $Ba_{0.4}Sr_{1.6}Mg_2Fe_{12}O_{22}$". In: *Physical Review B* 98.14 (2018), p. 144405.

[111] Chuankun Wang et al. "Magnetoelectric phase diagram and magnetic field-induced reversal of electric polarization in $Ba_{0.5}Sr_{1.5}Mg_{1.6}Co_{0.4}Fe_{12}O_{22}$ single crystal". In: *Journal of Alloys and Compounds* 886 (2021), p. 161266.

[112] H Hirori et al. "Single-cycle terahertz pulses with amplitudes exceeding 1 MV/cm generated by optical rectification in LiNbO 3". In: *Applied Physics Letters* 98.9 (2011), p. 091106.

[113] Martin van Exter, Ch. Fattinger, and D. Grischkowsky. "Terahertz time-domain spectroscopy of water vapor". In: *Opt. Lett.* 14.20 (Oct. 1989), pp. 1128–1130.

[114] Felix Büttner, Ivan Lemesh, and Geoffrey SD Beach. "Theory of isolated magnetic skyrmions: From fundamentals to room temperature applications". In: *Scientific Reports* 8.1 (2018), pp. 1–12.

[115] Xichao Zhang et al. "Skyrmion-electronics: writing, deleting, reading and processing magnetic skyrmions toward spintronic applications". In: *Journal of Physics: Condensed Matter* 32.14 (2020), p. 143001.

[116] Julie Grollier et al. "Neuromorphic spintronics". In: *Nature Electronics* 3.7 (2020), pp. 360–370.

[117] Takashi Kurumaji et al. "Skyrmion lattice with a giant topological Hall effect in a frustrated triangular-lattice magnet". In: *Science* 365.6456 (2019), pp. 914–918.

[118] Olivier Boulle et al. "Room-temperature chiral magnetic skyrmions in ultrathin magnetic nanostructures". In: *Nature Nanotechnology* 11.5 (2016), pp. 449–454.

[119] Constance Moreau-Luchaire et al. "Additive interfacial chiral interaction in multilayers for stabilization of small individual skyrmions at room temperature". In: *Nature Nanotechnology* 11.5 (2016), pp. 444–448.

[120] Anjan Soumyanarayanan et al. "Tunable room-temperature magnetic skyrmions in Ir/Fe/Co/Pt multilayers". In: *Nature Materials* 16.9 (2017), pp. 898–904.

[121] XZ Yu et al. "Transformation between meron and skyrmion topological spin textures in a chiral magnet". In: *Nature* 564.7734 (2018), pp. 95–98.

[122] Kai Litzius et al. "Skyrmion Hall effect revealed by direct time-resolved X-ray microscopy". In: *Nature Physics* 13.2 (2017), pp. 170–175.

[123] Joseph Barker and Oleg A Tretiakov. "Static and dynamical properties of antiferromagnetic skyrmions in the presence of applied current and temperature". In: *Physical Review Letters* 116.14 (2016), p. 147203.

[124] Takaaki Dohi et al. "Formation and current-induced motion of synthetic antiferromagnetic skyrmion bubbles". In: *Nature Communications* 10.1 (2019), pp. 1–6.

[125] FJ Morin. "Magnetic susceptibility of α Fe_2O_3 and α Fe_2O_3 with added titanium". In: *Physical Review* 78.6 (1950), p. 819.

[126] P. J. Besser, A. H. Morrish, and C. W. Searle. "Magnetocrystalline Anisotropy of Pure and Doped Hematite". In: *Physical Review* 153 (2 Jan. 1967), pp. 632–640.

[127] J M D Coey and George Sawatzky. "A study of hyperfine interactions in the system $(Fe_{1-x}Rh_x)_2O_3$ using the Mossbauer effect (Bonding parameters)". In: *Journal of Physics C: Solid State Physics* 4 (Mar. 2001), p. 2386.

[128] Hariom Jani et al. "Reversible hydrogen control of antiferromagnetic anisotropy in α-Fe_2O_3". In: *Nature Communications* 12.1 (2021), pp. 1–10.

[129] BT Thole, G Van Der Laan, and PH Butler. "Spin-mixed ground state of Fe phthalocyanine and the temperature-dependent branching ratio in X-ray absorption spectroscopy". In: *Chemical physics letters* 149.3 (1988), pp. 295–299.

[130] Christian Brouder. "Angular dependence of X-ray absorption spectra". In: *Journal of Physics: Condensed Matter* 2.3 (1990), p. 701.

[131] Maurizio Sacchi, Oumar Sakho, and Giorgio Rossi. "Strong dichroism in the Dy 3d→ 4f x-ray absorption at Dy/Si (111) interfaces". In: *Physical Review B* 43.1 (1991), p. 1276.

[132] MW Haverkort et al. "Magnetic versus crystal-field linear dichroism in NiO thin films". In: *Physical Review B* 69.2 (2004), p. 020408.

[133] Elke Arenholz et al. "Anisotropic x-ray magnetic linear dichroism at the Fe $L_2$3 edges in Fe_3O_4". In: *Physical Review B* 74.9 (2006), p. 094407.

[134] Hariom Jani et al. "Antiferromagnetic half-skyrmions and bimerons at room temperature". In: *Nature* 590.7844 (2021), pp. 74–79.

[135] Sebastian Mühlbauer et al. "Skyrmion lattice in a chiral magnet". In: *Science* 323.5916 (2009), pp. 915–919.

[136] XZ Yu et al. "Real-space observation of a two-dimensional skyrmion crystal". In: *Nature* 465.7300 (2010), pp. 901–904.

[137] Naoto Nagaosa and Yoshinori Tokura. "Topological properties and dynamics of magnetic skyrmions". In: *Nature Nanotechnology* 8.12 (2013), pp. 899–911.

[138] Shivaji Lal Sondhi et al. "Skyrmions and the crossover from the integer to fractional quantum Hall effect at small Zeeman energies". In: *Physical Review B* 47.24 (1993), p. 16419.

[139] Liang Fu, Charles L Kane, and Eugene J Mele. "Topological insulators in three dimensions". In: *Physical review letters* 98.10 (2007), p. 106803.

[140] David Hsieh et al. "Observation of unconventional quantum spin textures in topological insulators". In: *Science* 323.5916 (2009), pp. 919–922.

[141] M Zahid Hasan and Charles L Kane. "Colloquium: topological insulators". In: *Reviews of modern physics* 82.4 (2010), p. 3045.

[142] Xiao-Liang Qi and Shou-Cheng Zhang. "The quantum spin Hall effect and topological insulators". In: *Physics Today* 63 (2010), pp. 1–33.

[143] EJ Samuelsen and G Shirane. "Inelastic neutron scattering investigation of spin waves and magnetic interactions in α-Fe2O3". In: *physica status solidi (b)* 42.1 (1970), pp. 241–256.

[144] Romain Lebrun et al. "Long-distance spin-transport across the Morin phase transition up to room temperature in ultra-low damping single crystals of the antiferromagnet α-Fe_2O_3". In: *Nature Communications* 11.1 (2020), pp. 1–7.

[145] José Luis García-Palacios and Francisco J. Lázaro. "Langevin-dynamics study of the dynamical properties of small magnetic particles". In: *Phys. Rev. B* 58 (22 Dec. 1998), pp. 14937–14958.

[146] D. A. Garanin. "Fokker-Planck and Landau-Lifshitz-Bloch equations for classical ferromagnets". In: *Phys. Rev. B* 55 (5 Feb. 1997), pp. 3050–3057.

[147] Jun Miyawaki et al. "Dzyaloshinskii-Moriya interaction in $\alpha-Fe_2O_3$ measured by magnetic circular dichroism in resonant inelastic soft x-ray scattering". In: *Phys. Rev. B* 96 (21 Dec. 2017), p. 214420.

[148] EJ Samuelsen. "Spin waves in antiferromagnets with corundum structure". In: *Physica* 43.3 (1969), pp. 353–374.

[149] Albert W Sáenz. "Spin Waves in Exchange-Coupled Complex Magnetic Structures and Neutron Scattering". In: *Physical Review* 125.6 (1962), p. 1940.

[150] Duane C Wallace. "Spin waves in complex lattices". In: *Physical Review* 128.4 (1962), p. 1614.

[151] B Berg and Martin Lüscher. "Definition and statistical distributions of a topological number in the lattice O (3) σ-model". In: *Nuclear Physics B* 190.2 (1981), pp. 412–424.

[152] Riccardo Hertel and Claus M. Schneider. "Exchange Explosions: Magnetization Dynamics during Vortex-Antivortex Annihilation". In: *Phys. Rev. Lett.* 97 (17 Oct. 2006), p. 177202.

[153] M Blume and Doon Gibbs. "Polarization dependence of magnetic x-ray scattering". In: *Physical Review B* 37.4 (1988), p. 1779.

[154] Mathias Augustin et al. "Properties and dynamics of meron topological spin textures in the two-dimensional magnet $CrCl_3$". In: *Nature Communications* 12.1 (2021), pp. 1–9.